LIÈGE université
Sciences Appliquées

Stochastic Multiscale Modeling and Analysis of Polymer-Based Materials

A thesis submitted in partial fulfillment of the requirements
for the degree of Doctor of Philosophy (PhD) in Engineering Science

by

Juan Manuel CALLEJA VÁZQUEZ

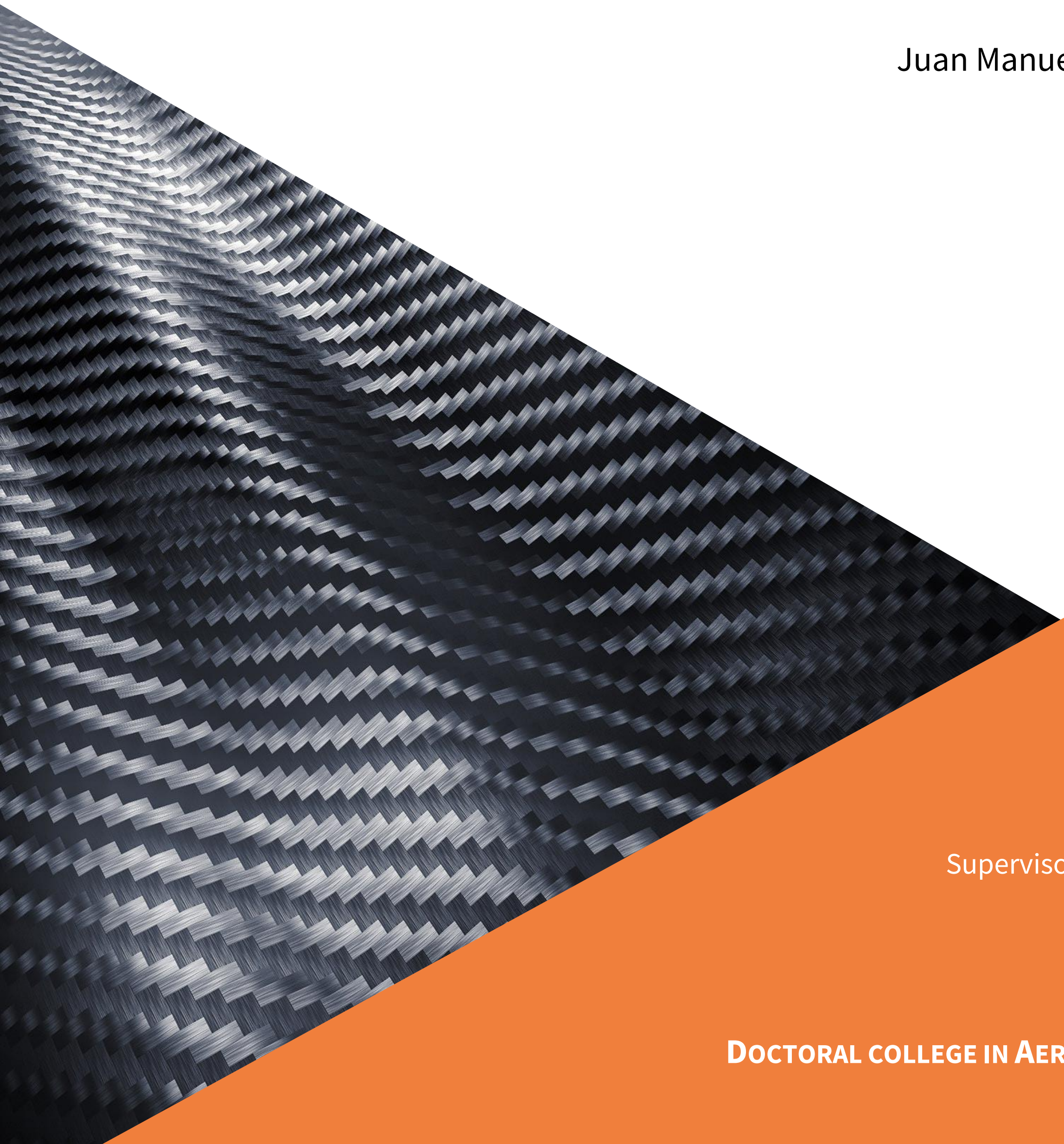

Supervisor: Ludovic NOELS

DOCTORAL COLLEGE IN AEROSPACE AND MECHANICS

FEBRUARY 2024

“*You see things; and you say 'Why?'*
But I dream things that never were; and I say 'Why not?' ”

George Bernard Shaw

UNIVERSITY OF LIÈGE

Abstract

Faculty of Applied Sciences
Aerospace and Mechanical Engineering Department

Doctor in Engineering Sciences

Stochastic Multiscale Modeling and Analysis of Polymer-Based Material

by Juan Manuel CALLEJA VÁZQUEZ

This Work focuses on the accurate and efficient modeling of polymer materials. In a first step, the large strain hyperelastic phenomenological constitutive model proposed by V.D. Nguyen et al. for the modeling of highly nonlinear, rate-dependent amorphous glassy polymers at isothermal conditions is enhanced with the introduction of new strain dependent bulk and shear moduli stiffening terms. This addition, allows the correct modeling of the elastic stiffening exhibited by some polymer materials, such as semi-crystalline polymers at large strains. While being able to accurately capture the behavior of highly non-linear polymers, large strain models can become prohibitive for the modeling of composite materials due to their high computational cost. To that end, this Thesis introduces a, possibly damage-enhanced, pressure-dependent based incremental-secant mean-field homogenization (MFH) scheme for two-phase composites. The incremental-secant formulation consists on a fictitious unloading of the material up to a stress-free state, in which a residual stress is attained in its phases. Then the secant method is performed in order to compute the mean stress fields of each phase. One of the main advantages of this method is the natural isotropicity of the secant tensors that allows defining the linear-comparison-composite (LCC). In this Work, we show that this isotropic nature is preserved for a non-associated pressure dependent plastic flow, making possible the direct definition of the LCC. Through several comparisons against full-field simulations and an experimental test, it is shown the ability of this model to capture the behavior of uni-directional (UD) composites, while reducing the computational cost of the large strain model by several orders of magnitude. This was used as basis for a surrogate for nonlinear stochastic multiscale analyses of two-phase composites. The homogenized stochastic behavior of the UD composite material is first characterized through full-field simulations on stochastic volume elements (SVE) of the material microstructure. Then, in order to conduct the stochastic nonlinear multiscale simulations, the microscale problem is substituted by a MF-ROM, whose properties are identified by an inverse process from the full-field SVE realizations. Homogenized stress-strain curves are used for the identification process of the nonlinear range. However, a loss of size objectivity is encountered once the strain softening onset is reached. This problem is addressed by introducing a calibration of the energy release rate obtained with a nonlocal MFH micromechanical model, allowing to scale the variability found on each SVE failure characteristics to the macroscale. The obtained random effective properties are then used as input of a data-driven stochastic model to generate the random fields used to feed the stochastic MF-ROM. The MF-ROM is then verified through nonlocal stochastic finite element method (SFEM) simulations against an experimental test and full-field simulations. The introduced innovations allows to conduct stochastic studies on the failure characteristics of material samples without the need for costly experimental campaigns, paving the way for more complete and affordable virtual testing.

Acknowledgements

Today is a special day for me, as after five years of journeying through a path full of ups and downs, I have managed to reach the finish line. On this challenging road, I never felt alone; I always had company. That's why today I am filled with gratitude to all those who accompanied me:

- To the FNRS scholarship program, and to the Actions de recherche concertées 2017 financed by Direction Générale de l'Enseignement non obligatoire de la Recherche scientifique, Direction de la Recherche scientifique, Communauté Francaise de Belgique and granted by Academie Universitaire Wallonie-Europe for the tremendous financial support they provided, enabling me to carry out this thesis.

- To the University of Liege for shaping me and offering me countless opportunities, and to all the professors who played a part in my knowledge enrichment.

- To my supervisor, Professor Ludovic Noels, for being by my side, guiding me academically with his professionalism and experience. Without his guidance, advice, training, unwavering support, and patience when I needed it most, I wouldn't have accomplished this work.

- To my research unit colleagues, Dr. Ling Wu, Dr. Van-Dung Nguyen, Dr. Nanda Gopala, Dr. Kevin Spilker, Dr. Tianyu Zhang, Mr. Vinayak Gholap, Mr. Ujwal Kishore Junaga and Dr. Bac Nam Vu and thesis committee member Dr. Laurent Adam for giving me guidelines that allowed me to continue on the right direction and encouraged me not to give up.

- I would also like to sincerely thank the members of the jury, Prof. Ludovic Noels, Dr. Ling Wu, Prof. Issam Doghri, Prof. Julien Yvonnet, Dr. Laurent Adam and Prof. Frédéric Collin for their agreement to be part of the jury for my PhD defense.

- To my friends and colleagues, because they were always there, sharing doubts, joys, and sorrows with me. Thank you for putting up with me and always providing encouragement.

- To my parents, for being by my side during those tough days and nights. Thank you for believing in me, for the advice and values you instilled in me, and for giving me understanding, affection, and love.

- To my grandparents, who have always kept me in their thoughts and prayers. They've been the embodiment of the hard work and courage I needed for this thesis. They taught me that with diligence and honesty, one can achieve anything.

I would also like to thank all those who will support me in the future. Because I look to tomorrow with optimism, and I know I'll always have a friendly hand to lean on.

Contents

List of Figures

List of Tables

List of Abbreviations

1W-SMP	**O**ne- **W**ay **S**hape **M**emory **P**olymer
2W-SMP	**T**wo- **W**ay **S**hape **M**emory **P**olymer
BC	**B**oundary **C**ondition
BVP	**B**oundary **V**alue **P**roblems
CMC	**C**eramic **M**atrix **C**omposites
DMA	**D**ynamic **M**echanical **A**nalysis
DMN	**D**eep **M**aterial **N**etwork
EDEAM	**E**lement-based **E**mpirical **A**pproximation **M**ethod
EP	**E**lasto- **P**lastic
FE	**F**inite **E**lement
FEM	**F**inite **E**lement **M**ethod
FFT	**F**ast **F**ourier **T**ransform
FSHP	**F**ast **S**tatistical **H**omogenization **P**rocedure
GSC	**G**eneralized **S**elf- **C**onsistent
LCC	**L**inear **C**omparison **C**omposite
MFH	**M**ean **F**ield **H**omogenization
MF-ROM	**M**ean **F**ield **R**educed **O**rder **M**odel
NN	**N**eural **N**etwork
NTFA	**N**onuniform **T**ransformation **F**ield **A**nalysis
NTFA-TSO	**N**onuniform **T**ransformation **F**ield **A**nalysis- **T**angent **S**econd- **O**rder
PBC	**P**eriodic **B**oundary **C**ondition
PO	**P**lastic **O**nset
RNN	**R**ecurrent **N**eural- **N**etwork
ROM	**R**educed **O**rder **M**odel
RVE	**R**epresentative **V**olume **E**lement
SEM	**S**canning **E**lectron **M**icroscope
SFEM	**S**tochastic **F**inite **E**lement **M**ethod
SMA	**S**hape **M**emory **A**lloys
SMP	**S**hape **M**emory **P**olymers
SVE	**S**tochastic **V**olume **E**lement
UD	**U**ni **D**irectional
VCFEM	**V**oronoi **C**ell **F**inite **E**lement **M**ethod
VEM	**V**irtual **E**lement **M**ethod

Chapter 1

Introduction

Since the first Wright Flyer flight in December 17th, 1903, the aeronautical sector has not stopped the search for faster, more efficient and safer flights. Over the years, the aeronautical sector has made great advancements in technology and safety, where material science has been a crucial part of this evolution. New materials have allowed for unimaginable weight reductions which directly translate into more efficiency, more payload capabilities and more design flexibility. However, with more than 46 million airline flights and 4.5 billion passengers worldwide per year (IATA, 2021), safety of transported people as well as flown over is paramount, and therefore, material and structural integrity is closely regulated. To this end, the airworthiness authorities such as the European aviation safety agency (EASA), the Federal aviation administration (FAA) or the international civil aviation organization (ICAO) impose a large certification campaign for the introduction of new materials in which the materials are tested under a wide variety of situations. These certifications follow what is called the building-block tests approach, also called pyramid of tests (Brunner, Alderliesten, and Pascoe, 2023; Division, 2017; Poulton, 2009) (see Fig. 1.1). The airworthiness authorities state that new technologies must be at least as safe as the already existing technologies, which means the introduction of new materials is always accompanied by a large and expensive testing campaign for thorough material properties and variability characterization.

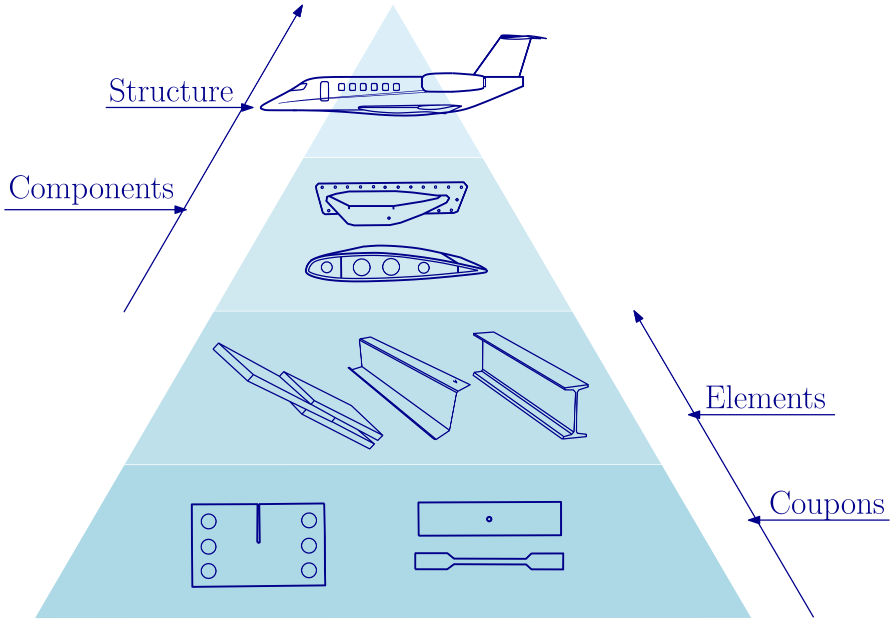

FIGURE 1.1: Aeronautical pyramid of tests. Brunner, Alderliesten, and Pascoe (2023)

With the search of the minimum weight to strength ratio, metallic materials have set themselves as the king of materials for aeronautical structures over many decades. However, this homogeneity has been disrupted by the introduction of composite materials. As an example, the A350 XWB has a composite material composition of more than 50% of the total materials used for its construction (Poulton, 2017). This disruption is caused by the many advantages of these materials over traditional metals and alloys, such as the lack of fatigue, lack of corrosion, low density and ability to tailor the properties in different directions by means of different combinations of plies. Nonetheless, these advantages do not come without some disadvantages that present a challenge to the industry, such as complex failure modes or scattered properties that can directly impact the structural integrity of the aircraft. While metals were mostly standardized, due to the highly tailoring possibilities of composites, which would technically allow for an infinite number of combinations, it is quite common for each company to end up developing a unique material system with a specific manufacturing process. This leads to a lack of standardization and therefore to longer and more complex testing campaigns. For this reason, the scientific and the industrial communities have realized that nondeterminism is a major issue which affects structural and material performance and reliability. One source of uncertainties is at the material level itself and its mechanical properties. Since experimental characterization alone would require an excessive number of tests, there is an increasing interest in stochastic virtual testing.

The next generation of aircrafts could see the arrival of new smart materials. Such is the case of shape memory polymers (SMPs). SMPs have potential applications in the aeronautical industry due to their ability to deform and recover their original shape in response to an external stimulus, such as heat or light (Sharma and Srinivas, 2020). SMPs can be used to create wings that can change shape in-flight (known as morphing wings), allowing aircraft to optimize their aerodynamic performance at different speeds and altitudes. For example, researchers have developed SMP-based wing flaps that can adjust their shape and position to control airflow and reduce drag. Similarly, these materials could be introduced to create deployable structures, such as antenna reflectors or solar panels, that can be compactly stowed during launch and then deploy to their full size and shape in orbit (Squibb, 2023; Wilson et al., 2020; Santo et al., 2014). The polyvalence of these materials makes them interesting for other implementations, such as the creation of surfaces that prevent ice from forming, or to shed ice that has already formed, reducing the risk of ice-related accidents in flight, or as a matrix material in composite repairs, as they can be shaped to fit complex geometries and then cured to retain that shape. This could help to extend the lifespan of aircraft components and reduce maintenance costs.

1.1 High-crosslinked epoxies and their modeling

One of the most common materials used as matrix phase in the composition of fiber reinforced composite materials is epoxy, a group of thermoset polymers. Epoxy is a large family of resins that presents great mechanical properties while exhibiting low moisture absorption and good degradation resistance, which makes them attractive for aeronautical applications.

The epoxy materials present a viscous nature that allows the resin to impregnate the mesh of fibers used for the composite reinforcement, minimizing the amount of gas bubbles inside the composite after processing. In order to solidify the composite, what is called a curing process is performed. The curing process is a chemical reaction that generate crosslinks between different polymer molecules. These crosslinks attach the molecules one to another impeding their sliding as shown in Fig. 1.2 and therefore making the resin to become solid. Several levels of crosslinks can be achieved through this hardening process, being the epoxies with higher crosslink density the ones with higher structural strength. In aeronautics, high-crosslinked epoxy resins are commonly used due to their good structural properties.

Many experimental works, such as Boyce, Arruda, and Jayachandran (1994), Buckley et al. (1994), Chen, Lu, and Cheng (2002), Fiedler et al. (2001), Hine et al. (2005), Lesser and Kody (1997), Morelle, Pardoen, and Bailly (2015), or Mulliken and Boyce (2006), have shown

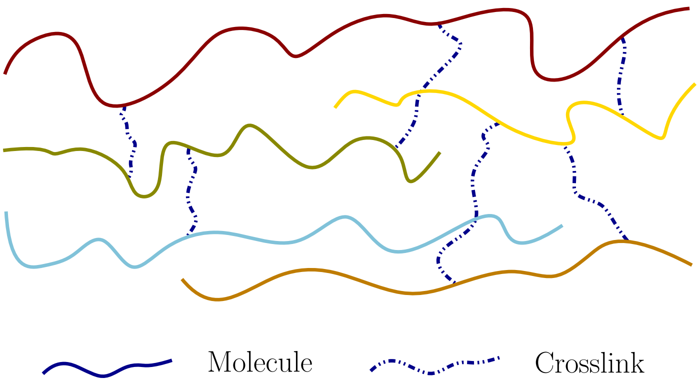

FIGURE 1.2: Representation of the molecules and crosslinks of a hardened epoxy.

that this amorphous glassy molecular composition of the epoxy makes its behavior quite complex, showing viscous behavior dependent on the deformation rate, dependency on temperature, and having a large difference between its tensile and compressive behaviors. One of the most noticeable differences is the higher peak values for compressive loadings when compared to the tensile ones, result of the hydro-static pressure dependency of these kind of materials. Different plastic stages can be observed in the strain-stress response of these materials. First, a plastic part is observed which leads to a first peak value, also called macro-yield point. Due to its amorphous glassy nature, at these strain deformations, molecules can be submitted to high internal loading provoking large modifications in their layout, and therefore, triggering plastic localization zones that appear as micro-shear bands. These bands propagate and create localization zones at the macro-structure, which for example in an experimental tensile test would be seen as a necking of the material sample. This micro-shear bands cause the apparition of a softening stage (Tomita and Adachi, 1997; Tomita and Lu, 2002; Lu and Ravi-Chandar, 1999; Morelle, Pardoen, and Bailly, 2015) in which the loading bearing capability of the material is reduced. Once this phenomenon stabilizes, the molecule chains start to slide and align themselves in the direction of highest positive strains causing an increase in the strain-stress curve at larger strain states before the final failure stage is reached. This phenomenon is generally called the rehardening stage. Polymers present a pressure-dependent behavior, which makes them tend to have higher peak stresses, failure stresses, and failure strains under compression than under tension at the same strain rate. Figure 1.3 shows the complete behavior of epoxy under compression. Most epoxies reach fracture before reaching the peak stress under tension (Fiedler et al., 2001; Morelle, Pardoen, and Bailly, 2015), so the softening and rehardening phenomena are not always present.

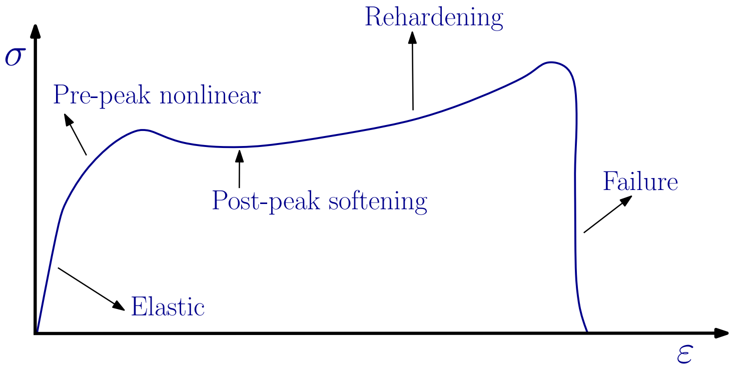

FIGURE 1.3: Schematic strain-stress behavior of an epoxy material under compression.

As already introduced, epoxy materials exhibit a high pressure dependency, making plasticity models based on the H. Tresca's (Tresca, 1864) or R. Von Mises'(Mises, 1913) yield criteria insufficient for their correct modeling. Pressure-sensitive models have been applied for decades, especially in the case of rock-like and porous materials. Some examples of basic pressure-dependent yield functions are the Mohr-Coulomb and the Drucker-Prager models. The Drucker-Prager model (Drucker and Prager, 1952) is one of the most recognized models inside the scientific community. This model is a generalization of the Mohr-Coulomb hypothesis and is based on the first and second invariants. When represented in the Haigh-Westergaard space, these pressure-dependent models differ from their pressure-insensitive counterparts in their cone-like shape (see Fig. 1.4), asymmetry introduced by the first invariant, that allows the modeling of the lower bearing capabilities of the material in tension than in a compressive stress state that present these pressure dependent materials.

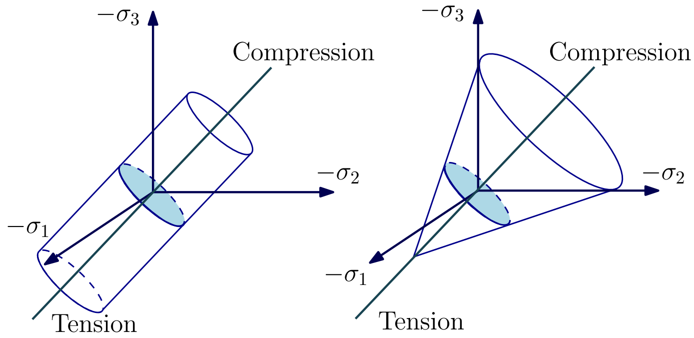

FIGURE 1.4: Representation of the Von Mises yield criterion on the right, and of the Drucker-Prager criterion on the right on the Haigh-Westergaard space.

Many of the plasticity models used nowadays derive from these basic models as for example the pressure-dependent model developed by Lee et al. (2021), which make use of the Drucker-Prager yield surface with a non-associated flow rule depending on the effective deviatoric stress and the hydrostatic stress, or the one used in the work by Cheng et al. (2015) which used a Drucker-Prager based pressure-dependent model into a limit analysis based on the bipotential theory in order to be able to implement the non-associated flow. Zhao et al. (2019) implemented this criterion in an incremental variational principle. The works by Guéry et al. (2008) and Shen et al. (2012) applied this yield model to homogenization techniques focused on the modeling of Callovo-Oxfordian argillites and clayey rocks respectively. The Modified Cam-Clay is another widely used model. This pressure-dependent plasticity model by Roscoe and Burland (Roscoe and Burland, 1968) forms a closed ellipsoid in the Haigh-Westergaard stress, which allows to avoid the theoretical complications that may be related to the Drucker-Prager model. It is widely used in the modeling of clay, as in the case of Islam and Gnanendran (2020), which developed a new yield surface based on this Modified Cam-Clay model with a non-associated flow rule-based elasto-viscoplastic model for isotropic clays. The work by Gao et al. (2011) focused on the modeling of pressure-dependent isotropic materials by introducing a yield surface which is a function of the hydrostatic stress as well as the second and third invariants of the stress deviator. The used plastic flow potential uses a similar definition to the yield surface, which also depends on the three stress invariants and three scalar parameters.

Due to the pressure-dependent nature of polymers, composite materials is a domain in which the use of asymmetric yield surfaces is very extended. Such is the case of Kaiser and Stommel (2014), which modelled pressure-dependency for short-fiber reinforced composites, or the model developed by Raghava, Caddell, and Yeh (1973), which is capable of accounting for pressure effects and differences in compressive and tensile yield strengths. This nonsymmetric yield surface was used in R. Balieu et al. (Balieu et al., 2013; Balieu et al., 2014). Similar to the Drucker-Prager criterion, this yield surface uses a critical combination of the first and the second invariant of the stress tensor in order to define plasticity. The tension-compression asymmetry found on this type of materials is modeled on this yield criterion by means of a parameter defined by its ratio. As polymers do not deform in an isochoric way, a non-associated viscoplastic potential flow depending on two parameters defining the volume variation for positive and negative hydrostatic pressures was used, allowing for an independent evolution of the positive and negative pressures. It appears that when considering a single-phase polymeric matrix, the Drucker-Prager yield criterion with a non-associated plastic flow is a widely used model by the research community and has been proven multiple-time to be successfully applied to many applications. This model was used in the works by Melro et al. (2013), Chevalier, Camanho, and Pardoen (2019) and V.D. Nguyen (Nguyen et al., 2016; Nguyen, Wu, and Noels, 2019). All these papers address the modeling of polymers used in composites and the obtained results were in good agreements with experiments.

Experiments on amorphous polymers indicate that the micro-structure of a polymer has a strong influence on the mechanical properties (Arruda, Boyce, and Jayachandran, 1995; G'Sell and Jonas, 1995; Zaïri, Woznica, and Naït-Abdelaziz, 2005), which means that these properties could change when used as matrix phase in a composite material. The reinforcement inclusions modify the spatial arrangement at the microstructure level, and therefore can have a big impact on the behavior of the epoxy phase, especially when reaching the failure phase. All macroscale cracks are a result of these microstructure variations, meaning that the mechanical behavior of the microstructure must be taken into account in the modeling of full macroscale composite materials, and hence the presence of the two phases of different behavior, for a correct representation. As full-field simulations accounting for all the inclusions is computationally unaffordable, multiscale approaches must be used to model these materials.

1.2 Homogenization techniques and damage representation

The use of composite materials has introduced new challenges within the industry, as the complex microstructure makes the use of direct numerical simulations unfeasible due to the high computational cost. As previously exposed, a multiscale approach represents the solution for accurate representations of composite materials with epoxy matrix phases. This approach comes into play to become a bridge between these different scales. The development of the multi-scale methods has paved the way to a better understanding of some important processes and creation of new methods such as microstructural deformation, homogenization of materials, damage and failure processes, or microstructure evolution.

The need for modeling in an efficient way the complexity of the microstructure of materials has made homogenization a very widespread technique, as shown by many reviews such as Kanouté et al. (2009), Geers, Kouznetsova, and Brekeclmans (2010), Llorca et al. (2011), Nemat-Nasser and Hori (2013) and Noels, Wu, and Adam (2016). It consists of methods that allow a strongly heterogeneous material to be substituted for an equivalent homogeneous one. This is achieved by obtaining an equivalent or effective response from a finite volume of material, which is generally assumed to be statistically homogeneous, a so-called representative volume element (RVE). The homogenization principle is based on the principle of scale separation, which states that the scale of the microstructure must be much smaller than the size of the considered RVE, and in turn must be much smaller than the length of the characteristic fluctuation in the macroscopic strain field (see Figure 1.5). While this principle is valid within the concept of local action of continuous mechanics, it is sometimes violated when a microstructural length scale tends to be large.

A great progress in homogenization techniques was made from the decade of the 50s to the 70s with works from Eshelby and Peierls (1957), Kröner (1958), Hashin and Shtrikman (1963), Hill (1963), Mori and Tanaka (1973) or Willis (1977a) as some examples. At first, these techniques focused in the elastic response of materials, being used to predict the apparent elastic response of heterogeneous material systems (Nemat-Nasser and Hori, 2013). Later, works such as the one by Hill (1965b), Kröner (1958) or Hutchinson (1977) started paving the way to the homogenization of

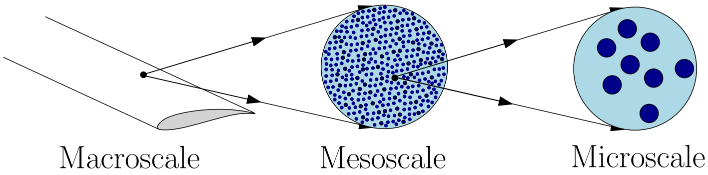

FIGURE 1.5: Scale separation from macrostructure to microstructure

nonlinear responses, which found an increase in interest and the apparition of many developments in elasto-plasticity, viscoplasticity and viscoelasticity in the decades of the 80s and the 90s. Some examples of these developments in the nonlinear modeling to be mentioned are P. Castañeda (Castaneda, 1991) with his work on the effective mechanical properties of nonlinear isotropic composites, Willis (1977b), Nemat-Nasser (Nemat-Nasser and Obata, 1986; Nemat-Nasser and Hori, 2013), Zaoui and Masson (2000) or Gurson (1977) with his well-known Gurson model.

The homogenization techniques could be divided into semi-analytical methods and numerical ones. While purely numerical approaches can yield accurate representations, the semi-analytical approaches allow to largely reduce the computational cost of simulations. Therefore, both approaches remain relevant nowadays. Some examples of semi-analytical methods are the generalized method of cells (GMC) which was reviewed by Aboudi (1996), the Transformation-Field Analysis (TFA) pioneered by Dvorak, Wafa, and Bahei-El-Din (1994), or its non-uniform transformation-field analysis extension (NTFA) developed by Michel and Suquet (2003). Regarding purely numerical methods, some examples are Ghosh et al. Voronoi cell finite element method (VCFEM) (Ghosh, Lee, and Moorthy, 1995), a purely numerical method which combines the asymptotic homogenization technique with the microstructural modeling using Voronoi cells, Lissenden and Arnold's method of cells (Lissenden and Arnold, 1997), and its generalizations by Michel, Moulinec, and Suquet (1999), Feyel (1999) or Terada et al. (2000).

To this day, homogenization techniques have grown inside the scientific community, having a widespread recognition, and becoming a more common research topic. Some of the currently most used homogenization techniques are the unit cell finite element (FE)-based computations (Wieckowski, 2000; Segurado, Llorca, and González, 2002; Ju and Wang, 2003; Carrere et al., 2004), the mean-field homogenization (MFH) method (Castaneda, 1991; Lahellec and Suquet, 2007a; Miehe, 2002; Doghri, Adam, and Bilger, 2010; Doghri et al., 2011; Berveiller and Zaoui, 1978; Hill, 1965b; Wu et al., 2013c), or the work by Kouznetsova, Brekelmans, and Baaijens (2001) in which a finite element model of the RVE was associated to each macro-scale integration point that led to the FE2 method (Kouznetsova, Brekelmans, and Baaijens, 2001; Kouznetsova, Geers, and Brekelmans, 2004; Matous et al., 2017; Geers et al., 2017). This FE2 method, while being a very flexible approach due to its nature, the need for the solving of a large number of microstructural boundary value problems makes this method an unrealistic option for real heterogeneous macroscale applications.

In order to cope with the issue of macroscale heterogeneous problems, projection-based reduced order models (ROM) are becoming a widespread alternative to the costly FE2 methodology, allowing a speeding up of the microscale solution with pre-offline computations. This method projects the governing equations into a suitably selected reduced order space where the microscale model is solved with a reduced number of unknown variables which are defined by means of proper orthogonal decomposition of the degrees-of-freedom (Yvonnet and He, 2007; Radermacher et al., 2016). The demanding computational cost of the internal forces arising from the assessment of local constitutive equations can be further decreased by the implementation of hyper-reduction techniques (Hernandez et al., 2014; Soldner et al., 2017; Oliver et al., 2017; Zahr, Avery, and Farhat, 2017).

Within the framework of model reduction through a micromechanics-based homogenization model, the nonuniform transformation field analysis (NTFA) (Michel and Suquet, 2009) employs pre-defined modes of internal variables obtained from pre-off-line full-field analyses. A tangent second-order (NTFA-TSO) expansion of the dissipation potential was then employed by Michel and Suquet (2016) to decrease the evolution equations associated with the reduced internal variables.

To avoid nonlinear pre-off-line computation, clusters of the micro-structure having similar elastic strain concentration tensors with respect to the applied deformation are homogenized using a self-consistent method (Liu, Bessa, and Liu, 2016). Although the use of such model reductions speeds up a multiscale simulation by several orders of magnitude, the reduction is still usually performed for a given deterministic micro-structure. Indeed, the required pre-offline computations can become prohibitive when several different micro-structures should be considered, in particular in the context of nonlinear responses such as irreversible deformations and/or damage and failure.

In order for multiscale simulations to become a reality in the nonlinear range, it is thus necessary to build surrogate models that can predict the homogenized properties of a given microstructure without actually solving it, or by solving a limited amount of them during an offline stage. This is the reason why machine learning and its application to computational mechanics have become an important topic of study. Once trained in an offline step, Machine Learning algorithms can approximate the behavior of real materials and RVEs responses, without solving constitutive laws or constitutive models (Nguyen and Noels, 2022; Ghaboussi and Sidarta, 1998; Lefik and Schrefler, 2003; Jung and Ghaboussi, 2006; Furukawa and Yagawa, 1998; Settgast et al., 2020), by only introducing some given variables of interest as inputs. Many examples of these applications can be found, such as the feed-forward implementation in the works by Le, Yvonnet, and He (2015), Fritzen, Fernández, and Larsson (2019), Yang, Tang, and Liu (2019) or Gorji et al. (2020).

In the work by Yvonnet, Monteiro, and He (2013), the macroscopic stress and elastic tangent tensors of heterogeneous materials are computed thanks to the developed nonconcurrent multiscale homogenization method. This method relies on a database that describes the variation of the strain energy density potential in the macroscopic right Cauchy-Green strain tensor space. The database values are computed through FEM simulations on a representative volume element. Then, the database is reduced by a tensor product approximation in order to accelerate the interpolations at the macroscopic scale. A continuous representation of the potential is obtained by an interpolation scheme, allowing the calculation of the macroscopic stress and elastic tangent tensors for macroscopic structures. In Bessa et al. (2017), a database of homogenized behaviors was obtained by varying microstructure entries and performing homogenization; the database is then used as entry of the neural network to predict the composite homogenized quantities. The main challenge faced by the so-called feed-forward neural network algorithms, in which information only flows forward, is the modeling of irreversible phenomena, meaning that complex loading cycles cannot be predicted by these machine learning algorithms. To this end, these feed-forward algorithms could be enriched in order to take into account these complex behaviors, such as in the case of the proper orthogonal decomposition feedforward neural network (PODFNN) proposed by Huang et al. (2020). Recurrent neural-networks (RNN) have seen an increase these last years due to its native ability to account for history-dependent behaviors. Recurrent neural-networks were successfully implemented in the works by Wu et al. (2020a), Wu and Noels (2022), Ghavamian and Simone (2019), Mozaffar et al. (2019), Gorji et al. (2020) or Logarzo, Capuano, and Rimoli (2021). One of the main concerns of these neural-network-based surrogate models is the large sampling space that must be used to train the algorithm, as predicting the behavior outside this training space would yield spurious results.

Another approach based on the use of machine learning algorithms is the so-called deep material network (DMN). Introduced by (Liu, Wu, and Koishi, 2019) for two-phase heterogeneous materials, this approach is capable of predicting nonlinear behaviors outside the sampling space thanks to the offline training of the two-phase laminate-based model that allows to take into account not only the behavior of the phases, but also their interaction. The DMN approach has been satisfactorily applied in the study of interface failure (Liu, 2020) and 3D microstructures (Liu and Wu, 2019). This method has been used as a basis for new works, such as the work by Gajek, Schneider, and Böhlke (2020), who presented a new online evaluation procedure based on energy minimization, or the work by Wu, Adam, and Noels (2021), who made use of a mean-field homogenization model in the material node for the study of woven composite materials (see Figure 1.6), achieving an important reduction on the number of needed mechanistic building blocks.

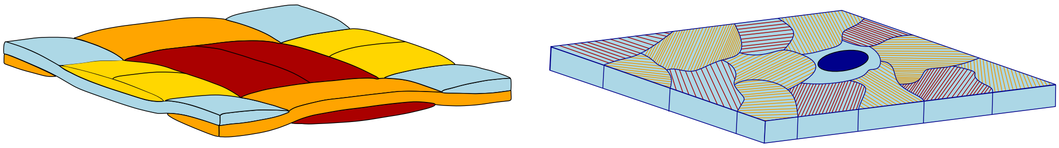

FIGURE 1.6: Woven composite homogenization.

Multiscale homogenization methods have improved over the years, and they are currently capable of accurately represent the behavior of composites in their elastic and nonlinear regimes as Pierard et al. (2007) shows. However, one of the most complex problems in multiscale modeling is the representation of damage. Damage is a phenomenon that crosses all length scales, and defining its scale transition has been proved not to be a straightforward task. Nowadays, damage is not a fully understood phenomenon, and therefore, it has not been easy to properly model its causes and evolution in a complete physical way, which explains the phenomenological nature of most of the damage models used currently in multiscale simulations.

The introduction of damage representation can cause some mathematical difficulties at the strain-softening onset, such as the loss of ellipticity in the governing equations as shown by the works by Llorca et al. (2011) or Geers, Kouznetsova, and Brekeclmans (2010). This loss of ellipticity causes the finite element solution to be nonunique, introducing a high mesh dependence. In order to address this issue, higher order terms could be introduced into the governing equations as presented in the review by De Borst et al. (1993), making possible an interaction between a given point and its surroundings through the introduction of a characteristic length associated with the failure mechanisms and microstructure of the studied material. This methodology has allowed the scientific community to address this challenge, not without the inconvenient of largely increasing the complexity of the base models, by introducing higher order terms and a characteristic length that allows to represent the failure mechanisms into the model allowing for an interaction between a given material point and the material surrounding it. Such is the case in the works by Bažant, Belytchko, and Chang (1984) with his nonlocal averaging approach, Zbib and Aifantis (1989) gradient-dependent flow theory, or De Borst (1991) with his reappraisal of the Cosserat continuum model, or other models such as the ones developed by Aifantis (1992), or by Svedberg and Runesson (1997) to name a few. Even though these formulations could circumvent the nonunique solution problem, these higher order terms introduce also the need to solve higher-order derivatives, increasing the complexity of these models. By formulating the nonlocal approach implicitly, a new nonlocal variable emanates as a result of the resolution of a new boundary value problem. This was proposed in the context of homogeneous materials by Peerlings et al. (1996); Peerlings et al. (1998); Geers (1997), which developed a new approach by implementing an implicit nonlocal formulation approach that allowed to make it fully nonlocal. Based on a weighted averaging integral, this approach introduces a new nonlocal variable that results from the resolution of the resolution of a boundary value problem.

These approaches mainly started as an implementation for direct numerical simulations, however, they have been successfully implemented in multiple works in the scope of multiscale simulations. Some examples of multiscale implementation of these nonlocal approaches are the constitutive model by Knockaert and Doghri (1999), which implemented a nonlocal constitutive model with gradients of internal variables for the one dimensional case, the Cosserat model was applied in the Mori-Tanaka model by Liu and Hu (2005) and Coenen, Kouznetsova, and Geers (2011a); Coenen, Kouznetsova, and Geers (2011b) who generalized the Massart et al. (Massart, Peerlings, and Geers, 2005; Massart, Peerlings, and Geers, 2007) nonlocal approach for masonry wall computations, showing the possibility to apply this approach to semi-analytical or numerical computational homogenizations. Wu et al. (2013c) implemented an implicit-gradient-enhanced approach of the incremental-secant MFH scheme, which permitted to account for damage in UD composite simulations while retaining the main benefits of the incremental-secant formulation.

When considering the case of damage on a composite material, complex damage formulations can be found for the modeling of full composites, such is the case of Barbero, Abdelal, and Caceres (2005), where the damage model depends on the combination of matrix, fiber and interphase damage models, constructing a second-order damage tensor and being necessary the use a fourth-order damage-effect tensor to compute the effective stress from the damaged one, or when accounting for different effects such as void nucleation caused by decohesion between phases, as in Östlund et al. (2014), where strain based failure criterion introduced by Haggblad et al. 2009 is used in a modified J2 yield criterion, which makes use of a single scalar localization function introduced to reduce the load bearing capability of the material. When a homogenization technique is considered, damage is modelled on each phase separately, as the response at the composite level inherits from the homogenization scheme (Wu et al., 2021). In the case of the strain driven damage of Costa et al. (2021), the model is capable of modeling several failure modes on composite by using only two damage variables (one for the matrix and one for the fiber), raising the question of the real need of more damage variables for a single-phase material since one variable is capable of capturing the most important damage modes dominated by the matrix phase while keeping a low number of mathematical operations. Most of the models developed for single-phase materials in the literature consider scalar damage, most of the time a single damage scale parameter, such are the cases in the work by Balieu et al. (2014), where a nonlocal version of the Gurson model which makes use of a local variable with a single scalar parameter is implemented. This is an alternative nonlocal formulation of the model proposed by Tvergaard and Needleman (1995); Tvergaard and Needleman (1998). Multi-mechanism nonlocal Gurson damage model was developed by Nguyen, Pardoen, and Noels (2020), and a multi-mechanisms nonlocal continuum based constitutive model for amorphous glassy polymers developed by Nguyen et al. (2016).

In the context of homogenization, the development of localization bands within the microstructure volume element introduces a loss of size objectivity at the strain-softening onset, and thus the absence of existence of a representative volume element. This issue has been studied in the past and avoided by making use of a representative quantity that allows to recover this size objectivity. Different quantities have been used during the years to address this problem, such as the traction-displacement jump softening response, the critical energy release rate or the fracture toughness of the material (Mosby and Matous, 2015; Phu Nguyen et al., 2010; Verhoosel et al., 2010; Wu et al., 2021; Nguyen, Wu, and Noels, 2019).

1.3 Stochastic multiscale methods

All materials, and more especially, composite materials, contain several microstructure uncretainities, such as geometric. These uncertainties propagate among the different scales, making one sample of a given material to behave differently to another sample of the same material. The homogenization of materials does not allow to take these effects into account. Stochastic finite element method (SFEM) is a way of approaching this problem (Ghanem and Spanos, 1991). This methodology is based on proper random fields (Charmpis, Schuëller, and Pellissetti, 2007) that allow representing the stochastic properties of the material. These random fields would have to be obtained from a large number of experiments in order to obtain accurate results, which is not always possible. In order to avoid this costly step, these random fields can be defined from micromechanical information (Charmpis, Schuëller, and Pellissetti, 2007; Ostoja-Starzewski and Wang, 1999) that contains the statistic properties of the uncertainties present on the microstructure of the material, being then possible to generate realistic virtual microstructures that contain the same stochastic properties as the real material.

The RVEs in which most homogenization techniques rely on, must be statistically representative of the microstructure, which means that its size varies with the sources of uncertainties. Some works have focused on the correct definition of this RVE for different heterogeneous material microstructures. Such is the case of the integrated framework using fast statistical homogenization procedure (FSHP) developed in Pingaro et al. (2019). The developed framework makes use of the virtual element method (VEM) and allows to efficiently converge towards the RVE size detection by solving a series of simulations. The FSHP has been used for the estimation of effective properties in a wide variety of random heterogeneous microstructures, such as for random porous materials (Pingaro, Reccia, and Trovalusci, 2019) or ceramic matrix composites (CMC) (Pingaro et al., 2023). In some cases, the existence of the definition of an RVE is impossible because of the large size required to be statistically representative of nonlinear behaviors (McDowell, 2010; Ostoja-Starzewski et al., 2007), meaning that the separation criterion for a multiscale analysis is not always met.

If the separation criterion is not met, the multiscale analysis should be performed based on multiple virtual microstructures called stochastic volume elements (SVEs) (Ostoja-Starzewski and Wang, 1999) (see Fig. 1.7). With the use of multiple SVEs, the homogenized properties depend on the location as well as on the applied boundary conditions as shown in Fig. 1.7 (Wu et al., 2018; Ostoja-Starzewski et al., 2007; Salmi et al., 2012; Trovalusci et al., 2015; Reccia et al., 2018; Ostoja-Starzewski, 2005; Hachemi et al., 2014).

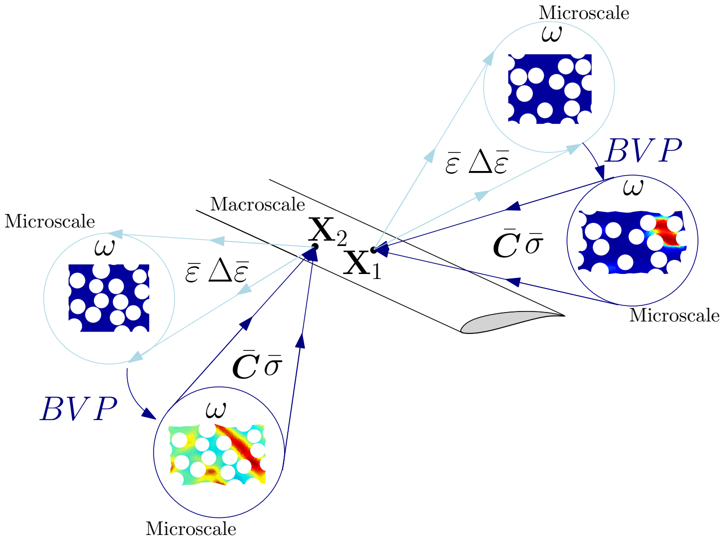

FIGURE 1.7: Nonlinear stochastic homogenization-based multiscale analysis schematic.

These SVEs are the means used to propagate the uncertainties from the microscale to the macroscale. Therefore, being capable of reproducing the internal structure and geometry of composite materials microstructure accounting for the uncertainties that they can contain is one of the main steps towards the development of stochastic multiscale models. These synthetic microstructures are extremely useful for studying the effects of micro-scale features and defects on the macro-scale properties and performance of the materials without the need of relying on real material samples. Different methods have been proposed for generating synthetic microstructures for multiple kinds of composite materials as shown in the review by Noels (2022).

In the case of UD composites, the main challenge is to capture the random distribution and interaction of the fibers, especially at high fiber volume fractions. Vaughan and McCarthy (2010) present a new method to generate realistic fiber distributions for high volume fraction composites, based on experimental data. The method uses a modified version of nearest neighbor distribution functions to define the distances between fibers. Melro, Camanho, and Pinho (2008) propose another model for generating the cross-section of composites with randomly distributed long fibers and high fiber volume fraction thanks to the development of a simple and fast algorithm modelling the random fiber distribution. Wu et al. (2018) develop a statistical method for generating realistic numerical models of the cross-section of unidirectional carbon fiber reinforced composites. The method uses SEM images of the cross-section to analyze the spatial distribution of the fibers and their interactions. The method then uses the copula framework to represent the empirical statistical descriptors as dependent variables and generate random microstructures that match the observed ones. These micro-structures are used as stochastic volume elements (SVEs) for further analysis. Similarly, synthetic microstructures for other types of microstructures have been developed over the years. One example is the case of woven composites, which present a more complex geometry and more sources of variability. the work by Blacklock et al. (2012) present a Monte Carlo algorithm that can generate realistic virtual specimens of textile composite materials based on data from computed tomography images. The algorithm models the textile reinforcement as one-dimensional tow loci in three-dimensional space, which can capture both periodic and stochastic variations in the tow geometry and defects. Tal and Fish (2016) present a methodology for generating a realistic volume element of a composite material with random micro-scale defects. The paper uses data from two-dimensional micrographs of a Sic/SiNC sample to statistically characterize the shape, size, orientation and distribution of the defects. The paper then uses a Monte-Carlo simulation to introduce three-dimensional ellipsoidal voids to a defect-free eight-harness weave model based on the statistical characteristics. The paper aims to create a volume element that has the same defect statistics as the micrographs. Another example is the work by Vanaerschot et al. (2013), which present a method for analyzing the stochastic nature of a textile reinforcement in a multi-ply laminate. The method, called reference period collation, separates the fiber characteristics into systematic trends and stochastic fluctuations. The results show that the in-plane centroid position of the tows is the most variable parameter. The paper also discusses how the fiber characteristics are influenced by the cross-over points within and between the plies.

Being these SVEs the main tool to propagate the effects of the microscale geometric uncertainties to the macroscale (Ostoja-Starzewski et al., 2007; Salmi et al., 2012; Trovalusci et al., 2015; Reccia et al., 2018), this means that in order to obtain accurate macroscale simulations, the mesh used in these simulations must have a size lower than the correlation length, which itself depends on the size of the SVE used to define the random properties of the microscale (Lucas et al., 2015). For linear behaviors it is possible to define mesoscale random fields of homogenized properties through offline simulations of the SVEs. This has ben done in works such as the one by Stefanou, Savvas, and Papadrakakis (2015), in which a method for linking the random variation of the microstructure geometry of two-phase composites with the effective material properties and the structural response at the macroscale was presented. This method combines the extended finite element method (XFEM) and Monte Carlo simulation (MCS) to compute the effective elastic modulus and Poisson's ratio of the composites. Another example is Stefanou et al. (2022). Using a covariance decomposition method, the reference creates sample functions of the random fields at the mesoscale level. Then, it uses Monte Carlo simulations to compute the response variability of different composite structures, being able to study how the uncertainty in the random field parameters influences the variability in the structural response. This approach was also used for the stochastic simulations of UD composites in the linear range in Wu et al. (2018). This reference proposes a two-step homogenization procedure that preserves the statistical content of the micro-scale random field in the meso-scale random field, which can be used in structural stochastic analyzes. In addition to only focusing in the stochastic simulations of composites in the linear range, the work by Hun et al. (2019) proposes a stochastic approach to model crack propagation in random heterogeneous media. To this end, the reference results and an estimation of the effect of the subscale randomness on the macroscopic response are obtained by performing Monte-Carlo simulations on microstructural samples. The stochastic model is then built to describe the mesoscopic elasticity as a non-Gaussian random field. This is then used in the phase-field approach to simulate the crack propagation within the material sample without the need to perform computational homogenization. The stochastic analysis of elastic heterogeneous materials was also addressed in Clément, Soize, and Yvonnet (2012), where a computational method for nonlinear stochastic homogenization of hyperelastic heterogeneous microstructures using a nonconcurrent multiscale approach was presented.

In the nonlinear range, the number of required SVE resolutions makes approaches such as the finite element square (FE^2) (Kouznetsova, Brekelmans, and Baaijens, 2001; Kouznetsova, Geers, and Brekelmans, 2004) method, which uses finite element (FE) simulations for the full-field analysis, unfeasible for these kinds of materials. Indeed, while being capable of yielding accurate predictions thanks to the explicit definition of the microstructures and the phases properties on the microscale BVP, multiscale approaches imply high computational requirements due to the explicit definition of the microstructure, imposing a strong constraint on the mesh level. For this reason, this methodology has been mainly used taking into account a deterministic microscale called representative volume element (RVE). For this reason, stochastic reduced models are widely used to conduct virtual testing in the nonlinear range. An example of this approach in the nonlinear range are the works by L. Wu et al. (Wu, Adam, and Noels, 2018; Wu et al., 2019), who extended their previous work (Wu et al., 2018) to the stochastic analysis of UD composites in the nonlinear range.

Another approach to perform stochastic simulations is the spectral stochastic FEM, a very computationally expensive but accurate method. This approach combines the spectral representation of stochastic processes with the discretization of the spatial domain. One example of implementation of this method is the work by Pivovarov, Steinmann, and Willner (2020), where a reduction of the main factors affecting the computational cost related to this approach was introduced. To this end, a hyper-reduction is performed through a new element-based modification of the element-based empirical approximation method (EDEAM), which is combined with the proper orthogonal decomposition incorporated into the spectral stochastic FEM.

In the past decades, the use of surrogate models has seen an increased interest, making stochastic multiscale simulations of complex nonlinear materials finally possible (See Figure 1.8). To this end, machine learning techniques have recently been employed as a powerful tool to construct accurate and efficient surrogate models, as only off-line microstructure computations would be needed to train the algorithm, and therefore to build the surrogate. In Hashemi, Safdari, and Sheidaei (2021), the database of thermal conductivities used for the training of the algorithm was obtained with the use of a fast Fourier transform (FFT) homogenization method on different microstructures identified through several features such as the volume fraction, size distribution, and aspect ratio. This dataset was used as an input for the training of a supervised machine learning. This surrogate model showed its capabilities not only predicting a given microstructure behavior, but also good inverse design capabilities. In the work by Lu et al. (2021), a data-driven FE^2 method was developed, for which a hybrid neural network (NN) interpolation scheme was introduced, achieving an improved accuracy of the NN surrogate and permitting to lower the number of RVE needed as database for the training of the NN to account for microstructure variations. Similarly, NN has been used in Lu et al. (2019), in which a data-driven multiscale method for anisotropic electrical responses has been developed, and in Fritzen, Fernández, and Larsson (2019), where its use in calibration of surrogate models is seen as promising.

The DMN approach by Liu, Wu, and Koishi (2019), has been also used as a basis in other works, such as in Huang et al. (2022), which introduced a microstructure-guided deep material

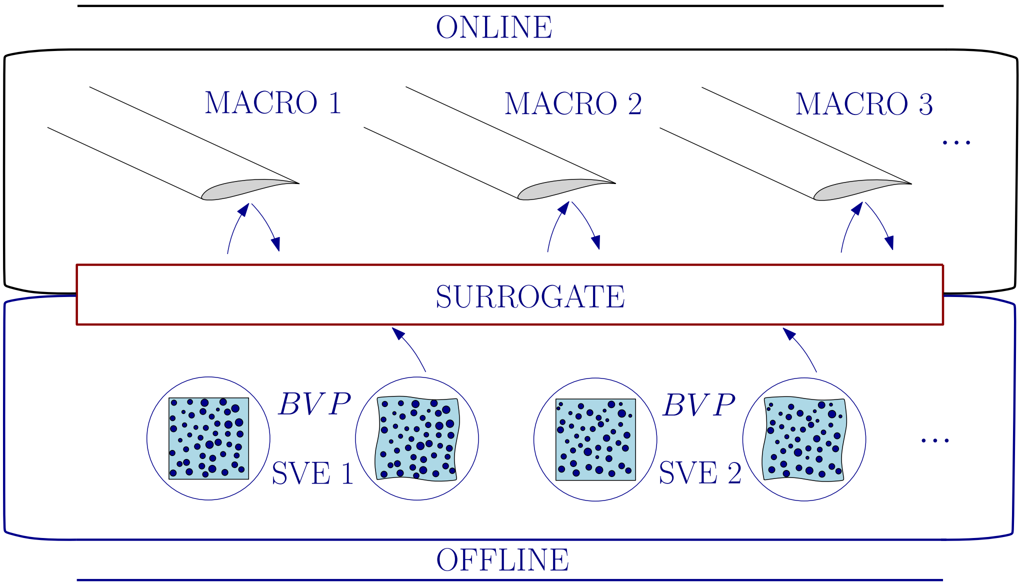

FIGURE 1.8: Scheme of a surrogate model approach.

network that avoided the need for further training to predict the nonlinear response of new microstructures, allowing for good accuracy while largely improving the efficiency of the modeling of heterogeneous materials with uncertainty.

As addressed in the review by Noels (2022), a wide variety of approaches can be found nowadays, underscoring the promising role of neural network-based surrogates in achieving stochastic multi-scale methods, such as the work by Rao and Liu (2020) with their three-dimensional deep convolution neural network (3D-CNN). The developed neural network is able to predict the linear anisotropic effective material properties of a given RVE with random inclusions by providing its image, and not using features as other approaches. While this method is not yet used in nonlinear stochastic multiscale analysis, it showcases the wide variety of new possibilities introduced by the neural networks in this field.

Most of the works emphasize the three main challenges especially when involving nonlinearities. The first challenge is the need for a rich synthetic database for effective training of the model. Creating such databases, implies the need of a substantial number of direct numerical simulations. The second main challenge is being able to relate the stochastic behavior at the macroscale to the uncertainties present at the microstructure. The third challenge is the modeling of the nonlinear range, and more specifically the stochastic modeling of the material failure. Nowadays, there is a clear lack of methods for the stochastic multiscale modeling of materials up to its complete failure. Some papers such as the one by Hun et al. (2019) address the crack propagation in random heterogeneous materials, but they treat the fracture stage as deterministic.

1.4 Objectives of the Thesis

The aim of this Work is to develop an efficient framework that allows the scientific and industry communities to further improve the virtual testing of polymeric composites. To that end, a methodology that allows to take the microstructure variability of the material into account must be used, so that irreversible behaviors such as plasticity and/or damage and failure and behavioral variability can naturally be taken into account.

When the microstructures involve geometrical properties and material responses that may vary, traditional multiscale approaches coupled with Monte-Carlo simulations cannot be envisioned because of the overwhelming computational cost. For nonlinear materials and complex geometries such as woven composites, computational homogenization (FE^2) (Kouznetsova, Geers, and Brekelmans, 2002), which solves boundary value problems (BVP) at both scales using full-field analyzes such as finite elements reveals itself to be an accurate methodology, however, as previously mentioned, the resolution of the two BVP should be concurrent, involving a high computational cost, and therefore, making its use prohibitive in the case of a deterministic complex 3D problem. In order to circumvent this problem, this Work focused on the development of MFH based ROM for composite materials. To that end, we first need to have accurate simulation of composite volume elements, which requires an accurate model of the polymeric matrix. Then the MFH ought to be able to capture the complex behavior of the matrix, such as its pressure-dependent response. Finally, the stochastic micromechanics ROM have to be developed to represent the composite response variability, including during the failure stage.

This Thesis will start generalizing the finite strain nonlocal damaged-enhanced viscoelastic-viscoplastic constitutive model developed by Nguyen et al. (2016) introducing bulk and shear moduli stiffening terms. This introduction will allow us to consider a wider range of polymers as it will be exemplified by briefly exploring the modeling of shape memory polymers and their stiffening behavior at large strains as reported by Srivastava, Chester, and Anand (2010).

The second goal of this Thesis is to develop a mean-field homogenization framework capable of correctly capture the behavior of two-phase composites with a pressure dependent matrix phase up to its failure with a view to efficient stochastic studies of this type of composites. The incremental-secant-based MFH model developed by L. Wu et al. (Wu et al., 2017; Wu, Doghri, and Noels, 2015; Wu et al., 2013a; Wu et al., 2013c; Wu et al., 2012) is here used as the basis methodology. This methodology allows to avoid a common problem for most MFH schemes: the need for an isotropization step to avert the over stiff predictions. Being able to obtain good predictions in plasticity and avoiding this isotropization step has been shown to not be a straightforward task. This Work implements a MFH scheme that allows to take elasto-plastic behaviors with pressure-dependency into account, permitting to consider damaging phases and to remain accurate under nonproportional loading conditions, while maintaining the intrinsic advantages of the incremental-secant scheme: the isotropic nature of the linear-comparison composite (LCC) instantaneous stiffness tensor circumvents and makes the isotropization step unnecessary, resulting into a simplified implementation of the material constitutive material law. Similarly to the approach followed in the works by V.D. Nguyen et al. (Nguyen et al., 2016; Nguyen, Wu, and Noels, 2019), this Thesis implements the enhanced Drucker-Prager model described in Section 2 in combination to a non-associated flow rule that allows to control the evolution of the plastic-Poisson's ratio.

This pressure-dependent MFH model is then used as a surrogate model for the construction of a UD composite stochastic reduced order model, which represents the third objective of this Thesis. As shown in Figure 1.9, by constructing a micro-informatics model of the microstructure using statistical indicators, homogenized behaviors can be predicted in a stochastic way. The homogenized stochastic behavior of the studied composite is first characterized through full-field simulations of stochastic volume elements (SVEs) of the material microstructure, permitting to capture and characterize the effect of the microstructural geometrical uncertainties. Then, by applying an inverse identification process on each SVE realization, the random effective properties needed by the pressure-dependent incremental-secant mean-field homogenization formulation are obtained and used to feed the data-driven stochastic MF-ROM used to perform stochastic finite element method (SFEM) simulations.

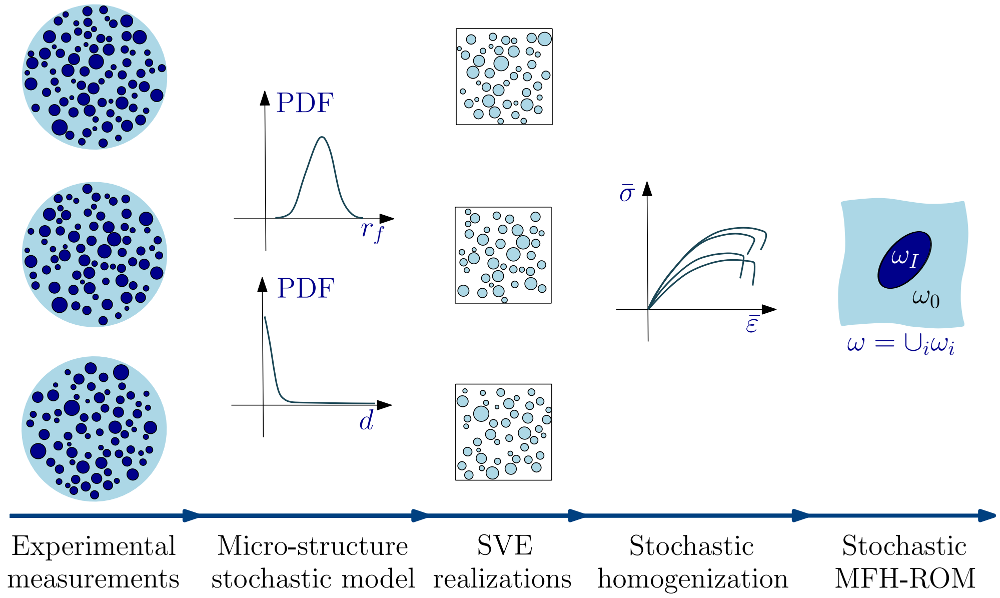

FIGURE 1.9: UD composite ROM methodology.

Such methodology was developed in the works by L. Wu et al. (Wu et al., 2018; Wu et al., 2019) for pressure independent composite materials. The new developed damaged-enhanced pressure-dependent MFH model allow to complete this ROM with pressure dependency and the ability to recover the size objectivity of the solution after the failure onset by introducing a new calibration step based on the critical energy release rate of the material. The calibration step will consist on an iterative process that will compute the failure-damage surrogate model parameters required to recover the same critical energy release rate obtained during the full-field realizations (as shown in Fig. 1.10). The addition of this new step means the stochastic MF-ROM is now able to naturally assess the stochasticity of the material failure.

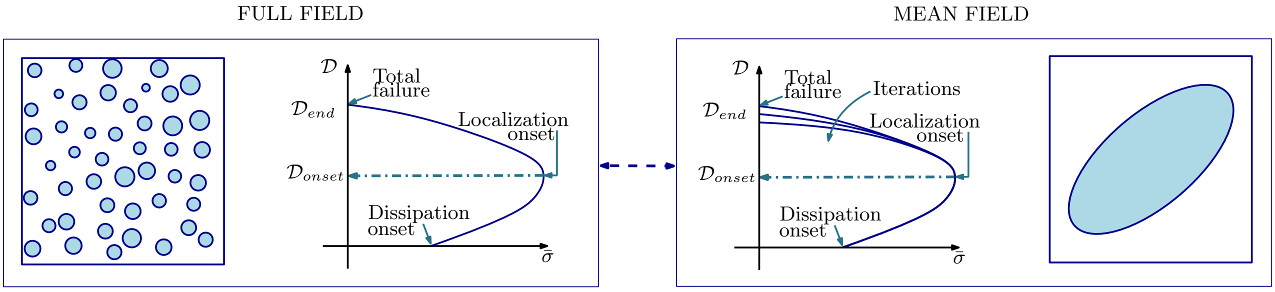

FIGURE 1.10: Iterative calibration of the MFH model to reach the critical energy release rate of the SVE realization.

The MF-ROM accelerates the prediction of the variability in a structural response by several orders of magnitude, allowing to efficiently study particular quantities of interest (QoI), e.g. a structure strength, with a given confidence range studied in terms of the microstructure.

1.5 Scientific novelties

- The correct modeling of the elastic stiffening observed for some polymers at large strains is addressed. This is performed by means of the addition of bulk and shear moduli stiffening terms to the large strain nonlocal damaged-enhanced viscoelastic-viscoplastic constitutive model developed in Nguyen et al. (2016).

- The developed MFH scheme allows to take elasto-plastic behaviors with pressure-dependency into account while maintaining the intrinsic advantages of the incremental-secant scheme: the isotropic nature of the LCC instantaneous stiffness tensor circumvents and makes the isotropization step unnecessary, and results into a simplified implementation of the material constitutive material law.
- The developed pressure-dependent MFH is used as a basis of an incremental-secant based stochastic MF-ROM for UD composites constructed from MFH parameters obtained through an inverse identification process, making possible stochastic simulations capable of accounting for the pressure-dependent behavior of epoxy matrices.
- The MFH loss of size objectivity after the localization onset is addressed. This recovery of the size objectivity of the damaged-enhanced MFH model after the softening onset is performed by taking the energy release rate of the studied material as a reference value for the definition of the MFH nonlocal damage evolution law.

The following articles were published in the scope of this Thesis:

- Calleja Vázquez, JM, Wu, L, Nguyen, V-D, Noels, L. An incremental-secant mean-field homogenization model enhanced with a non-associated pressure-dependent plasticity model. Int J Numer Methods Eng. 2022; 123(19): 4616–4654. doi:10.1002/nme.7048
- Calleja Vázquez, JM, Wu, L, Nguyen, V-D, Noels, L. A micromechanical mean-field homogenization surrogate for the stochastic multiscale analysis of composite materials failure. Int J Numer Methods Eng. 2023; 1-63. doi: 10.1002/nme.7344

1.6 Thesis outline

This Thesis will present the work performed during this PhD in a linear way, allowing the reader to understand the reasoning behind this Work. This document is divided into five chapters:

- Chapter 1: Introduction

This chapter introduces the general context and the motivation of the study carried in this Thesis. Focusing on composite materials, the high-crosslinked epoxies are introduced showing their pressure-dependent behavior. The techniques used in computational mechanics in order to model pressure-dependent plastic behaviors are then introduced and reviewed, followed by an introduction to homogenization techniques.

- Chapter 2: Generalized large strain nonlocal damage enhanced viscoelastic viscoplastic constitutive model for semi-crystalline and glassy polymers

This Chapter presents a generalized framework for the modeling of glassy and semi-crystalline polymers. Here, the nonlocal damage formulation used for the softening of the material and the enhanced large strain nonlocal damage enhanced viscoelastic viscoplastic constitutive model are recalled (Nguyen et al., 2016). This enhanced constitutive model will feature the introduction of bulk and shear moduli stiffening terms, which will allow to correctly capture the stiffening behavior observed in some polymers, such as semi-crystalline shape memory polymers. The constitutive model is based on a generalized Maxwell viscoelastic model completed by pressure-dependent non-associated viscoplastic Perzyna approach. This Chapter will develop the implementation of the large strain nonlocal damaged-enhanced viscoelastic-viscoplastic constitutive model in a FE framework. Finally, the Chapter will end by testing the efficiency of the introduced enhancements in the constitutive model against real tests on DMA samples of the shape memory polymer PCL76-4MAL/FUR 3 wt%CNT.

- Chapter 3: Incremental-Secant implementation of a possibly damaged enhanced non-associated pressure-dependent plasticity model

This chapter starts by introducing some MFH generalities, which will build the path to the introduction of the incremental-secant based MFH. Then, the pressure-dependent plasticity model used in this Thesis and the MFH resolution in the nonlocal FE framework are addressed before showing the performance of this methodology through the verification of its predictions against FE simulations and experiments.

- Chapter 4: A micromechanical mean-field homogenization surrogate for the stochastic multiscale analysis of composite materials failure

The fourth chapter starts by the definition of the meso-scale boundary value problem followed by the multiscale homogenization scale transition. Then, the inverse identification process used for the obtention of the MFH parameter dataset is presented followed by a statistical analysis of these parameters. These parameters will then be used for the generation of proper random fields that allow the construction of the stochastic-ROM. This chapter will finalize by showing the capabilities of the reduced order model on several applications.

- Chapter 5: Conclusion and future perspectives

Finally, this chapter will discuss and analyze the different results obtained at each step of this Work, allowing to have a more general view of the achievements of this Thesis and the points that are still to be addressed and improved in future works.

Chapter 2

Generalized large strain nonlocal damage enhanced viscoelastic viscoplastic constitutive model for polymers[1]

Epoxies are a group of thermoset polymers that are commonly used as the matrix phase in fiber reinforced composite materials. Their properties have made these group of materials to gain popularity in the aeronautical industry these last decades. As previously presented, the amorphous glassy molecular composition of epoxies results in complex behaviors. It has been shown these materials are found to be dependent on factors such as deformation rate and temperature, with a large difference between tensile and compressive behaviors. In particular, compressive loadings exhibit higher peak values due to the hydrostatic pressure dependency exhibited by this family of materials.

Amorphous glassy polymers, such as epoxies, exhibit different plastic stages in their strain-stress response, with micro-shear bands causing a softening stage and reduction in loading bearing capability before the rehardening stage caused by the alignment of the molecule chains is reached. This complex behavior makes viscoelastic constitutive models, such as the widely used generalized Kelvin model (Zhang and Moore, 1997) and the generalized Maxwell model (Reese and Govindjee, 1998; Buhan and Frey, 2011; Takagi et al., 2008), or other well-known models such as the Schapery model (Haj-Ali and Muliana, 2004; Zhang et al., 2022), or the fractional model (Schiessel et al., 1995; Hajikarimi et al., 2022), to be insufficient for the correct modeling of polymers. In order to properly represent the glassy polymer behavior, plasticity, softening, and failure must be taken into account. As a result, complex constitutive models are necessary to fully model its behavior.

Viscoplasticity has been an extensive subject of study for the scientific community, which has approached this phenomenon in multiple ways. Some works focused on a physical approach in order to model these materials (Boyce, Parks, and Argon, 1988; Arruda, Boyce, and Jayachandran, 1995; Tervoort et al., 1997; Govaert, Timmermans, and Brekelmans, 1999). The main drawback of these models is the large amount of parameters they require, which translates on a complex testing campaign required for the calibration of the model. The use of phenomenological models (Krempl, McMahon, and Yao, 1986; Bodner and Partom, 1975; Perzyna, 1971) can drastically reduce the number of parameters to be calibrated. This lower calibration complexity makes this approach highly attractive for the modeling of this kind of materials. As an example, many examples of this modeling approach can be observed in the study of polymers as shown in the works (Colak, 2005; Bodner and Partom, 1975; Frank and Brockman, 2001; Zairi et al., 2008). One of the most stablished models in the viscoplastic theory is the phenomenological viscoplastic model introduced by Perzyna (1971). Several works such as the ones by Van Der Sluis, Schreurs, and Meijer (2001), Kim and Muliana (2010), Al-Rub, Tehrani, and Darabi (2015) or Nguyen et

---

[1] Part of this chapter is an adapted version of the paper (Gulasik et al., 2023), while the main concept is from (Nguyen et al., 2016)

al. (2016) successfully introduced this viscoplastic approach for the modeling of the viscoplastic effect on these materials.

Damage-enhanced viscoelastic-viscoplastic models, in which a viscoelastic model can be used together with a phenomenological viscoplastic model, allow to have a full representation of the behavior of these polymers. This approach yielded good results in multiple publications, as shown in the works by Al-Rub, Tehrani, and Darabi (2015), Zairi et al. (2008), Krairi and Doghri (2014), Chowdhury, Benzerga, and Talreja (2008), Chowdhury, Talreja, and Benzerga (2008), Nguyen et al. (2016), Zhao et al. (2021), Liu et al. (2022), Carvalho, Coda, and Sanches (2023) or Narayanan, Pramanik, and Arockiarajan (2023).

Nguyen et al. (2016) addressed the complex behavior of glassy polymers with his large strain nonlocal damaged-enhanced pressure-dependent viscoelastic-viscoplastic constitutive model. This model is a hyperelastic viscoelastic-viscoplastic-damage constitutive model based on a multimechanism nonlocal damage continuum to model the matrix phase of the composite material. This model showed great capabilities to mimic real epoxy materials like the high-crosslinked RTM6 epoxy resin (Nguyen, Wu, and Noels, 2019) thanks to the introduction of the pressure-dependency. In this approach, different models are used depending on the strain level. At small strains, an enhanced generalized Maxwell model is used to capture the viscoelastic behavior. When the strain exceeds a certain limit characterized by a pressure-sensitive yield function, the material enters a viscoplastic region. In this region, the plastic flow is governed by a non-associated Perzyna-type flow rule, which considers the pressure-sensitive yield function and a quadratic flow potential. The damage evolution inside the material is taken into account in a Lemaitre-Chaboche style, also called continuum damage mechanics (CDM) approach (Lemaitre and Chaboche, 1994) using a nonlocal formulation. This nonlocal formulation allows to circumvent the ill-posedness of the boundary value problem after the localization stage.

The behavior of some hyperelastic polymers like the shape memory polymers, can present a characteristic elastic stiffening behavior at high deformations as observed by Srivastava, Chester, and Anand (2010). This behavior was not captured by the model introduced by Nguyen et al. (2016), which accounted for linear terms in its elastic definition. The aim of this Chapter is to present an enhanced version of the large strain nonlocal damaged-enhanced viscoelastic-viscoplastic constitutive model developed by Nguyen et al. (2016) for the modeling of such polymer materials. This enhancement consists in the introduction of bulk and shear moduli stiffening terms, which will allow to capture the elastic stiffening observed in polymers such as SMPs. This generalization of the original model will allow to better capture the wide range of properties that can be observed in polymeric materials.

This Chapter will start by presenting the nonlocal damage formulation used for the softening of the material. Then, the viscoelastic-viscoplastic constitutive model enhanced with the new bulk and shear moduli stiffening terms will be presented. To that end, first the kinematics framework of the studied problem will be briefly presented, followed by the introduction of the generalized Maxwell viscoelastic model. Then, viscoplastic part of the model will consist on the presentation of the non-associated Perzyna approach used for the viscous modeling, followed by the definition of the pressure-dependent yield surface and the flow potential, and the hardening modeling. Finally, this Chapter will end by presenting the implementation of the large strain nonlocal damaged-enhanced viscoelastic-viscoplastic constitutive model.

2.1 Nonlocal damage formulation

Let us briefly present the nonlocal mechanics of a studied body ω with a reference configuration ω_{ref} and boundary $\partial\omega_{\text{ref}}$. Considering a volumetric force $\mathbf{\Omega}$ applied to the body ω, its boundary can be divided into Newman ($\partial_N\omega_{\text{ref}}$) and Dirichlet ($\partial_D\omega_{\text{ref}}$) boundaries. A surface traction $\mathbf{T}_b$ is applied on boundary $\partial_N\omega_{\text{ref}}$, while the boundary $\partial_D\omega_{\text{ref}}$ is set to a displacement $\boldsymbol{u}_b$. In this case, considering $\boldsymbol{N}$ the unit outward normal to the body boundary $\partial\omega_{\text{ref}}$ and $\mathbf{P}$ the first Piola-Kirchhoff stress tensor, the equilibrium equations of the studied body ω write:

$$\begin{cases} \mathbf{P}\cdot\boldsymbol{\nabla}_0 = -\boldsymbol{\Omega} & \text{on } \omega_{\text{ref}}, \\ \boldsymbol{u} = \boldsymbol{u}_b & \text{on } \partial_D\omega_{\text{ref}}, \text{ and} \\ \mathbf{P}\cdot\boldsymbol{N} = \mathbf{T}_b & \text{on } \partial_N\omega_{\text{ref}}. \end{cases} \tag{2.1}$$

where $\boldsymbol{\nabla}_0$ stands for the gradient operator with respect to the reference configuration and $\boldsymbol{u}$ refers to the displacement.

Elasto-plastic materials are history dependent. In order to account for these history and path dependent irreversibilities, a set of internal variables $\boldsymbol{q}$ is used. The material constitutive law that completes the set of equations governing the studied problem writes:

$$\mathbf{P} = \mathbf{P}(\mathbf{F}(t);\boldsymbol{q}(\tau),\tau\in[0,t]), \tag{2.2}$$

where $\mathbf{F}$ stands for the deformation gradient tensor.

In the work by Nguyen et al. (2016), the damage effect within the material is taken into account in a Lemaitre-Chaboche style (Lemaitre and Chaboche, 1994). This damage formulation accounts for the evolution of damage within the studied material through an internal scalar D, whose value ranges from 0 to 1, where 1 stands for a fully damaged material, and 0 for a undamaged material.

The evolution of this scalar is governed by an evolution law which writes:

$$\dot{D} = \mathfrak{D}\left(D,\mathbf{F}(t);\boldsymbol{q}(\tau),\tau\in[0,t]\right). \tag{2.3}$$

Assuming the material strain in its undamaged state equals the current strain state (Lemaitre, 1985), the first Piola-Kirchhoff writes in terms of the scalar D and the effective Piola-Kirchhoff as:

$$\mathbf{P} = (1-D)\,\hat{\mathbf{P}}, \tag{2.4}$$

where the effective Piola-Kirchhoff stress is governed by the undamaged material constitutive law:

$$\hat{\mathbf{P}} = \hat{\mathbf{P}}\left(\mathbf{F}(t);\boldsymbol{q}(\tau),\tau\in[0,t]\right). \tag{2.5}$$

The evolution law presented in Eq. (2.3) allows to locally define the value of the damage scalar for a given strain history, however, once the strain softening occurs, the boundary value problem is no longer well-posed. This formulation will therefore yield mesh dependent results and damage localization. In order to solve this problem, Peerlings et al. (1996) introduced a nonlocal implicit approach that allowed to circumvent this issue. Instead of considering the local value of a given internal variable q at a material point in a position $\boldsymbol{x}_{\text{ref}}$, this approach takes an average of this quantity over a characteristic volume ω_c:

$$\breve{q}(\boldsymbol{x}_{\text{ref}}) = \frac{1}{\omega_c}\int_{\omega_c} q(\boldsymbol{Y})\theta(\boldsymbol{r})d\omega, \tag{2.6}$$

where $\boldsymbol{Y}$ stands for a position belonging to the characteristic volume ω_c, $d\omega$ is the differential volume, and where $\theta(\boldsymbol{r})$ stands for the weight function that accounts for the level of influence of a point at a radius $\boldsymbol{r} = \boldsymbol{x}_{\text{ref}} - \boldsymbol{Y}$ belonging to the characteristic volume ω_c as shown in Fig. 2.1.

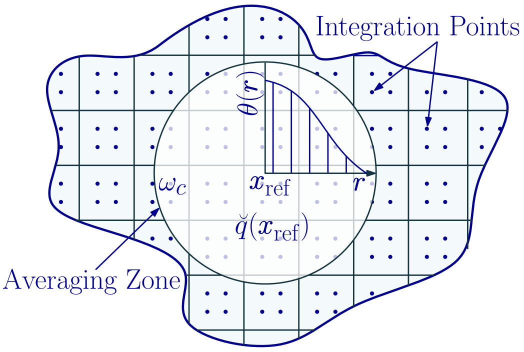

FIGURE 2.1: Graphic representation of the nonlocal averaging of variable q over a volume ω_c.

It was shown in Peerlings et al. (1996); Peerlings et al. (2001), that this expression with θ, the Green's function can be expressed as a Helmoltz-type equation:

$$\breve{q}(\boldsymbol{x}_{\text{ref}}, t) - l^2 \Delta_0 \breve{q} = q, \tag{2.7}$$

where l stands for the characteristic length of the studied material. Making use of this nonlocal variable, the evolution of the damage scalar D will write:

$$\dot{D} = \mathfrak{D}\left(D, \mathbf{F}(t), \mathcal{Q}(t); \boldsymbol{q}(\tau), \tau \in [0, t]\right) \dot{\mathcal{Q}}, \tag{2.8}$$

where $\boldsymbol{q}$ is the vector with the undamaged internal variables, and $\mathcal{Q}$ is a monotonically increasing nonlocal variable which writes:

$$\mathcal{Q} = \max\left[\mathcal{Q}_0, \breve{q}; 0 \le \tau \le t\right]. \tag{2.9}$$

As already introduced in Chapter 1 and shown in Fig. 2.2, multiple investigations (Boyce, Arruda, and Jayachandran, 1994; Buckley et al., 1994; Chen, Lu, and Cheng, 2002; Fiedler et al., 2001; Hine et al., 2005; Lesser and Kody, 1997; Morelle, Pardoen, and Bailly, 2015; Mulliken and Boyce, 2006) have shown a very complex behavior that depends on various external factors such as hydrostatic pressure, temperature or deformation rate. In order to present the modeling strategy used for the damage of these materials, let us consider uniaxial loading conditions. As it can be seen from Fig. 2.2, Multiple stages can be observed from this response, from which we can observe two major damage-related stages: The post-peak softening and the failure stages.

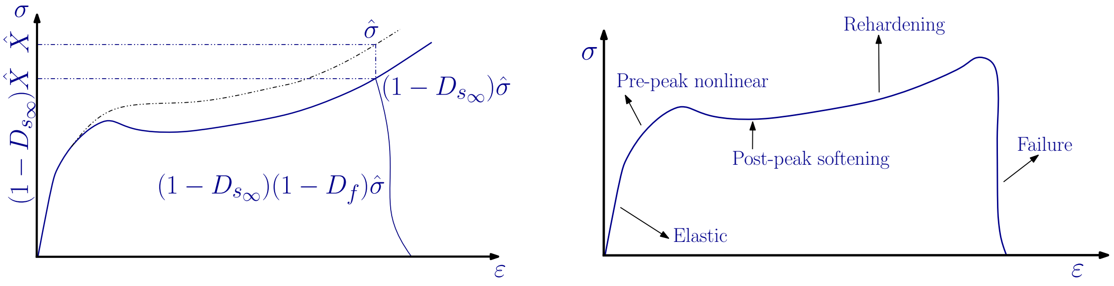

FIGURE 2.2: Schematic representation of a typical amorphous glassy polymer stress-strain curve for a uniaxial compressive monotonic loading condition on the right and graphic representation of the damage modeling used in (Nguyen et al., 2016) on the left

In order to model these stages, a two-step damage modeling is used (see Fig. 2.2). In order to model the post-peak softening, a softening damage variable D_s will be used, while a failure damage variable D_f will later be triggered in order to model the failure of the epoxy material. Using these two damage variables, the damage variable D writes:

$$D = 1 - (1 - D_s)(1 - D_f), \tag{2.10}$$

rewriting Eq. (2.4) as:

$$\mathbf{P} = (1 - D_s)\,(1 - D_f)\,\hat{\mathbf{P}}. \tag{2.11}$$

In order to avoid the previously mentioned problems that local damage can introduce, both damage scalars will be defined in an implicit nonlocal formulation. This formulation is then completed with natural boundary conditions for the respective nonlocal variables used for each damage. The softening damage will therefore write:

$$\begin{cases} \breve{q}_s(\boldsymbol{x}, t) - l_s^2 \Delta_0 \breve{q}_s = q_s, \\ \dot{D}_s = \mathfrak{D}_s \left(D_s, \mathbf{F}(t), \mathcal{Q}_s(t); \boldsymbol{q}(\tau), \tau \in [0, t]\right) \dot{\mathcal{Q}}_s, \\ \mathcal{Q}_s(t) = \max\left[\mathcal{Q}_{s0}, \breve{q}_s; 0 \leq \tau \leq t\right], \\ \boldsymbol{\nabla}_0 \breve{q}_s \cdot \boldsymbol{N} = 0 \text{ on } \partial\omega_{\text{ref}}, \end{cases} \tag{2.12}$$

where l_s stands for the softening characteristic size. Equivalently, the failure damage D_f will be formulated as:

$$\begin{cases} \breve{q}_f(\boldsymbol{x}, t) - l_f^2 \Delta_0 \breve{q}_f = q_f, \\ \dot{D}_f = \mathfrak{D}_f \left(D_f, \mathbf{F}(t), \mathcal{Q}_f(t); \boldsymbol{q}(\tau), \tau \in [0, t]\right) \dot{\mathcal{Q}}_f, \\ \mathcal{Q}_f(t) = \max\left[\mathcal{Q}_{f0}, \breve{q}_f; 0 \leq \tau \leq t\right], \\ \boldsymbol{\nabla}_0 \breve{q}_f \cdot \boldsymbol{N} = 0 \text{ on } \partial\omega_{\text{ref}}, \end{cases} \tag{2.13}$$

where l_f stands for the failure characteristic size. This nonlocal formulation of the damage allows a complete uncoupling of the damage variables and the constitutive behavior of the material, permitting a high degree of flexibility of the model.

2.2 Viscoelastic-viscoplastic constitutive model

Having a material point which initially was at a reference point $\boldsymbol{x}_{\text{ref}}$ and is currently at position $\boldsymbol{x}$, the deformation gradient tensor $\mathbf{F}$ is defined as:

$$\mathbf{F} = \frac{\partial \boldsymbol{x}}{\partial \boldsymbol{x}_{\text{ref}}}, \tag{2.14}$$

where the deformed configuration $\boldsymbol{x}$ is a two-point mapping depending on the reference configuration and time t: $\boldsymbol{x} = \boldsymbol{x}(\boldsymbol{x}_{\text{ref}}, t)$. Defining the displacement vector $\boldsymbol{u} = \boldsymbol{x} - \boldsymbol{x}_{\text{ref}}$, the deformation gradient tensor $\mathbf{F}$ writes:

$$\mathbf{F} = \boldsymbol{x} \otimes \boldsymbol{\nabla}_0 = \mathbf{1} + \boldsymbol{u} \otimes \boldsymbol{\nabla}_0, \tag{2.15}$$

where $\mathbf{1}$ stands for the second-order identity tensor, and $\boldsymbol{\nabla}_0$ stands for the gradient operator with respect to the reference configuration.

This Section will now present the viscoelastic-viscoplastic constitutive model that will be used for the modeling of the glassy amorphous polymers. This Section will start by briefly presenting the strain-stress measures before presenting the viscoelastic and viscoplastic models. Finally, this Section will present how the model is implemented numerically, displaying the predictor-corrector steps to follow its solution.

2.2.1 Logarithmic strain-stress measures

The deformation gradient $\mathbf{F}$ can be divided into viscoelastic $\mathbf{F}^{\text{ve}}$ and viscoplastic $\mathbf{F}^{\text{vp}}$ gradients, such that:

$$\mathbf{F} = \mathbf{F}^{\text{ve}} \cdot \mathbf{F}^{\text{vp}}. \tag{2.16}$$

These deformation gradients are then used for the definition of the right Cauchy strain tensor and the viscoelastic right Cauchy strain tensor, which write:

$$\mathbf{C} = \mathbf{F}^{T} \cdot \mathbf{F}, \quad \mathbf{C}^{\text{ve}} = \mathbf{F}^{\text{ve}T} \cdot \mathbf{F}^{\text{ve}}, \tag{2.17}$$

or again using Eqs. (2.16, 2.17) as:

$$\mathbf{C} = \mathbf{F}^{\text{vp}T} \cdot \mathbf{C}^{\text{ve}} \cdot \mathbf{F}^{\text{vp}}. \tag{2.18}$$

These definitions of the right Cauchy strain tensors can then be used to define the logarithmic strain operator for the total and viscoelastic terms:

$$\mathbf{E} = \frac{1}{2} \ln \mathbf{C}, \text{ and } \mathbf{E}^{\text{ve}} = \frac{1}{2} \ln \mathbf{C}^{\text{ve}}. \tag{2.19}$$

If an irrotational viscoplastic flow is assumed, which means that the anti-symmetric part of the viscoplastic spatial gradient of velocity $\mathbf{L}^{\text{vp}}$ vanishes ($\mathbf{W}^{\text{vp}} = 0$), the viscoplastic strain rate tensor $\dot{\boldsymbol{\varepsilon}}^{\text{vp}}$ will be equal to $\mathbf{L}^{\text{vp}}$, being possible to write:

$$\dot{\boldsymbol{\varepsilon}}^{\text{vp}} = \mathbf{L}^{\text{vp}} = \dot{\mathbf{F}}^{\text{vp}} \cdot \mathbf{F}^{\text{vp}-1}. \tag{2.20}$$

This Eq. (2.20) allows us to find an expression for the plastic evolution, which yields:

$$\dot{\mathbf{F}}^{\text{vp}} = \dot{\boldsymbol{\varepsilon}}^{\text{vp}} \cdot \mathbf{F}^{\text{vp}}. \tag{2.21}$$

The hyperelastic formulation of this model is based on the assumption of the existence of an elastic potential depending on the logarithmic viscoelastic strain operator $\Psi(\mathbf{E}^{\text{ve}})$, from which the effective Kirchhoff stress $\hat{\boldsymbol{\kappa}}$ and the effective corotational Kirchhoff stress $\hat{\boldsymbol{\tau}}$ can be defined as:

$$\dot{\Psi} = \hat{\boldsymbol{\kappa}} : \mathbf{L}^{\text{ve}} = \hat{\boldsymbol{\tau}} : \dot{\mathbf{E}}^{\text{ve}}, \tag{2.22}$$

or solving for $\hat{\boldsymbol{\kappa}}$:

$$\hat{\boldsymbol{\kappa}} = 2\mathbf{F}^{\text{ve}} \cdot \frac{\partial \Psi}{\partial \mathbf{C}^{\text{ve}}} \cdot \mathbf{F}^{\text{ve}T} = \mathbf{F}^{\text{ve}-T} \cdot \hat{\boldsymbol{\tau}} \cdot \mathbf{F}^{\text{ve}T}. \tag{2.23}$$

We note that in order for $\hat{\boldsymbol{\tau}}$ to be the effective Kirchhoff stress expressed in the viscoelastic corotational space, we need to assume that $\mathbf{C}^{\text{ve}}$ and $\hat{\boldsymbol{\tau}}$ permute, which is not the case for the viscous terms as discussed later.

After the definition of the deformation gradients $\mathbf{F}^{\text{ve}}$ and $\mathbf{F}^{\text{vp}}$ and the Kirchhoff stress, it is then possible to define the first Piola-Kirchhoff stress $\hat{\mathbf{P}}$ as:

$$\hat{\mathbf{P}} = \hat{\boldsymbol{\kappa}} \cdot \mathbf{F}^{-T} = 2\mathbf{F}^{\text{ve}} \cdot \frac{\partial \Psi}{\partial \mathbf{C}^{\text{ve}}} \cdot \mathbf{F}^{\text{vp}-T} = \mathbf{F}^{\text{ve}} \cdot \mathbf{S}^{\text{ve}} \cdot \mathbf{F}^{\text{vp}-T} = \mathbf{F}^{\text{ve}-T} \cdot \hat{\boldsymbol{\tau}} \cdot \mathbf{F}^{\text{vp}-T}, \tag{2.24}$$

where $\mathbf{S}^{\text{ve}}$ writes:

$$\mathbf{S}^{\text{ve}} = \hat{\boldsymbol{\tau}} : \mathcal{L} \text{ with } \mathcal{L} = \left.\frac{\partial \ln \mathbf{C}^{\text{ve}}}{\partial \mathbf{C}^{\text{ve}}}\right|_{\mathbf{C}^{\text{ve}}(t)}. \tag{2.25}$$

In the case for which the logarithm is evaluated following an approximation:

$$\ln(\mathbf{1}+\mathbf{A}) = \mathbf{A} - \frac{\mathbf{A}^2}{2} + \frac{\mathbf{A}^3}{3} - \frac{\mathbf{A}^4}{4} + \ldots, \tag{2.26}$$

being $\mathbf{A}$ an arbitrary second-order tensor. The derivative $\mathcal{L}$ is computed from this approximation.

2.2.2 Viscoelasticity and Kirchhoff stress

One of the most consolidated mechanical models of viscoelasticity is the Maxwell model. Pioneered by (Maxwell, 1867), this model is built connecting an elastic spring with a viscous dashpot as shown in Fig. 2.3. This model allows then to represent not only the static behavior of the material, but also to take into account the rate dependency of its response.

FIGURE 2.3: Schematic representation of the viscoelastic Maxwell model.

As in the work by V.D. Nguyen et al. (Nguyen et al., 2016; Simo, 1987), an enhanced viscoelastic potential based on this generalized Maxwell model in the is used in this Thesis. The model contain N+1 springs (see Fig. 2.4) with elastic potentials Ψ_∞ and Ψ_i, and N dashpots with dissipation functions Υ_i:

$$\Psi\left(\mathbf{E}^{\mathrm{ve}}; \boldsymbol{q}_1, \ldots, \boldsymbol{q}_N\right) = \Psi_\infty + \sum_{i=1}^{N}\left[\Psi_i\left(\mathbf{E}^{\mathrm{ve}}\right) + \Upsilon_i\left(\mathbf{E}^{\mathrm{ve}}; \boldsymbol{q}_i\right)\right], \tag{2.27}$$

where $i = 1, ..., N$.

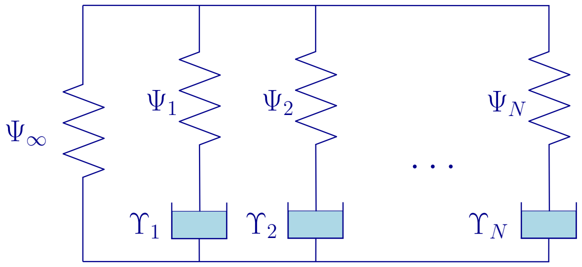

FIGURE 2.4: Schematic representation of the generalized viscoelastic Maxwell model.

The N Maxwell spring potentials are modeled with a bi-logarithmic potential function which writes:

$$\Psi_i\left(\mathbf{C}^{\mathrm{ve}}\right) = \frac{\kappa_i}{2}\ln^2 J^{\mathrm{ve}} + \mu_i\left(\mathbf{E}^{\mathrm{ve}}\right)^{\mathrm{dev}} : \left(\mathbf{E}^{\mathrm{ve}}\right)^{\mathrm{dev}} \text{ with } i = 1, \ldots, N, \tag{2.28}$$

where κ_i and μ_i stand for the bulk and shear moduli of the material with $i = 1, ..., N$.

In the present Work, Ψ_∞ is modified to account for bulk and shear moduli terms that directly depend on the evolution of E^{ve}. The term Ψ_∞ therefore writes:

$$\Psi_\infty\left(\mathbf{C}^{\mathrm{ve}}\right) = \int_0^{\operatorname{tr}\mathbf{E}^{\mathrm{ve}}} \kappa_\infty\left(\operatorname{tr}\mathbf{E}^{\mathrm{ve}\prime}\right)\operatorname{tr}\mathbf{E}^{\mathrm{ve}\prime} d\operatorname{tr}\mathbf{E}^{\mathrm{ve}\prime} + \int_0^{(\mathbf{E}^{\mathrm{ve}})^{\mathrm{dev}}} 2\mu_\infty(|\mathbf{E}^{\mathrm{ve}\prime}|)(\mathbf{E}^{\mathrm{ve}\prime})^{\mathrm{dev}} : d\operatorname{tr}\mathbf{E}^{\mathrm{ve}\prime}, \tag{2.29}$$

where $\operatorname{tr}(\bullet)$ is the trace operator, $(\bullet)^{\mathrm{dev}} = (\bullet) - (\bullet)^{\mathrm{vol}}$ is the deviatoric operator, being $(\bullet)^{\mathrm{vol}} = 1/3\operatorname{tr}(\bullet)\mathbf{1}$, where $\mathbf{1}$ stands for the second-order identity tensor; and κ_∞ and μ_∞ are the nonlinear bulk and shear moduli respectively of the purely elastic branch. This nonlinearity added to the original model presented in Nguyen et al. (2016) allows to recover the stiffening behavior observed on some polymers at a large deformation (Srivastava, Chester, and Anand, 2010). The new expressions for the nonlinear bulk and shear moduli write:

$$\kappa_\infty = \hat{\kappa}_\infty \left[1 + \underbrace{V_\kappa \left[\tanh\left(\frac{\vartheta_\kappa}{3} (\operatorname{tr} \mathbf{E}^{\text{ve}})^2 - \zeta_\kappa \right) + \tanh(\zeta_\kappa) \right]}_{f_\kappa(\operatorname{tr}\mathbf{E}^{\text{ve}})} \right], \text{and} \tag{2.30}$$

$$\mu_\infty = \hat{\mu}_\infty \left[1 + \underbrace{V_\mu \left[\tanh\left(\vartheta_\mu (\mathbf{E}^{\text{ve}})^{\text{dev}} : (\mathbf{E}^{\text{ve}})^{\text{dev}} - \zeta_\mu \right) + \tanh(\zeta_\mu) \right]}_{f_\mu(\mathbf{E}^{\text{ve}})^{\text{dev}}} \right], \tag{2.31}$$

being $\hat{\mu}_\infty$ and $\hat{\kappa}_\infty$ the linear shear and bulk moduli at infinitesimal strain, and V_κ, V_μ, ϑ_κ, ϑ_μ, ζ_κ and ζ_μ are the parameters to model the evolution of the bulk and shear moduli. The introduction of these six parameters allows a maximum generalization of the enhanced bulk and shear moduli, and gives the model the ability to capture a wide range of elastic stiffening behaviors.

For the modeling of the viscous dashpots, quadratic dissipating functions are used (Nguyen et al., 2016; Simo, 1987):

$$\Upsilon_i(\mathbf{E}^{\text{ve}}, \boldsymbol{q}_i) = -\boldsymbol{q}_i : \mathbf{E}^{\text{ve}} + \frac{1}{18\kappa_i} (\operatorname{tr} \boldsymbol{q}_i)^2 + \frac{1}{4\mu_i} (\boldsymbol{q}_i)^{\text{dev}} : (\boldsymbol{q}_i)^{\text{dev}} \text{ with } i = 1, \dots, N. \tag{2.32}$$

The internal variables $\boldsymbol{q}_i$ allow to account for the viscoelastic effect and their evolution is characterized by a retardation action (Simo, 1987):

$$\begin{aligned} (\dot{\boldsymbol{q}}_i)^{\text{dev}} &= \frac{2\mu_i}{g_i} (\mathbf{E}^{\text{ve}})^{\text{dev}} - \frac{1}{g_i} (\boldsymbol{q}_i)^{\text{dev}}, \\ \operatorname{tr} \dot{\boldsymbol{q}}_i &= \frac{3\kappa_i}{k_i} \operatorname{tr} \mathbf{E}^{\text{ve}} - \frac{1}{k_i} \operatorname{tr} \boldsymbol{q}_i, \end{aligned} \tag{2.33}$$

where g_i and k_i are respectively the characteristic relaxation times for the deviatoric and volumetric terms.

The effective corotational Kirchhoff stress can be computed as the derivative of the viscoelastic potential $\Psi_i(\mathbf{E}^{\text{ve}})$ with respect to the viscoelastic logarithmic strain measure $\mathbf{E}^{\text{ve}}$:

$$\hat{\boldsymbol{\tau}} = \frac{\partial \Psi}{\partial \mathbf{E}^{\text{ve}}}. \tag{2.34}$$

Finally, the viscous terms can be found by integration as:

$$\begin{aligned} (\boldsymbol{q}_i)^{\text{dev}} &= \frac{2\mu_i}{g_i} \int_{-\infty}^{t} \exp\left(-\frac{t-s}{g_i} \right) (\mathbf{E}^{\text{ve}})^{\text{dev}}(s) ds, \text{ and} \\ \frac{1}{3} \operatorname{tr} \boldsymbol{q}_i &= \frac{\kappa_i}{k_i} \int_{-\infty}^{t} \exp\left(-\frac{t-s}{k_i} \right) \operatorname{tr} \mathbf{E}^{\text{ve}}(s) ds, \end{aligned} \tag{2.35}$$

yielding:

$$\boldsymbol{q}_i = (\boldsymbol{q}_i)^{\text{dev}} + (\boldsymbol{q}_i)^{\text{vol}}. \tag{2.36}$$

As it can be observed from the previous equations, the corotational Kirchhoff stress can be directly divided into a deviatoric and a volumetric contribution as:

$$\hat{\boldsymbol{\tau}} = (\hat{\boldsymbol{\tau}})^{\text{dev}} + (\hat{\boldsymbol{\tau}})^{\text{vol}}. \tag{2.37}$$

Introducing Eq. (2.27) into Eq. (2.34), the effective corotational Kirchhoff stress writes:

$$\left\{ \begin{array}{l} (\hat{\boldsymbol{\tau}})^{\mathrm{dev}} = 2\mu_{\infty}(\mathbf{E}^{\mathrm{ve}})^{\mathrm{dev}}(t) + \int_{-\infty}^{t} 2\mu(t-s) : \frac{\mathrm{d}}{\mathrm{d}s}(\mathbf{E}^{\mathrm{ve}})^{\mathrm{dev}}(s)ds, \\ \frac{1}{3}\operatorname{tr}\hat{\boldsymbol{\tau}} = \kappa_{\infty}\operatorname{tr}\mathbf{E}^{\mathrm{ve}}(t) + \int_{-\infty}^{t} \kappa(t-s)\frac{\mathrm{d}}{\mathrm{d}s}\operatorname{tr}\mathbf{E}^{\mathrm{ve}}(s)ds, \end{array} \right. \tag{2.38}$$

where:

$$\mu(t) = \sum_{i=1}^{N} \mu_i \exp\left(-\frac{t}{g_i}\right), \text{ and } \kappa(t) = \sum_{i=1}^{N} \kappa_i \exp\left(-\frac{t}{k_i}\right). \tag{2.39}$$

Using the definition of the derivative $\mathcal{L}$ (see Eq. (2.25)), the expression for the first Piola-Kirchhoff stress follows Eq. (2.24).

2.2.3 Viscoplasticity

After presenting the viscoelastic constitutive law, the next step consists in the modeling of the viscoplastic stage. This Section will start presenting the viscous modeling strategy, followed by the definition of the used pressure-dependent yield surface, the flow potential and the extended yield condition. Finally, the hardening modeling strategy will be introduced.

Viscoplastic flow The viscoelastic model that has been presented thus far is applicable within the elastic range. The boundary of this validity, which signifies the shift from elasticity to plasticity, is established by the yield condition F. In order to model the viscous behavior of these polymer materials, a non-associated Perzyna-type (Perzyna, 1971) viscoplastic flow is used to define the viscoplastic strain rate:

$$\dot{\boldsymbol{\varepsilon}}^{\mathrm{vp}} = \underbrace{\frac{1}{\eta}\langle F\rangle^{\frac{1}{\gamma}}}_{\lambda}\mathbf{Q}, \tag{2.40}$$

where η is the material viscosity parameter, λ is the consistency parameter, γ is the rate sensitivity exponent, $\mathbf{Q}$ is the normal to the plastic flow potential G, to be further defined $\left(\mathbf{Q} = \frac{\partial G}{\partial \hat{\boldsymbol{\tau}}}\right)$ and $\langle \bullet \rangle = \frac{1}{2}(\bullet + |\bullet|)$. Fixing the material viscosity parameter η to 0, the rate-independent case can be recovered if desired. It is worth noting that as a non-associated flow rule is used, the flow potential G differs from the yield surface F.

By introducing the consistency parameter λ, it becomes possible to formulate the viscoplastic extended yield function that can represent rate-dependent materials. This can be expressed in a generalized form as follows:

$$\bar{F} = F - (\eta\lambda)^{\gamma} \leq 0. \tag{2.41}$$

As it is shown in figure 2.5, three different regions can therefore be defined. The first region will be delimited by the yield function F. This region is called the viscoelastic region, as the material behaves in a viscoelastic way. While the material state lies inside this region, the yield function F and the extended yield condition $\bar{F}$ remain the same. Once the plastic limit is surpassed, i.e. $F > 0$, plasticity starts to develop and the yield surface F will be modified. The new definition of the extended viscoplastic yield function is obtained through a Kuhn-Tucker-type condition computed with the use of the consistency parameter λ:

$$\lambda\bar{F} = 0,\ \lambda \geq 0,\ \text{and } \bar{F} \leq 0. \tag{2.42}$$

The third region would belong to a $\bar{F} > 0$ case, which is a no-access region.

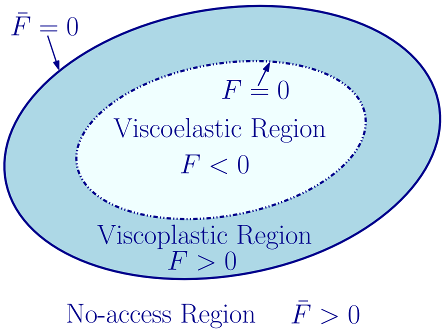

FIGURE 2.5: Schematic representation of the viscoelastic-viscoplastic yield surface regions.

Yield surface The Drucker-Prager yield surface model is a well-known yield criterion whose yield surface not only varies with respect to the second invariant, but also presents a dependence on the hydrostatic stress, showing a cone-like shaped yield surface (see Figure 2.6).

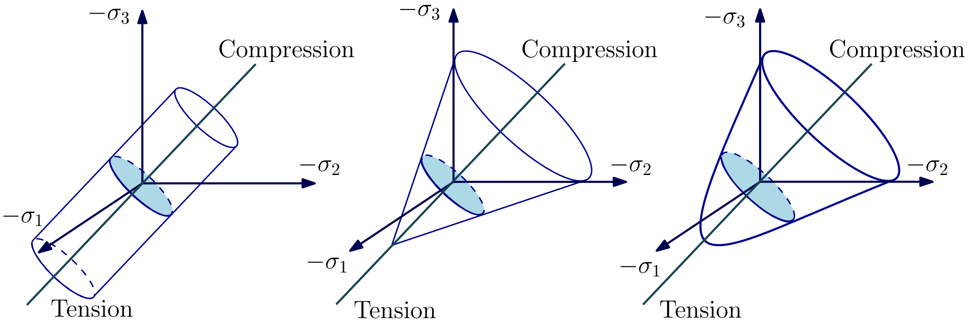

FIGURE 2.6: Graphical representation of the von Mises (left), the pressure-dependent Drucker-Prager (center) and Nguyen et al. (2016) (right) yield surfaces on the stress space.

This yield surface was later extended multiple times to represent accurately different material behaviors. The used yield function for the modeling of plasticity represents a power-enhanced version of the original Drucker-Prager. This criterion was used by Nguyen et al. (2016), who applied it to the case of amorphous glassy polymers, developing a hyperelastic viscoelastic-viscoplastic-damage constitutive model based on a multimechanism nonlocal damage continuum. The developed power-enhanced version of the Drucker-Prager is then capable of not only representing materials following the classical Drucker-Prager yield surface or the Melro et al. (2013) yield surface, but also more complex power yield surfaces. This model has the capabilities to mimic real epoxy materials like the high-crosslinked RTM6 epoxy resin (Nguyen, Wu, and Noels, 2019).

This allows for a more versatile and adaptable approach to modeling plasticity, which is of crucial importance when studying materials that exhibit rate-dependent behavior or have other complex characteristics. This yield surface is written in terms of a combined stress tensor $\boldsymbol{\phi}$ written in terms of the effective corotational Kirchhoff stress and the corotational backstress tensor $\hat{\mathbf{b}}$ as:

$$\boldsymbol{\phi} = \hat{\boldsymbol{\tau}} - \hat{\mathbf{b}}. \tag{2.43}$$

In order to account for the pressure dependency, the Drucker-Prager yield function depends on the first and second invariants of the combined stress tensor. The coefficients that complete the yield function are found by accounting for two different yield conditions at different pressure states as shown by Nguyen et al. (2016), where uniaxial tension and compression were used. This enhanced Drucker-Prager yield function writes:

$$\begin{cases} F(\boldsymbol{\phi}) = a_2\left(\phi^{\mathrm{eq}}\right)^{\alpha} - a_1\hat{\phi} - a_0 \leq 0, \\ a_2 = \frac{1}{\sigma_c^{\alpha}}; a_1 = 3\frac{m^{\alpha}-1}{m+1}\frac{1}{\sigma_c}; a_0 = \frac{m^{\alpha}+m}{m+1}, \\ \phi^{\mathrm{eq}} = \sqrt{\frac{3}{2}(\boldsymbol{\phi})^{\mathrm{dev}} : (\boldsymbol{\phi})^{\mathrm{dev}}}, \\ \hat{\phi} = \frac{1}{3}\operatorname{tr}\boldsymbol{\phi} = \frac{1}{3}\operatorname{tr}\hat{\boldsymbol{\tau}} - \frac{1}{3}\operatorname{tr}\hat{\mathbf{b}}, \end{cases} \tag{2.44}$$

where the exponent α is a material constant, $\operatorname{tr}\boldsymbol{\phi} = \boldsymbol{\phi}_{ii}$ and σ_c represents the isotropic compressive yield stress. Finally, $m = \frac{\sigma_t}{\sigma_c}$ is the ratio between the current compressive and tensile yield stresses, where σ_t represents the current tensile yield stress. The evolution of the tensile and compressive yield stresses will be dictated by a tensile (H_t) and a compressive (H_c) hardening functions respectively, and the evolution of the backstress tensor will be ruled by a kinematic hardening evolution law (H_b).

It is worth noting that as shown in Nguyen et al. (2016), the exponent α must satisfy the inequality $\alpha \geq 0$ in order to ensure the positive semidefinite condition of the Hessian:

$$\frac{\partial^2 F}{\partial\hat{\boldsymbol{\tau}}\partial\hat{\boldsymbol{\tau}}} = a_2\alpha\left(\phi^{\mathrm{eq}}\right)^{\alpha-1}\frac{\partial^2\phi^{\mathrm{eq}}}{\partial\hat{\boldsymbol{\tau}}\partial\hat{\boldsymbol{\tau}}} + a_2\alpha(\alpha-1)\left(\phi^{\mathrm{eq}}\right)^{\alpha-2}\frac{\partial\phi^{\mathrm{eq}}}{\partial\hat{\boldsymbol{\tau}}} \otimes \frac{\partial\phi^{\mathrm{eq}}}{\partial\hat{\boldsymbol{\tau}}}. \tag{2.45}$$

Flow potential and extended yield condition Following previous contributions (Al-Rub, Tehrani, and Darabi, 2015; Melro et al., 2013; Vogler, Rolfes, and Camanho, 2013), a non-associated flow rule is used for the correct capturing of the polymer behavior. The flow rule will then evolve in a direction normal to a plastic flow potential, which writes:

$$G = \phi^{\mathrm{eq}\,2} + \beta\hat{\phi}^2, \tag{2.46}$$

where β is a material parameter. This flow potential allows a correct control of the Poisson effect during plasticity. A plastic Poisson's ratio ν_p yields from this potential flow, modeling the volumetric plastic deformation. At the plastic flow onset, this ν_p writes (Melro et al., 2013):

$$\nu_p = \frac{9-2\beta}{18+2\beta}. \tag{2.47}$$

Once the plastic flow onset is reached, the plastic Poisson's ratio decreases from this value as plasticity evolves within the material.

The non-associated flow being defined, it is now possible to find the direction of the plastic flow normal to the plastic flow potential. This normal direction writes:

$$\mathbf{Q} = \frac{\partial G}{\partial\hat{\boldsymbol{\tau}}} = 3(\boldsymbol{\phi})^{\mathrm{dev}} + \frac{2\beta}{3}\hat{\phi}\mathbf{1}. \tag{2.48}$$

To consider the non-reversible nature of a process, it is necessary to incorporate an internal variable as the reference value. In this Work, this internal variable is chosen to be the equivalent plastic strain p. The reason for using this variable is that it allows quantifying the amount of plastic deformation that has occurred in a material, being an ideal indicator of the level of plasticity that it has sustained. The evolution of this plastic strain writes:

$$\dot{p} = k\sqrt{\dot{\boldsymbol{\varepsilon}}^{\mathrm{vp}} : \dot{\boldsymbol{\varepsilon}}^{\mathrm{vp}}} = k\lambda\sqrt{6\phi^{\mathrm{eq}\,2} + \frac{4}{3}\beta^2\hat{\phi}^2}, \tag{2.49}$$

where k is defined in terms of the plastic Poisson's ratio ν_p as:

$$k = \frac{1}{\sqrt{1+2\nu_p^2}} \quad ; \quad k = \sqrt{\frac{2}{3}} \quad \text{if incompressible flow rule.} \tag{2.50}$$

It is then possible to rewrite the extended yield condition presented in Eq. (2.41) as:

$$\bar{F} = \left(\frac{\phi^{\mathrm{eq}}}{\sigma_c}\right)^{\alpha} - 3\frac{m^{\alpha}-1}{m+1}\frac{\hat{\phi}}{\sigma_c} - \frac{m^{\alpha}+m}{m+1} - \left(\frac{\eta\dot{p}}{k\sqrt{6\phi^{\mathrm{eq}\,2}+\frac{4}{3}\beta^2\hat{\phi}^2}}\right)^{\gamma} \leq 0. \tag{2.51}$$

As it can be deduced from Eq. (2.51), the equivalent plastic deformation $\dot{p}$ allows to account for the rate dependent effects of the material.

Hardening modeling As already introduced, the hardening will be modeled through the effect of three hardening laws: the compressive and tensile isotropic hardenings, which will control the evolution of the compressive and tensile yield stresses, and the asymmetric plastic flow behavior and the kinematic hardening, which will model the evolution of the backstress tensor $\hat{\boldsymbol{b}}$.

The hardening evolution laws defining the evolution of the compressive and tensile isotropic yield stresses are defined as a function of the equivalent plastic strain $\dot{p}$ as:

$$\begin{cases} \dot{\sigma}_c = H_c(p)\dot{p}, \text{ with } \sigma_c(p=0) = \sigma_c^0, \\ \dot{\sigma}_t = H_t(p)\dot{p}, \text{ with } \sigma_t(p=0) = \sigma_t^0. \end{cases} \tag{2.52}$$

H_c and H_t, respectively stand for the compressive and tensile isotropic hardening moduli.

Finally, the kinematic hardening allows to describe the evolution of the corotational backstress tensor during the plastic evolution. The backstress tensor evolution writes:

$$\dot{\hat{\boldsymbol{b}}} = kH_b(p)\mathbf{D}^{\mathrm{vp}} \text{ with } \hat{\boldsymbol{b}}(p=0) = \mathbf{0}, \tag{2.53}$$

where H_b represents the kinematic hardening modulus.

2.3 Constitutive model implementation

To demonstrate the numerical implementation of the constitutive model, let us consider a particular time step $n+1$. The time increment between this step and the previous step is represented by Δt_n, such that the current time can be expressed as $t_{n+1} = t_n + \Delta t_n$. For the sake of conciseness, the subscript indicating the current time step $n+1$ will be omitted.

At time t_{n+1} the first Piola-Kirchhoff stress tensor writes:

$$\hat{\mathbf{P}} = \mathbf{F}^{\mathrm{ve}} \cdot \mathbf{S}^{\mathrm{ve}} \cdot \mathbf{F}^{\mathrm{vp}-T}, \tag{2.54}$$

where $\mathbf{S}^{\mathrm{ve}}$ (Eq. (2.25)) writes:

$$\mathbf{S}^{\mathrm{ve}} = \hat{\boldsymbol{\tau}} : \mathcal{L} \text{ with } \mathcal{L} = \left.\frac{\partial \ln \mathbf{C}^{\mathrm{ve}}}{\partial \mathbf{C}^{\mathrm{ve}}}\right|_{\mathbf{C}^{\mathrm{ve}}(t)}, \tag{2.55}$$

and where the derivative $\mathcal{L}$ is approximated following Eq. (2.26).

The viscous terms are found by integrating the expression given in Eq. (2.35). For the deviatoric part, one has:

$$(\boldsymbol{q}_i)^{\mathrm{dev}} = 2\mu_i(\mathbf{E}^{\mathrm{ve}})^{\mathrm{dev}} - \underbrace{\int_{-\infty}^{t} 2\mu_i \exp\left(-\frac{t-s}{g_i}\right)\frac{\mathrm{d}}{\mathrm{d}s}(\mathbf{E}^{\mathrm{ve}})^{\mathrm{dev}}(s)ds}_{\mathbf{A}_i}, \tag{2.56}$$

where $\mathbf{A}_i$ can be approximated using the midpoint rule as shown by Nguyen et al. (2016), yielding:

$$\begin{aligned}\mathbf{A}_i &= \int_{-\infty}^{t} 2\mu_i \exp\left(-\frac{t-s}{g_i}\right)\frac{\mathrm{d}}{\mathrm{d}s}(\mathbf{E}^{\mathrm{ve}})^{\mathrm{dev}}(s)ds \\ &\approx \mathbf{A}_{in}\exp\left(-\frac{\Delta t_n}{g_i}\right) + 2\mu_i \exp\left(-\frac{\Delta t_n}{2g_i}\right)\left((\mathbf{E}^{\mathrm{ve}})^{\mathrm{dev}} - (\mathbf{E}_n^{\mathrm{ve}})^{\mathrm{dev}}\right).\end{aligned} \tag{2.57}$$

The deviatoric term of the corotational Kirchhoff stress obtained in Eq.(2.38) can be found following equivalent computations to the ones used for $\operatorname{dev}\boldsymbol{q}_i$, obtaining:

$$(\hat{\boldsymbol{\tau}})^{\mathrm{dev}} = 2\mu_\infty(\mathbf{E}^{\mathrm{ve}})^{\mathrm{dev}} + \sum_{i=1}^{N}\mathbf{A}_i. \tag{2.58}$$

We note that the presence of the terms $\mathbf{A}_i$ does not allow to demonstrate the commutativity of $\boldsymbol{C}^{\mathrm{ve}}$ and $\hat{\boldsymbol{\tau}}$, see discussion on Eq. (2.23).

Similarly for the volumetric terms one has:

$$\frac{1}{3}\operatorname{tr}\boldsymbol{q}_i = \kappa_i \operatorname{tr}\mathbf{E}^{\mathrm{ve}} - \underbrace{\int_{-\infty}^{t}\kappa_i \exp\left(-\frac{t-s}{k_i}\right)\frac{\mathrm{d}}{\mathrm{d}s}\operatorname{tr}\mathbf{E}^{\mathrm{ve}}(s)ds}_{B_i}, \tag{2.59}$$

where, following equivalent computations as the ones followed for $\mathbf{A}_i$ one can find:

$$B_i = B_{in}\exp\left(-\frac{\Delta t_n}{k_i}\right) + \kappa_i \exp\left(-\frac{\Delta t_n}{2k_i}\right)\left(\operatorname{tr}\mathbf{E}^{\mathrm{ve}} - \operatorname{tr}\mathbf{E}_n^{\mathrm{ve}}\right). \tag{2.60}$$

As for the deviatoric term of $\hat{\boldsymbol{\tau}}$, it is therefore possible to find the expression for the volumetric term:

$$\frac{1}{3}\operatorname{tr}\hat{\boldsymbol{\tau}} = \kappa_\infty \operatorname{tr}\mathbf{E}^{\mathrm{ve}} + \sum_{i=1}^{N} B_i. \tag{2.61}$$

The corotational Kirchhoff stress can then be written by dividing it into its volumetric and deviatoric terms as:

$$\hat{\boldsymbol{\tau}} = (\hat{\boldsymbol{\tau}})^{\mathrm{dev}} + (\hat{\boldsymbol{\tau}})^{\mathrm{vol}}. \tag{2.62}$$

Introducing the expression of A_i Eq. (2.57) into Eq. (2.58) and using Eq. (2.31), the deviatoric part of the corotational Kirchhoff stress writes:

$$(\hat{\boldsymbol{\tau}})^{\mathrm{dev}} = \underbrace{2\hat{\mu}_\infty(\mathbf{E}^{\mathrm{ve}})^{\mathrm{dev}} + \sum_{i=1}^{N}\mathbf{A}_i}_{(\hat{\boldsymbol{\tau}}_0)^{\mathrm{dev}}} + \underbrace{2\hat{\mu}_\infty f_\mu((\mathbf{E}^{\mathrm{ve}})^{\mathrm{dev}})(\mathbf{E}^{\mathrm{ve}})^{\mathrm{dev}}}_{(\hat{\boldsymbol{\tau}}_c)^{\mathrm{dev}}}, \tag{2.63}$$

where $(\hat{\boldsymbol{\tau}}_0)^{\mathrm{dev}}$ is the term that is found in Nguyen et al. (2016), and $(\hat{\boldsymbol{\tau}}_c)^{\mathrm{dev}}$ is the deviatoric enhancement term that accounts for the nonlinear elastic response.

Carrying equivalent computations for the volumetric part using Eq. (2.30), one can find:

$$\frac{1}{3}\operatorname{tr}\hat{\boldsymbol{\tau}} = \underbrace{\hat{\kappa}_\infty \operatorname{tr}\mathbf{E}^{\mathrm{ve}} + \sum_{i=1}^{N} B_i}_{\frac{1}{3}\operatorname{tr}\hat{\boldsymbol{\tau}}_0} + \underbrace{\hat{\kappa}_\infty f_\kappa(\operatorname{tr}\mathbf{E}^{\mathrm{ve}})\operatorname{tr}\mathbf{E}^{\mathrm{ve}}}_{\frac{1}{3}\operatorname{tr}\hat{\boldsymbol{\tau}}_c}, \tag{2.64}$$

where $\frac{1}{3}\operatorname{tr}\hat{\boldsymbol{\tau}}_0$ is the term that is found in Nguyen et al. (2016), and $\frac{1}{3}\operatorname{tr}\hat{\boldsymbol{\tau}}_c$ is the pressure enhancement term.

During the time interval between t_n and t_{n+1}, the corotational Kirchhoff stress $\hat{\boldsymbol{\tau}}$, the viscoelastic deformation gradient $\mathbf{F}^{\mathrm{ve}}$, and the viscoplastic deformation gradient $\mathbf{F}^{\mathrm{vp}}$ are calculated using a predictor-corrector scheme. The scheme involves two stages, known as the viscoelastic predictor and viscoplastic corrector stages.

2.3.1 Viscoelastic predictor

The computation of the step $t_n \rightarrow t_{n+1}$ starts by a pure viscoelastic step in which a viscoelastic predictor state is obtained. First, the plastic deformation tensor $\mathbf{F}^{\mathrm{vp\,tr}}$ is assimilated to the previous step value $\mathbf{F}_n^{\mathrm{vp\,tr}}$, being possible to obtain the viscoelastic deformation gradient predictor as:

$$\mathbf{F}^{\mathrm{ve\,tr}} = \mathbf{F} \cdot \mathbf{F}^{\mathrm{vp\,tr}-1}. \tag{2.65}$$

Therefore, at this stage, the viscoelastic logarithmic operator will correspond to the quantity obtained through the current predictor of the plastic deformation tensor:

$$\mathbf{E}^{\mathrm{ve}} = \mathbf{E}^{\mathrm{ve\,tr}} = \frac{1}{2} \ln \mathbf{C}^{\mathrm{ve\,tr}}. \tag{2.66}$$

Using these new predictor values, the predictor of the corotational Kirchhoff stress writes:

$$\hat{\boldsymbol{\tau}}^{\mathrm{tr}} = (\hat{\boldsymbol{\tau}}^{\mathrm{tr}})^{\mathrm{dev}} + (\hat{\boldsymbol{\tau}}^{\mathrm{tr}})^{\mathrm{vol}} = (\hat{\boldsymbol{\tau}}_0{}^{\mathrm{tr}})^{\mathrm{dev}} + (\hat{\boldsymbol{\tau}}_0^{\mathrm{tr}})^{\mathrm{vol}} + (\hat{\boldsymbol{\tau}}_c{}^{\mathrm{tr}})^{\mathrm{dev}} + (\hat{\boldsymbol{\tau}}_c^{\mathrm{tr}})^{\mathrm{vol}}. \tag{2.67}$$

In this Equation, the deviatoric part of $\hat{\boldsymbol{\tau}}_0^{\mathrm{tr}}$ writes:

$$(\hat{\boldsymbol{\tau}}_0^{\mathrm{tr}})^{\mathrm{dev}} = 2\mu_e (\mathbf{E}^{\mathrm{ve\,tr}})^{\mathrm{dev}} - 2\left(\mu_e - \hat{\mu}_\infty\right)(\mathbf{E}_n^{\mathrm{ve}})^{\mathrm{dev}} + \sum_{i=1}^{N} \left[\mathbf{A}_{in} \exp\left(-\frac{\Delta t_n}{g_i}\right)\right], \tag{2.68}$$

where:

$$\mu_e = \hat{\mu}_\infty + \sum_{i=1}^{N} \mu_i \exp\left(-\frac{\Delta t_n}{2 g_i}\right). \tag{2.69}$$

The nonlinear deviatoric term writes:

$$(\hat{\boldsymbol{\tau}}_c^{\mathrm{tr}})^{\mathrm{dev}} = 2\hat{\mu}_\infty f_\mu((\mathbf{E}^{\mathrm{ve\,tr}})^{\mathrm{dev}})(\mathbf{E}^{\mathrm{ve\,tr}})^{\mathrm{dev}}, \tag{2.70}$$

while the volumetric term writes:

$$\frac{1}{3} \operatorname{tr} \hat{\boldsymbol{\tau}}_0^{\mathrm{tr}} = \kappa_e \operatorname{tr} \mathbf{E}^{\mathrm{ve\,tr}} - \left(\kappa_e - \hat{\kappa}_\infty\right) \operatorname{tr} \mathbf{E}_n^{\mathrm{ve}} + \sum_{i=1}^{N} \left[B_{in} \exp\left(-\frac{\Delta t_n}{k_i}\right)\right], \tag{2.71}$$

where:

$$\kappa_e = \hat{\kappa}_\infty + \sum_{i=1}^{N} \kappa_i \exp\left(-\frac{\Delta t_n}{2 k_i}\right), \tag{2.72}$$

with the nonlinear term:

$$\frac{1}{3} \operatorname{tr} \hat{\boldsymbol{\tau}}_c^{\mathrm{tr}} = \hat{\kappa}_\infty f_\kappa(\operatorname{tr} \mathbf{E}^{\mathrm{ve\,tr}}) \operatorname{tr} \mathbf{E}^{\mathrm{ve\,tr}}. \tag{2.73}$$

The predictor of the combined stress tensor is then written as:

$$\boldsymbol{\phi}^{\mathrm{tr}} = \hat{\boldsymbol{\tau}}^{\mathrm{tr}} - \hat{\mathbf{b}}_n = (\hat{\boldsymbol{\tau}}_0^{\mathrm{tr}})^{\mathrm{dev}} - \hat{\mathbf{b}}_n + (\hat{\boldsymbol{\tau}}_c^{\mathrm{tr}})^{\mathrm{dev}} + (\hat{\boldsymbol{\tau}}_0^{\mathrm{tr}})^{\mathrm{vol}} + (\hat{\boldsymbol{\tau}}_c^{\mathrm{tr}})^{\mathrm{vol}}. \tag{2.74}$$

Dividing $\boldsymbol{\phi}^{\text{tr}}$ into its deviatoric and volumetric terms one has:

$$(\boldsymbol{\phi}_0^{\text{tr}})^{\text{dev}} = (\hat{\boldsymbol{\tau}}_0^{\text{tr}})^{\text{dev}} - (\hat{\mathbf{b}}_n)^{\text{dev}}, \tag{2.75}$$

$$(\boldsymbol{\phi}_c^{\text{tr}})^{\text{dev}} = (\hat{\boldsymbol{\tau}}_c^{\text{tr}})^{\text{dev}}, \tag{2.76}$$

$$\hat{\phi}_0^{\text{tr}} = \frac{1}{3}\operatorname{tr}\boldsymbol{\phi}_0^{\text{tr}} = \frac{1}{3}\operatorname{tr}\hat{\boldsymbol{\tau}}_0^{\text{tr}} - \frac{1}{3}\operatorname{tr}\hat{\mathbf{b}}_n, \text{ and} \tag{2.77}$$

$$\hat{\phi}_c^{\text{tr}} = \frac{1}{3}\operatorname{tr}\boldsymbol{\phi}_c^{\text{tr}} = \frac{1}{3}\operatorname{tr}\hat{\boldsymbol{\tau}}_c^{\text{tr}}. \tag{2.78}$$

At the end of the predictor step, the yield condition is verified to satisfy the condition $F(\boldsymbol{\phi}^{\text{tr}}) \leq 0$. If this condition is not satisfied, a correction step is performed.

2.3.2 Viscoplastic correction

If the yield condition is not satisfied, plasticity is occurring within the material, and therefore, the accumulated plastic strain p should evolve. During this correction step, the plastic strain p is updated to satisfy the extended yield condition $\bar{F}$ Eq. (2.51).

Using the radial return mapping algorithm (Simo and Hughes, 2006), the viscoplastic deformation gradient writes:

$$\mathbf{F}^{\text{vp}} = \exp(\Gamma\mathbf{Q})\mathbf{F}_n^{\text{vp}}, \tag{2.79}$$

where Γ is defined as:

$$\Gamma = \int_{t_n}^{t} \lambda(t)dt. \tag{2.80}$$

This allows to correct the elastic deformation gradient and the right Cauchy tensor as:

$$\mathbf{F}^{\text{ve}} = \mathbf{F}\cdot\mathbf{F}^{\text{vp}-1} = \mathbf{F}\cdot\mathbf{F}_n^{\text{vp}-1}[\exp(\Gamma\mathbf{Q})]^{-1}, \tag{2.81}$$

$$\mathbf{C}^{\text{ve}} = [\exp(\Gamma\mathbf{Q})]^{-T}\cdot\mathbf{C}^{\text{ve}\,\text{tr}}\cdot[\exp(\Gamma\mathbf{Q})]^{-1}, \tag{2.82}$$

being possible to find the corrected expression for the viscoelastic logarithmic strain measure:

$$\mathbf{E}^{\text{ve}} = \mathbf{E}^{\text{ve}\,\text{tr}} - \Gamma\mathbf{Q}. \tag{2.83}$$

Applying the correction to the deviatoric and volumetric terms of the corotational Kirchhoff one has:

$$(\hat{\boldsymbol{\tau}})^{\text{dev}} = (\hat{\boldsymbol{\tau}}_0)^{\text{dev}} + (\hat{\boldsymbol{\tau}}_c)^{\text{dev}}, \text{ and} \tag{2.84}$$

$$\frac{1}{3}\operatorname{tr}\hat{\boldsymbol{\tau}} = \frac{1}{3}\operatorname{tr}\hat{\boldsymbol{\tau}}_0 + \frac{1}{3}\operatorname{tr}\hat{\boldsymbol{\tau}}_c, \tag{2.85}$$

where:

$$(\hat{\boldsymbol{\tau}}_0)^{\text{dev}} = 2\mu_e\left(\mathbf{E}^{\text{ve}\,\text{tr}} - \Gamma\mathbf{Q}\right)^{\text{dev}} - 2\left(\mu_e - \hat{\mu}_\infty\right)(\mathbf{E}_n^{\text{ve}})^{\text{dev}} + \sum_{i=1}^{N}\left[\mathbf{A}_{in}\exp\left(-\frac{\Delta t_n}{g_i}\right)\right], \tag{2.86}$$

which can be simplified to:

$$(\hat{\boldsymbol{\tau}}_0)^{\text{dev}} = (\hat{\boldsymbol{\tau}}_0^{\text{tr}})^{\text{dev}} - 2\mu_e\Gamma(\mathbf{Q})^{\text{dev}}. \tag{2.87}$$

The deviatoric nonlinear term reads:

$$(\hat{\boldsymbol{\tau}}_c)^{\text{dev}} = 2\hat{\mu}_\infty f_\mu((\mathbf{E}^{\text{ve tr}} - \Gamma\mathbf{Q}))^{\text{dev}}(\mathbf{E}^{\text{ve tr}} - \Gamma\mathbf{Q})^{\text{dev}}, \tag{2.88}$$

and the volume terms becomes:

$$\frac{1}{3}\operatorname{tr}\hat{\boldsymbol{\tau}}_0 = \kappa_e \operatorname{tr}(\mathbf{E}^{\text{ve tr}} - \Gamma\mathbf{Q}) - (\kappa_e - \hat{\kappa}_\infty)\operatorname{tr}\mathbf{E}_n^{\text{ve}} + \sum_{i=1}^{N}\left[B_{in}\exp\left(-\frac{\Delta t_n}{k_i}\right)\right], \tag{2.89}$$

which can be simplified to:

$$\frac{1}{3}\operatorname{tr}\hat{\boldsymbol{\tau}}_0 = \frac{1}{3}\operatorname{tr}\hat{\boldsymbol{\tau}}_0^{\text{tr}} - \kappa_e\Gamma\operatorname{tr}\mathbf{Q}, \tag{2.90}$$

while the nonlinear part eventually reads:

$$\frac{1}{3}\operatorname{tr}\hat{\boldsymbol{\tau}}_c = \hat{\kappa}_\infty f_k(\operatorname{tr}(\mathbf{E}^{\text{ve tr}} - \Gamma\mathbf{Q}))\operatorname{tr}(\mathbf{E}^{\text{ve tr}} - \Gamma\mathbf{Q}). \tag{2.91}$$

Eqs. (2.84) and (2.85) can therefore be written as:

$$(\hat{\boldsymbol{\tau}})^{\text{dev}} = \Delta(\hat{\boldsymbol{\tau}}_c)^{\text{dev}} + (\hat{\boldsymbol{\tau}}^{\text{ve tr}})^{\text{dev}} - 2\mu_e\Gamma(\mathbf{Q})^{\text{dev}}, \tag{2.92}$$

where $\Delta(\hat{\boldsymbol{\tau}}_c)^{\text{dev}} = (\hat{\boldsymbol{\tau}}_c)^{\text{dev}} - (\hat{\boldsymbol{\tau}}_c^{\text{tr}})^{\text{dev}}$, and:

$$\frac{1}{3}\operatorname{tr}\hat{\boldsymbol{\tau}} = \Delta(\frac{1}{3}\operatorname{tr}\hat{\boldsymbol{\tau}}_c) + \frac{1}{3}\operatorname{tr}\hat{\boldsymbol{\tau}}^{\text{tr}} - \kappa_e\Gamma\operatorname{tr}\mathbf{Q}, \tag{2.93}$$

where $\Delta(\frac{1}{3}\operatorname{tr}\hat{\boldsymbol{\tau}}_c) = \frac{1}{3}\operatorname{tr}\hat{\boldsymbol{\tau}}_c - \frac{1}{3}\operatorname{tr}\hat{\boldsymbol{\tau}}_c^{\text{tr}}$.

Finally, following Eq. (2.53), the backstress tensor is corrected as:

$$\hat{\mathbf{b}} = \hat{\mathbf{b}}_n + kH_b\Gamma\mathbf{Q}. \tag{2.94}$$

Using these new corrected expressions for $\hat{\boldsymbol{\tau}}$ and $\hat{\mathbf{b}}$ and making use of the definition of the normal $\mathbf{Q}$ found in Eq. (2.48), it is then possible to find the corrected expressions for $(\boldsymbol{\phi})^{\text{dev}}$, $\hat{\phi}$ and ϕ^{eq}:

$$(\boldsymbol{\phi})^{\text{dev}} = (\hat{\boldsymbol{\tau}})^{\text{dev}} - (\hat{\mathbf{b}})^{\text{dev}} = \Delta(\hat{\boldsymbol{\tau}}_c)^{\text{dev}} + (\boldsymbol{\phi}^{\text{tr}})^{\text{dev}} - 2\mu_e\Gamma(\mathbf{Q})^{\text{dev}} - kH_b\Gamma(\mathbf{Q})^{\text{dev}}, \tag{2.95}$$

being possible to express the updated value of $\boldsymbol{\phi}$ as:

$$(\boldsymbol{\phi})^{\text{dev}} = \frac{(\boldsymbol{\phi}^{\text{tr}})^{\text{dev}} + \Delta(\hat{\boldsymbol{\tau}}_c)^{\text{dev}}}{u}, \tag{2.96}$$

where $u = 1 + 6\breve{\mu}\Gamma$ and $\breve{\mu} = \mu_e + \frac{k}{2}H_b$. As a result, one can evaluate the equivalent combined stress following:

$$\phi^{\text{eq}} = \sqrt{\frac{3}{2}\frac{(\boldsymbol{\phi}^{\text{tr}})^{\text{dev}} + \Delta(\hat{\boldsymbol{\tau}}_c)^{\text{dev}}}{u} : \frac{(\boldsymbol{\phi}^{\text{tr}})^{\text{dev}} + \Delta(\hat{\boldsymbol{\tau}}_c)^{\text{dev}}}{u}} = \frac{(\boldsymbol{\phi}^{\text{tr}} + \Delta(\hat{\boldsymbol{\tau}}_c)^{\text{dev}})^{\text{eq}}}{u}. \tag{2.97}$$

Similarly, the volumetric term of $\hat{\boldsymbol{\tau}}$ writes:

$$\hat{\phi} = \frac{1}{3}\operatorname{tr}\hat{\boldsymbol{\tau}} - \frac{1}{3}\operatorname{tr}\hat{\mathbf{b}} = \Delta(\frac{1}{3}\operatorname{tr}\hat{\boldsymbol{\tau}}_c) + \hat{\phi}^{\mathrm{tr}} - \kappa_e\Gamma\operatorname{tr}\mathbf{Q} - \frac{1}{3}kH_b\Gamma\operatorname{tr}\mathbf{Q}. \tag{2.98}$$

Again, making use of the definition of $\mathbf{Q}$, Eq.(2.48), and solving for $\hat{\phi}$, it is possible to write it as:

$$\hat{\phi} = \frac{\hat{\phi}^{\mathrm{tr}} + \Delta(\frac{1}{3}\operatorname{tr}\hat{\boldsymbol{\tau}}_c)}{v}, \tag{2.99}$$

where $v = 1 + 2\beta\breve{\kappa}\Gamma$ and $\breve{\kappa} = \kappa_e + \frac{k}{3}H_b$.

With these corrections, Eq. (2.48) is rewritten as:

$$\mathbf{Q} = \frac{3((\boldsymbol{\phi}^{\mathrm{tr}})^{\mathrm{dev}} + \Delta(\hat{\boldsymbol{\tau}}_c)^{\mathrm{dev}})}{u} + \frac{2\beta}{3}\frac{\hat{\phi}^{\mathrm{tr}} + \Delta(\frac{1}{3}\operatorname{tr}\hat{\boldsymbol{\tau}}_c)}{v}\mathbf{1}. \tag{2.100}$$

The equivalent plastic deformation p can be now computed. Integrating Eq. (2.49) and making use of Eq. (2.80), its increment is approximated as:

$$\Delta p = k\Gamma\sqrt{\mathbf{Q}:\mathbf{Q}} = k\Gamma\underbrace{\sqrt{6\phi^{\mathrm{eq}\,2} + \frac{4}{3}\beta^2\hat{\phi}^2}}_{A}. \tag{2.101}$$

Using the corrected values of ϕ^{eq} and $\hat{\phi}$, it is possible to rewrite A as:

$$A = \sqrt{6\left(\frac{((\boldsymbol{\phi}^{\mathrm{tr}})^{\mathrm{dev}} + \Delta(\hat{\boldsymbol{\tau}}_c)^{\mathrm{dev}})^{\mathrm{eq}}}{u}\right)^2 + \frac{4}{3}\beta^2\left(\frac{\hat{\phi}^{\mathrm{tr}} + \Delta(\frac{1}{3}\operatorname{tr}\hat{\boldsymbol{\tau}}_c)}{v}\right)^2}. \tag{2.102}$$

The corrected extended yield condition $\bar{F}$ (Eq. 2.51) writes:

$$\bar{F} = a_2\left(\frac{((\boldsymbol{\phi}^{\mathrm{tr}})^{\mathrm{dev}} + \Delta(\hat{\boldsymbol{\tau}}_c)^{\mathrm{dev}})^{\mathrm{eq}}}{u}\right)^{\alpha} - a_1\frac{\hat{\phi}^{\mathrm{tr}} + \Delta(\frac{1}{3}\operatorname{tr}\hat{\boldsymbol{\tau}}_c)}{v} - a_0 - \left(\frac{\eta\Delta p}{\Delta t k\sqrt{6\phi^{\mathrm{eq}2} + \frac{4}{3}\beta^2\hat{\phi}^2}}\right)^{\gamma} = 0. \tag{2.103}$$

Using Eq. (2.101), and solving for Γ, one find that:

$$\Gamma = \frac{\Delta p}{k\sqrt{6(\phi^{\mathrm{eq}})^2 + \frac{4}{3}\beta^2\hat{\phi}^2}} = \frac{\Delta p}{kA}, \tag{2.104}$$

being possible to write $\bar{F}$ as:

$$\bar{F} = a_2\left(\frac{((\boldsymbol{\phi}^{\mathrm{tr}})^{\mathrm{dev}} + \Delta(\hat{\boldsymbol{\tau}}_c)^{\mathrm{dev}})^{\mathrm{eq}}}{u}\right)^{\alpha} - a_1\frac{\hat{\phi}^{\mathrm{tr}} + \Delta(\frac{1}{3}\operatorname{tr}\hat{\boldsymbol{\tau}}_c)}{v} - a_0 - \left(\eta\frac{\Gamma}{\Delta t}\right)^{\gamma} = 0. \tag{2.105}$$

To find the value of the only unknown variable in Eq. (2.105), Γ, the equation is solved using an iterative Newton-Raphson algorithm, for which it is necessary to compute:

$$\frac{\mathrm{d}\bar{F}}{\mathrm{d}\Gamma} = \frac{\partial\bar{F}}{\partial\Delta p}\frac{\partial\Delta p}{\partial\Gamma} + \frac{\partial\bar{F}}{\partial\Gamma}, \tag{2.106}$$

where $\frac{\partial\bar{F}}{\partial\Delta p}$, $\frac{\partial\Delta p}{\partial\Gamma}$ and $\frac{\partial\bar{F}}{\partial\Gamma}$ are developed in Appendix A.

At each step, a new value of $\frac{1}{3}\operatorname{tr}\hat{\boldsymbol{\tau}}_c$ shall therefore be computed, which, as shown by Eq. (2.91), depends on the corrected logarithmic strain measure $(\mathbf{E}^{\mathrm{ve\,tr}} - \Gamma\mathbf{Q})$. The dependency of the corrected logarithmic strain measure on the normal $\mathbf{Q}$, makes it dependent on the value that is being updated $\frac{1}{3}\operatorname{tr}\hat{\boldsymbol{\tau}}_c$, making it required the use of a secondary Newton Raphson iterative loop at fixed Γ. To this end, a new function J_v is defined as:

$$0 = J_v = \hat{\kappa}_\infty f_\kappa(\operatorname{tr}(\mathbf{E}^{\mathrm{ve\,tr}} - \Gamma\mathbf{Q}))\operatorname{tr}(\mathbf{E}^{\mathrm{ve\,tr}} - \Gamma\mathbf{Q}) - \frac{1}{3}\operatorname{tr}\hat{\boldsymbol{\tau}}_c, \tag{2.107}$$

where making use of Eq. (2.100):

$$\operatorname{tr}\mathbf{Q} = 2\beta\frac{\hat{\phi}^{\mathrm{tr}} + \Delta(\frac{1}{3}\operatorname{tr}\hat{\boldsymbol{\tau}}_c)}{v}. \tag{2.108}$$

The Jacobian of Eq. (2.107) at fixed Γ and using $\left.\frac{\partial(\operatorname{tr}\mathbf{Q}}{\partial(\frac{1}{3}\operatorname{tr}\hat{\boldsymbol{\tau}}_c)}\right|_\Gamma = \frac{2\beta}{v}$ writes:

$$\left.\frac{\partial J_v}{\partial(\frac{1}{3}\operatorname{tr}\hat{\boldsymbol{\tau}}_c)}\right|_\Gamma = -\frac{2\beta\Gamma}{v}\hat{\kappa}_\infty[\operatorname{tr}(\mathbf{E}^{\mathrm{ve\,tr}} - \Gamma\mathbf{Q})f'_\kappa + f_\kappa] - 1, \tag{2.109}$$

where f'_κ follows from Eq. (2.30) and writes;

$$f'_\kappa(\operatorname{tr}\mathbf{E}^{\mathrm{ve}}) = \frac{\partial f_\kappa}{\partial\operatorname{tr}\mathbf{E}^{\mathrm{ve}}} = \frac{2V_\kappa\vartheta_\kappa}{3}\left[1 - \tanh^2\left(\frac{\vartheta_\kappa}{3}(\operatorname{tr}\mathbf{E}^{\mathrm{ve}})^2 - \zeta_\kappa\right)\right]\operatorname{tr}\mathbf{E}^{\mathrm{ve}}. \tag{2.110}$$

A similar approach is followed for the deviatoric part following Eq. (2.88). Let us define the new function $\mathbf{J}_{dev}$:

$$0 = \mathbf{J}_{dev} = 2\hat{\mu}_\infty f_\mu((\mathbf{E}^{\mathrm{ve\,tr}} - \Gamma\mathbf{Q})^{\mathrm{dev}})(\mathbf{E}^{\mathrm{ve\,tr}} - \Gamma\mathbf{Q})^{\mathrm{dev}} - (\hat{\boldsymbol{\tau}}_c)^{\mathrm{dev}}, \tag{2.111}$$

where following Eq. (2.100) one has:

$$\mathbf{Q}^{\mathrm{dev}} = 3\frac{(\hat{\boldsymbol{\phi}}^{\mathrm{tr}})^{\mathrm{dev}} + \Delta(\hat{\boldsymbol{\tau}}_c)^{\mathrm{dev}}}{u}, \text{ and } \left.\frac{\partial\mathbf{Q}^{\mathrm{dev}}}{\partial(\hat{\boldsymbol{\tau}}_c)^{\mathrm{dev}}}\right|_\Gamma = \frac{3}{u}\left(\boldsymbol{I} - \frac{1}{3}\mathbf{1}\otimes\mathbf{1}\right), \tag{2.112}$$

where $\boldsymbol{I}$ stands for the fourth order identity tensor.

The Jacobian of $\mathbf{J}_{dev}$ therefore writes;

$$\left.\frac{\partial\mathbf{J}_{dev}}{\partial(\hat{\boldsymbol{\tau}}_c)^{\mathrm{dev}}}\right|_\Gamma = -\frac{6\Gamma}{u}\hat{\mu}_\infty\left[(\mathbf{E}^{\mathrm{ve\,tr}} - \Gamma\mathbf{Q})^{\mathrm{dev}}\otimes\mathbf{f}'_\mu + f_\mu\left(\boldsymbol{I} - \frac{1}{3}\mathbf{1}\otimes\mathbf{1}\right)\right] - \left(\boldsymbol{I} - \frac{1}{3}\mathbf{1}\otimes\mathbf{1}\right), \tag{2.113}$$

where the derivative $\mathbf{f}'_\mu$ follows from Eq. (2.31) and writes:

$$\mathbf{f}'_\mu((\mathbf{E}^{\mathrm{ve}})^{\mathrm{dev}}) = \frac{\partial f_\mu}{\partial(\mathbf{E}^{\mathrm{ve}})^{\mathrm{dev}}} = 2V_\mu\vartheta_\mu[1 - \tanh^2(\vartheta_\mu(\mathbf{E}^{\mathrm{ve}})^{\mathrm{dev}} : (\mathbf{E}^{\mathrm{ve}})^{\mathrm{dev}} - \zeta_\mu)](\mathbf{E}^{\mathrm{ve}})^{\mathrm{dev}}. \tag{2.114}$$

The scheme presented in Fig. 2.7 shows a summary of the plastic correction algorithm presented hereabove.

Once all the updated values are computed, it is possible to compute the updated first Piola-Kirchhoff stress $\hat{\mathbf{P}}$ using Eq. (2.54). Finally, the effective tangent operator $\hat{\mathbf{L}} = \frac{\partial\hat{\mathbf{P}}}{\partial\mathbf{F}}$ can be obtained as:

$$\hat{\mathbf{L}} = \frac{\partial\hat{\mathbf{P}}}{\partial\mathbf{F}} = \frac{\partial\mathbf{F}^{\mathrm{ve}}}{\partial\mathbf{F}}{}^{2}\cdot\left(\mathbf{S}^{\mathrm{ve}}\cdot\mathbf{F}^{\mathrm{vp-T}}\right) + \mathbf{F}^{\mathrm{ve}}\cdot{}^{1}\frac{\partial\mathbf{S}^{\mathrm{ve}}}{\partial\mathbf{F}}{}^{2}\cdot\mathbf{F}^{\mathrm{vp-T}} + (\mathbf{F}^{\mathrm{ve}}\cdot\mathbf{S}^{\mathrm{ve}})\cdot\frac{\partial\mathbf{F}^{\mathrm{vp-T}}}{\partial\mathbf{F}}. \tag{2.115}$$

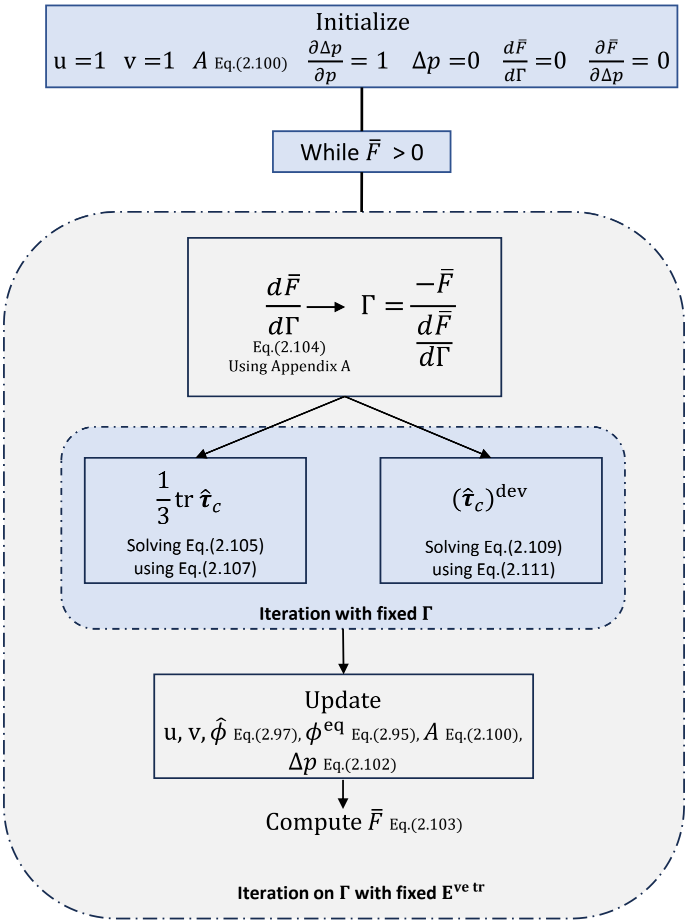

FIGURE 2.7: Plastic correction algorithm summary.

where $^i \cdot (\cdot^i)$ stands for the i^{th} left (right) dot product operator of two tensors considering the i^{th} index of the left (right) tensor. The derivatives required to compute the effective tangent operator $\hat{\mathbf{L}}$ can be found in Appendix A.

The numerical implementation of the here developed constitutive model was performed modifying the original C++ code of the pressure dependent model developed by Nguyen et al. (2016). The new strain dependent elastic stiffening introduces changes in the definition of the viscoelastic predictor and mainly in the viscoplastic correction, where the code is modified to account for the additional two new Newton Raphson loops which allow to find the volumetric and deviatoric terms of $\hat{\boldsymbol{\tau}}_c$. In addition, all the involved derivatives were adapted to account for the newly introduced terms. This code implementation allows to seamlessly switch from the original model to the enhanced without any further inconvenience.

2.4 SMP viscoelastic modeling

Polymers is a large family of materials that offers a wide range of properties and behaviors that allows its introduction to a large range of applications. One kind of polymer that is gaining interest in the scientific community is the shape memory polymer family. The concept of elastic memory was first introduced by Vernon et al. in their patent (Vernon and Vernon, U.S. Patent , 1941) when they observed that a styrene methacrylate resin could change shape when heated and cooled. Its properties were temporary shape fixation and recovery of the original shape. It was the beginning of a newly discovered a class of smart materials called shape memory polymers (SMPs). The shape memory effect can be observed in a wide variety of polymers, including thermoplastic and thermoset. Each of these polymers has unique properties that make them suitable for different applications and manufacturing processes. These polymers can change shape in response to certain stimuli, such as thermal phase transition. In this method, the polymer is deformed to a temporary shape by an external application of force, such as the application of pressure or stretching. After unloading the material, the polymer is heated above its phase transition or activation temperature, which is the temperature at which the polymer undergoes the phase transition and returns to its original shape.

For many fields of engineering, this discovery has been of major importance. Scientists have shown interest in the better understanding of its characteristics, and engineers have used the SMPs different and interesting applications in a wide variety of sectors. Self-regenerating materials, smart fabrics, reticular structures, solar cells, self-deployable structures, sensors, pipes, biomedical devices, among other applications, benefit from the introduction of SMPs (Sánchez et al., 2022; Zende, Ghase, and Jamdar, 2023).

Depending on the nature of the SMP used, the shape memory effect may be unidirectional or one-way or bidirectional, or two-way SMPs (see Figs. 2.8 and 2.9). Unidirectional SMPs (1W-SMPs) are designed to change from an initial shape to a specific final shape in one direction only, and then return to their original shape when the appropriate stimulus (such as temperature) is activated. However, once they have returned to the original shape, they cannot change shape without reprogramming. On the other hand, bidirectional SMPs (2W-SMPs) are programmed to change between two different final shapes in two opposite directions. This means that the material can change from an initial shape to an end shape 1 and subsequently return to the initial shape or change to end shape 2. Within the group of the 2W-SMPs, semi-crystalline polymers in particular, have a unique property in that they elongate during the crystallization phase when a constant stress is applied to them as shown in the experiments by Defize et al. (2012) and Sánchez et al. (2022). By reheating the sample under the same stress, the polymer can return to its initial high-temperature deformation state. Similarly, by cooling the sample under constant stress, the low-temperature deformation state can be recovered.

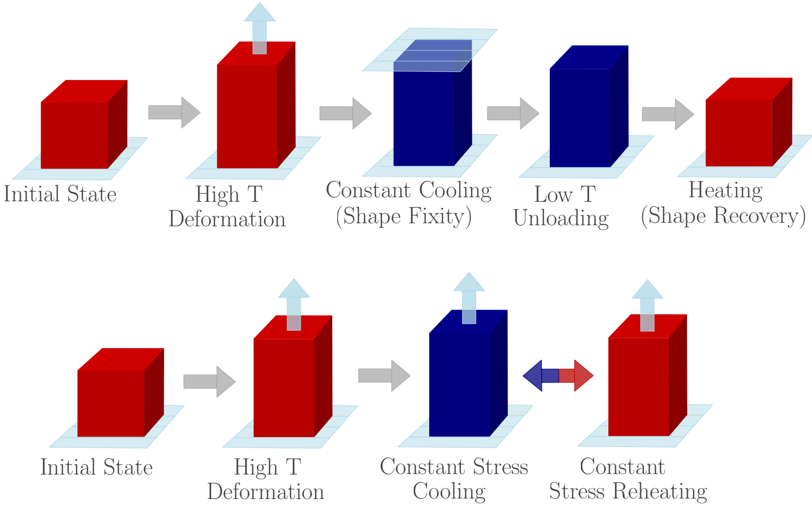

FIGURE 2.8: One way shape-memory behavior on top, and two-way shape-memory polymer behavior below.

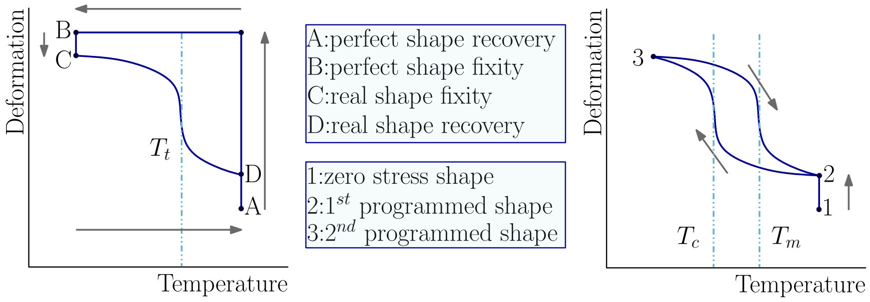

FIGURE 2.9: One way shape-memory behavior shown in a deformation-temperature plot on the left, and deformation-temperature plot of a two-way shape-memory polymer on the right.

Some polymers, such as shape memory polymers, exhibit elastic stiffening at high deformations, as observed by Srivastava, Chester, and Anand (2010). In order to demonstrate the advantages of the introduced correction, this model will be directly compared with results obtained in laboratory tests. A test campaign was conducted to investigate the shape memory behavior of a semicrystalline polymer, PCL76-4MAL/FUR 3 wt%CNT (Gulasik et al., 2023). This polymer was created as a thermoreversible network through the synthesis of star-shaped precursors based on PCL (polycaprolactone) containing terminal groups FUR (furano) or MAL (maleimide) via a Diels-Alder (DA) process. These precursors were co-precipitated with multi-walled carbon nanotubes (MWCNT) in a 3% weight ratio. This process is detailed in the work by Houbben et al. (2023). Thermomechanical cycles of uniaxial stress were studied using a dynamic mechanical analysis (DMA) testing machine, DMA Q800 (TA Instruments), on samples measuring approximately 1050.54mm^3. Since a DMA testing machine was employed, it is assumed that temperature and deformation were uniform within the sample, and numerical analysis was performed at a material point.

A viscoelastic-viscoplastic model for shape memory polymers was developed in the work by Gulasik et al. (2023); however, the elastic stiffening of the viscoelastic response observed during uniaxial tests above the transition temperature could not be captured. For this reason, the here developed enhanced version was developed. This Section will show the performance of the introduced enhanced terms and how this behavior can now be captured.

2.4.1 Model calibration

Shape memory polymers present very distinct behaviors at different temperatures, which allows them showing the so-called shape memory effect. The temperature difference introduces changes in the material microstructure. This Section aims to calibrate the hereabove presented model showing its capability of correctly capturing the elastic stiffening exhibited by these type of materials at large strains. To that end, two different tests will be used as reference in order to capture the behavior of this semi-crystalline polymer above the melting temperature of the crystalline phase and below the crystallization temperature of this phase. In particular it will be shown that considering the elastic stiffening is required in order to capture the viscoelastic response above the melting temperature. These tests will also give us the opportunity to directly compare the original model against the new enhanced model with the bulk and shear moduli stiffening terms.

2.4.1.1 Cyclic uniaxial tensile test at 65°C

The first test[2] consists of a cyclic uniaxial tensile test on DMA samples to assess material properties at high temperatures (65°C) under different stress levels: 0.6 MPa, 1.0 MPa, and 1.4

---

[2] This test was performed by Maxime Houbben and published in Gulasik et al. (2023)

MPa. The results of this test are presented in Fig. 2.10. Initially, the samples were heated to 65°C and held at this temperature for 10 minutes to achieve stabilization. The test was conducted by applying an initial deformation to eliminate any thermal expansion. Once a uniform temperature was reached, a constant rate load of 0.06 MPa/min was applied until reaching 0.6 MPa. Once this stress level was reached, the sample was suddenly released and left to rest for 5 minutes. This process was repeated four times, followed by the same procedure with the other stress levels. Resting times of 10 and 15 minutes were used for the 1.0 MPa and 1.4 MPa stresses, respectively. In the case of the 1.4 MPa stress level, some slippage at the grips was observed, as shown in Fig. 2.10(b). It was also noted that the material stiffness decreased even for the same stress level, suggesting damage to the material.

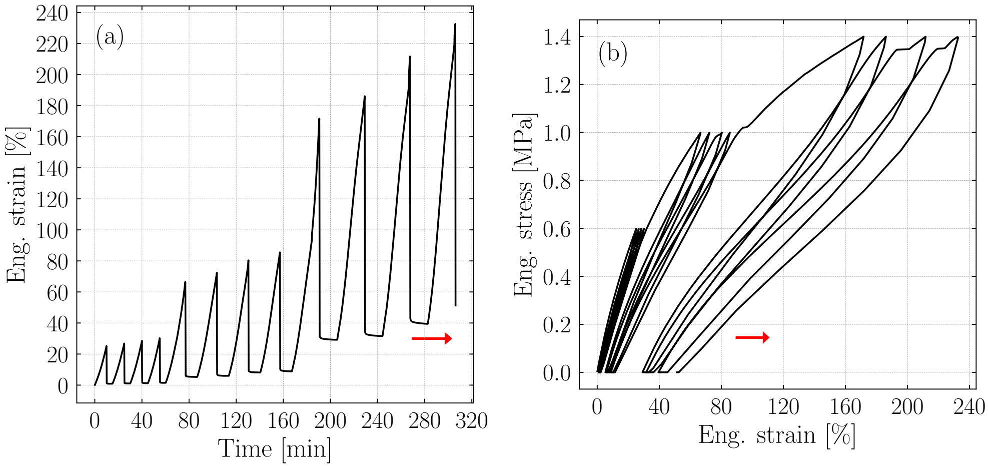

FIGURE 2.10: Experimental cyclic uni-axial tensile test measured at 65°C on the DMA samples: (a) Time-strain; and (b) Strain-stress curves. Experimental data from Gulasik et al. (2023)

Calibration was performed with reference to the first cycle shown in Fig. 2.10(a). In this first cycle, excessive permanent deformation is observed, which disappears in subsequent cycles at 0.6 MPa. This phenomenon represents the adaptation of the specimen to the load, a common behavior in polymers. In order to demonstrate the capability of the added bulk and shear stiffening terms in the original model, plasticity and damage evolution in the material are not required at this load level, simplifying the calibration of the model. The material properties were calibrated using the first test cycle to prevent the stiffness reduction, as illustrated in Fig. 2.11. Due to the limited available experimental data information, it was decided to use the same values for the parameters governing the bulk and shear moduli. The calibrated properties using two viscous branches are shown in Table 2.1.

TABLE 2.1: Constitutive model inputs and identified parameters for PCL76-4MAL/FUR 3 wt%CNT at 65^{o}C.

Property	**Value**	**Unit**
Young's moduli	$E_\infty = 3.15$, $E_1 = 0.181$, $E_2 = 0.181$	[MPa]
Bulk modulus stiffening	$V_\kappa = 3.89$, $\theta_\kappa = 1.09$, $\zeta_\kappa = 1.34$	[-]
Shear modulus stiffening	$V_\mu = 3.89$, $\theta_\mu = 1.09$, $\zeta_\mu = 1.34$	[-]
Bulk-shear relaxation times of viscous branches	$k_1 = g_1 = 8.15$, $k_2 = g_2 = 115.05$	[s]
Poisson's ratio	$\nu = 0.26$	[-]

It is evident that the obtained results closely approximate the behavior of the experimental test. In the Figure 2.11, a mild viscoelasticity is observed when the sample is suddenly released.

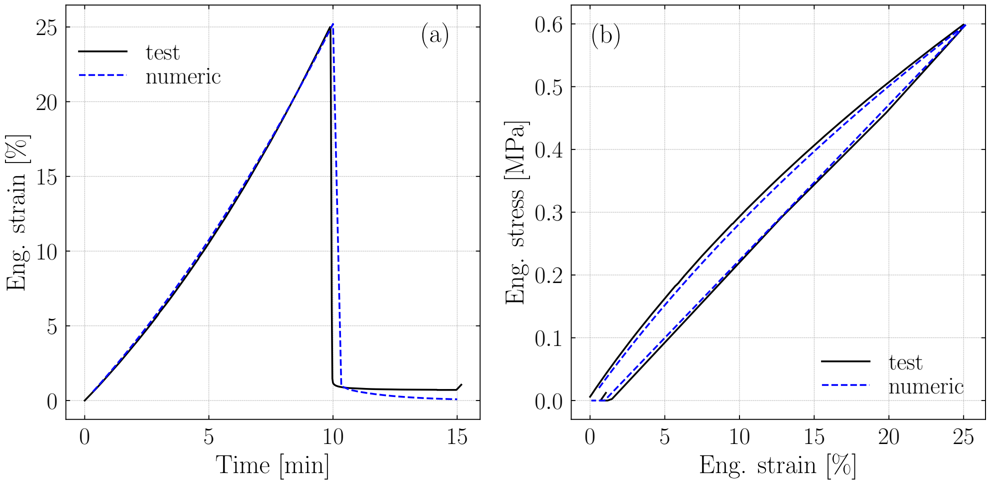

FIGURE 2.11: Experimental cyclic uni-axial tensile test vs. numerical result from our model obtained at 65°C: (a) Time-strain; and (b) Strain-stress curves. Experimental data from Gulasik et al. (2023).

2.4.1.2 Cyclic uniaxial tensile test at 0°C

Similar to the tests at 65°C, the material was tested at a temperature of 0°C under the same loading cycles as the previous test (see Fig. 2.12). In this test[3], the sample was cooled to 0°C and held at that temperature for 20 minutes to stabilize it, after which the initial thermal expansion was removed by resetting the deformation. As in the previous test, the material was loaded at a constant rate of 0.06 MPa/min to 0.6 MPa, followed by a sudden release. Then, the material was isothermally held at 0°C for 15 minutes. This loading cycle was repeated four times for each stress level.

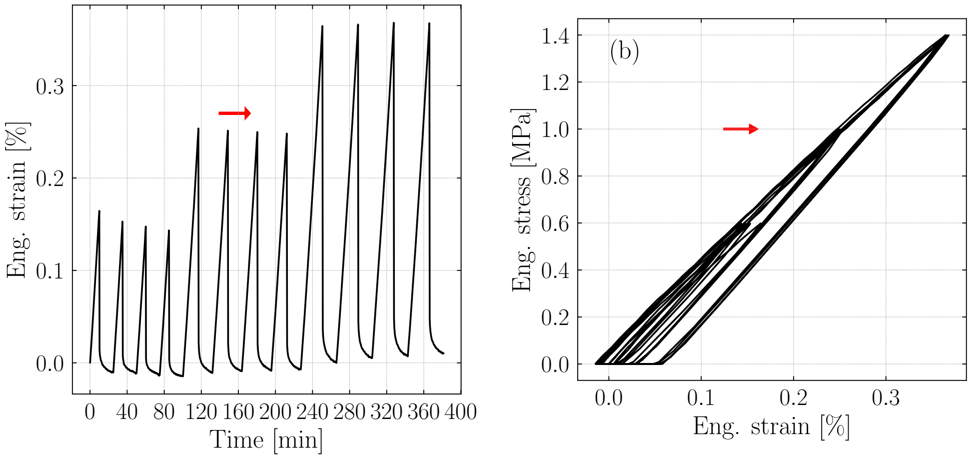

FIGURE 2.12: Experimental cyclic uni-axial tensile test measured at 0°C: (a) Time-strain; and (b) Strain-stress curves. Experimental data from Gulasik et al. (2023).

In this case, the stiffness of the crystallized phase is much higher than that of the melted phase, and a viscous effect can still be observed during the loading cycles. As for the previous case, it was decided to use the same values for the parameters governing the bulk and shear

---

[3] Test performed by Maxime Houbben and published in Gulasik et al. (2023)

moduli due to the limited experimental data information available. The calibrated viscoelastic properties are reported in Table 2.2.

TABLE 2.2: Constitutive model inputs and identified parameters for PCL76-4MAL/FUR 3 wt%CNT at 0^{o}C.

Property	**Value**	**Unit**
Young's moduli	$E_\infty = 383$, $E_1 = 89$, $E_2 = 90$	[MPa]
Bulk modulus stiffening	$V_\kappa = 1.37$, $\theta_\kappa = 0.685$, $\zeta_\kappa = 0.822$	[-]
Shear modulus stiffening	$V_\mu = 1.37$, $\theta_\mu = 0.685$, $\zeta_\mu = 0.822$	[-]
Bulk-shear relaxation times of vicous branches	$k_1 = g_1 = 8.15$, $k_2 = g_2 = 83.55$	[s]
Poisson's ratio	$\nu = 0.26$	[-]

The comparison of experimental test results and numerical model results for the first cycle at the highest stress level are shown in Fig. 2.13. The model is capable of accurately capturing the viscoelastic and hysteresis behavior, as illustrated in Fig. 2.13(b).

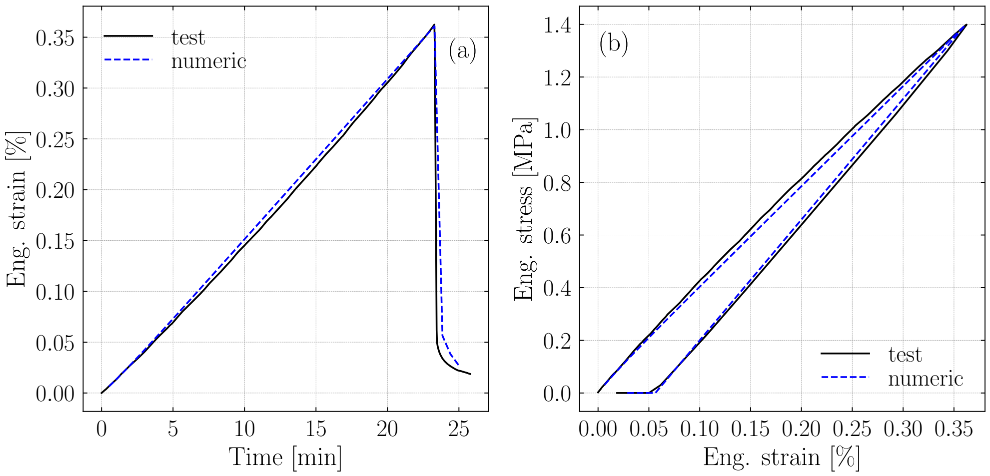

FIGURE 2.13: Experimental cyclic uni-axial tensile test vs. numerical result from our model obtained at 0°C: (a) Time-strain; and (b) Strain-stress curves. Experimental data from Gulasik et al. (2023).

2.4.2 Elastic stiffening at large deformation

After the viscoelastic calibrating the model and showing its capability to correctly capture the viscoelastic behavior of the material at different temperatures, this Section will focus on the ability of the bulk and shear moduli stiffening introduced in the original model to capture the large deformation stress states. To this end, the material was tested at 60°C, a temperature above the melting temperature of the crystalline phase. Therefore, the material properties reported in Table 2.1 obtained for the calibration of the material at 65°C will be used for the numerical simulations. The tests presented in this Section were load controlled with three different levels: 0.623 MPa, 0.973 MPa and 1.723 MPa. In order to avoid the damage evolution in the material observed in the cyclic test at high temperature, different specimens were used for each test.

The test started by heating the material sample to a temperature of 60°C. After 10 minutes allowing the sample to stabilize, the effect of the thermal expansion is removed by resetting the strain of the sample. Then, the sample is loaded isothermally at a rate of 0.06 MPa/min up to the final load level. The results of these tests and a direct comparison to the obtained numerical response can be observed in Fig. 2.14. In order to complete the understanding of the effect introduced by the bulk and shear moduli stiffening, the curves obtained using the original viscoelastic model without the introduction of these terms are added to the Figure.

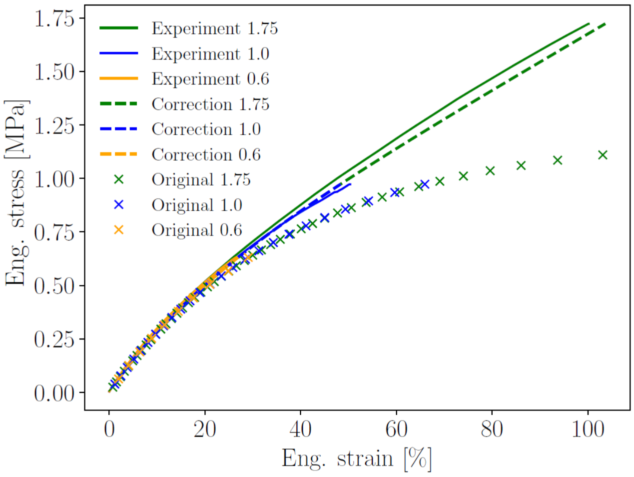

FIGURE 2.14: Engineering strain-Engineering stress curves of isothermal loads at a rate of 0.06 MPa/min up to the targeted stress of three different material samples. Comparison between experimental results, original viscoelastic model and bulk and shear moduli correction enhanced viscoelastic model. Experimental data from Gulasik et al. (2023).

Even though a slight stiffer behavior was shown by the sample used for the test in which the sample specimen was loaded up to 1.75MPa due to variations in the microstructure of the used samples, it is possible to observe the capability of the calibrated model of correctly capturing the stiffening behavior observed in the semi-crystalline polymer at large deformations of up to 100% engineering strain. The direct comparison between the enhanced model and the original one clearly shows the efficiency of the introduced bulk and shear stiffening terms capturing this behavior.

2.5 Summary

The complex behavior of the materials belonging to the family of polymers makes necessary the use of complex material models. This chapter presented an enhanced version of the large strain nonlocal damaged-enhanced viscoelastic-viscoplastic constitutive model developed by Nguyen et al. (2016) for the modeling of glassy polymer materials. The introduction of the bulk and shear moduli stiffening terms allows the model to capture the elastic stiffening observed on some hyperelastic polymer like the SMPs. This constitutive model uses a generalized Maxwell for the viscoelastic stage at low strains. The transition from the viscoelastic to the viscoplastic is bounded by an enhanced Drucker-Prager pressure dependent yield function. This enhanced version permits the representation of wide range of behaviors thanks to its ability to model different power yield surfaces including the classical Drucker-Prager yield surface. The viscoplastic flow was governed by a non-associated flow rule following a quadratic flow potential that allows a correct control of the Poisson effect during plasticity. The viscous effects were modeled through a non-associated Perzyna-type viscous model.

Damage was introduced into the model using a nonlocal implicit gradient formulation in order to circumvent the problem of the loss of solution uniqueness. Polymer materials exhibit a multi-stage nature of the damage evolution. With the goal of being able to mimic this behavior, a two-step damage model ruled by two softening damage scalar variables was used. First, a softening damage D_s permits the modeling of the post-peak softening. Then, once the failure stage is reached, a failure damage D_f is added to the damage definition. The damage evolution laws as well as the hardening laws will be developed later in Chapter 4, where the model is used to perform the full field simulations of the fiber reinforced RTM6 SVEs that will allow to conduct the stochastic multiscale simulations.

In order to show the efficiency of the bulk and shear moduli stiffening terms introduced in the model, the model was calibrated to mimic the behavior of the semicrystalline polymer, PCL76-4MAL/FUR 3 wt%CNT. Even though the uniqueness of the parameter calibration is difficult to proove due to the limited amount of experimental data, the purpose of this Section is to show the capability of the newly introduced elastic hardening to mimic the observed behavior of these kinds of materials for two extreme cases. A direct comparison between the results obtained with the enhanced model and the results obtained in experimental tests and using the original model clearly exposes the capability of the model to capture the elastic stiffening behavior shown by this material.

A more thorough calibration of the model was carried out in the work by Gulasik et al. (2023), where the introduction of this enhanced constitutive model in a phenomenological model for SMP allows the use of more experimental data to calibrate the here developed model. These bulk and shear moduli stiffening terms makes the model the perfect constitutive ingredient for a phenomenological model as exploited by Gulasik et al. (2023). This reference focuses on the modeling of highly nonlinear polymers exhibiting one-way and two-way shape memory effects under phase change. As shown in the 1D analogy of the model shown in Figure 2.15, this reference treats the semi-crystalline polymer as a two-phase composite material comprising a semi-crystalline (CR) phase and an amorphous (a) phase.

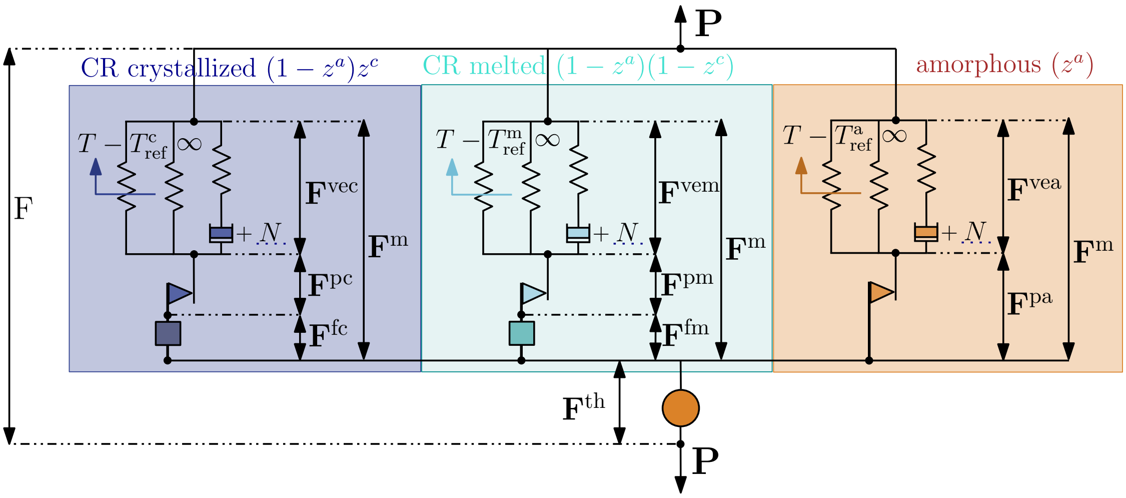

FIGURE 2.15: 1D analogy of the SMP constitutive model used by Gulasik et al. (2023).

The polymer operates above the T_g of the amorphous phase, assuming that the amorphous phase maintains a constant volume fraction (z^a) and constant material properties without undergoing phase changes with temperature. The temperature range of interest includes T_c and T_m, enabling the shape memory behavior through the phase transition of the crystalline phase. The crystalline phase is further divided into two phases: the crystallized phase (c) and the melted phase (m). The crystallized phase becomes active at low temperatures, while the melted phase becomes active at high temperatures, with both phases contributing during the phase transition. The volume fractions of the phases vary based on temperature and strain, following a temperature and strain dependent function (z^c) that represents the volume fraction of the glassy phase. Finally, the volume fractions of each phase, relative to the reference volume, are expressed as:

$$\begin{aligned} v^{\mathrm{c}} &= \left(1 - z^{\mathrm{a}}\right)\left(z^{\mathrm{c}}\right) \\ v^{\mathrm{m}} &= \left(1 - z^{\mathrm{a}}\right)\left(1 - z^{\mathrm{c}}\right) \\ v^{\mathrm{a}} &= \left(z^{\mathrm{a}}\right) \end{aligned} \tag{2.116}$$

The here developed model is used as constitutive model governing the mechanical deformation gradient of each of the branches together with other deformation measures to model temporary (imperfect shape fixity) and permanent (imperfect shape recovery) deformations in a thermomechanical loading cycle. In this work, the plasticity modeling developed in this Chapter is used to model plastic flow during the phase changes. This work is able to naturally capture the SMP behavior at different temperatures, including the load-dependent and anisotropic thermal expansion observed during the transition temperatures and permits to capture one-way and two-way shape memory effects as shown in Fig. 2.16.

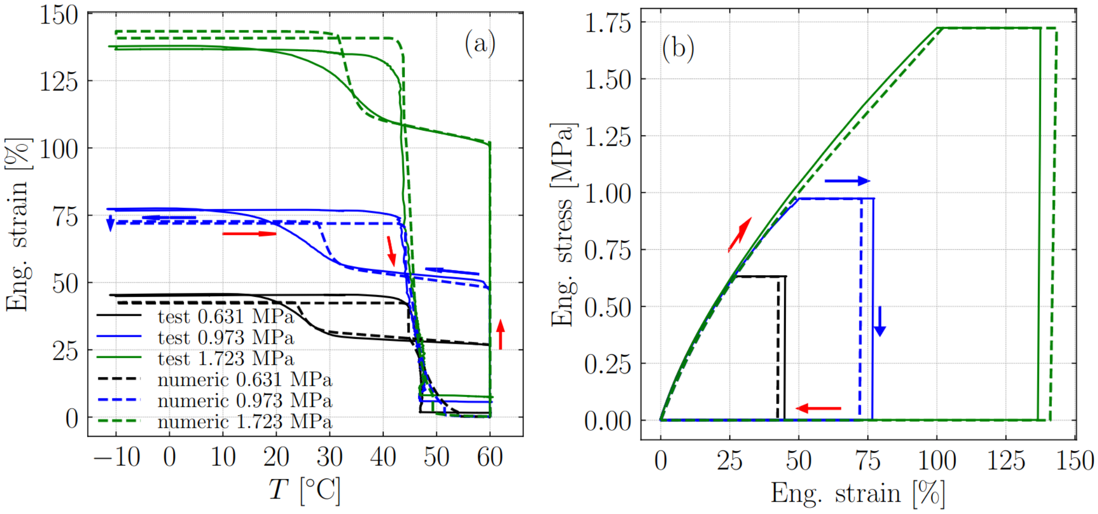

Figure 2.16: Two-Way Shape Memory test on DMA sample vs. numerical result under thermomechanical loading: (a) Temperature-strain; (b) Strain-stress curves. Results from Gulasik et al. (2023)

This Figure shows a direct comparison between experimental tests and the results obtained with the model developed in Gulasik et al. (2023). Starting at a temperature of 60°C, the sample is loaded isothermally at a rate of 0.06 MPa/min up to the final load level. Then, the specimen is cooled down to -10°C at a rate of 3°C/min, after which the specimen is suddenly unloaded. Finally, the specimen is heated up back to 60°C at a rate of 3°C/min. As observed, the model is capable of correctly capture the two-way behavior of the polymer, including the elastic stiffening observed in the first phase of the test and the apparent negative thermal expansion coefficient of the polymer before crystallization.

Chapter 3

Incremental-Secant implementation of a possibly damaged enhanced non-associated pressure-dependent plasticity model[1]

Among the homogenization methods recalled in Chapter 1, MFH is a semi-analytical technique developed to obtain efficient modeling of multi-phase composites. The main goal the of mean-field homogenization is to avoid the computation of the detailed microstrain or microstress fields by assuming relations between the volume averages of the strain and stress fields of each material phase. Some of the advantages that MFH presents over other homogenization techniques are its easiness of implementation in a FE code as a material law, its semi-analytical nature, and low computational requirements. The purpose of this Chapter is to extent the MFH to the pressure-dependent plasticity model presented in Chapter 2 but formulated in a small-strain setting.

The fundamental solution derived by J.D. Eshelby for single ellipsoidal inclusions (Eshelby and Peierls, 1957) served as a basis for the first mean-field homogenization (MFH) methods for linear-elastic cases and it is still considered as one of the most important solutions used in MFH. Most of the current models are still based on this fundamental solution, among which we can find the self-consistent model, (Kröner, 1958; Hill, 1965b; Hill, 1965a) which is mostly applicable for high inclusion volume fractions or poly-crystalline materials, the incremental or differential models (Maalej, Imene El Ghezal, and Doghri, 2013), or the Mori-Tanaka (M-T) model (Mori and Tanaka, 1973; Benveniste, 1987). By using similar steps to the ones used by Eshelby and Peierls (1957) on its single inclusion solution and applying it to a multiple-inclusions RVE, the M-T model is one of the most widely used MFH models for low and moderate inclusion volume fractions due to its ease of use and accurate predictions for two-phase composite materials. However, not all MFH methods are directly based on the Eshelby solution, as it is the case of the composite sphere assemblage proposed by Hashin (1962), the generalized self-consistent (GSC) model by Christensen and Lo (1979), which was based on the composite sphere assemblage and, the double inclusion model (Hori and Nemat-Nasser, 1993), that took inspiration from the GSC model formulating the ellipsoidal inclusions similarly to the M-T model.

Even though MFH models were initially developed for linear behaviors, they can be extended in order to represent material nonlinearities with very low computational cost. The most common approach is the definition of a linear comparison composite (LCC) (Talbot and Willis, 1985; Hill, 1965b). An LCC is a fictitious material defined from linear phases with the same behavior as the linearized behavior of the studied material. The LCC can be defined through different approaches, as for example through direct linearization of the nonlinear constitutive models of the material phases or through variational formulations. The single potential approach pioneered by Ponte Castañeda (Castaneda, 1991; Castaneda, 1992), the two-potential approach by Lahellec and Suquet (Lahellec and Suquet, 2007a; Lahellec and Suquet, 2007b) or the incremental

---

[1] This chapter is an adapted version of the paper (Calleja Vázquez et al., 2022)

variational (Miehe, 2002; Brassart et al., 2011; Brassart et al., 2012; Boudet et al., 2016; Lucchetta et al., 2019; Lucchetta et al., 2021) formulations are some examples of variational formulations. The direct linearization approach for the definition of the LCC is used in the secant formulation by Berveiller and Zaoui (1978), Tandon and Weng (1988), and so forth, to represent viscoplastic behaviors under proportional and monotonic loading conditions. Other approaches are the affine formulation (Molinari, Canova, and Ahzi, 1987; Masson et al., 2000; Pierard and Doghri, 2006) which is valid for arbitrary loading history of viscoplastic models, the incrementally affine formulation (Doghri, Adam, and Bilger, 2010; Miled et al., 2013), or the incremental-tangent formulation (Hutchinson and Hill, 1970; Hill, 1965b; Doghri and Ouaar, 2003; Mercier, Kowalczyk-Gajewska, and Czarnota, 2019), which allow representing arbitrary loading. There is one main drawback when using the affine, incrementally-affine and incremental-tangent formulations, which is the anisotropicity of their tangent operators. This generally leads to a stiff behavior, yielding inaccurate MFH predictions. In order to improve the MFH solution, it is possible to isotropize the tangent operators when computing the strain concentration tensors (Chaboche, Kanouté, and Roos, 2005; Haddad, Doghri, and Pierard, 2022). This step is not needed in the case of the incremental-secant linearization (Wu et al., 2017; Wu et al., 2013c; Wu et al., 2013a) since its material operators are isotropic by nature. The incremental-secant linearization first applies a fictitious elastic unloading to the studied composite material at a given step configuration. While the composite material reaches a zero-stress state, this is not the case for each of the phases, as these can have a residual stress. Then, the composite is reloaded until reaching the new composite configuration in the next step. The secant operators of each phase, which are naturally isotropic, are then used to define the LCC. This formulation allows for good accuracy in nonproportional loading conditions and damage-enhanced elasto-plastic cases as shown in the work by Wu et al. (2013a). In order to avoid the loss of ellipticity in the governing equations at the strain-softening onset, a nonlocal damage approach based on a Lemaitre-Chaboche approach was successfully introduced in the model.

The incremental-secant approach was developed by Wu et al. (Wu et al., 2013c; Wu et al., 2013a) by considering J2 plasticity in the different phases, meaning this approach was only valid for pressure insensitive materials. However, to be representative of the behavior of polymer-based materials, the phases response should account for a pressure dependent behavior. Such is the case for amorphous glassy polymers, which can present a high pressure dependence. This behavior was studied and modeled on fully discretized microstructures by Nguyen et al. (Nguyen et al., 2016; Nguyen, Wu, and Noels, 2019), who implemented a hyperelastic viscoelastic-viscoplastic-damage constitutive model based on a multimechanism nonlocal damage continuum to model the matrix phase of the composite material. This model showed great capabilities to mimic real epoxy materials like the high-crosslinked RTM6 epoxy resin (Nguyen, Wu, and Noels, 2019). However, the resolution time of this full discretization remains prohibitive, motivating the development of MFH embedding pressure-dependent phases. The behavior of polymeric material can be captured by considering a yield surface written in terms of the pressure and equivalent stress in combination with a non-associated plastic potential flow depending on the same two parameters defining the volume variation during plastic flow (Nguyen et al., 2016; Nguyen, Wu, and Noels, 2019; Melro et al., 2013; Chevalier, Camanho, and Pardoen, 2019). In this Work, it is thus intended to model the matrix phase of the composite material with the power-enhanced version of the pressure dependent yield surface in combination with the non-associated plastic potential developed by Nguyen et al. (2016) and recalled in Chapter 2. The anisotropic and more complex behavior of the composite material naturally arises from the homogenization process.

Pressure-sensitive models have been applied in homogenization methods, especially in homogenization of rock-like and porous materials, where taking into consideration the hydrostatic pressure effect on the material behavior is of crucial importance. Such is the case of Guéry et al. (2008), who developed a two-step homogenization procedure to study the behavior of callovo-oxfordian argillites or Shen et al. (2012) who studied the mechanical behavior of clayey rocks with a plastic compressible porous matrix. In order to capture the pressure sensitive behavior of these materials, the Drucker-Prager-based yield criterion was used in both works, which based their nonlinear homogenization techniques on an adaptation of the incremental method proposed by Hill (1965b), which formulates the macroscopic tangent operator accounting for nonlinear local behaviors on each phase of the composite. One of the main drawbacks of this procedure is the stiff behavior that the homogenized results present at the macroscopic level. In order to solve this problem, both works opted to implement an isotropization technique to improve the obtained material response. Composite materials are also a domain in which the hydrostatic pressure effects are important. An example is the work by Kaiser and Stommel (2014), which focused on improving the modeling of short fiber reinforced thermoplastics by using the quadratic yield formulation proposed by Kolling et al. (2005). This yield criterion was implemented in the second moment incremental formulation-based MFH approach developed for elastic-plastic composites by Doghri et al. (2011). Recently, this model has been used in the work by Naili and Doghri (2023), where a predictive micromechanical approach for analyzing porous materials with elasto-plastic matrices is developed. As for the previous cases, an isotropization step was needed in order to avoid over-stiff behaviors, for which the isotropization proposed by Bornert, Bretheau, and Gilormini (2001) was applied. Other approaches such as introducing a pressure sensitivity in the damage evolution law have been studied, although, wrong predictions were obtained. Such is the case of Krairi (2015), who proved that the introduction of pressure-sensitivity in the damage law evolution was not enough to capture the correct pressure effect on the studied materials.

The aim of this Work is to develop a pressure-dependent MFH by implementing the constitutive model developed in Chapter 2, this time in an infinitesimal strain formulation, in Wu et al. (Wu et al., 2013c; Wu et al., 2013a) incremental-secant approach. We will show that the incremental-secant approach allows defining naturally isotropic operators for pressure-sensitive models, circumventing the need for an isotropization step as in other formulations. We will also show that the approach inherits the benefits of the incremental-secant approach, that is, its ability to consider damaging phases and to remain accurate under nonproportional loading conditions. The model is completed with the possibility to account for damage in the matrix phase by using an implicit nonlocal approach, which avoids the loss of ellipticity that is found in local formulations once the strain softening onset is reached. The implementation enables thus to take into account this pressure-dependent behavior observed in polymer-based materials while keeping the mentioned advantages.

Regarding the structure of this Chapter, Section 3.1 starts by presenting a recall of MFH incremental-secant generalities. When considering homogenization of composite materials through a MFH scheme, scalar damage variables can be considered in each phase in order to capture the composite response (Wu et al., 2021). In this Work, we consider the damage of the matrix phase only since we are interested in accounting for the effect of the pressure-dependent yield surface on the homogenization scheme. In that case, it was shown by Nguyen et al. (2016), model in which the constitutive model recalled in Chapter 2 was based, that a scalar damage variable framed in a Lemaitre-Chaboche damage model was able to capture the failure of high-crosslinked polymer materials, including in 3D tests with barreling effects. As in the model recalled in Chapter 2, which was developed by Nguyen et al. (2016), the authors also considered a second damage variable to capture the post peak saturated softening observed under compressive loading, which is neglected in the present work: introducing this second scalar damage variable in the model does not require to modify the formulation since an equivalent damage variable can be obtained from two damage evolution laws. Then, Section 3.2 opens with a brief introduction of the pressure-sensitive yield function used and continues with its mathematical implementation in the residual incremental-secant approach. Section 3.3 introduces then the pressure-sensitive mean-field homogenization scheme. This MFH scheme is later verified in Section 3.4 for the elasto-plastic and damage-enhanced elasto-plastic cases by comparing the MFH predictions to full-field FE simulations on 2D UD composite RVE and 3D composites reinforced with spherical inclusions. In Section 3.5, the approach is further validated against a macroscale transverse compression experiment performed on a UD composite sample.

3.1 MFH recall

In this Section, a brief presentation of the basis of the MFH method using the Mori-Tanaka assumption is provided. Then, the incremental-secant MFH is recalled introducing the residual and zero incremental-secant operators.

3.1.1 MFH generalities

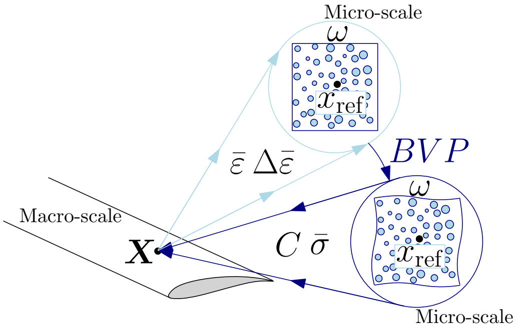

FIGURE 3.1: Multiscale simulation scheme.

Considering a multiscale problem (Figure 3.1), two different scales are present: the macroscale and the microscale. At the macroscale, either the macrostrain $\bar{\boldsymbol{\varepsilon}}$ or the macrostress $\bar{\boldsymbol{\sigma}}$ is known at a given point $\boldsymbol{X}$ and the unknown quantity is obtained by solving a microscale boundary-value problem (BVP). This point $\boldsymbol{X}$, from a microscale perspective, represents a set of points $\boldsymbol{x}_{\text{ref}}$ that belongs to a RVE domain, such that $\boldsymbol{x}_{\text{ref}} \in \omega$, with a boundary $\partial\omega$. As a two-phase composite material is taken into account, the subindex 0 represents the matrix subdomain ω_0 and the subindex I the inclusion subdomain ω_{I}.

As already stated, the MFH assumes relations between volume averages of the stress or strain fields of each phase, which avoids the high computational requirements needed for the complete resolution of the microstrain/microstress fields. The average stress ($\boldsymbol{\sigma}_i$) and strain ($\boldsymbol{\varepsilon}_i$) of a given phase ω_i can be computed as:

$$\begin{aligned} \boldsymbol{\sigma}_i &= \frac{1}{|\omega_i|}\int_{\omega_i} \boldsymbol{\sigma}(\boldsymbol{x}_{\text{ref}})dV, \\ \boldsymbol{\varepsilon}_i &= \frac{1}{|\omega_i|}\int_{\omega_i} \boldsymbol{\varepsilon}(\boldsymbol{x}_{\text{ref}})dV, \end{aligned} \tag{3.1}$$

where dV stands for the differential volume. The scale transition is written as a relation between the macrostrains and macrostresses and the RVE average strains. In the studied case of two-phase isothermal composite material, having the matrix (v_0) and inclusion (v_{I}) volume fractions such that $v_0 + v_{\text{I}} = 1$, the scale transition can be rewritten as:

$$\begin{cases} \bar{\boldsymbol{\varepsilon}} = v_0\boldsymbol{\varepsilon}_0 + v_{\text{I}}\boldsymbol{\varepsilon}_{\text{I}}, \\ \bar{\boldsymbol{\sigma}} = v_0\boldsymbol{\sigma}_0 + v_{\text{I}}\boldsymbol{\sigma}_{\text{I}}. \end{cases} \tag{3.2}$$

3.1.1.1 Linear behavior

Completing Eq. (3.2) with the constitutive laws of each of the phases one can write:

$$\begin{cases} \boldsymbol{\sigma}_0 = \boldsymbol{C}_0^{\mathrm{el}} : \boldsymbol{\varepsilon}_0, \\ \boldsymbol{\sigma}_{\mathrm{I}} = \boldsymbol{C}_{\mathrm{I}}^{\mathrm{el}} : \boldsymbol{\varepsilon}_{\mathrm{I}}, \end{cases} \tag{3.3}$$

where the constitutive material tensors $\boldsymbol{C}_i^{\mathrm{el}}$ are considered to be uniform per phase.

The MFH scheme reduces the complexity of the SVE formulation, by assuming a simplified morphology of the SVE in which only an ellipsoidal inclusion defined by the geometrical property (I) and volume fraction (v_{I}) is embedded into the matrix phase. By defining a strain concentration tensor $\boldsymbol{B}^{\epsilon}$, it is possible to link the strain averages of the matrix and inclusion phases:

$$\boldsymbol{\varepsilon}_{\mathrm{I}} = \boldsymbol{B}^{\epsilon}\left(\mathrm{I}, \boldsymbol{C}_0^{\mathrm{el}}, \boldsymbol{C}_{\mathrm{I}}^{\mathrm{el}}\right) : \boldsymbol{\varepsilon}_0, \tag{3.4}$$

where I stands for the geometrical information of the inclusions required to define $\boldsymbol{B}^{\epsilon}$.

Due to its good performance for two-phase composite materials for which the matrix can be identified, the Mori-Tanaka (M-T) model (Mori and Tanaka, 1973) is used to define the strain concentration. Assuming this model, the strain concentration $\boldsymbol{B}^{\epsilon}$ reads:

$$\boldsymbol{B}^{\epsilon}\left(\mathrm{I}, \boldsymbol{C}_0^{\mathrm{el}}, \boldsymbol{C}_{\mathrm{I}}^{\mathrm{el}}\right) = \left\{\boldsymbol{I} + \boldsymbol{S}\left(\mathrm{I}, \boldsymbol{C}_0^{\mathrm{el}}\right) : \left[\left(\boldsymbol{C}_0^{\mathrm{el}}\right)^{-1} : \boldsymbol{C}_{\mathrm{I}}^{\mathrm{el}} - \boldsymbol{I}\right]\right\}^{-1}, \tag{3.5}$$

where $\boldsymbol{S}$ stands for the Eshelby tensor (Eshelby and Peierls, 1957) that depends on the geometry of the inclusions (I) and the matrix elastic operator $\boldsymbol{C}_0^{\mathrm{el}}$, and $\boldsymbol{I}$ is the fourth order identity tensor.

For the case of linear elastic composites, Eqs. (3.2, 3.3 and 3.4) can be used to write the following constitutive equation:

$$\bar{\boldsymbol{\sigma}} = \bar{\boldsymbol{C}}^{\mathrm{el}}\left(\mathrm{I}, \boldsymbol{C}_0^{\mathrm{el}}, \boldsymbol{C}_{\mathrm{l}}^{\mathrm{el}}, v_{\mathrm{l}}\right) : \bar{\boldsymbol{\varepsilon}}, \tag{3.6}$$

where $\bar{\boldsymbol{C}}^{\mathrm{el}}$ writes:

$$\bar{\boldsymbol{C}}^{\mathrm{el}}\left(\mathrm{I}, \boldsymbol{C}_0^{\mathrm{el}}, \boldsymbol{C}_{\mathrm{I}}^{\mathrm{el}}, v_{\mathrm{l}}\right) = \left[v_{\mathrm{I}}\boldsymbol{C}_{\mathrm{I}}^{\mathrm{el}} : \boldsymbol{B}^{\epsilon}\left(\mathrm{I}, \boldsymbol{C}_0^{\mathrm{el}}, \boldsymbol{C}_{\mathrm{I}}^{\mathrm{el}}\right) + v_0\boldsymbol{C}_0^{\mathrm{el}}\right] : \left[v_{\mathrm{I}}\boldsymbol{B}^{\epsilon}\left(\mathrm{I}, \boldsymbol{C}_0^{\mathrm{el}}, \boldsymbol{C}_{\mathrm{I}}^{\mathrm{el}}\right) + v_0\boldsymbol{I}\right]^{-1}. \tag{3.7}$$

3.1.1.2 Nonlinear behavior

As already stated in the Introduction, the MFH method was extended to nonlinear behaviors through the use of a Linear Comparison Composite. This LCC is a fictitious material with linear phases, whose behavior is the same as the linearized behavior of the original composite material. Therefore, considering a material with a matrix phase with virtual elastic operator $\boldsymbol{C}_0^{\mathrm{LCC}}$ and inclusions phase with virtual elastic operator $\boldsymbol{C}_{\mathrm{I}}^{\mathrm{LCC}}$, it is possible to write the MFH equations of a linear composite material. In this case, the relation between the incremental strains of both phases Eq. (3.4) can be written as:

$$\Delta\boldsymbol{\varepsilon}_{\mathrm{I}} = \boldsymbol{B}^{\epsilon}\left(\mathrm{I}, \boldsymbol{C}_0^{\mathrm{LCC}}, \boldsymbol{C}_{\mathrm{I}}^{\mathrm{LCC}}\right) : \Delta\boldsymbol{\varepsilon}_0, \tag{3.8}$$

and the relations between the macro and the micro strains and stresses Eq. (3.2) write:

$$\begin{cases} \Delta\bar{\boldsymbol{\varepsilon}} = v_0\Delta\boldsymbol{\varepsilon}_0 + v_{\mathrm{I}}\Delta\boldsymbol{\varepsilon}_{\mathrm{I}}, \\ \bar{\boldsymbol{\sigma}} = v_0\boldsymbol{\sigma}_0 + v_{\mathrm{I}}\boldsymbol{\sigma}_{\mathrm{I}}. \end{cases} \tag{3.9}$$

By using the virtual elastic operators $\boldsymbol{C}_0^{\mathrm{LCC}}$ and $\boldsymbol{C}_{\mathrm{I}}^{\mathrm{LCC}}$ of the LCC, the Mori-Tanaka model (Mori and Tanaka, 1973) that defines $\boldsymbol{B}^{\epsilon}$ is rewritten as:

$$\boldsymbol{B}^{\epsilon} = \left\{\boldsymbol{I} + \boldsymbol{S} : \left[\left(\boldsymbol{C}_0^{\mathrm{LCC}}\right)^{-1} : \boldsymbol{C}_{\mathrm{I}}^{\mathrm{LCC}} - \boldsymbol{I}\right]\right\}^{-1}. \tag{3.10}$$

Several approaches have been developed to define this LCC, as for example through linearization of the nonlinear constitutive models of the material phases (Berveiller and Zaoui, 1978; Tandon and Weng, 1988) or through variational formulations (Castaneda, 1991; Lahellec and Suquet, 2007a; Miehe, 2002; Brassart et al., 2011; Boudet et al., 2016; Lucchetta et al., 2019). Other approaches are the affine formulation (Molinari, Canova, and Ahzi, 1987; Masson et al., 2000; Pierard and Doghri, 2006), the incrementally affine formulation (Doghri, Adam, and Bilger, 2010; Miled et al., 2013), or the incremental-tangent formulation (Hutchinson and Hill, 1970; Hill, 1965b; Doghri and Ouaar, 2003; Mercier, Kowalczyk-Gajewska, and Czarnota, 2019). These formulations yield anisotropic formulations of their tangent operators, leading to stiff predictions of the material behavior and therefore needing an isotropization step (Chaboche, Kanouté, and Roos, 2005). This step is not needed in the case of the incremental-secant linearization (Wu et al., 2017; Wu et al., 2013c; Wu et al., 2013a; Haddad, Doghri, and Pierard, 2022; Calleja Vázquez et al., 2022) since its material operators are isotropic by nature. In this Work, the incremental-secant formulation is used.

3.1.2 Incremental-secant MFH (Wu et al., 2013a)

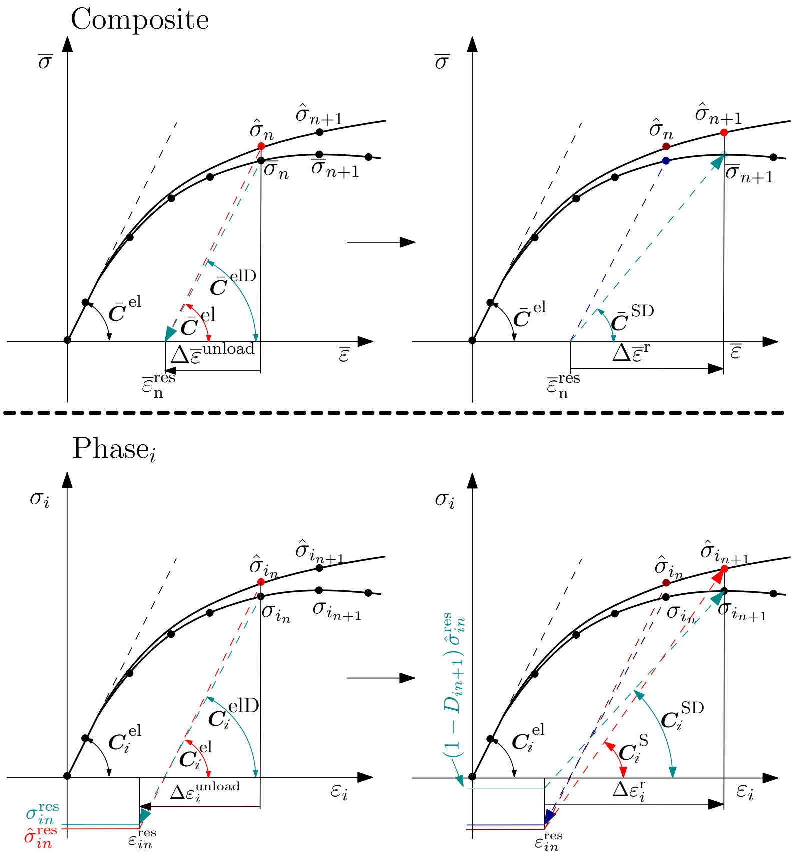

FIGURE 3.2: Composite and phase elastic unloading and loading processes for LCC definition for damage-enhanced elasto-plastic materials. Virtual elastic unloading on the left pictures and incremental-secant loading on the right pictures.

Let us consider a time step interval $[t_n, t_{n+1}]$ in which strain increments $\Delta\bar{\boldsymbol{\varepsilon}}_{n+1}$ and $\Delta\boldsymbol{\varepsilon}_{i_{n+1}}$ are applied to the composite material and its phases respectively, such that the total strain at t_{n+1} yields:

$$\bar{\boldsymbol{\varepsilon}}_{n+1} = \bar{\boldsymbol{\varepsilon}}_n + \Delta\bar{\boldsymbol{\varepsilon}}_{n+1} \text{ and } \boldsymbol{\varepsilon}_{i_{n+1}} = \boldsymbol{\varepsilon}_{i_n} + \Delta\boldsymbol{\varepsilon}_{i_{n+1}}. \tag{3.11}$$

The damage effect is introduced by a single scalar value (D_i) with a Lemaitre-Chaboche approach. In this case, the elasto-plastic (EP) flow is evaluated in the apparent stress state. The concept of effective stress ($\hat{\boldsymbol{\sigma}}_i$) is therefore introduced, having:

$$\hat{\boldsymbol{\sigma}}_i = \frac{\boldsymbol{\sigma}_i}{1 - D_i}. \tag{3.12}$$

Let us detail the operations carried at each step.

3.1.2.1 Virtual elastic unloading

As recalled in the introduction, the incremental-secant approach first virtually unloads the composite material to a zero-stress state (see Figure 3.2), but this is not necessarily the case for the phases composing the composite material, since each sees a residual stress ($\hat{\boldsymbol{\sigma}}_{i_n}^{\text{res}}$) and a residual strain tensor ($\boldsymbol{\varepsilon}_{i_n}^{\text{res}}$).

One thus defines the unloading and residual stress states as:

$$\begin{cases} \Delta\boldsymbol{\varepsilon}_i^{\text{unload}} = \boldsymbol{\varepsilon}_{i_n} - \boldsymbol{\varepsilon}_{i_n}^{\text{res}} \\ \bar{\boldsymbol{\sigma}}_n^{\text{res}} = 0 = \bar{\boldsymbol{\sigma}}_n - \bar{\boldsymbol{C}}^{\text{elD}} : \Delta\bar{\boldsymbol{\varepsilon}}^{\text{unload}}, \\ \hat{\boldsymbol{\sigma}}_{i_n}^{\text{res}} = \hat{\boldsymbol{\sigma}}_{i_n} - \boldsymbol{C}_i^{\text{el}} : \Delta\boldsymbol{\varepsilon}_i^{\text{unload}}, \end{cases} \tag{3.13}$$

being $\boldsymbol{\varepsilon}_{i_n}^{\text{res}}$ the phase strain reached at this composite zero-stress state, $\Delta\bar{\boldsymbol{\varepsilon}}^{\text{unload}} = \bar{\boldsymbol{\varepsilon}}_n - \bar{\boldsymbol{\varepsilon}}_n^{\text{res}}$, where $\bar{\boldsymbol{\varepsilon}}_n^{\text{res}}$ is the composite strain when reaching the zero-stress state, and where $\bar{\boldsymbol{C}}^{\text{elD}}$ is the macroscale damaged elastic operator, which is evaluated from $\boldsymbol{C}_i^{\text{elD}}$, the phase damaged elastic operators, following:

$$\bar{\boldsymbol{C}}^{\text{elD}}\left(\text{I},\, \boldsymbol{C}_0^{\text{elD}}, \boldsymbol{C}_{\text{I}}^{\text{elD}}\right) = \left[v_{\text{I}}\boldsymbol{C}_{\text{I}}^{\text{elD}} : \boldsymbol{B}^{\epsilon}\left(\text{I}, \boldsymbol{C}_0^{\text{elD}}, \boldsymbol{C}_{\text{I}}^{\text{el}}\right) + v_0\boldsymbol{C}_0^{\text{elD}}\right] : \left[v_{\text{I}}\boldsymbol{B}^{\epsilon}\left(\text{I}, \boldsymbol{C}_0^{\text{elD}}, \boldsymbol{C}_{\text{I}}^{\text{elD}}\right) + v_0\boldsymbol{I}\right]^{-1}$$
$$\text{and } \boldsymbol{C}_i^{\text{elD}} = (1 - D_{i_n})\boldsymbol{C}_i^{\text{el}}. \tag{3.14}$$

In this Work, we consider the damage of the matrix phase only since we are interested in accounting for the effect of the pressure-dependent yield surface on the homogenization scheme. Assuming damage is only present in the matrix phase of the composite material from now on, it is possible to write the final system of equations as:

$$\begin{cases} \bar{\boldsymbol{\sigma}}_n - \bar{\boldsymbol{C}}^{\text{elD}}\left(\text{I}, \boldsymbol{C}_0^{\text{elD}}, \boldsymbol{C}_{\text{I}}^{\text{el}}\right) : \Delta\bar{\boldsymbol{\varepsilon}}^{\text{unload}} = 0, \\ \Delta\bar{\boldsymbol{\varepsilon}}^{\text{unload}} = v_0\Delta\boldsymbol{\varepsilon}_0^{\text{unload}} + v_{\text{I}}\Delta\boldsymbol{\varepsilon}_{\text{I}}^{\text{unload}}, \\ \Delta\boldsymbol{\varepsilon}_{\text{I}}^{\text{unload}} = \boldsymbol{B}^{\epsilon}(\text{I}, \boldsymbol{C}_0^{\text{elD}}, \boldsymbol{C}_{\text{I}}^{\text{el}}) : \Delta\boldsymbol{\varepsilon}_0^{\text{unload}}, \\ 0 = \bar{\boldsymbol{\sigma}}^{\text{res}} = v_0\boldsymbol{\sigma}_0^{\text{res}} + v_{\text{I}}\boldsymbol{\sigma}_{\text{I}}^{\text{res}}. \end{cases} \tag{3.15}$$

At time t_n, and at unloaded state, the effective stress tensors write:

$$\begin{cases} \hat{\boldsymbol{\sigma}}_{i_n} = \frac{\boldsymbol{\sigma}_{i_n}}{(1-D_{i_n})}, \\ \hat{\boldsymbol{\sigma}}_{i_n}^{\text{res}} = \frac{\boldsymbol{\sigma}_{i_n}^{\text{res}}}{(1-D_{i_n})}. \end{cases} \tag{3.16}$$

3.1.2.2 Incremental-secant loading

The virtually unloaded composite material is then reloaded, until reaching the new stress-state. The computation of this reloading is made by defining a LCC subjected to a strain increment $\Delta\bar{\boldsymbol{\varepsilon}}_{n+1}^{\text{r}}$ from which the stress tensor is computed. Considering the residual strain tensors, Eq.

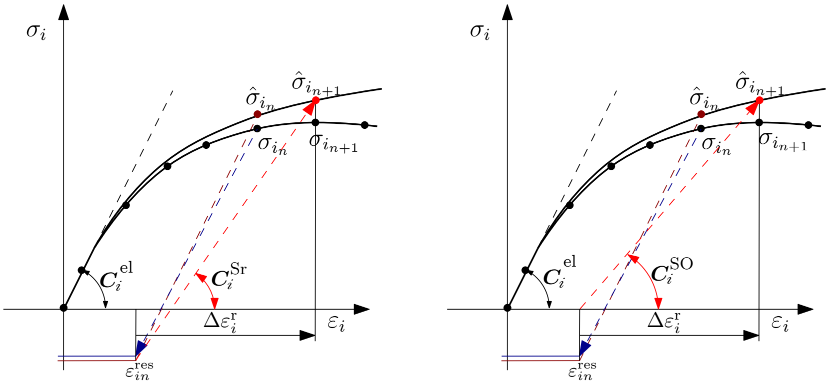

FIGURE 3.3: Graphical representation of the definition of the residual-secant operator (left) and the zero-secant operator (right).

(3.11) can be rewritten as:

$$\begin{cases} \bar{\boldsymbol{\varepsilon}}_{n+1} = \bar{\boldsymbol{\varepsilon}}_n^{\text{res}} + \Delta\bar{\boldsymbol{\varepsilon}}_{n+1}^{\text{r}}, \\ \boldsymbol{\varepsilon}_{i_{n+1}} = \boldsymbol{\varepsilon}_{in}^{\text{res}} + \Delta\boldsymbol{\varepsilon}_{i_{n+1}}^{\text{r}}, \end{cases} \tag{3.17}$$

where $\Delta\boldsymbol{\varepsilon}_{i_{n+1}}^{\text{r}}$ is the phase strain increment from the residual strain to the new strain $\boldsymbol{\varepsilon}_{n+1}$ and where $\Delta\bar{\boldsymbol{\varepsilon}}_{n+1}^{\text{r}}$ is the composite strain increment from the residual strain to the new strain $\bar{\boldsymbol{\varepsilon}}_{n+1}$ as shown graphically in Figure 3.3.

The phases effective stress tensor at t_{n+1} can be defined from the stress increment such that:

$$\hat{\boldsymbol{\sigma}}_{i_{n+1}} = \hat{\boldsymbol{\sigma}}_{in}^{\text{res}} + \Delta\hat{\boldsymbol{\sigma}}_{i_{n+1}}^{\text{r}}, \tag{3.18}$$

being $\Delta\hat{\boldsymbol{\sigma}}_{i_{n+1}}^{\text{r}}$ defined as:

$$\Delta\hat{\boldsymbol{\sigma}}_{i_{n+1}}^{\text{r}} = \boldsymbol{C}_{i_{n+1}}^{\text{Sr}} : \Delta\boldsymbol{\varepsilon}_{i_{n+1}}^{\text{r}}, \tag{3.19}$$

where $\boldsymbol{C}_i^{\text{Sr}}$ is the residual-incremental-secant operator of the elasto-plastic material. The computation of this residual-incremental-secant operator is detailed later in this Section, but its physical interpretation is illustrated in Figure 3.3. It is then possible to write the apparent stress tensor as:

$$\boldsymbol{\sigma}_{i_{n+1}} = \left(1 - D_{i_{n+1}}\right) \hat{\boldsymbol{\sigma}}_{in}^{\text{res}} + \boldsymbol{C}_{i_{n+1}}^{\text{SDr}} : \Delta\boldsymbol{\varepsilon}_{i_{n+1}}^{\text{r}}, \tag{3.20}$$

where the damaged incremental-secant operator is defined as:

$$\boldsymbol{C}_{i_{n+1}}^{\text{SDr}} = \left(1 - D_{i_{n+1}}\right) \boldsymbol{C}_{i_{n+1}}^{\text{Sr}}. \tag{3.21}$$

The residual macro scale incremental-secant operator can then be defined as:

$$\bar{\boldsymbol{C}}^{\text{SDr}} = \left[v_{\text{I}} \boldsymbol{C}_{\text{I}}^{\text{Sr}} : \boldsymbol{B}^{\epsilon}\left(\text{I}, \boldsymbol{C}_0^{\text{SDr}}, \boldsymbol{C}_{\text{I}}^{\text{Sr}}\right) + v_0 \boldsymbol{C}_0^{\text{SDr}}\right] : \left[v_{\text{I}} \boldsymbol{B}^{\epsilon}\left(\text{I}, \boldsymbol{C}_0^{\text{SDr}}, \boldsymbol{C}_{\text{I}}^{\text{Sr}}\right) + v_0 \boldsymbol{I}\right]^{-1}. \tag{3.22}$$

With the macro scale incremental-secant operator defined, it is possible to compute the macro scale stress tensor as:

$$\bar{\boldsymbol{\sigma}}_{n+1} + v_0\left(D_{0_{n+1}} - D_{0_n}\right) \hat{\boldsymbol{\sigma}}_{0_n}^{\text{res}} = \bar{\boldsymbol{C}}_{n+1}^{\text{SDr}}\left(\text{I}, \boldsymbol{C}_{0_{n+1}}^{\text{SDr}}, \boldsymbol{C}_{\text{I}_{n+1}}^{\text{Sr}}, v_{\text{I}}\right) : \Delta\bar{\boldsymbol{\varepsilon}}_{n+1}^{\text{r}}. \tag{3.23}$$

As lengthily discussed by Wu et al. (Wu et al., 2017; Wu et al., 2013a; Wu et al., 2013c), when considering only first statistical moments, the incremental-secant method main limitation is the over-stiff results predicted when studying composites whose elasto-plastic inclusions are much stiffer than the matrix phase during the plastic flow. It was shown for a wide variety of test cases that by neglecting the residual stress in the matrix phase, see Figure 3.3, this over-stiffness was counterbalanced. This is called the zero-incremental secant method. The need for this zero-incremental secant can be circumvented with the use of second statistical moments (Wu et al., 2017). In the zero-incremental case, the new effective stress tensor would be defined by means of the zero secant operator $\boldsymbol{C}_i^{\mathrm{S0}}$ as:

$$\hat{\boldsymbol{\sigma}}_{i_{n+1}} = \boldsymbol{C}_i^{\mathrm{S0}} : \Delta\boldsymbol{\varepsilon}_{i_{n+1}}^{\mathrm{r}}, \tag{3.24}$$

Using $\boldsymbol{C}^{\mathrm{S}}$, standing for either $\boldsymbol{C}^{\mathrm{Sr}}$ or $\boldsymbol{C}^{\mathrm{S0}}$, and $\boldsymbol{C}^{\mathrm{SD}}$ for either $\boldsymbol{C}^{\mathrm{SDr}}$ or $\boldsymbol{C}^{\mathrm{SD0}}$ we can define the LCC using the strain concentration tensor:

$$\boldsymbol{B}^{\epsilon}\left(\mathrm{I}, \left(1 - D_{0_{n+1}}\right)\boldsymbol{C}_0^{\mathrm{S}}, \boldsymbol{C}_{\mathrm{I}}^{\mathrm{S}}\right), \tag{3.25}$$

being possible to close the system of equations that writes:

$$\begin{cases} \Delta\bar{\boldsymbol{\varepsilon}}_{n+1}^{\mathrm{r}} = v_0 \Delta\boldsymbol{\varepsilon}_{0_{n+1}}^{\mathrm{r}} + v_{\mathrm{I}} \Delta\boldsymbol{\varepsilon}_{\mathrm{I}_{n+1}}^{\mathrm{r}}, \\ \Delta\boldsymbol{\varepsilon}_{\mathrm{I}_{n+1}}^{\mathrm{r}} = \boldsymbol{B}^{\epsilon}\left(\mathrm{I}, \boldsymbol{C}_{0_{n+1}}^{\mathrm{SD}}, \boldsymbol{C}_{\mathrm{I}_{n+1}}^{\mathrm{S}}\right) : \Delta\boldsymbol{\varepsilon}_{0_{n+1}}^{\mathrm{r}}, \\ \boldsymbol{C}_{0_{n+1}}^{\mathrm{SD}} = (1 - D_{0_{n+1}})\boldsymbol{C}_{0_{n+1}}^{\mathrm{S}}, \\ \bar{\boldsymbol{\sigma}}_{n+1} = v_0\left(1 - D_{0_{n+1}}\right)\hat{\boldsymbol{\sigma}}_{0_{n+1}} + v_{\mathrm{I}}\hat{\boldsymbol{\sigma}}_{\mathrm{I}_{n+1}}. \end{cases} \tag{3.26}$$

3.1.2.3 Phase constitutive behavior

Finally, the phase responses obey the damage-enhanced elasto-plastic law:

$$\begin{cases} \hat{\boldsymbol{\sigma}}_i(t) = \hat{\boldsymbol{\sigma}}_i\left(\boldsymbol{\varepsilon}_i(t); \boldsymbol{q}(\tau), \tau \in [0, t]\right), \\ D_i(t) = D_i\left(\boldsymbol{\varepsilon}_i(t); \boldsymbol{q}(\tau), \check{\boldsymbol{q}}(\tau), \tau \in [0, t]\right), \end{cases} \tag{3.27}$$

where $\boldsymbol{q}$ is a set of internal variables and $\check{\boldsymbol{q}}$ is their nonlocal counterpart used to avoid the mesh dependency of the solution.

In the work by Wu et al. (2017), the J2 yield surface was used for the development of the MFH model. While the model showed an excellent performance against full-field simulations, the J2 plasticity model is not able to capture the high pressure dependency observed in real life composite materials with a polymer-based matrix. This pressure dependency affects not only the tension-compression yield asymmetry, but also the behavior of the material when introducing triaxiality effects. Let us take as an example a small 2D UD composite material sample of 45x45 μm^2 with an RTM6 matrix, using the model with pressure sensitive yield surface reported in Chapter 2. To this end, the model using the calibration of the parameters performed in the work by Nguyen, Wu, and Noels (2019) is used. As shown in Fig. 3.4, after calibration, the J2-based MFH model is able to capture the behavior of the material when undergoing uniaxial loading in direction 11. The strain evolution obtained from this simulation ($\varepsilon 11_{ref}$ and $\varepsilon 22_{ref}$) is taken as reference. As soon as we start constraining the strain evolution of the sample across direction 22 up to $\varepsilon_{22} = 0$, and hence increasing the triaxiality within the sample, we observe how the MFH is not able to capture the correct behavior anymore. This highlights how crucial accounting for pressure-dependency is when studying these materials, and represents the motivation behind the here developed pressure-dependent MFH model.

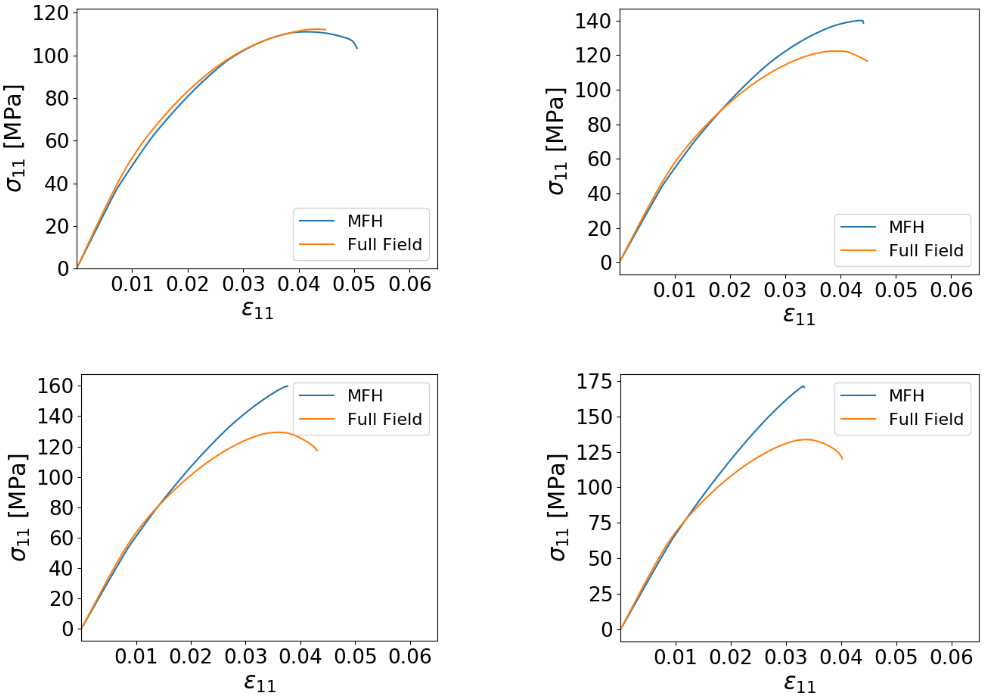

FIGURE 3.4: Full-Field and MFH behavior comparison for different load conditions. On the top left, uniaxial loading is applied to the sample. On the top right, a strain evolution $\varepsilon_{11} = \varepsilon_{11_{ref}}$ and $\varepsilon_{22} = 3/4\varepsilon_{22_{ref}}$ is applied. On the bottom, $\varepsilon_{11} = \varepsilon_{11_{ref}}$ and $\varepsilon_{22} = 1/4\varepsilon_{22_{ref}}$ is applied on the left, and $\varepsilon_{11} = \varepsilon_{11_{ref}}$ and $\varepsilon_{22} = 0$ on the right.

3.2 Pressure sensitive phase material law (Calleja Vázquez et al., 2022)

In this Chapter, with a view to its embedding in a MFH scheme, the power-enhanced yield version of the Drucker-Prager criterion presented in Chapter 2 is implemented at the phase level in an incremental-secant approach for elasto-plastic and damage enhanced cases. To this end, the model is reformulated in a small-strain setting. For the sake of conciseness, the subscript referring to the phase is omitted.

3.2.1 Pressure-dependent model in a small-strain setting

The Drucker-Prager yield function consists of a linear combination of the two first invariants, making it dependent on the hydrostatic pressure. Nguyen et al. (2016) enhanced this model by adding an exponent ($\alpha \geq 1$) in the octahedral term. Considering that the plastic flow is written in the effective stress space in case of damage, the yield criterion reads:

$$F\left(\hat{\boldsymbol{\sigma}}, p\right) = \frac{\left((\hat{\boldsymbol{\sigma}})^{\mathrm{eq}}\right)^{\alpha}}{\sigma_c^{\alpha}} - 3\frac{m^{\alpha}-1}{(m+1)\sigma_c}\hat{\phi} - \frac{m^{\alpha}+m}{m+1} \leq 0, \tag{3.28}$$

where the superscript “eq” stands for the equivalent von Mises effective stress, $\hat{\phi} = 1/3\,\mathrm{tr}(\hat{\boldsymbol{\sigma}})$, σ_c represents the current compressive yield stress and $m = \frac{\sigma_t}{\sigma_c}$ is the ratio between the current tensile and compressive yield stresses. With a view to the damage-enhanced case, the yield surface is written in the effective space.

The exponent α observed in the first term of the yield criterion allows recovering different power yield surfaces. It is possible to observe that when α is set to one, the classical Drucker-

Prager yield criterion is recovered. For the case in which a value of $\alpha = 2$ is used, the paraboloidal yield surface studied by Melro et al. (2013) is recovered. The ratio between the current yield stresses permits to model the effect of a tension-compression flow asymmetry.

In order to correctly capture the complex behavior of polymers, the use of a non-associated flow rule is normally integrated (Al-Rub, Tehrani, and Darabi, 2015; Melro et al., 2013; Vogler, Rolfes, and Camanho, 2013). This means that, contrary to the case of an associate flow rule in which the plastic flow evolves taking into account the gradient of the yield function, the non-associated flow rule follows a direction normal to a plastic flow potential. In this Work, as in Nguyen et al. (2016), a quadratic flow potential is used in order to be able to control the Poisson's ratio during the plastic process. This plastic flow potential is written as (Melro et al., 2013):

$$G = (\hat{\boldsymbol{\sigma}}^{\mathrm{eq}})^2 + \beta \hat{\phi}^2, \tag{3.29}$$

where β is a material parameter. This flow potential permits modeling the volumetric plastic deformation with what is called a plastic Poisson's ratio. At the plastic flow onset, the plastic Poisson's ratio writes:

$$\nu_p = \frac{9 - 2\beta}{18 + 2\beta}. \tag{3.30}$$

This combination of the modified Drucker-Prager yield surface coupled with the use of the flow potential described by Melro et al. (2013) was proven to yield satisfactory results and to be able of accurately representing the pressure-dependent plastic behavior of high-crosslinked epoxies such as the RTM6 in previous works, and allows to easily match a wide variety of pressure-dependent behaviors thanks to the modifications applied to the original criterion. This flexibility and proven performance made this an ideal option for this Work and future implementations of this scheme.

The direction of the flow is then defined as $\mathbf{Q} = \frac{\partial G}{\partial \hat{\boldsymbol{\sigma}}}$ and can be evaluated (Nguyen et al., 2016) as:

$$\mathbf{Q} = \frac{\partial G}{\partial \hat{\boldsymbol{\sigma}}} = 3\hat{\boldsymbol{\sigma}}^{\mathrm{dev}} + \frac{2\beta}{3}\hat{\boldsymbol{\sigma}}^{\mathrm{vol}}, \tag{3.31}$$

where $\hat{\boldsymbol{\sigma}}^{\mathrm{vol}} = \hat{\phi}\mathbf{1}$, with "vol"standing for the volume operator $(\bullet)^{\mathrm{vol}} = \frac{1}{3}\mathrm{tr}(\bullet)\mathbf{1}$ with $\mathbf{1}$ being the second order identity tensor and where "dev" stands for the deviatoric operator $(\bullet)^{\mathrm{dev}} = \bullet - (\bullet)^{\mathrm{vol}}$.

The plastic flow evolution can be written as:

$$\dot{\boldsymbol{\varepsilon}}^{\mathrm{p}} = \dot{\Gamma}\mathbf{Q}, \tag{3.32}$$

where Γ is related to the equivalent plastic strain rate as:

$$\dot{p} = k\sqrt{\dot{\boldsymbol{\varepsilon}}^{\mathrm{p}} : \dot{\boldsymbol{\varepsilon}}^{\mathrm{p}}} = k\dot{\Gamma}\sqrt{\boldsymbol{Q} : \boldsymbol{Q}}; \tag{3.33}$$

and (Melro et al., 2013):

$$k = \frac{1}{\sqrt{1 + 2\nu_p^2}} \quad ; \quad k = \sqrt{\frac{2}{3}} \quad \text{if incompressible flow rule.} \tag{3.34}$$

3.2.2 Residual incremental-secant pressure-dependent model implementation

This Section frames this pressure-dependent model into the incremental-secant framework step by step. First the elastic trial is developed, following with the radial return mapping used for the plastic process, finishing with the definition of the secant tensors.

3.2.2.1 Elastic trial

First, an elastic flow is assumed to compute a trial effective stress tensor $\hat{\boldsymbol{\sigma}}^{\mathrm{tr}}_{n+1}$. Using the relations developed in Section 3.1.2, the trial effective stress tensor reads:

$$\hat{\boldsymbol{\sigma}}^{\mathrm{tr}}_{n+1} = \hat{\boldsymbol{\sigma}}_n + \boldsymbol{C}^{\mathrm{el}} : \Delta\boldsymbol{\varepsilon}_{n+1} = \hat{\boldsymbol{\sigma}}_n + \boldsymbol{C}^{\mathrm{el}} : \left(\Delta\boldsymbol{\varepsilon}^{\mathrm{r}}_{n+1} + \boldsymbol{\varepsilon}^{\mathrm{res}}_n - \boldsymbol{\varepsilon}_n\right) = \hat{\boldsymbol{\sigma}}^{\mathrm{res}}_n + \boldsymbol{C}^{\mathrm{el}} : \Delta\boldsymbol{\varepsilon}^{\mathrm{r}}_{n+1}, \tag{3.35}$$

where the elastic operator $\boldsymbol{C}^{\mathrm{el}}$, being isotropic, can be expressed in terms of its volumetric and deviatoric components as:

$$\boldsymbol{C}^{\mathrm{el}} = 3\kappa^{\mathrm{el}}\boldsymbol{I}^{\mathrm{vol}} + 2\mu^{\mathrm{el}}\boldsymbol{I}^{\mathrm{dev}}, \tag{3.36}$$

where the volume and deviatoric fourth order tensors write $\boldsymbol{I}^{\mathrm{vol}} \equiv \frac{1}{3}\mathbf{1}\otimes\mathbf{1}$ and $\boldsymbol{I}^{\mathrm{dev}} = \boldsymbol{I} - \boldsymbol{I}^{\mathrm{vol}}$, κ^{el} is the elastic compressibility modulus and μ^{el} is the elastic shear modulus.

The pressure-sensitive yield criterion is then verified to check whether an elastic or a plastic flow is occurring, with

$$F^{\mathrm{tr}}\left(\hat{\boldsymbol{\sigma}}^{\mathrm{tr}}_{n+1}, p_n\right) = \frac{\left(\left(\hat{\boldsymbol{\sigma}}^{\mathrm{tr}}_{n+1}\right)^{\mathrm{eq}}\right)^{\alpha}}{\sigma_c^{\alpha}} - 3\frac{m^{\alpha}-1}{(m+1)\sigma_c}\hat{\phi}^{\mathrm{tr}}_{n+1} - \frac{m^{\alpha}+m}{m+1} \leq 0, \tag{3.37}$$

where $\sigma_c = \sigma_0^c + R(p)$ where p is the accumulated plastic strain and $R(p)$ the hardening law in terms of p. In this Chapter, the ratio $\frac{\sigma_t}{\sigma_c}$ is considered to be constant during the hardening, and the hardening law is defined with respect to the compressive behavior. This assumption is not restrictive for the methodology.

If the yield criterion is fulfilled, then the trial effective stress $\hat{\boldsymbol{\sigma}}^{\mathrm{tr}}_{n+1} = \hat{\boldsymbol{\sigma}}_{n+1}$, $p_{n+1} = p_n$ and the secant operator $\boldsymbol{C}^{\mathrm{Sr}} = \boldsymbol{C}^{\mathrm{el}}$.

3.2.2.2 Radial return mapping

If the yield criterion is not fulfilled ($F^{\mathrm{tr}} > 0$), a plastic correction must be applied:

$$\hat{\boldsymbol{\sigma}}_{n+1} = \hat{\boldsymbol{\sigma}}^{\mathrm{tr}}_{n+1} - \boldsymbol{C}^{\mathrm{el}} : \Delta\boldsymbol{\varepsilon}^{\mathrm{p}}. \tag{3.38}$$

Following Wu et al. (Wu et al., 2013c; Wu et al., 2013a), the normal direction shown in Eq. (3.31) is modified as:

$$\begin{aligned}\mathbf{Q}_{n+1} &= 3\left(\boldsymbol{C}^{\mathrm{Sr}} : \Delta\boldsymbol{\varepsilon}^{\mathrm{r}}_{n+1}\right)^{\mathrm{dev}} + \frac{2\beta}{3}\left(\boldsymbol{C}^{\mathrm{Sr}} : \Delta\boldsymbol{\varepsilon}^{\mathrm{r}}_{n+1}\right)^{\mathrm{vol}} \\ &= 3\left(\hat{\boldsymbol{\sigma}}_{n+1} - \hat{\boldsymbol{\sigma}}^{\mathrm{res}}_n\right)^{\mathrm{dev}} + \frac{2\beta}{3}\left(\hat{\boldsymbol{\sigma}}_{n+1} - \hat{\boldsymbol{\sigma}}^{\mathrm{res}}_n\right)^{\mathrm{vol}}.\end{aligned} \tag{3.39}$$

As discussed by Wu et al. (2019), for infinitesimal strain increments $\Delta\boldsymbol{\varepsilon} \to 0$ for a single phase material, this expression $\mathbf{Q}_{n+1}$ tends to the normal of the yield surface. At the trial state, $\mathbf{Q}^{\mathrm{tr}}_{n+1}$ writes:

$$\begin{aligned}\mathbf{Q}^{\mathrm{tr}}_{n+1} &= 3\left(\boldsymbol{C}^{\mathrm{el}} : \Delta\boldsymbol{\varepsilon}^{\mathrm{r}}_{n+1}\right)^{\mathrm{dev}} + \frac{2\beta}{3}\left(\boldsymbol{C}^{\mathrm{el}} : \Delta\boldsymbol{\varepsilon}^{\mathrm{r}}_{n+1}\right)^{\mathrm{vol}} \\ &= 3\left(\hat{\boldsymbol{\sigma}}^{\mathrm{tr}}_{n+1} - \hat{\boldsymbol{\sigma}}^{\mathrm{res}}_n\right)^{\mathrm{dev}} + \frac{2\beta}{3}\left(\hat{\boldsymbol{\sigma}}^{\mathrm{tr}}_{n+1} - \hat{\boldsymbol{\sigma}}^{\mathrm{res}}_n\right)^{\mathrm{vol}}.\end{aligned} \tag{3.40}$$

Since $\boldsymbol{C}^{\mathrm{el}}$ is isotropic, $\boldsymbol{C}^{\mathrm{el}} : \Delta\boldsymbol{\varepsilon}^{\mathrm{p}} = \left(3\kappa^{\mathrm{el}}\boldsymbol{I}^{\mathrm{vol}} + 2\mu^{\mathrm{el}}\boldsymbol{I}^{\mathrm{dev}}\right) : \Delta\boldsymbol{\varepsilon}^{\mathrm{p}}$, where the plastic strain increment reads:

$$\Delta\boldsymbol{\varepsilon}^{\mathrm{p}} = \Gamma\mathbf{Q}, \tag{3.41}$$

with the plastic multiplier Γ related to the increment in accumulated plastic strain deformation as:

$$\Delta p = k\Gamma\sqrt{\mathbf{Q}:\mathbf{Q}} = k\Gamma\sqrt{6\left(\left(\hat{\boldsymbol{\sigma}}_{n+1}-\hat{\boldsymbol{\sigma}}_n^{\mathrm{res}}\right)^{\mathrm{eq}}\right)^2+\frac{4}{3}\beta^2\left(\hat{\phi}_{n+1}-\hat{\phi}_n^{\mathrm{res}}\right)^2}. \tag{3.42}$$

Decomposing the normal into its deviatoric and volumetric parts ($\mathbf{Q}_{n+1} = \mathbf{Q}_{n+1}^{\mathrm{dev}} + \mathbf{Q}_{n+1}^{\mathrm{vol}}$) and following the developments in Nguyen et al. (2016) one can rewrite the plastic correction shown in Eq. (3.38) as:

$$\left(\hat{\boldsymbol{\sigma}}_{n+1}\right)^{\mathrm{dev}} = \left(\hat{\boldsymbol{\sigma}}_{n+1}^{\mathrm{tr}}\right)^{\mathrm{dev}} - 2\mu^{\mathrm{el}}\Gamma\mathbf{Q}_{n+1}^{\mathrm{dev}}, \text{ and} \tag{3.43}$$

$$\left(\hat{\boldsymbol{\sigma}}_{n+1}\right)^{\mathrm{vol}} = \left(\hat{\boldsymbol{\sigma}}_{n+1}^{\mathrm{tr}}\right)^{\mathrm{vol}} - 3\kappa^{\mathrm{el}}\Gamma\mathbf{Q}_{n+1}^{\mathrm{vol}}, \text{ or} \tag{3.44}$$

$$\hat{\phi}_{n+1} = \hat{\phi}_{n+1}^{\mathrm{tr}} - 3\kappa^{\mathrm{el}}\Gamma\frac{2\beta}{3}\left(\hat{\phi}_{n+1}-\hat{\phi}_{n+1}^{\mathrm{res}}\right). \tag{3.45}$$

Equations (3.43) and (3.44) can also be written as:

$$\left(\hat{\boldsymbol{\sigma}}_{n+1}-\hat{\boldsymbol{\sigma}}_n^{\mathrm{res}}\right)^{\mathrm{dev}} = \left(\hat{\boldsymbol{\sigma}}_{n+1}^{\mathrm{tr}}-\hat{\boldsymbol{\sigma}}_n^{\mathrm{res}}\right)^{\mathrm{dev}} - 2\mu^{\mathrm{el}}\Gamma\mathbf{Q}_{n+1}^{\mathrm{dev}}, \text{ and} \tag{3.46}$$

$$\left(\hat{\boldsymbol{\sigma}}_{n+1}-\hat{\boldsymbol{\sigma}}_n^{\mathrm{res}}\right)^{\mathrm{vol}} = \left(\hat{\boldsymbol{\sigma}}_{n+1}^{\mathrm{tr}}-\hat{\boldsymbol{\sigma}}_n^{\mathrm{res}}\right)^{\mathrm{vol}} - 3\kappa^{\mathrm{el}}\mathbf{Q}_{n+1}^{\mathrm{vol}}. \tag{3.47}$$

Using Eq. (3.39), these two equations are respectively rewritten:

$$\begin{aligned}\left(\hat{\boldsymbol{\sigma}}_{n+1}-\hat{\boldsymbol{\sigma}}_n^{\mathrm{res}}\right)^{\mathrm{dev}} &= \left(\hat{\boldsymbol{\sigma}}_{n+1}^{\mathrm{tr}}-\hat{\boldsymbol{\sigma}}_n^{\mathrm{res}}\right)^{\mathrm{dev}} - 2\mu^{\mathrm{el}}\Gamma\left(3\left(\hat{\boldsymbol{\sigma}}_{n+1}-\hat{\boldsymbol{\sigma}}_n^{\mathrm{res}}\right)^{\mathrm{dev}}\right)\\ &= \frac{\left(\hat{\boldsymbol{\sigma}}_{n+1}^{\mathrm{tr}}-\hat{\boldsymbol{\sigma}}_n^{\mathrm{res}}\right)^{\mathrm{dev}}}{1+6\mu^{\mathrm{el}}\Gamma},\end{aligned} \tag{3.48}$$

and

$$\begin{aligned}\left(\hat{\boldsymbol{\sigma}}_{n+1}-\hat{\boldsymbol{\sigma}}_n^{\mathrm{res}}\right)^{\mathrm{vol}} &= \left(\hat{\boldsymbol{\sigma}}_{n+1}^{\mathrm{tr}}-\hat{\boldsymbol{\sigma}}_n^{\mathrm{res}}\right)^{\mathrm{vol}} - 3\kappa^{\mathrm{el}}\Gamma\left(\frac{2\beta}{3}\left(\hat{\boldsymbol{\sigma}}_{n+1}-\hat{\boldsymbol{\sigma}}_n^{\mathrm{res}}\right)^{\mathrm{vol}}\right)\\ &= \frac{\left(\hat{\boldsymbol{\sigma}}_{n+1}^{\mathrm{tr}}-\hat{\boldsymbol{\sigma}}_n^{\mathrm{res}}\right)^{\mathrm{vol}}}{\left(1+2\kappa^{\mathrm{el}}\Gamma\beta\right)}.\end{aligned} \tag{3.49}$$

It is then possible to use Eqs. (3.48) and (3.49) to find the relation between $\mathbf{Q}_{n+1}$, Eq. (3.39), and $\mathbf{Q}_{n+1}^{\mathrm{tr}}$, Eq. (3.40), which writes:

$$\mathbf{Q}_{n+1} = 3\frac{\left(\hat{\boldsymbol{\sigma}}_{n+1}^{\mathrm{tr}}-\hat{\boldsymbol{\sigma}}_n^{\mathrm{res}}\right)^{\mathrm{dev}}}{1+6\mu^{\mathrm{el}}\Gamma} + \frac{2\beta}{3}\frac{\left(\hat{\boldsymbol{\sigma}}_{n+1}^{\mathrm{tr}}-\hat{\boldsymbol{\sigma}}_n^{\mathrm{res}}\right)^{\mathrm{vol}}}{\left(1+2\kappa^{\mathrm{el}}\Gamma\beta\right)}, \tag{3.50}$$

or when separated into their deviatoric and volumetric terms:

$$\mathbf{Q}_{n+1}^{\mathrm{dev}} = \frac{1}{1+6\mu^{\mathrm{el}}\Gamma}\left(\mathbf{Q}_{n+1}^{\mathrm{tr}}\right)^{\mathrm{dev}} \quad ; \quad \mathbf{Q}_{n+1}^{\mathrm{vol}} = \frac{1}{1+2\kappa^{\mathrm{el}}\Gamma\beta}\left(\mathbf{Q}_{n+1}^{\mathrm{tr}}\right)^{\mathrm{vol}}. \tag{3.51}$$

At this stage, the pressure-sensitive yield criterion is rewritten as:

$$F\left(\hat{\boldsymbol{\sigma}}\right) = \left(\frac{\left(\hat{\boldsymbol{\sigma}}_{n+1}-\hat{\boldsymbol{\sigma}}_n^{\mathrm{res}}+\hat{\boldsymbol{\sigma}}_n^{\mathrm{res}}\right)^{\mathrm{eq}}}{\sigma_c}\right)^{\alpha} - 3\frac{m^{\alpha}-1}{\left(m+1\right)\sigma_c}\left(\hat{\phi}_{n+1}-\hat{\phi}_n^{\mathrm{res}}+\hat{\phi}_n^{\mathrm{res}}\right) - \frac{m^{\alpha}+m}{m+1} = 0. \tag{3.52}$$

Making use of the Eqs. (3.48) and (3.49), since only the deviatoric parts are involved when evaluating the equivalent operator, Eq. (3.52) can be expressed in terms of $\hat{\boldsymbol{\sigma}}^{\text{tr}}$, $\hat{\boldsymbol{\sigma}}^{\text{res}}$ and Γ as:

$$F\left(\hat{\boldsymbol{\sigma}}^{\text{tr}},\Gamma\right)=\left(\frac{\left(\frac{\hat{\boldsymbol{\sigma}}^{\text{tr}}_{n+1}-\hat{\boldsymbol{\sigma}}^{\text{res}}_{n}}{1+6\mu^{\text{el}}\Gamma}+\hat{\boldsymbol{\sigma}}^{\text{res}}_{n}\right)^{\text{eq}}}{\sigma_c}\right)^{\alpha}-3\frac{m^{\alpha}-1}{(m+1)\,\sigma_c}\left(\frac{\hat{\phi}^{\text{tr}}_{n+1}-\hat{\phi}^{\text{res}}_{n}}{1+2\kappa^{\text{el}}\Gamma\beta}+\hat{\phi}^{\text{res}}_{n}\right)-\frac{m^{\alpha}+m}{m+1}=0. \tag{3.53}$$

In order to find the expression of the plastic multiplier Γ, a Newton-Raphson algorithm is used. Using this final expression of the yield criterion Eq. (3.53), the derivative with respect to Γ writes:

$$\begin{aligned}\frac{dF}{d\Gamma}=&\left[-\frac{\alpha}{\sigma_c^{\alpha+1}}\frac{\partial R(\Delta p)}{\partial\Delta p}\left(\left(\frac{\hat{\boldsymbol{\sigma}}^{\text{tr}}_{n+1}-\hat{\boldsymbol{\sigma}}^{\text{res}}_{n}}{1+6\mu^{\text{el}}\Gamma}+\hat{\boldsymbol{\sigma}}^{\text{res}}_{n}\right)^{\text{eq}}\right)^{\alpha}\right.\\&\left.+3\frac{m^{\alpha}-1}{(m+1)\sigma_c^{2}}\frac{\partial R(\Delta p)}{\partial\Delta p}\left(\frac{\hat{\phi}^{\text{tr}}_{n+1}-\hat{\phi}^{\text{res}}_{n}}{1+2\kappa^{\text{el}}\Gamma\beta}+\hat{\phi}^{\text{res}}_{n}\right)\right]\frac{\partial\Delta p}{\partial\Gamma}+\frac{\partial F}{\partial\Gamma},\end{aligned} \tag{3.54}$$

where, from Eqs. (3.42, 3.48, 3.49), one has:

$$\begin{aligned}\frac{\partial\Delta p}{\partial\Gamma}=&\,k\sqrt{6\left(\left(\frac{\hat{\boldsymbol{\sigma}}^{\text{tr}}_{n+1}-\hat{\boldsymbol{\sigma}}^{\text{res}}_{n}}{1+6\mu^{\text{el}}\Gamma}\right)^{\text{eq}}\right)^{2}+\frac{4\beta^{2}}{3}\left(\frac{\hat{\phi}^{\text{tr}}_{n+1}-\hat{\phi}^{\text{res}}_{n}}{1+2\kappa^{\text{el}}\Gamma\beta}\right)^{2}}\\&-\frac{k\Gamma}{2\sqrt{6\left(\left(\frac{\hat{\boldsymbol{\sigma}}^{\text{tr}}_{n+1}-\hat{\boldsymbol{\sigma}}^{\text{res}}_{n}}{1+6\mu^{\text{el}}\Gamma}\right)^{\text{eq}}\right)^{2}+\frac{4\beta^{2}}{3}\left(\frac{\hat{\phi}^{\text{tr}}_{n+1}-\hat{\phi}^{\text{res}}_{n}}{1+2\kappa^{\text{el}}\Gamma\beta}\right)^{2}}}\left[72\mu^{\text{el}}\frac{\left(\left(\hat{\boldsymbol{\sigma}}^{\text{tr}}_{n+1}-\hat{\boldsymbol{\sigma}}^{\text{res}}_{n}\right)^{\text{eq}}\right)^{2}}{\left(1+6\mu^{\text{el}}\Gamma\right)^{3}}\right.\\&\left.+\frac{16\beta^{3}\kappa^{\text{el}}}{3}\frac{\left(\hat{\phi}^{\text{tr}}_{n+1}-\hat{\phi}^{\text{res}}_{n}\right)^{2}}{\left(1+2\kappa^{\text{el}}\Gamma\beta\right)^{3}}\right],\end{aligned} \tag{3.55}$$

and

$$\begin{aligned}\frac{\partial F}{\partial\Gamma}=&-\alpha\left(\frac{\left(\frac{\hat{\boldsymbol{\sigma}}^{\text{tr}}_{n+1}-\hat{\boldsymbol{\sigma}}^{\text{res}}_{n}}{1+6\mu^{\text{el}}\Gamma}+\hat{\boldsymbol{\sigma}}^{\text{res}}_{n}\right)^{\text{eq}}}{\sigma_c}\right)^{\alpha-1}\frac{9\mu^{\text{el}}\left(\hat{\boldsymbol{\sigma}}^{\text{tr}}_{n+1}-\hat{\boldsymbol{\sigma}}^{\text{res}}_{n}\right)^{\text{dev}}:\left(\frac{\hat{\boldsymbol{\sigma}}^{\text{tr}}_{n+1}-\hat{\boldsymbol{\sigma}}^{\text{res}}_{n}}{1+6\mu^{\text{el}}\Gamma}+\hat{\boldsymbol{\sigma}}^{\text{res}}_{n}\right)^{\text{dev}}}{\sigma_c\left(1+6\mu^{\text{el}}\Gamma\right)^{2}\left(\frac{\hat{\boldsymbol{\sigma}}^{\text{tr}}_{n+1}-\hat{\boldsymbol{\sigma}}^{\text{res}}_{n}}{1+6\mu^{\text{el}}\Gamma}+\hat{\boldsymbol{\sigma}}^{\text{res}}_{n}\right)^{\text{eq}}}\\&+3\frac{m^{\alpha}-1}{(m+1)\,\sigma_c}\left(\frac{\hat{\phi}^{\text{tr}}_{n+1}-\hat{\phi}^{\text{res}}_{n}}{\left(1+2\kappa^{\text{el}}\Gamma\beta\right)^{2}}2\kappa^{\text{el}}\beta\right).\end{aligned} \tag{3.56}$$

Finally, the algorithmic operator $\boldsymbol{C}^{\text{alg}}=\frac{\partial\hat{\boldsymbol{\sigma}}}{\partial\boldsymbol{\varepsilon}}$ is given in Appendix B.1.

3.2.2.3 Radial return mapping neglecting the residual stress

In the case in which the residual stress is neglected when defining the LCC, see Section 3.1.2, the normal direction shown in Eq. (3.31) is the classical direction:

$$\mathbf{Q}_{n+1}=3\left(\hat{\boldsymbol{\sigma}}_{n+1}\right)^{\text{dev}}+\frac{2\beta}{3}\left(\hat{\boldsymbol{\sigma}}_{n+1}\right)^{\text{vol}}. \tag{3.57}$$

At the trial state, $\mathbf{Q}^{\mathrm{tr}}_{n+1}$ writes:

$$\mathbf{Q}^{\mathrm{tr}}_{n+1} = 3\left(\hat{\boldsymbol{\sigma}}^{\mathrm{tr}}_{n+1}\right)^{\mathrm{dev}} + \frac{2\beta}{3}\left(\hat{\boldsymbol{\sigma}}^{\mathrm{tr}}_{n+1}\right)^{\mathrm{vol}}. \tag{3.58}$$

The plastic multiplier Γ is therefore related to the increment in accumulated plastic strain deformation as:

$$\Delta p = k\Gamma\sqrt{\mathbf{Q}:\mathbf{Q}} = k\Gamma\sqrt{6\left(\left(\hat{\boldsymbol{\sigma}}_{n+1}\right)^{\mathrm{eq}}\right)^2 + \frac{4}{3}\beta^2\left(\hat{\phi}_{n+1}\right)^2}. \tag{3.59}$$

The relation between $\mathbf{Q}_{n+1}$ and $\mathbf{Q}^{\mathrm{tr}}_{n+1}$ neglecting the residual stress writes:

$$\mathbf{Q}_{n+1} = 3\frac{\left(\hat{\boldsymbol{\sigma}}^{\mathrm{tr}}_{n+1}\right)^{\mathrm{dev}}}{1+6\mu^{\mathrm{el}}\Gamma} + \frac{2\beta}{3}\frac{\left(\hat{\boldsymbol{\sigma}}^{\mathrm{tr}}_{n+1}\right)^{\mathrm{vol}}}{\left(1+2\kappa^{\mathrm{el}}\Gamma\beta\right)}. \tag{3.60}$$

The pressure-dependent yield criterion is then expressed in terms of $\hat{\boldsymbol{\sigma}}^{\mathrm{tr}}$ and Γ as: :

$$F\left(\hat{\boldsymbol{\sigma}}^{\mathrm{tr}},\Gamma\right) = \left(\frac{\left(\frac{\hat{\boldsymbol{\sigma}}^{\mathrm{tr}}_{n+1}}{1+6\mu^{\mathrm{el}}\Gamma}\right)^{\mathrm{eq}}}{\sigma_c}\right)^{\alpha} - 3\frac{m^{\alpha}-1}{(m+1)\sigma_c}\left(\frac{\hat{\phi}^{\mathrm{tr}}_{n+1}}{1+2\kappa^{\mathrm{el}}\Gamma\beta}\right) - \frac{m^{\alpha}+m}{m+1} = 0. \tag{3.61}$$

The plastic multiplier Γ is then computed, as in the case in which the residual is considered, by means of a Newton-Raphson algorithm, with the derivatives following from Eqs. (3.54 - 3.56) without the residual stress.

The updated expressions when neglecting the residual stress of $\frac{dF}{d\Gamma}$, Eq. (3.54), $\frac{\partial \Delta p}{\partial \Gamma}$, Eq. (3.55), $\frac{\partial F}{\partial \Gamma}$, Eq. (3.56), and of $\boldsymbol{C}^{\mathrm{alg}} = \frac{\partial \hat{\boldsymbol{\sigma}}}{\partial \boldsymbol{\varepsilon}}$ are given in Appendix B.1.

3.2.2.4 Definition of the secant operators in the elasto-plastic case

Knowing Γ and therefore $\hat{\boldsymbol{\sigma}}_{n+1}$, $\boldsymbol{C}^{\mathrm{Sr}}$ can be computed using Eqs. (3.18) and (3.38). Indeed, one has:

$$\begin{aligned}\Delta\hat{\boldsymbol{\sigma}}^{\mathrm{r}}_{n+1} &= \boldsymbol{C}^{\mathrm{Sr}} : \Delta\boldsymbol{\varepsilon}^{\mathrm{r}}_{n+1} = \boldsymbol{C}^{\mathrm{el}} : \Delta\boldsymbol{\varepsilon}^{\mathrm{r}}_{n+1} - \boldsymbol{C}^{\mathrm{el}} : \Delta\boldsymbol{\varepsilon}^{\mathrm{p}} \\ &= \boldsymbol{C}^{\mathrm{el}} : \Delta\boldsymbol{\varepsilon}^{\mathrm{r}}_{n+1} - 2\mu^{\mathrm{el}}\Gamma\mathbf{Q}^{\mathrm{dev}}_{n+1} - 3\kappa^{\mathrm{el}}\Gamma\mathbf{Q}^{\mathrm{vol}}_{n+1}.\end{aligned} \tag{3.62}$$

Using the relation Eq. (3.51) between $\mathbf{Q}_{n+1}$ and $\mathbf{Q}^{\mathrm{tr}}_{n+1}$:

$$\Delta\hat{\boldsymbol{\sigma}}^{\mathrm{r}}_{n+1} = \boldsymbol{C}^{\mathrm{el}} : \Delta\boldsymbol{\varepsilon}^{\mathrm{r}}_{n+1} - 2\mu^{\mathrm{el}}\Gamma\frac{1}{1+6\mu^{\mathrm{el}}\Gamma}\left(\mathbf{Q}^{\mathrm{tr}}_{n+1}\right)^{\mathrm{dev}} - 3\kappa^{\mathrm{el}}\Gamma\frac{1}{1+2\kappa^{\mathrm{el}}\Gamma\beta}\left(\mathbf{Q}^{\mathrm{tr}}_{n+1}\right)^{\mathrm{vol}}, \tag{3.63}$$

which, using Eq. (3.40), can be rewritten as:

$$\Delta\hat{\boldsymbol{\sigma}}^{\mathrm{r}}_{n+1} = \boldsymbol{C}^{\mathrm{el}} : \Delta\boldsymbol{\varepsilon}^{\mathrm{r}}_{n+1} - \frac{6\mu^{\mathrm{el}}\Gamma}{1+6\mu^{\mathrm{el}}\Gamma}\left(\boldsymbol{C}^{\mathrm{el}} : \Delta\boldsymbol{\varepsilon}^{\mathrm{r}}_{n+1}\right)^{\mathrm{dev}} - \frac{2\beta\kappa^{\mathrm{el}}\Gamma}{1+2\kappa^{\mathrm{el}}\Gamma\beta}\left(\boldsymbol{C}^{\mathrm{el}} : \Delta\boldsymbol{\varepsilon}^{\mathrm{r}}_{n+1}\right)^{\mathrm{vol}}, \tag{3.64}$$

or again

$$\Delta\hat{\boldsymbol{\sigma}}^{\mathrm{r}}_{n+1} = \left[\boldsymbol{C}^{\mathrm{el}} - \frac{6\mu^{\mathrm{el}}\Gamma}{1+6\mu^{\mathrm{el}}\Gamma}\left(\boldsymbol{I}^{\mathrm{dev}} : \boldsymbol{C}^{\mathrm{el}}\right) - \frac{2\beta\kappa^{\mathrm{el}}\Gamma}{1+2\kappa^{\mathrm{el}}\Gamma\beta}\left(\boldsymbol{I}^{\mathrm{vol}} : \boldsymbol{C}^{\mathrm{el}}\right)\right] : \Delta\boldsymbol{\varepsilon}^{\mathrm{r}}_{n+1}. \tag{3.65}$$

Having that the effective stress increment is defined as $\Delta\hat{\boldsymbol{\sigma}}^{\mathrm{r}}_{n+1} = \boldsymbol{C}^{\mathrm{Sr}} : \Delta\boldsymbol{\varepsilon}^{\mathrm{r}}_{n+1}$, $\boldsymbol{C}^{\mathrm{Sr}}$ is identified to be:

$$\boldsymbol{C}^{\mathrm{Sr}} = \boldsymbol{C}^{\mathrm{el}} - \frac{6\mu^{\mathrm{el}}\Gamma}{1+6\mu^{\mathrm{el}}\Gamma}\left(\boldsymbol{I}^{\mathrm{dev}} : \boldsymbol{C}^{\mathrm{el}}\right) - \frac{2\beta\kappa^{\mathrm{el}}\Gamma}{1+2\kappa^{\mathrm{el}}\Gamma\beta}\left(\boldsymbol{I}^{\mathrm{vol}} : \boldsymbol{C}^{\mathrm{el}}\right). \tag{3.66}$$

Since $\boldsymbol{C}^{\mathrm{el}}$ is isotropic, so is the residual-incremental-secant operator of the LCC ($\boldsymbol{C}^{\mathrm{Sr}}$) and it is possible to write:

$$\boldsymbol{C}^{\mathrm{el}} = 3\kappa^{\mathrm{el}}\boldsymbol{I}^{\mathrm{vol}} + 2\mu^{\mathrm{el}}\boldsymbol{I}^{\mathrm{dev}}; \text{ and } \boldsymbol{C}^{\mathrm{Sr}} = 3\kappa_s^{\mathrm{r}}\boldsymbol{I}^{\mathrm{vol}} + 2\mu_s^{\mathrm{r}}\boldsymbol{I}^{\mathrm{dev}}, \tag{3.67}$$

where the expressions for κ_s^{r} and μ_s^{r} are respectively:

$$\kappa_s^{\mathrm{r}} = \kappa^{\mathrm{el}} - \frac{2\beta{\kappa^{\mathrm{el}}}^2\Gamma}{1+2\kappa^{\mathrm{el}}\Gamma\beta} \quad ; \text{ and } \quad \mu_s^{\mathrm{r}} = \mu^{\mathrm{el}} - \frac{6{\mu^{\mathrm{el}}}^2\Gamma}{1+6\mu^{\mathrm{el}}\Gamma}. \tag{3.68}$$

This finding means that the isotropic nature of the LCC secant tensors is preserved for the case of non-associated pressure dependent plastic flow, which avoids the need for the isotropization step during the MFH process.

In the case the zero-incremental-secant approach is considered, that is, when the residual stress is neglected, the zero-incremental-secant operator would be defined by taking into account the residual strain, but neglecting the residual stress, such that $\hat{\boldsymbol{\sigma}}$ would be defined as:

$$\hat{\boldsymbol{\sigma}} = \boldsymbol{C}^{\mathrm{S0}} : \Delta\boldsymbol{\varepsilon}_{n+1}^{\mathrm{r}}, \tag{3.69}$$

where $\boldsymbol{C}^{\mathrm{S0}}$ writes:

$$\boldsymbol{C}^{\mathrm{S0}} = 3\kappa_s^0\boldsymbol{I}^{\mathrm{vol}} + 2\mu_s^0\boldsymbol{I}^{\mathrm{dev}}, \tag{3.70}$$

with the expressions for κ_s^0 and μ_s^0

$$\kappa_s^0 = \kappa^{\mathrm{el}} - \frac{2\beta{\kappa^{\mathrm{el}}}^2\Gamma}{1+2\kappa^{\mathrm{el}}\Gamma\beta} \quad ; \text{ and } \quad \mu_s^0 = \mu^{\mathrm{el}} - \frac{6{\mu^{\mathrm{el}}}^2\Gamma}{1+6\mu^{\mathrm{el}}\Gamma}. \tag{3.71}$$

These expressions are similar to Eq. (3.68), where Γ does not take into account the residual in its definition.

3.2.2.5 Definition of the secant operators in the damage-enhanced elasto-plastic case

In the damage-enhanced case, the damage present at the next time step D_{n+1} should now be computed using the chosen nonlocal damage model, Eq. (3.27). Section 3.4 particularizes the damage evolution law used in this Work. Once the new damage state is known, it is possible to compute the LCC's damage-enhanced residual-incremental-secant operator and the final stress as:

$$\boldsymbol{C}^{\mathrm{SDr}} = (1-D_{n+1})\,\boldsymbol{C}^{\mathrm{Sr}}, \text{ with} \tag{3.72}$$

$$\boldsymbol{\sigma}_{n+1} = (1-D_{n+1})\,\hat{\boldsymbol{\sigma}}_n^{\mathrm{res}} + \boldsymbol{C}^{\mathrm{SDr}} : \Delta\boldsymbol{\varepsilon}_{n+1}^{\mathrm{r}}. \tag{3.73}$$

Equation (3.72) implies that the damaged shear and bulk moduli are then written as:

$$\begin{aligned} \kappa_s^{\mathrm{Dr}} &= (1-D_{n+1})\left(\kappa^{\mathrm{el}} - \frac{2\beta{\kappa^{\mathrm{el}}}^2\Gamma}{1+2\kappa^{\mathrm{el}}\Gamma\beta}\right), \\ \mu_s^{\mathrm{Dr}} &= (1-D_{n+1})\left(\mu^{\mathrm{el}} - \frac{6{\mu^{\mathrm{el}}}^2\Gamma}{1+6\mu^{\mathrm{el}}\Gamma}\right). \end{aligned} \tag{3.74}$$

In the case the zero-incremental-secant approach is used, the damage-enhanced zero-incremental-secant operator and the final stress would write:

$$\boldsymbol{C}^{\mathrm{SD0}} = (1-D_{n+1})\,\boldsymbol{C}^{\mathrm{S0}}, \text{ with} \tag{3.75}$$

$$\boldsymbol{\sigma}_{n+1} = \boldsymbol{C}^{\mathrm{SD0}} : \Delta\boldsymbol{\varepsilon}^{\mathrm{r}}_{n+1}. \tag{3.76}$$

In this case, the damaged shear and bulk moduli, as for the previous case, write:

$$\begin{aligned} \kappa_s^{\mathrm{D0}} &= (1 - D_{n+1}) \left(\kappa^{\mathrm{el}} - \frac{2\beta {\kappa^{\mathrm{el}}}^2 \Gamma}{1 + 2\kappa^{\mathrm{el}}\Gamma\beta} \right), \\ \mu_s^{\mathrm{D0}} &= (1 - D_{n+1}) \left(\mu^{\mathrm{el}} - \frac{6 {\mu^{\mathrm{el}}}^2 \Gamma}{1 + 6\mu^{\mathrm{el}}\Gamma} \right). \end{aligned} \tag{3.77}$$

In the following Sections, $\boldsymbol{C}^{\mathrm{S}}$, κ_s, μ_s and $\boldsymbol{C}^{\mathrm{SD}}$, κ_s^{D} and μ_s^{D} respectively stand either for $\boldsymbol{C}^{\mathrm{Sr}}$, Eq. (3.67), κ_s^{r}, μ_s^{r}, Eq. (3.68), $\boldsymbol{C}^{\mathrm{SDr}}$, Eq. (3.72), κ_s^{Dr} and μ_s^{Dr}, Eq. (3.74), or for $\boldsymbol{C}^{\mathrm{S0}}$, Eq. (3.70), κ_s^{0}, μ_s^{0}, Eq. (3.71), $\boldsymbol{C}^{\mathrm{SD0}}$, Eq. (3.75), κ_s^{D0} and μ_s^{D0}, Eq. (3.77).

The developed residual and zero incremental-secant MFH pressure-dependent models, as well as the used damage evolution model were introduced in the C++ core of the CM3 in-house code.

3.3 MFH resolution within a nonlocal FE framework

In this Section, a general description of the "first-order moment" based MFH process is presented and then the complete pressure sensitive MFH computation scheme is exposed and detailed step by step.

Making use of nonlocal damage in the matrix phase, one can write the governing equations of the homogenized material for the interval $[t_n, t_{n+1}]$ as:

$$\nabla \cdot \bar{\boldsymbol{\sigma}}^T_{n+1} + \bar{\boldsymbol{f}}_{n+1} = \mathbf{0}, \tag{3.78}$$

where $\bar{\boldsymbol{f}}$ stands for the macroscale body force vector.

By using an implicit nonlocal form of elasto-plasticity (Peerlings et al., 1996) to define the nonlocal internal variables, the matrix governing equations are completed by the Helmholtz-type equation that relates the internal variable $p_0 \in \boldsymbol{q}_i$ and its nonlocal counterpart $\breve{p}_0 \in \breve{\boldsymbol{q}}_i$:

$$\breve{p}_{0_{n+1}} - \boldsymbol{\nabla}_0 \cdot \left(\boldsymbol{c}_{\mathrm{g}} \cdot \boldsymbol{\nabla}_0 \breve{p}_{0_{n+1}} \right) = p_{0_{n+1}} \quad \text{for} \quad \omega_0, \tag{3.79}$$

where p_0 is a representation of the matrix plastic strain, $\breve{p}_0$ stands for a representation of the homogenized matrix nonlocal accumulated plastic strain and where for an isotropic medium (Wu et al., 2015), $\boldsymbol{c}_{\mathrm{g}} = \mathrm{diag}\left(l_c^2; l_c^2; l_c^2\right)$, being l_c the characteristic length scale. It is now possible to rewrite Eq. (3.27) in a nonlocal form as:

$$\boldsymbol{\sigma}_i(t) = \boldsymbol{\sigma}_i\left(\boldsymbol{\varepsilon}_i(t), \breve{\boldsymbol{q}}_i(\tau); \boldsymbol{q}_i(\tau), \tau \in [0, t]\right). \tag{3.80}$$

In this Work, we consider the damage of the matrix phase only since we are interested in accounting for the effect of the pressure-dependent yield surface on the homogenization scheme. The formulation can be extended to account for fiber failure by considering a scalar damage variable in the inclusion phase in order to capture the composite response (Wu et al., 2021). As shown by Wu et al. (2012), the system of equations composed by Eqs. (3.78) and (3.79) can be solved by combining a weak finite element form with Newton-Raphson linearization technique. During this Newton-Raphson resolution, the macrostrain increment $\Delta\bar{\boldsymbol{\varepsilon}}_{n+1}$ and the nonlocal matrix plastic strain $\breve{p}_{0_{n+1}}$ are the degrees of freedom arising from the weak form discretization. The total macro strain tensor $\bar{\boldsymbol{\varepsilon}}_n$ and the internal state variables (including p_{0_n}) at the initial state of the time interval are known from the previous time step resolution. The homogenized stress $\bar{\boldsymbol{\sigma}}_{n+1}$ as well as its derivatives are evaluated by the MFH model.

Therefore knowing the macrostrain increment $\Delta\bar{\boldsymbol{\varepsilon}}_{n+1}$, it is possible to compute the strain increment that is seen by the LCC $\Delta\bar{\boldsymbol{\varepsilon}}^{\mathrm{r}}_{n+1}$ (see Section 3.1.2):

$$\Delta\bar{\boldsymbol{\varepsilon}}^{\mathrm{r}}_{n+1} = \bar{\boldsymbol{\varepsilon}}_{n} + \Delta\bar{\boldsymbol{\varepsilon}}_{n+1} - \bar{\boldsymbol{\varepsilon}}^{\mathrm{res}}_{n} . \tag{3.81}$$

By defining the LCC operators $\boldsymbol{C}^{\mathrm{LCC}}_{\mathrm{I}}$ and $\boldsymbol{C}^{\mathrm{LCC}}_{0}$ making use of the isotropic linear comparison operators $\boldsymbol{C}^{\mathrm{S}}_{\mathrm{I}}$ and $\boldsymbol{C}^{\mathrm{SD}}_{0}$, the MFH process can be summed up by the relation between the phases and composite strains and stresses and the direct relation between the strain phases via a concentration tensor $\boldsymbol{B}^{\epsilon}$:

$$\begin{aligned} \Delta\bar{\boldsymbol{\varepsilon}}^{\mathrm{r}}_{n+1} &= v_0 \Delta\boldsymbol{\varepsilon}^{\mathrm{r}}_{0_{n+1}} + v_{\mathrm{I}} \Delta\boldsymbol{\varepsilon}^{\mathrm{r}}_{\mathrm{I}_{n+1}} \, , \\ \bar{\boldsymbol{\sigma}}_{n+1} &= v_0 \boldsymbol{\sigma}_{0_{n+1}} + v_{\mathrm{I}} \boldsymbol{\sigma}_{\mathrm{I}_{n+1}} \, , \\ \Delta\boldsymbol{\varepsilon}^{\mathrm{r}}_{\mathrm{I}_{n+1}} &= \boldsymbol{B}^{\epsilon}\left(\mathrm{I}, \boldsymbol{C}^{\mathrm{SD}}_{0}, \boldsymbol{C}^{\mathrm{S}}_{\mathrm{I}}\right) : \Delta\boldsymbol{\varepsilon}^{\mathrm{r}}_{0_{n+1}} . \end{aligned} \tag{3.82}$$

The system resolution follows the next steps:

1. In order to solve this set of equations, the strain increment of the inclusions phase is initialized: $\Delta\bar{\boldsymbol{\varepsilon}}^{\mathrm{r}}_{n+1} \rightarrow \Delta\boldsymbol{\varepsilon}^{\mathrm{r}}_{\mathrm{I}_{n+1}}$. Then, the following scheme is solved iteratively:
   (a) The constitutive material law of the inclusions is called and computed using the phase strain increment tensor $\Delta\boldsymbol{\varepsilon}^{\mathrm{r}}_{\mathrm{I}_{n+1}}$ and the internal variables at t_n. This updates the inclusion phase stress $\boldsymbol{\sigma}_{\mathrm{I}_{n+1}}$, internal variables, incremental-secant operator $\boldsymbol{C}^{\mathrm{Sr}}_{\mathrm{I}_{n+1}}$ and "consistent" anisotropic operator $\boldsymbol{C}^{\mathrm{alg}}_{\mathrm{I_{n+1}}} = \frac{\partial\boldsymbol{\sigma}_{\mathrm{I}_{n+1}}}{\partial\Delta\boldsymbol{\varepsilon}_{\mathrm{I}_{n+1}}}$ reported in Appendix B.1.

   (b) It is now possible to compute the matrix average strain as:

   $$\Delta\boldsymbol{\varepsilon}^{\mathrm{r}}_{0_{n+1}} = \frac{\left(\Delta\bar{\boldsymbol{\varepsilon}}^{\mathrm{r}}_{n+1} - v_{\mathrm{I}}\Delta\boldsymbol{\varepsilon}^{\mathrm{r}}_{\mathrm{I}_{n+1}}\right)}{v_0} . \tag{3.83}$$

   (c) Then, the constitutive material law of the matrix described in Section 3.2 is called using the strain tensor increment $\Delta\boldsymbol{\varepsilon}^{\mathrm{r}}_{0_{n+1}}$ and the internal state variables at t_n. This gives the updated matrix stress $\boldsymbol{\sigma}_{0_{n+1}}$, damage state $D_{0_{n+1}}$, internal variables and the consistent and incremental-secant operators $\boldsymbol{C}^{\mathrm{alg}}_{0_{n+1}}$, $\boldsymbol{C}^{\mathrm{algD}}_{0_{n+1}} = \left(1 - D_{0_{n+1}}\right)\boldsymbol{C}^{\mathrm{alg}}_{0}$ and $\boldsymbol{C}^{\mathrm{SD}}_{0_{n+1}}$.

   (d) Knowing the matrix incremental-secant operator, the Eshelby tensor $\boldsymbol{S}\left(\mathrm{I}, \boldsymbol{C}^{\mathrm{SD}}_{0_{n+1}}\right)$ is evaluated.

   (e) For the time interval $[t_n, t_{n+1}]$ the strain increment of the composite material and the nonlocal plastic strain of the matrix ($\Delta\bar{\boldsymbol{\varepsilon}}^{\mathrm{r}}_{n+1}$ and $\Delta\breve{p}_{0_{n+1}}$) are known and the stress residual vector $\boldsymbol{F}$ of the system of Eqs. (3.82), see Appendix B.2, is evaluated:

   $$\boldsymbol{F} = \boldsymbol{C}^{\mathrm{SD}}_{0_{n+1}} : \left[\Delta\boldsymbol{\varepsilon}^{\mathrm{r}}_{\mathrm{I}_{n+1}} - \frac{1}{v_0}\boldsymbol{S}^{-1} : \left(\Delta\boldsymbol{\varepsilon}^{\mathrm{r}}_{\mathrm{I}_{n+1}} - \Delta\bar{\boldsymbol{\varepsilon}}^{\mathrm{r}}_{n+1}\right)\right] - \boldsymbol{C}^{\mathrm{S}}_{\mathrm{I}_{n+1}} : \Delta\boldsymbol{\varepsilon}^{\mathrm{r}}_{\mathrm{I}_{n+1}} . \tag{3.84}$$

   (f) The inclusion strain increment is thus corrected following:

   $$\Delta\boldsymbol{\varepsilon}^{\mathrm{r}}_{\mathrm{I}_{n+1}} \leftarrow \Delta\boldsymbol{\varepsilon}^{\mathrm{r}}_{\mathrm{I}_{n+1}} - \boldsymbol{J}^{-1} : \boldsymbol{F}, \tag{3.85}$$

   where the Jacobian $\boldsymbol{J}$ is given in Appendix B.2.

   (g) Then, a new iteration is started, going back to step (a) until $|\boldsymbol{F}| \leq$ Tol.

2. Once convergence is reached:

(a) Compute the internal variables and the homogenized stress:

$$\bar{\boldsymbol{\sigma}}_{n+1} = v_0 \boldsymbol{\sigma}_{0_{n+1}} + v_{\mathrm{I}} \boldsymbol{\sigma}_{\mathrm{I}_{n+1}} \,. \tag{3.86}$$

(b) Using the "consistent" tangent operators $\bar{\boldsymbol{C}}^{\mathrm{alg}} = \frac{\partial \bar{\boldsymbol{\sigma}}}{\partial \bar{\boldsymbol{\varepsilon}}}$ and $\boldsymbol{C}_{\breve{p}} = \frac{\partial \bar{\boldsymbol{\sigma}}}{\partial \breve{p}_0}$, with

$$\bar{\boldsymbol{C}}^{\mathrm{alg}}_{n+1} = v_{\mathrm{I}} \boldsymbol{C}^{\mathrm{alg}}_{\mathrm{I}} : \frac{\partial \boldsymbol{\varepsilon}_{\mathrm{I}}}{\partial \bar{\boldsymbol{\varepsilon}}} + v_0 \left(\boldsymbol{C}^{\mathrm{algD}}_0 - \hat{\boldsymbol{\sigma}}_0 \otimes \frac{\partial D_0}{\partial \boldsymbol{\varepsilon}_0} \right) : \frac{\partial \boldsymbol{\varepsilon}_0}{\partial \bar{\boldsymbol{\varepsilon}}}, \text{ and} \tag{3.87}$$

$$\boldsymbol{C}_{\breve{p}} = v_{\mathrm{I}} \boldsymbol{C}^{\mathrm{alg}}_{\mathrm{I}} : \frac{\partial \boldsymbol{\varepsilon}_{\mathrm{I}}}{\partial \breve{p}_0} + v_0 \left(\boldsymbol{C}^{\mathrm{algD}}_0 - \hat{\boldsymbol{\sigma}}_0 \otimes \frac{\partial D}{\partial \boldsymbol{\varepsilon}_0} \right) : \frac{\partial \boldsymbol{\varepsilon}_0}{\partial \breve{p}} - v_0 \hat{\boldsymbol{\sigma}}_0 \frac{\partial D_0}{\partial \breve{p}_0}, \tag{3.88}$$

the consistent linearization of the homogenized stress can be computed:

$$\delta \bar{\boldsymbol{\sigma}} = \bar{\boldsymbol{C}}^{\mathrm{alg}} : \delta \bar{\boldsymbol{\varepsilon}} + \boldsymbol{C}_{\breve{p}} \delta \breve{p}_0. \tag{3.89}$$

The expressions of $\boldsymbol{C}^{\mathrm{alg}}_i$ are given in Appendix B.1, the expressions of $\frac{\partial \boldsymbol{\varepsilon}_i}{\partial \bar{\boldsymbol{\varepsilon}}}$ and $\frac{\partial \boldsymbol{\varepsilon}_i}{\partial \breve{p}_0}$ are given in Appendix B.2 and the expressions of $\frac{\partial D_0}{\partial \boldsymbol{\varepsilon}_0}$ and $\frac{\partial D_0}{\partial \breve{p}_0}$ are given in Appendix B.5.

In order to solve the weak form (Eqs. (3.78) and (3.79)), one also needs the linearization of p_0 which writes:

$$\delta p_0 = \frac{\partial p_0}{\partial \bar{\boldsymbol{\varepsilon}}} \delta \bar{\boldsymbol{\varepsilon}} + \frac{\partial p_0}{\partial \breve{p}_0} \delta \breve{p}_0, \tag{3.90}$$

where the derivative of p_0 with respect to the strain is indirectly related to the plastic multiplier, as shown in Eqs. (3.55) and (3.42) through

$$\frac{\partial p_0}{\partial \bar{\boldsymbol{\varepsilon}}} = \frac{\partial p_0}{\partial \Gamma_0} \frac{\partial \Gamma_0}{\partial \boldsymbol{\varepsilon}_0} \frac{\partial \boldsymbol{\varepsilon}_0}{\partial \bar{\boldsymbol{\varepsilon}}}, \tag{3.91}$$

with $\frac{\partial p_0}{\partial \Gamma_0}$ obtained from Eq. (3.55), $\frac{\partial \Gamma_0}{\partial \boldsymbol{\varepsilon}_0}$ from Appendix B.1 and $\frac{\partial \boldsymbol{\varepsilon}_0}{\partial \bar{\boldsymbol{\varepsilon}}}$ from Appendix B.2. The derivative $\boldsymbol{C}_p = \frac{\partial p_0}{\partial \breve{p}_0}$ is given in Appendix B.1.

3. Then, the unloading step is performed, obtaining the needed composite material, matrix and inclusion phases, residual strains $\left(\bar{\boldsymbol{\varepsilon}}^{\mathrm{res}}_{n+1}, \boldsymbol{\varepsilon}^{\mathrm{res}}_{0_{n+1}}, \text{ and } \boldsymbol{\varepsilon}^{\mathrm{res}}_{\mathrm{I_{n+1}}} \right)$, the inclusions residual stress $\boldsymbol{\sigma}^{\mathrm{res}}_{\mathrm{I_{n+1}}}$ and the matrix phase effective residual stress $\hat{\boldsymbol{\sigma}}^{\mathrm{res}}_{0_{n+1}}$ required for the next loading increment. To this end:

   (a) Considering a pure virtual elastic process, the composite material is unloaded up to a zero-stress state. The residual strain of the composite is then computed following Eq. (3.15), yielding

$$\bar{\boldsymbol{\varepsilon}}^{\mathrm{res}}_{n+1} = \bar{\boldsymbol{\varepsilon}}_{n+1} - \Delta \bar{\boldsymbol{\varepsilon}}^{\mathrm{unload}}_{n+1} = \bar{\boldsymbol{\varepsilon}}_{n+1} - \left(\bar{\boldsymbol{C}}^{\mathrm{elD}}_{n+1} \right)^{-1} : \bar{\boldsymbol{\sigma}}_{n+1}. \tag{3.92}$$

   (b) Once the residual strain of the composite is known, the matrix and inclusion phase residual stresses are computed as:

$$\begin{aligned} \boldsymbol{\varepsilon}^{\mathrm{res}}_{0_{n+1}} &= \boldsymbol{\varepsilon}_{0_{n+1}} - \Delta \boldsymbol{\varepsilon}^{\mathrm{unload}}_{0_{n+1}} \\ &= \boldsymbol{\varepsilon}_{0_{n+1}} - \left[v_{\mathrm{I}} \boldsymbol{B}^{\epsilon}(\mathrm{I}, \boldsymbol{C}^{\mathrm{elD}}_0, \boldsymbol{C}^{\mathrm{el}}_{\mathrm{I}}) + v_0 \boldsymbol{I} \right]^{-1} : \Delta \bar{\boldsymbol{\varepsilon}}^{\mathrm{unload}}_{n+1} \,, \text{ and} \end{aligned} \tag{3.93}$$

$$\begin{aligned} \boldsymbol{\varepsilon}^{\mathrm{res}}_{\mathrm{I_{n+1}}} &= \boldsymbol{\varepsilon}_{\mathrm{I}_{n+1}} - \Delta \boldsymbol{\varepsilon}^{\mathrm{unload}}_{\mathrm{I_{n+1}}} \\ &= \boldsymbol{\varepsilon}_{\mathrm{I}_{n+1}} - \boldsymbol{B}^{\epsilon}(\mathrm{I}, \boldsymbol{C}^{\mathrm{elD}}_0, \boldsymbol{C}^{\mathrm{el}}_{\mathrm{I}}) : \left[v_{\mathrm{I}} \boldsymbol{B}^{\epsilon}(\mathrm{I}, \boldsymbol{C}^{\mathrm{elD}}_0, \boldsymbol{C}^{\mathrm{el}}_{\mathrm{I}}) + v_0 \boldsymbol{I} \right]^{-1} : \Delta \bar{\boldsymbol{\varepsilon}}^{\mathrm{unload}}_{n+1} \,. \end{aligned} \tag{3.94}$$

(c) The residual stress of the inclusion phase and the effective stress of the matrix phase are then computed as:

$$\hat{\boldsymbol{\sigma}}^{\mathrm{res}}_{0_{n+1}} = \hat{\boldsymbol{\sigma}}_{0_{n+1}} - \boldsymbol{C}^{\mathrm{el}}_{0_{n+1}} : \Delta\boldsymbol{\varepsilon}^{\mathrm{unload}}_{0_{n+1}} \text{ , and} \tag{3.95}$$

$$\boldsymbol{\sigma}^{\mathrm{res}}_{\mathrm{I_{n+1}}} = \boldsymbol{\sigma}_{\mathrm{I}_{n+1}} - \boldsymbol{C}^{\mathrm{el}}_{\mathrm{I}_{n+1}} : \Delta\boldsymbol{\varepsilon}^{\mathrm{unload}}_{\mathrm{I_{n+1}}} \,. \tag{3.96}$$

The MFH resolution in the nonlocal FE framework made use of the C++ code developed for the paper by Wu et al. (2017). The code was adapted to account for the new definition of the incremental secant tensors, as well as all the required derivatives in the process. This implementation permits the user to easily switch from the original J2 based incremental secant MFH to the here developed pressure-dependent model.

3.4 Verification of the MFH scheme prediction with direct FE simulations

Once the pressure-dependent damage-enhanced incremental-secant MFH model has been developed, its accuracy is verified against finite-element full-field simulations. To this end, random UD composite volume element with different volume fractions and spherical inclusions-reinforced composites are used considering elastic, elasto-plastic and damage-enhanced phases.

For the direct numerical simulations, we consider periodic boundary conditions (PBC) for displacement field and the nonlocal variables. The use of this boundary condition improves the convergence rate even for nonperiodic structures, as shown in the work by Nguyen et al. (2012). However, when considering failure, multiple localization bands could appear at the failure onset when this kind of boundary condition is used. This is not the case under tensile loading conditions for which this condition is valid, since in those cases the failure band is perpendicular to the loading direction (Nguyen, Wu, and Noels, 2019). While remaining out of the onset of localization, the PBC conditions are still valid for all test cases. Another problem after localization onset is the loss of size objectivity and thus the absence of existence of a representative volume element (RVE). In order to recover this size objectivity, a new reference quantity, such as the energy release rate, must be used as a target in order to correctly define the failure stage of the material (Verhoosel et al., 2010; Nguyen, Wu, and Noels, 2019). This case will be treated in Chapter 4. We note that because of the use of a nonlocal damage evolution law, MFH is energy consistent during localization since the characteristic length can be evaluated to recover the right amount of dissipated energy during failure (Wu et al., 2021). Nevertheless, the MFH response during localization cannot be compared to the direct finite element response since the latter depends on the size of the volume element.

In order to be able to mathematically discuss the discrepancies found on the loading test cases, an error measurement scheme is implemented in order to give a more quantitative assessment of the errors found in the MFH predictions on the composite response as well as on the phases responses. To this end, the error on a stress component i is evaluated following:

$$\%\Delta_i = \frac{\int_{\mathrm{Cycle}} |\langle \sigma_{i_{\mathrm{RVE}}} \rangle - \sigma_{i_{\mathrm{MFH}}}| \, d\varepsilon_i}{\int_{\mathrm{Cycle}} |\langle \sigma_{i_{\mathrm{RVE}}} \rangle| \, d\varepsilon_i} \times 100 \,, \tag{3.97}$$

where $\sigma_{i_{\mathrm{RVE}}}$ is the corresponding component of the full-field simulation stress tensor, and $\sigma_{i_{\mathrm{MFH}}}$ stands for the corresponding component of the MFH simulation stress tensor. In order to avoid additive problems, $d\varepsilon_i$ is always taken as positive, including during unloading path. For the phases error, the mean of the inclusion and matrix response errors are considered and added.

3.4.1 Matrix and inclusions material properties

In this Work, two-phase composites are studied. The spherical inclusions phase is modeled as an isotropic elastic material, the fiber inclusions phase is modeled as a transversely isotropic elastic material and the matrix as an elasto-plastic, possibly damage-enhanced, material. This phase is modeled with the pressure-dependent-based incremental-secant law introduced in Section 3.2 using an exponential hardening for the plastic stage of the matrix response:

$$R_0(p_0) = h_0\left(1 - e^{-m_0 p_0}\right) . \tag{3.98}$$

The evolution law used to model the damaged-enhanced phase is divided into two contributions: A softening damage (D_s) and a failure damage (D_f). The softening damage models the damage evolution up to the strain-softening onset writing:

$$\Delta D_s = \frac{D_{\text{onset}}}{p_{\text{onset}}} \Delta \breve{p}_0 , \tag{3.99}$$

where D_{onset} and p_{onset} are the matrix damage and the accumulated plastic strain at the strain-softening onset respectively. The failure damage D_f contribution starts after the matrix strain-softening onset. This law permits to model the failure characteristics of the material by accelerating the development of damage. The failure damage D_f writes:

$$\Delta D_f = \alpha_{\text{Dam}}\left(\breve{p}_0 + \Delta\breve{p}_0 - p_{\text{onset}}\right)^{\beta_{\text{Dam}}} \Delta\breve{p}_0, \quad \text{if} \quad \breve{p}_0 > p_{\text{onset}} . \tag{3.100}$$

Finally, the used matrix damage evolution law D_0 writes:

$$\Delta D_0 = \begin{cases} \Delta D_s, & \text{if} \quad \breve{p}_0 \leq p_{\text{onset}} , \\ \Delta D_s + \Delta D_f, & \text{if} \quad \breve{p}_0 > p_{\text{onset}} . \end{cases} \tag{3.101}$$

The damage law derivatives are given in Appendix B.5. This Lemaitre-Chaboche damage formulation in which the damage history is taken into account by means of scalar variables was already used for the modeling of high-crosslinked polymer materials, usually found in composite materials, and proved to be able to represent accurately the damage evolution as well as failure for different test cases, including 3D test with barreling effects (Nguyen et al., 2016). In this latter reference, one scalar damage variable captures the material failure, and one scalar damage variables captures the post-peak saturated softening observed under compressive loading. The two scalar damage variables follow different damage evolution laws and can be reformulated under a single damage variable in a Lemaitre-Chaboche model. Therefore, for the sake of simplicity, we consider a single damage variable in this Work.

The properties used for the inclusion phase are the same as the properties used in Nguyen, Wu, and Noels (2019) (UD300/CHS carbon fiber) and the matrix properties were chosen so that it matches the RTM6 epoxy resin behavior studied by Nguyen et al. (2016). The inclusions and matrix phases properties are reported in Tables 3.1, 3.2 and 3.3.

TABLE 3.1: Inclusion phase properties for UD composite.

Inclusions phase properties [Unit]	**Value**
Longitudinal Young's modulus E^{L} [GPa]	230
Transverse Young's modulus E^{T} [GPa]	40
Transverse Poisson's ratio ν^{TT} [-]	0.2
Longitudinal transverse Poisson's ratio ν^{LT} [-]	0.215
Transverse shear modulus μ^{TT} [GPa]	16.7
Longitudinal transverse shear modulus μ^{LT} [GPa]	24

TABLE 3.2: Inclusion phase properties for 3D spherical inclusion reinforced composite.

Inclusions phase properties [Unit]	**Value**
Young's modulus E [GPa]	230
Poisson's ratio ν [-]	0.215

TABLE 3.3: Matrix phase properties.

Matrix phase properties [Unit]	**Value**
Young's modulus E [MPa]	2450
Poisson's ratio ν [-]	0.38
Initial Yield σ_0 [MPa]	48
Yield ratio m [-]	0.85
Initial plastic Poisson's ratio ν_p [-]	0.3
Hardening parameter h_0 [MPa]	164
Hardening parameter m_0 [-]	36.5
Damage parameter p_{onset} [-]	0.14
Damage parameter D_{onset} [-]	0.35
Damage parameter α_{Dam} [-]	18
Damage parameter β_{Dam} [-]	2.5

3.4.2 2D MFH verification with UD composite RVE

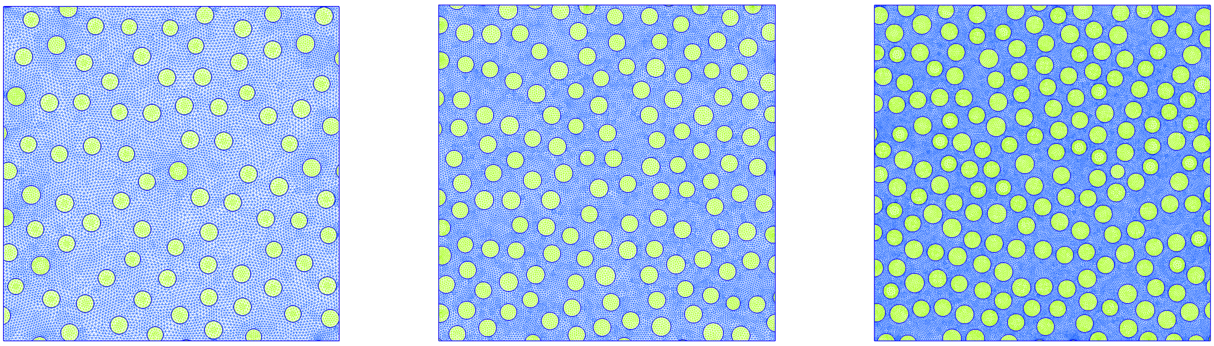

FIGURE 3.5: 18% (left) 28% (center) 40% (right) volume fraction square UD RVE of 150μm side length with second order mesh. Matrix phase in blue and fiber phase in green.

In this Section, the 2D performance of the developed MFH scheme is studied by comparing the MFH predictions for different volume fractions with its RVE full-field FE simulation counterpart. The elasto-plastic and the damage-enhanced elasto-plastic cases are studied in different test settings, which include uniaxial tension cycles, biaxial tension, shear and nonproportional loading. The considered RVEs are square UD samples of 150 μm, see Figure 3.5, generated using the generation process developed by Wu et al. (2018). Three different square RVEs of 150μm side length with different volume fractions were used in order to test the MFH capabilities for different volume fractions ranging from 18% to 40%. As in the work by Nguyen, Wu, and Noels (2019), in order to correctly account for the effect of fibers in the direct FE simulations, the matrix phase considers a nonlocal matrix $\boldsymbol{c}_{\text{g}} = \text{diag}(l_c^2)$ with $l_c = 3.2\mu m$, value that represents the average radius of fiber. All the 2D FE tests were carried out with the third dimension constrained so that plane strain conditions are used.

3.4.2.1 Elasto-plastic case

The first verification is made without taking damage into account. As already mentioned, in order to check the validity of the MFH scheme for different levels of volume fractions, three different samples with 18%, 28% and 40% have been tested, see Figure 3.5.

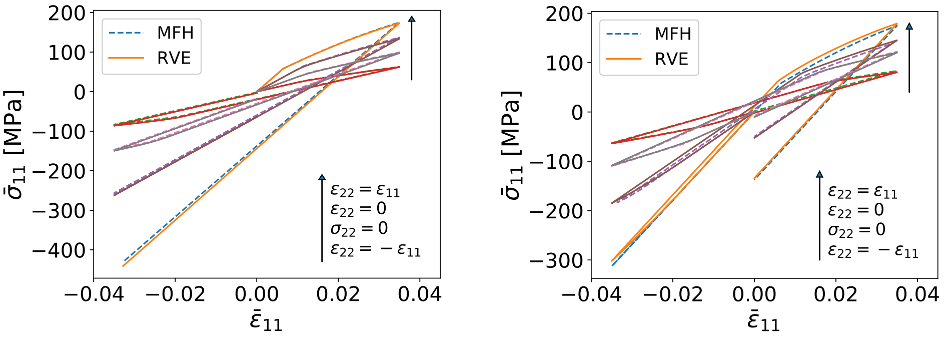

FIGURE 3.6: Stress-strain curves of tension-compression cycle tests on the elasto-plastic 2D UD sample with 18% inclusion volume fraction. Cycles with different triaxiality levels starting with tension on the left and starting with compression on the right.

Pressure-dependency test In order to test the pressure-dependent MFH scheme performance under different hydrostatic pressure conditions, four different strain evolution paths have been used in the two main directions of the 18% RVE. The strain evolution in the 11 direction is kept the same for all the tests while the loading condition in the 22 direction sees different constraints, introducing an added pressure effect in the $\bar{\varepsilon}_{22} = -\bar{\varepsilon}_{11}$, $\bar{\varepsilon}_{22} = \bar{\varepsilon}_{11}$ and $\bar{\varepsilon}_{22} = 0$ cases, or keeping the material free to deform in the 22 direction ($\bar{\sigma}_{22} = 0$). For the 11 direction, two different loading paths are tested, first performing a tension-compression complete cycle, and then a compression-tension complete cycle. The obtained results are shown in Figure 3.6.

As Figure 3.6 shows, for the tension-compression loading cycle, the MFH scheme is able to accurately capture the behavior of the two-phase composite material for all the tested cases. As it is possible to observe, the pressure-dependent scheme is capable of predicting correctly the tension-compression flow asymmetry capturing the different behaviors of the composite under different hydrostatic pressure conditions. The same is observed in the compression-tension loading cycle. The overall prediction of the MFH model is very satisfactory for all the tested cases.

Volume fraction effect After testing the pressure-dependency feature of the model, the effect of the fiber volume fraction is studied. The first test performed is a small deformation cyclic uniaxial tension-compression test (plane-strain in 33-direction) on the UD composite RVE. The obtained stress-strain curves can be observed in Figure 3.7.

As it can be seen, the MFH yields accurate results for the three volume fractions tested. From Figure 3.7 it can be said that the lower the volume fraction the more accurate the MFH prediction is, being the average composite stress predicted by the MFH scheme in the tension stage accurate compared to the finite element simulation. It is possible to observe a slope difference in the elastic phases of the cycle. In order to further investigate this slope difference, we compute the slopes found at each elastic phase of the loading cycle. As Table 3.4 shows, most of the difference between the full-field simulation and the MFH slope can already be found in the first elastic loading stage, which points to the effect of the Mori-Tanaka assumption whose accuracy decreases with the increase of the volume fraction. Besides, even though small-strain constitutive behaviors were used in the FE code, the latter is framed in a finite strain setting, which causes large local deformations to appear in the matrix between two close positioned fibers,

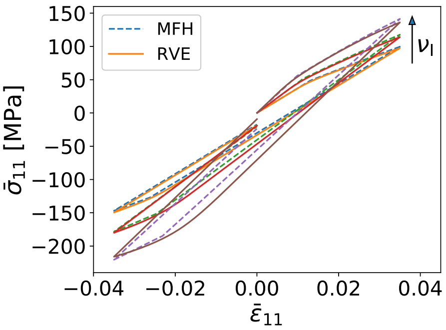

FIGURE 3.7: Stress-strain curves of the uniaxial tension test on the elasto-plastic 2D UD samples with fiber volume fractions of 18%, 28% and 40%.

TABLE 3.4: Slopes of the different elastic phases of the uniaxial cycle for the 2D elasto-plastic MFH and Full-Field simulations for the 3 different volume fractions.

Simulation 18%	**Load [MPa]**	**Unload [MPa]**	**Reload [MPa]**	**Avg Slope Error**
Full-Field	3736.72	3736.71	3736.71	
MFH	3707.26	3707.26	3707.26	0.78%
Simulation 28%	**Load [MPa]**	**Unload [MPa]**	**Reload [MPa]**	**Avg Slope Error**
Full-Field	4597.38	4599.38	4599.44	
MFH	4527.25	4527.25	4527.25	1.55%
Simulation 40%	**Load [MPa]**	**Unload [MPa]**	**Reload [MPa]**	**Avg Slope Error**
Full-Field	5904.17	5908.07	5908.10	
MFH	5634.16	5634.16	5634.16	4.58%

and which leads to a slope discrepancy between the elastic loading and elastic unloading phases of the direct numerical simulation.

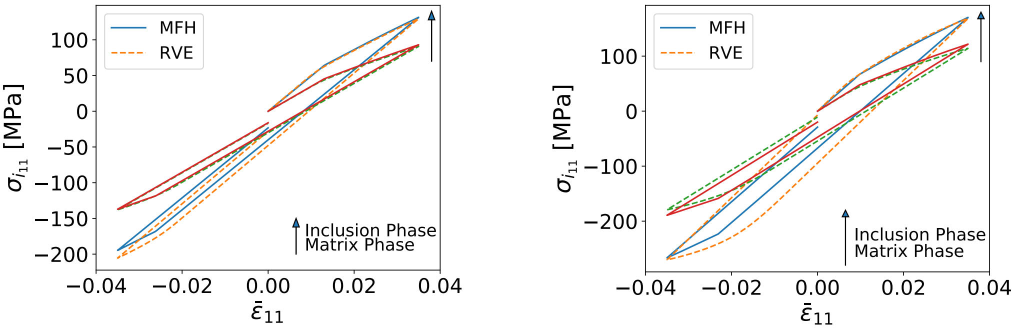

FIGURE 3.8: Fiber and matrix phase stress - composite strain curves of the uniaxial tension test on the elasto-plastic 2D UD samples with fiber volume fractions of 18% (left) and 40% (right).

Figure 3.8 shows a more detailed comparison between the MFH prediction and the Full-Field simulation by presenting the averaged stress obtained for each of the phases of the composite with respect to the composite strain evolution. It is possible to observe the good agreement of the matrix phase response, being the lower volume fraction case more accurate than the 40% volume fraction one. A higher discrepancy is found in the fiber phase, in which the slope discrepancy observed in the composite response is also seen in this phase prediction. Following the error measurement methodology previously presented, it is possible to have a deeper understanding of the found discrepancies. Table 3.5 shows that a 1.29% total average error was found for the lowest fiber volume fraction and a 2.90% in the 40% volume fraction case. An averaged total error ranging between 1.9% and 4.33% is found in the detailed phases responses, when increasing the fiber volume fraction. Even though some differences are present as already exposed, they are small enough to conclude that the MFH scheme is capable of satisfactorily predicting the composite behavior.

TABLE 3.5: Error percentages for different stress components for the 2D elasto-plastic cyclic loading conditions and for different fiber volume fractions.

Test and volume fraction	**Composite 11**	**Phases 11**
Uniaxial; 18%	1.296%	1.901%
Uniaxial; 28%	1.482%	2.184%
Uniaxial; 40%	2.895%	4.334%
	Composite 11	**Phases 11**
Biaxial Cycle; 18%	1.464%	1.764%
Biaxial Cycle; 28%	1.180%	2.765%
Biaxial Cycle; 40%	1.907%	2.745%
	Composite 22	**Phases 22**
Biaxial Cycle; 18%	1.033%	1.114%
Biaxial Cycle; 28%	1.151%	2.32%
Biaxial Cycle; 40%	2.001%	2.094%
	Composite 12	**Phases 12**
Shear Cycle; 18%	1.270%	2.437%
Shear Cycle; 28%	2.037%	2.923%
Shear Cycle; 40%	3.444%	4.812%
	Composite 11	**Phases 11**
Nonproportional $\varepsilon_{22} \neq 0$; 18%	4.380%	4.595%
Nonproportional $\varepsilon_{22} \neq 0$; 40%	8.046%	8.993%
	Composite 12	**Phases 12**
Nonproportional $\varepsilon_{22} \neq 0$; 18%	2.603%	4.129%
Nonproportional $\varepsilon_{22} \neq 0$; 40%	5.634%	7.656%
	Composite 11	**Phases 11**
Nonproportional $\varepsilon_{22} = 0$; 18%	4.656%	4.566%
Nonproportional $\varepsilon_{22} = 0$; 40%	9.088%	9.178%
	Composite 12	**Phases 12**
Nonproportional $\varepsilon_{22} = 0$; 18%	3.056%	5.029%
Nonproportional $\varepsilon_{22} = 0$; 40%	7.136%	7.039%

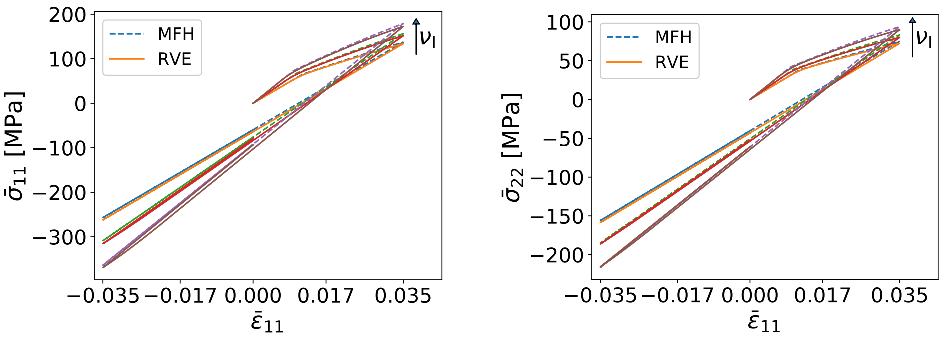

FIGURE 3.9: Loading and transverse direction stress-strain curves for biaxial loading tests ($\bar{\varepsilon}_{22} = 0$) on elasto-plastic 2D UD RVE samples with 18%, 28% and 40% fiber volume fractions.

The next step in the verification is to perform biaxial tension tests in order to verify the MFH model under different triaxiality conditions. In these biaxial tension tests, the strain in the tension-compression direction 11 is modified while the transverse loading direction 22 remains constant at zero strain ($\bar{\varepsilon}_{22} = 0$). As in the previous test, RVE with different volume fractions were used in order to test the MFH performance at different volume fractions. The obtained results can be observed in Figure 3.9. The MFH shows a good agreement with the obtained responses for all the volume fractions tested and is further corroborated by the error values shown in Table 3.5. As in the uniaxial tension test, the higher the volume fraction, the larger the difference in the slope of the unloading/compression phase. The stress in the transverse-loading direction shows how the MFH model is also capable of correctly predicting the behavior of the composite in the 22 direction. The homogenization is therefore capable of predicting a correct composite behavior under different internal pressures showing the ability of the MFH to capture the pressure-dependence of the simulated material.

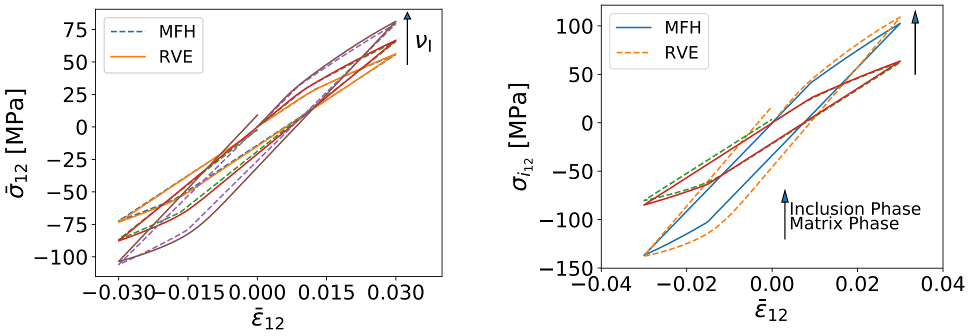

FIGURE 3.10: Stress-strain curves of shear cycle tests on elasto-plastic 2D UD samples with fiber volume fractions of 18%, 28% and 40% (left) and matrix and fiber phase stress - composite strain curves of the cyclic shear test on the elasto-plastic 2D UD sample with fiber volume fraction of 40% (right).

Once loading in the two in-plane directions has been studied, shear strain is the next verification step. Shear is a loading condition in which, due to the kind of deformation applied to the composite, when high volume fractions of fibers are present, large deformations in the matrix are observed. As for the previous test, three different RVEs with volume fractions ranging from 18% to 40% were tested in order to assess the performance of the MFH model. Figure 3.10 shows again good MFH predictions of the composite behavior for all three tested RVEs. As in the previous tests, more accurate results are obtained for the lower volume fraction RVEs than for the higher volume fraction ones. The MFH model shows a slight underestimation of the stress in the first phase of the loading cycle. As for the previous tension tests, the higher the volume fraction, the higher the difference of the elastic slope in the sample response. Closely studying the responses obtained for each of the phases with respect to the composite strain state shown in Figure 3.10, it can be observed how, as for the case of the uniaxial tension test, the matrix phase behavior is correctly captured over the entire path, just showing a small underestimation of the minimum stress reached during the compression phase. This is not the case for the fiber phase, which shows higher discrepancies between the predicted and the full-field response. Most of this discrepancy comes from the fiber phase strain evolution predicted by the MFH, in which the total strain seen by this phase is underestimated compared to the strain observed in the full-field simulation. Detailed error values are reported in Table 3.5 and one can conclude that the MFH is capable of predicting correctly the behavior of a shear loaded composite with the total average errors remaining below 3.5% for all volume fractions.

Nonproportional loading case The incremental-secant approach developed by Wu et al. (2013a) is known for its good accuracy in nonproportional loading cases. Nonproportional loading conditions on the 18% and 40% RVE is now being tested to see how the implemented incremental-secant pressure-dependent MFH model is capable of predicting the behavior of the composite under this condition. Two different tests have been performed, in which tension-compression and shear are applied with different loading for the transverse strain direction. The strain evolutions are depicted in Figures 3.11 and 3.12.

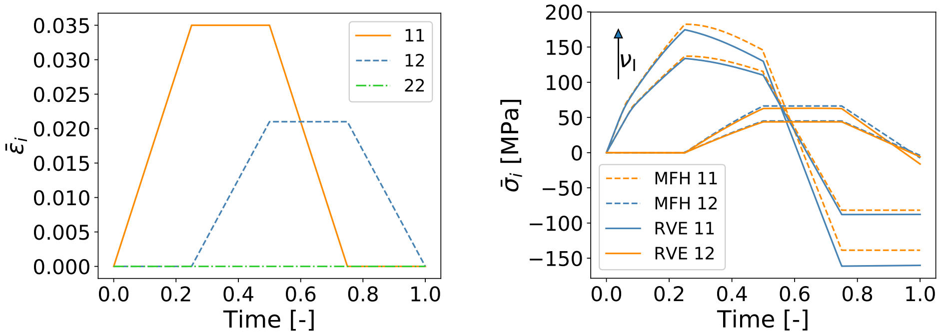

FIGURE 3.11: Strain-time evolution (left) and stress-time response evolution (right) of 18% and 40% fiber volume fraction elasto-plastic 2D UD samples loaded nonproportionally with $\bar{\varepsilon}_{22} = 0$.

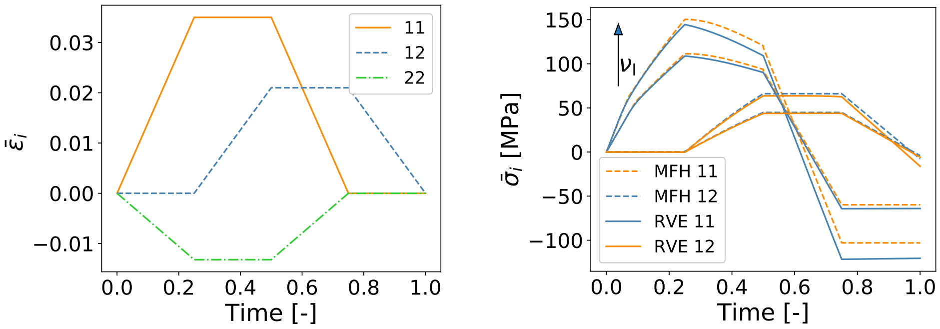

FIGURE 3.12: Strain-time evolution (left) and stress-time response evolution (right) of 18% and 40% volume fraction elasto-plastic 2D UD samples loaded nonproportionally with $\bar{\varepsilon}_{22} \neq 0$.

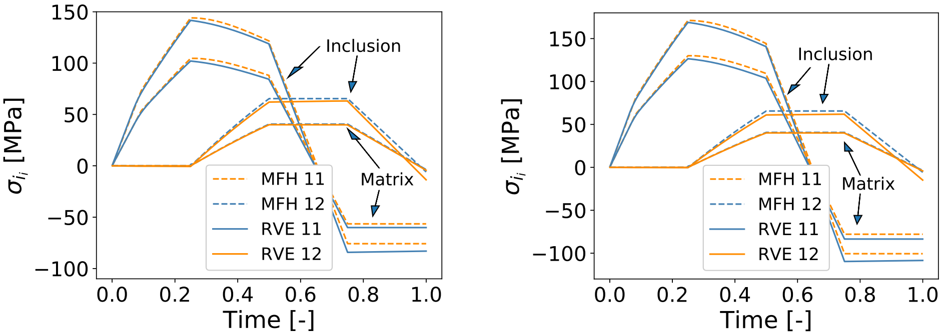

FIGURE 3.13: Phase stress - time curve of the nonproportional test, with $\bar{\varepsilon}_{22} \neq 0$ on the left and with $\bar{\varepsilon}_{22} = 0$ on the right, on the elasto-plastic 2D UD sample with fiber volume fraction of 18%.

As the results show in Figures 3.11 and 3.12, the MFH model presents a good prediction of the composite behavior obtained by the FE simulations. In the first phase of the loading cycle, as already shown in the tension-compression and biaxial tests, a very good agreement between the MFH prediction and the full-field simulation is found for both cases, being the MFH solution slightly stiffer than the full-field one. Then, completing the first half of the test, the shear loading shows a good prediction in both cases for the stress evolution in the longitudinal and shear components. The second half of the test starts by an unloading in the

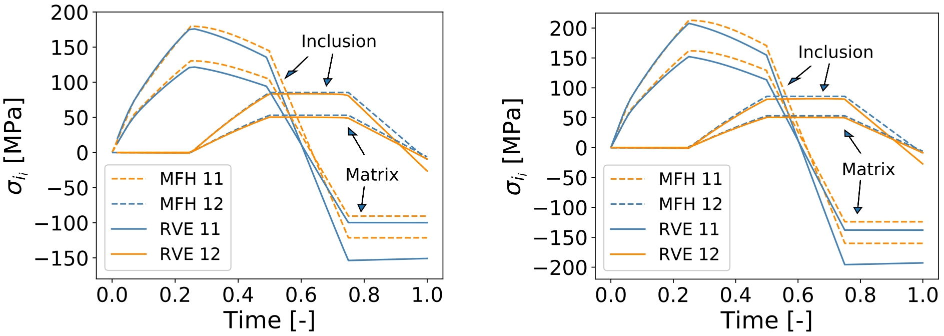

FIGURE 3.14: Phase stress - time curve of the nonproportional test, with $\bar{\varepsilon}_{22} \neq 0$ on the left and with $\bar{\varepsilon}_{22} = 0$ on the right, on the elasto-plastic 2D UD sample with fiber volume fraction of 40%.

longitudinal direction. A small underestimation of the average stress in both components is observed. However, this difference can be considered as relatively small. Finally, in the shear unload phase of the load cycle, one can observe a slight slope difference between the full-field and MFH simulations, being this larger for the highest volume fraction RVE. Figures 3.14 and 3.13 show a detailed look at each phase behavior for the 18% and 40% volume fraction RVEs on the full-field simulation and the MFH prediction. As in previous cases, the matrix phase behavior is better captured than the inclusion phase, where the largest discrepancies are found during the 11 direction unloading stage after the shear loading. Table 3.5 shows that although discrepancies are added up during the full loading cycle, these remain reasonable on both the composite and the phases averaged errors. The general picture for both test cases shows how the pressure-dependent incremental-secant MFH model is capable of performing accurately under nonproportional loading for different triaxiality levels.

3.4.2.2 Damage-enhanced elasto-plastic case

The next step is to verify the MFH predictions when accounting for damage-enhanced elasto-plastic phases. All the following tests were performed using periodic boundary conditions for the displacement and for the involved nonlocal variables, and the displacement in the normal direction was constrained so that plane strain conditions are recovered. The 40% volume fraction RVE sample, see Figure 3.5, was used in all the tests shown in this Section as it is found to be the most challenging case for the MFH model.

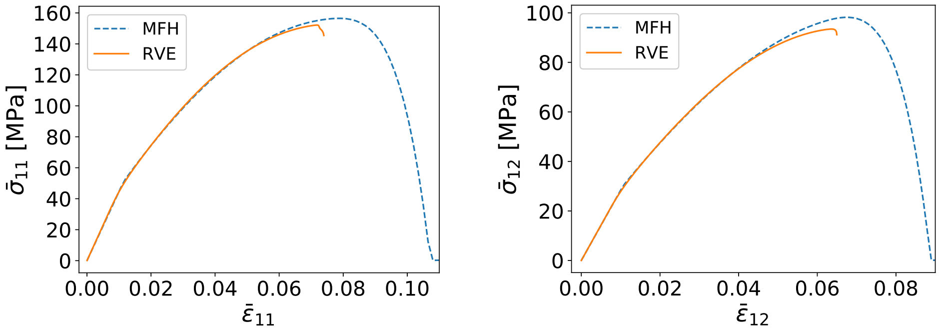

FIGURE 3.15: Stress-strain curves for the damage-enhanced uniaxial loading test on a 40% 2D UD sample (left), and damage-enhanced shear loading test on a 40% 2D UD sample (right).

In order to test the MFH prediction performance in the damaged-enhanced case, the results for the uniaxial and shear loading cases are shown herein. When loading the composite up to its failure onset, Figure 3.15, it is possible to observe a disagreement between both simulations as the

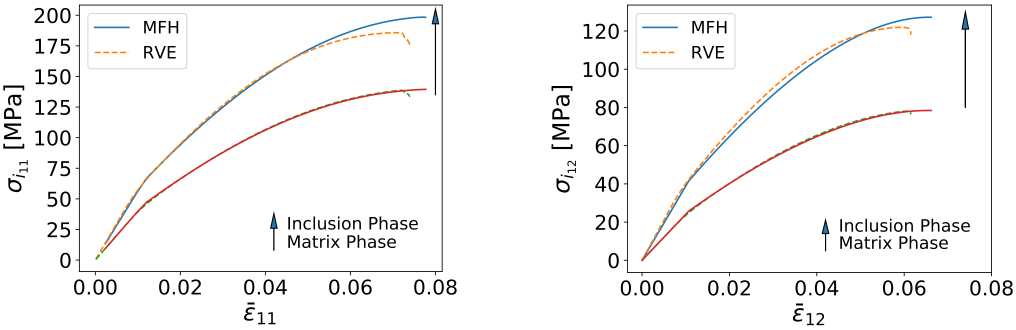

FIGURE 3.16: Matrix and fiber phase stress - composite strain curves of the uniaxial tension test (left) and shear (right) on the damage-enhanced elasto-plastic 2D UD sample with fiber volume fraction of 40%.

MFH model shows a stiffer behavior when reaching the strain-softening onset, especially in the shear loading case, where a 4.2% difference can be found on the reached maximum stress value. As previously mentioned, the periodic boundary conditions are suitable for all cases while remaining out of the localization onset, but once this onset is reached, the PBC suitability can be degraded in the case of shear loading, as multiple shear bands appear. After this localization onset, a loss of size objectivity appears for direct numerical simulation and the results cannot be compared with the MFH which does not suffer from this drawback since the energy dissipation, within a multiscale framework, is governed by the nonlocal characteristic length (Wu et al., 2021). This will be addressed in Chapter 4. Figure 3.16 shows a detailed comparison of the phases average stress between the full-field simulation and the MFH prediction. It is possible to observe how the matrix response is correctly captured up to the failure onset, being the difference between both negligible. In the case of the fiber phase, the MFH prediction shows a stiffer behavior when reaching the softening onset on both test cases, however it is possible to conclude that both phases behaviors were correctly represented by the MFH scheme.

Even though a slight slope difference is encountered in the averaged stress evolution in the composite and must be taken into account, one can conclude that the pressure-dependent MFH method is able to correctly predict the composite behavior under damaging process. A more extensive study for the damaged-enhanced case accounting for other type of loading conditions such as biaxial loading and nonproportional loading can be found in Appendix B.6.

3.4.3 Spherical inclusions-reinforced matrix

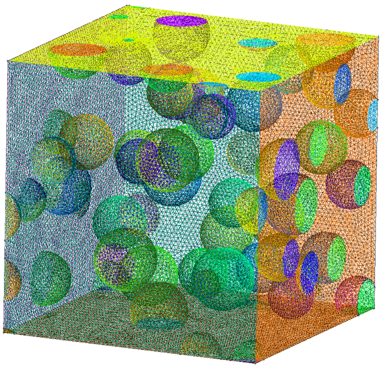

FIGURE 3.17: 3D RVE with 20% spherical inclusions and 100 μm side length meshed with a second order mesh.

After verifying the accuracy of the MFH scheme in 2D, the MFH methodology is tested in 3D with a matrix reinforced with spherical inclusions. As for the 2D case, cyclic tests are performed in order to assess the accuracy of the MFH methodology in 3D. A 20% volume fraction cubic RVE with around 40 spherical inclusions and 100 μm side length is used, as it was proved to be representative enough of the studied composite. The used RVE can be observed in Figure 3.17. As in the 2D case, periodic boundary conditions for the displacement and for the nonlocal variables involved are used in all the performed tests.

3.4.3.1 Elasto-plastic case

As for the 2D case, the elasto-plastic case is studied in the first place. This Section presents equivalent tests to the ones performed in the UD composite case which allow testing the MFH performance under different conditions, including nonproportional loading.

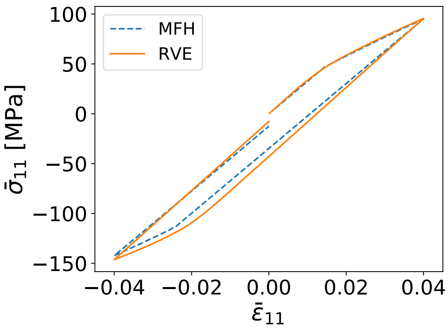

FIGURE 3.18: Stress-strain curves of a uniaxial tension test on an elasto-plastic 3D RVE with spherical inclusions.

TABLE 3.6: Error percentages for different stress components for the 3D elasto-plastic cases.

Test and volume fraction	**Composite 11**	**Phases 11**
Uniaxial 20%	2.637%	3.932%
	Composite 11	**Phases 11**
Triaxial 20%	2.142%	2.251%
	Composite 22	**Phases 22**
Triaxial 20%	1.724%	2.195%
	Composite 12	**Phases 12**
Shear low strain 20%	1.014%	1.637%
Shear high strain 20%	1.623%	2.386%
	Composite 11	**Phases 11**
Nonproportional 20%	4.063%	4.236%
	Composite 12	**Phases 12**
Nonproportional 20%	3.109%	4.764%

Uniaxial, triaxial and shear loading The first test performed is low strain cyclic uniaxial loading ($\bar{\boldsymbol{\sigma}}_{22} = \bar{\boldsymbol{\sigma}}_{33} = 0$). In this test the sample is loaded up to a 4% strain and then symmetrically compressed before returning to a zero-strain state. The obtained results represented in Figure 3.18 show a satisfactory prediction of the composite behavior in the entire cycle. In the first quarter of the simulation in which the loading is carried out, the stress evolution is correctly captured by the MFH method. Then, in the unloading/compression phase, the slight difference in stress evolution slope already seen in the 2D case is recovered, showing a small underestimation of the absolute stress of the composite. The total errors are reported in Table 3.6.

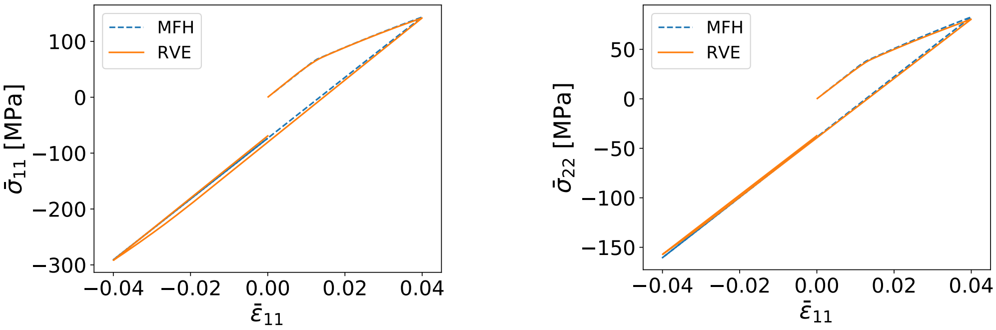

FIGURE 3.19: 11 and 22 direction stress-strain curves of a triaxial loading test on an elasto-plastic 3D RVE with spherical inclusions.

In order to check the MFH accuracy under different composite pressure conditions, triaxial loading is now tested. In this test, the sample is strained in the longitudinal direction (11) and the strain in the other two main directions (22 and 33) is set to be constant at zero strain. The obtained results presented in Figure 3.19 show a good match between the full-field FE simulations and the MFH prediction with a total error below 2.2% as stated in Table 3.6. Even though, the difference in the slope seen at the unloading/compression stage is still observed, this is less pronounced than in the 2D case, and the overall MFH prediction in this 3D case can be considered as accurate.

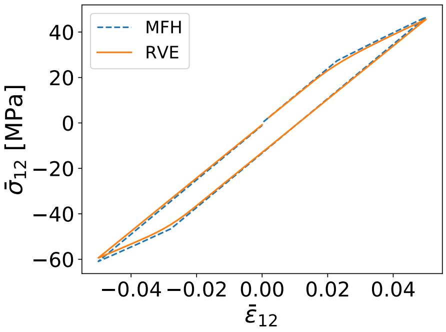

FIGURE 3.20: Stress-strain curves of a shear cycle test on an elasto-plastic 3D RVE with spherical inclusions.

After the uniaxial and triaxial cases have been tested, pure shear loading is tested. The obtained results are shown in Figures 3.20 and 3.21. Figure 3.20 shows a good agreement between the full-field simulation and the MFH prediction. As it can be observed, with a full-cycle error of 1% (Table 3.6), the result is more accurate than the one obtained in the 2D case. Two different shear tests were performed in order to check the performance of the MFH model under different strain percentage conditions. The obtained results show a similar performance for both tests, verifying the correct MFH performance even under higher strain loading paths. Looking at Figure 3.21 which shows the obtained responses of each of the phases for the full-field and MFH simulations in the case of the wider shear deformation cycle, once again, a good prediction of the matrix behavior is observed, however a higher difference is found between both simulations for the fiber response, especially in the plastic compressive phase.

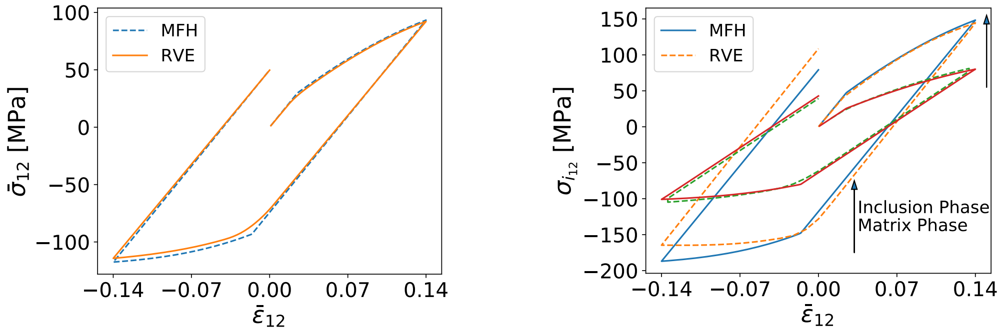

FIGURE 3.21: Stress-strain curves of a shear cycle test on an elasto-plastic 3D RVE with spherical inclusions (left) and its respective matrix and fibre phase stress - composite strain curves (right).

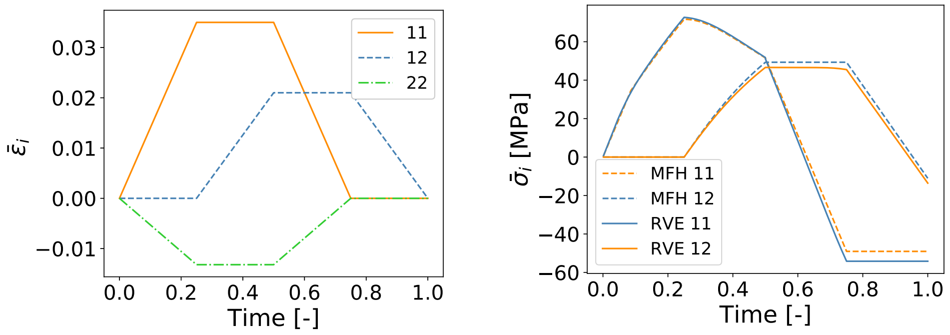

FIGURE 3.22: 11 and 12 component stress-strain curves for a nonproportional loading test on an elasto-plastic 3D RVE with spherical inclusions.

Nonproportional loading Finally, in order to complete the verification of the performance of the MFH model in a three-dimensional case, a nonproportional loading test is performed. Figure 3.22 shows the applied strain constraints and the obtained response for the longitudinal and shear components. Figure 3.22 shows a satisfactory response prediction for both components. The obtained results, with a full cycle error of about 4.1% for the response in 11, see Table 3.6, are comparable to those obtained in the 2D case, being the stress of the material slightly overestimated along the entire loading path and finding a small slope difference between the full-field simulation solution and the MFH prediction.

3.4.3.2 Damage enhanced elasto-plastic case

When damage was considered in the matrix phase in the 2D case, the MFH method showed a good agreement between its prediction and the full-field FE simulation results. This Section now briefly shows the performance of the pressure-sensitive MFH method when damage-enhanced elasto-plasticity is taken into account in the matrix phase of the composite.

The first verification test carried out is uniaxial loading, for which the same test as the one performed for the elasto-plastic case is used. As it can be observed in Figure 3.23, a good MFH result is obtained. The loading path is perfectly captured by the MFH model, correctly following the entire stress evolution. Then, the unloading/compression phase shows a small difference in slope as in the previous cases, which makes the MFH prediction to slightly underestimate the absolute minimum stress reached in the test. However, this difference can be seen as negligible as the stress evolution is satisfactorily captured over the complete cycle.

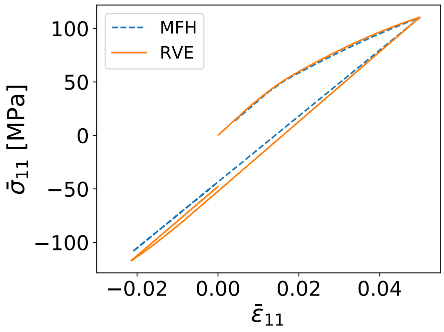

FIGURE 3.23: Stress-strain curves of a damage-enhanced uniaxial loading test on a 3D RVE with spherical inclusions.

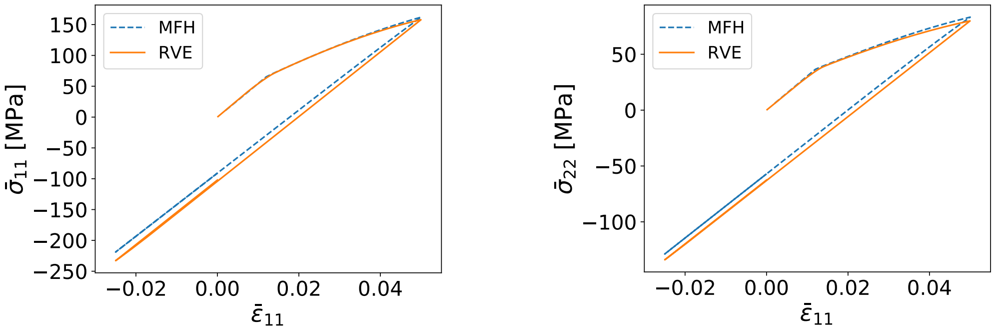

FIGURE 3.24: 11 and 22 component stress-strain curves for a damage-enhanced triaxial loading test on a 3D RVE with spherical inclusions.

To complete this brief verification of the damage-enhanced 3D case, triaxial loading conditions are taken into account, which allow us to verify the correct performance of the MFH method under different pressure conditions. As illustrated in Figure 3.24, this simulation shows a good longitudinal 11 prediction of the stress evolution as for the elasto-plastic case. The transverse direction shows a slight overestimation of the prediction in the loading path; however, this is small enough to consider the MFH prediction as satisfactory.

TABLE 3.7: Error percentages for different stress components for the 3D damage-enhanced cases.

Test and volume fraction	**Composite 11**	**Phases 11**
Uniaxial 20%	2.386%	3.932%
	Composite 11	**Phases 11**
Triaxial 20%	4.028%	4.194%
	Composite 22	**Phases 22**
Triaxial 20%	3.274%	3.723%

Table 3.7 shows how the pressure-dependent MFH method accurately predicts the damage-enhanced elasto-plastic cases. Similar differences to the ones seen in the 2D case were found, being the slope difference in the unloading-compression phase between the full-field and the MFH simulation smaller than in the 2D cases. As for the 2D cases, the MFH scheme has shown good accuracy in the 3D cases.

3.5 Experimental compression test

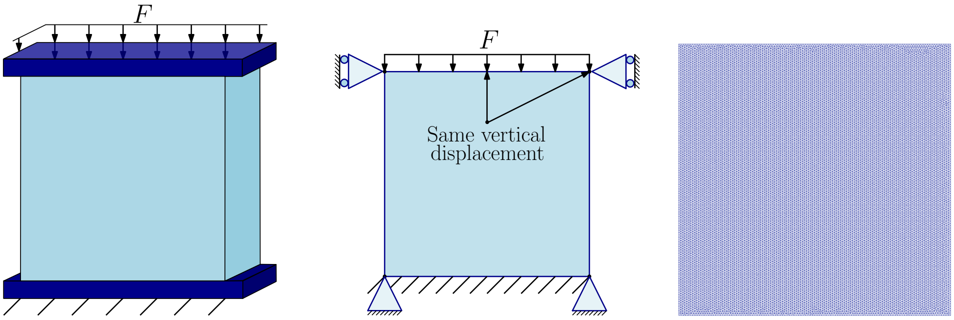

FIGURE 3.25: Experimental setup used in Chevalier, Camanho, and Pardoen (2019) on the left, boundary conditions in the middle and second-order mesh on the right used for the MFH multiscale simulation.

Being the performance of the MFH scheme tested at the microscale, in order to complete the MFH validation, a macroscale transverse compression test is studied. To that end, the compression test performed on a UD composite cube sample by Chevalier, Camanho, and Pardoen (2019) is used. For these tests, cubic specimens of UD composite with 10 mm edge length were transversely compressed until reaching failure. In order to simulate this experimental test numerically at an affordable computational cost, a representation of this macroscale test was performed using a 2D square of 10x10 mm. Figure 3.25 shows a comparison between the experimental and numerical setups. For the multiscale MFH simulation, an unstructured second-order mesh is considered, see Figure 3.25.

An inclusion volume fraction of 40% is considered since this is the experimentally measured one. The material properties of both phases were identified by Nguyen, Wu, and Noels (2019) for viscoelastic-viscoplastic models. Since in the present Chapter we did not consider the viscous effects, in order to recover the same behavior, a correction is applied to the used Young's modulus. The applied correction is computed by considering the instantaneous Young's modulus (Nguyen et al., 2016):

$$E = E_{\infty} + \sum_{i=1}^{N} E_i \mathrm{exp}\left(\frac{t}{\tau_i}\right), \tag{3.102}$$

where E_i, $i = \infty$, $1...N$, and τ_i, $i = 1...N$ are the moduli and time constants of the N Maxwell branches. Using the parameters identified by Nguyen, Wu, and Noels (2019), since the elastic part of the experimental test conducted at $\dot{\varepsilon} = 10^{-4}s^{-1}$ took place in a time of around 150s, the matrix Young's modulus is increased to 2.85 GPa. The other parameters are reported in Tables 3.1 and 3.3. A nonlocal length of 80 μm is used in the multiscale simulation. This nonlocal value, as well as the post failure onset damage parameters should be calibrated (Nguyen, Wu, and Noels, 2019) in order to recover the measured experimental energy release rate G_c following the approach set by Wu et al. (2021), as it will be explained and conducted in Chapter 4.

In transverse loading, the matrix dominates the mechanical response of the composite. Figure 3.26 shows an accurate prediction of the elasto-plastic behavior of the composite cube, successfully capturing the transition from elasticity to plasticity on the macrosample as well as representing a similar plastic evolution. The MFH prediction shows a slightly stiffer behavior, when reaching the failure onset, phenomenon that was also observed in the results of Section 3.4.2.2, however this could be due to the simple damage evolution used in this Chapter, as well as the use of the simplified two-dimensional sample coupled with plane strain.

The failure mode observed experimentally is compared to the numerical predictions in Figure 3.27. As it can be seen, similar failure patterns can be observed between both results, in which

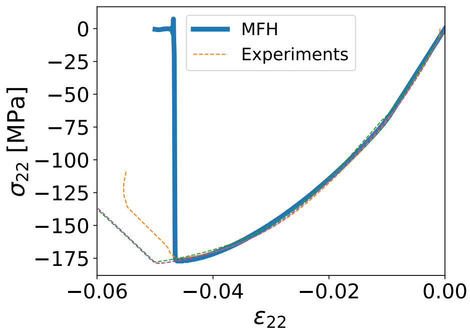

FIGURE 3.26: MFH multiscale and experimental stress-strain curves: experimental tests at $\dot{\varepsilon} = 10^{-4}s^{-1}$ taken from Chevalier, Camanho, and Pardoen (2019).

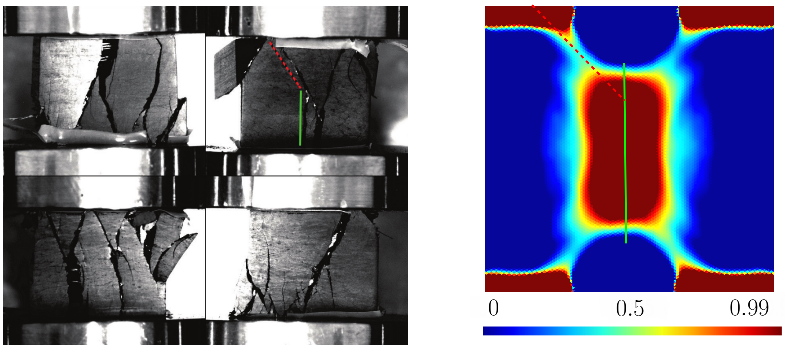

FIGURE 3.27: Surfaces of the cubic UD specimens after failure as shown in Chevalier, Camanho, and Pardoen (2019) on the left: the green and red lines emphasize the transition between a tensile stress dominated crack propagation to a shear one. Reprinted from Composite Structures, 209, J. Chevalier and P.P. Camanho and F. Lani and T. Pardoen, Multi-scale characterization and modelling of the transverse compression response of unidirectional carbon fiber reinforced epoxy, 160-176, Copyright (2022), with permission from Elsevier. Damage [-] contour plot on the deformed sample with a displacement factor of 10 predicted by the multiscale MFH simulations on the right.

two distinctive fracture directions are found due to the transition from a tensile stress to a shear one.

3.6 Summary

In this Chapter, the incremental-secant MFH process developed by L. Wu et al. (Wu et al., 2013c; Wu et al., 2013a) was extended by framing a pressure-dependent yield criterion in an incremental-secant formulation. This yield criterion allows capturing the behavior of pressure-sensitive materials such as some epoxy resins while retaining the advantages of using an incremental-secant approach.

It was proved how the isotropic nature of the secant tensors defining the linear-comparison-composite is preserved for the case of a non-associated pressure-dependent plastic flow. This finding is of crucial importance, as it avoids the isotropization step found in most approaches and allows for accurate MFH predictions. This implementation was completed with the possibility to account for damage by using an implicit nonlocal approach, avoiding the loss of ellipticity that is found in local formulations.

This implementation has shown the accurate prediction capabilities of the pressure-sensitive residual incremental-secant MFH model in the 2D and 3D cases when considering pure elasto-plasticity and in the damage-enhanced case. Slight discrepancies in the slope of the stress evolution between unloading/compression stages were found in the simulations. The Mori-Tanaka assumption is the principal cause of this phenomenon, with the higher the volume fraction, the higher the discrepancy between the full-field simulation and the MFH prediction. Another cause to this discrepancy is caused by the difference in the matrix material model implementation: although small macroscale deformation simulations were performed, in the direct simulations the matrix phase can show large deformations locally when two inclusions are close to each other, and therefore resulting in large local deformation.

In the next chapter, this MFH model will be used to construct a mean-field stochastic reduced order model (MF-ROM) (Wu et al., 2019), which will allow to perform macroscale simulations of composites with pressure-dependent matrix materials accounting for the inherent stochastic properties caused by geometrical perturbations in the microstructure.

Chapter 4

A micromechanical Mean-Field Homogenization surrogate for the stochastic multiscale analysis of composite materials failure[1]

The inherent complexity of the manufacture of composite materials constitutes a major concern for all those industries in which the use of these materials has recently been introduced. Many of these industries need a thorough characterization of the properties and characteristics of the used materials for certification purposes, for which a large number of tests is normally needed. This costly step could be largely reduced by means of virtual testing, being possible to characterize the variability in the performance and the main properties of these materials without the need of real-life testing campaigns. As already discussed and developed in Chapters 1 and 3, while MFH allows to obtain efficient modeling of multi-phase composites, it does not account for the uncertainty effects of the microstructure.

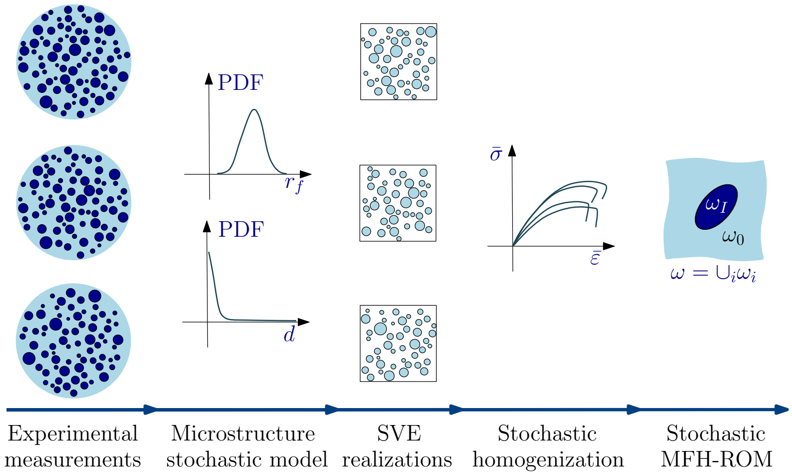

FIGURE 4.1: Schematic representation of the generation of the stochastic MF-ROM. r_f stands for fiber radius, d stands for the fiber nearest distance, $\bar{\boldsymbol{\sigma}}$ and $\bar{\varepsilon}$ stand for the homogenized macro-stress and strains, and ω_i stand for the phases i that compose the composite ω.

In the work by Wu, Adam, and Noels (2018), a surrogate model for linear elasticity was developed by using the mean-field homogenization (MFH) theory for the stochastic ROM definition. The uncertainties are contained in a vector of random parameters that will define the effective material properties which are identified by an inverse analysis performed on the full-field SVE simulations. In the work by Wu et al. (2019), the stochastic micromechanics model serving as mesoscale surrogate model for UD composite materials was further extended to non-linear behaviors. The geometric microscale information was obtained through SEM images of

---

[1] This chapter is an adapted version of the paper (Calleja Vázquez et al., 2023)

real UD materials, and then used to build synthetic microstructures and SVEs of arbitrary size and number (Wu et al., 2018) to perform the full-field simulation campaign. The homogenized responses were then obtained from these SVE realizations and used as the input of an inverse identification process that allows identifying the random effective parameters of the stochastic MFH micromechanical surrogate, which serves as a surrogate that can be used as input for SFEM analysis. However, the method was not able to account for failure. Besides, when modeling complex loading conditions, some discrepancies were found in the composite material response under different internal pressure conditions.

The purpose of this Chapter is to develop a stochastic mean-field reduced order model (MF-ROM) capable of modeling the nonlinear and the post-strain softening behaviors of two-phase UD composite materials and to generate a database used to feed random fields for SFEM analyses. In order to be able to consider complex stress state, the pressure-dependent MFH scheme developed in Chapter 3 is considered.

As previously stated, the obtained homogenized behavior of the SVE is not representative once the strain softening onset is reached, because of the loss of size objectivity of the SVE response encountered beyond this point, meaning the homogenized stress-strain curves no longer represent a valid quantity for the identification process. In order to be able to recover this size objectivity, the inverse process must rely on a new reference quantity (Verhoosel et al., 2010; Nguyen, Wu, and Noels, 2019). As already exposed in Chapter 1, this issue has been addressed in the past thanks to the use of different quantities, such as the traction-displacement jump softening response, the critical energy release rate or the fracture toughness of the material. In this Chapter, as when used in multiscale simulations the MFH is mesh insensitive during this phase because of the nonlocal formulation of the damage evolution law, the critical energy release rate (G_c) has been chosen as the parameter used to recover this size objectivity. The critical energy release rate is then extracted from each SVE realization, permitting to upscale the variabilities found in the failure stage of each SVE to the macroscale through a calibration of the MFH micromechanical surrogate model. This will allow the stochastic MF-ROM to correctly predict not only the effect of the variabilities in the linear and nonlinear stages, but also the variabilities and characteristics of the failure stage.

The Chapter is divided into 5 Sections where the different steps of the generation of the MF-ROM are detailed. In this Work, the steps 1 and 2 of Fig. 4.1 are completed using the developed microstructure stochastic model in Wu et al. (2018). Section 4.1 focuses on the full-field SVE realizations step, from which the data needed for the surrogate construction will be extracted (see steps 3 and 4 of Fig. 4.1). This Section uses the polymer large-strain model developed in Chapter 2 and presents the mathematical basis of the microscale problem and the scale transition of the obtained results of the performed finite element simulations. Then, Section 4.2 focuses on the identification of the MFH surrogate model parameters, which takes the MFH developed in Chapter 3. In this Work, the nonlocal incremental secant scheme is used in order to model the nonlinear behavior of the composite material including its failure. The inverse identification of the model parameters used for the definition of the MF-ROM completes this Section. The inverse identification (see step 5 of Fig. 4.1) is detailed for the elastic and pressure-dependent nonlinear stages of the material response and is completed with the implementation of a calibration process allowing to recover the size objectivity once the strain softening onset is reached. This identification process is then applied to the UD composite SVE realizations in order to construct the MF-ROM, being possible to show a comparison between the predicted MFH responses and the full field SVE results in order to evaluate the accuracy of the inverse-identification process. The identification of parameters is performed for SVE samples of 45×45 μm^2 and 25×25 μm^2, which allows verifying the size consistency of the presented methodology. The obtained effective random parameters are analyzed in Section 4.3, which ends with a brief introduction of the data-driven sampling method used to obtain proper random fields needed for the construction of the stochastic MF-ROM and a comparison between the distributions of the identified and the generated data. This MF-ROM is then applied to the resolution of stochastic simulations in Section 4.4. To this end, two test cases will be used. First, transverse loading tests performed on ply realizations are used as test cases to show the performance of MF-ROM and to assess the results obtained through the two property field discretizations corresponding to the two SVE lengths, by comparing the results with full-field realizations. Then, the validity of the MF-ROM is tested directly against a real-life transverse compression test on a UD composite material, previously presented in Section 3.5.

4.1 SVE realizations and their apparent responses

In this Work a homogenization-based nonlinear stochastic multiscale analysis is performed. Several scales are involved in this analysis. As shown in Figs. 1.7 and 4.1, the homogenized responses seen at the macroscale level are obtained from the microscale resolution. This section will present the main equations governing the relation between the different scales. First, the scale transition and a brief recall of the computational homogenization basics are presented. When performing the SVE simulations, large local deformations appear in the matrix regions embedded between two contiguous fibers. Therefore, a finite strain setting has to be considered at the SVE level although the homogenized strain remains limited to a few percents. Finally, this Section concludes with the generation of the full-field SVE realizations and the extraction of their responses, including during their failure stage.

4.1.1 Microscale boundary value problem

Let us consider a point $\boldsymbol{X}$ belonging to the macroscale volume Ω. In the multiscale analysis based on homogenization, the deformation gradient tensor $\bar{\mathbf{F}}$ and its increment $\dot{\bar{\mathbf{F}}}$ are obtained from the macroscale boundary value problem (BVP). Then, the BVP resolution of the microscale volume element with domain $\boldsymbol{x}_{\text{ref}} \in \omega$, which represents a point of the studied macrostructure $\boldsymbol{X}$, allows the macro-stress tensor $\bar{\boldsymbol{\sigma}}$ to be evaluated.

The position $\boldsymbol{x}$ of a material particle at time t is defined as a two-point mapping of its initial position at the reference configuration $\boldsymbol{x}_{\text{ref}}$ such that: $\boldsymbol{x} = \boldsymbol{x}(\boldsymbol{x}_{\text{ref}}, t)$. Defining the displacement vector $\boldsymbol{u} = \boldsymbol{x} - \boldsymbol{x}_{\text{ref}}$, the deformation gradient tensor $\mathbf{F}$ writes:

$$\mathbf{F} = \boldsymbol{x} \otimes \boldsymbol{\nabla}_0 = \mathbf{1} + \boldsymbol{u} \otimes \boldsymbol{\nabla}_0, \tag{4.1}$$

where $\mathbf{1}$ stands for the second-order identity tensor, and $\boldsymbol{\nabla}_0$ stands for the gradient operator with respect to the reference configuration. The energetically conjugate to the deformation gradient tensor, the first Piola-Kirchhoff stress $\mathbf{P}$, is used as the stress measure.

The microscale is composed of different phases ω_i, having that $\cup_i \omega_i = \omega$. Assuming that classical continuum mechanics applies, the equilibrium equations read:

$$\begin{cases} \mathbf{P} \cdot \boldsymbol{\nabla}_0 = \mathbf{0} & \forall \boldsymbol{x}_{\text{ref}} \in \omega, \\ \boldsymbol{T} = \mathbf{P} \cdot \boldsymbol{N} & \forall \boldsymbol{x}_{\text{ref}} \in \partial\omega, \end{cases} \tag{4.2}$$

where $\boldsymbol{T}$ is the surface traction on boundary $\partial\omega$ with outward unit normal $\boldsymbol{N}$. The material constitutive law is written as:

$$\mathbf{P} = \mathbf{P}\left(\mathbf{F}(t); \boldsymbol{q}(\tau), \tau \in [\ 0, t\ ]\right). \tag{4.3}$$

Plasticity makes deformation to be a path-dependent process, being then necessary to take the strain history into account. To that end, a set of internal variables $\boldsymbol{q}$ that stores this history dependence is used. In the case of a damage-enhanced material, the strain softening implies a mesh dependency of the result if a local formulation is used. In order to avoid this mesh dependency, the implicit nonlocal model (Peerlings et al., 1996; Peerlings et al., 1998; Geers et al., 1998; Peerlings et al., 2001) is used to define the nonlocal internal variables $\breve{\boldsymbol{q}}$. This formulation states that the relation between the internal variable $q_i \in \boldsymbol{q}$ and its nonlocal counterpart $\breve{q}_i \in \breve{\boldsymbol{q}}$ follow a Helmholtz-type equation, which writes:

$$\breve{q}_i(\boldsymbol{x}_{\text{ref}}, t) - \boldsymbol{\nabla}_0 \cdot (\boldsymbol{c}_{\text{g}}(\boldsymbol{x}_{\text{ref}}) \cdot \boldsymbol{\nabla}_0 \breve{q}_i(\boldsymbol{x}_{\text{ref}}, t)) = q_i(\boldsymbol{x}_{\text{ref}}, t) \quad \forall \boldsymbol{x}_{\text{ref}} \in \omega, \tag{4.4}$$

where, for an isotropic medium (Wu et al., 2015), $\boldsymbol{c}_{\text{g}} = \text{diag}\left(l^2; l^2; l^2\right)$, being l_c the characteristic length scale. It is now possible to rewrite Eq. (4.3) in a nonlocal form:

$$\mathbf{P} = \mathbf{P}\left(\mathbf{F}(t); \breve{\boldsymbol{q}}(\tau), \boldsymbol{q}(\tau), \tau \in [\ 0, t\ ]\right). \tag{4.5}$$

4.1.2 Scale transition and computational homogenization

To ensure consistency between scales, the Hill-Mandel condition, which guarantees deformation power consistency, is used. Expressing it in terms of the macroscopic first Piola-Kirchhoff stress tensor $\overline{\mathbf{P}}$ and the macroscopic deformation gradient tensor $\overline{\mathbf{F}}$, one has:

$$\overline{\mathbf{P}} : \dot{\overline{\mathbf{F}}} = \langle \mathbf{P} : \dot{\mathbf{F}} \rangle_\omega = \frac{1}{|\omega|} \int_{\partial\omega} \dot{\boldsymbol{u}} \cdot \boldsymbol{T} dA, \tag{4.6}$$

where ω stands for the volume element of volume $|\omega|$, $\partial\omega$ stands for its external boundary, $\langle \bullet(\boldsymbol{x}_{\text{ref}}) \rangle_\omega = \frac{1}{|\omega|} \int_\omega \bullet(\boldsymbol{x}_{\text{ref}}) d\omega$ is the volume average, $d\omega$ represents the differential volume and dA represents the differential area. This condition allows us to write the weak form equations:

$$\begin{cases} \langle \mathbf{P} : (\dot{\boldsymbol{u}} \otimes \boldsymbol{\nabla}_0) \rangle_\omega - \overline{\mathbf{P}} : \dot{\overline{\mathbf{F}}} = 0, \\ \left\langle (\breve{q}_i - q_i)\dot{\breve{q}}_i + (\boldsymbol{c}_{\text{g}} \cdot \boldsymbol{\nabla}_0 \breve{q}_i) \cdot \boldsymbol{\nabla}_0 \dot{\breve{q}}_i \right\rangle_\omega = 0. \end{cases} \tag{4.7}$$

The macroscopic quantities can then be estimated by performing the average over the studied volume. By further integrating by parts and applying the Gauss theorem using Eq. (4.6), one gets:

$$\begin{cases} \dot{\overline{\mathbf{F}}} = \langle \dot{\mathbf{F}} \rangle_\omega = \frac{1}{|\omega|} \int_{\partial\omega} \dot{\boldsymbol{u}} \otimes \boldsymbol{N} dA, \\ \overline{\mathbf{P}} = \langle \mathbf{P} \rangle_\omega = \frac{1}{|\omega|} \int_{\partial\omega} \boldsymbol{T} \otimes \boldsymbol{x}_{\text{ref}} dA. \end{cases} \tag{4.8}$$

Contrarily to those quantities for which the scale transition $\bar{\bullet} = \langle \bullet(\boldsymbol{x}_{\text{ref}}) \rangle_\omega$ is performed in the homogenization step, this is the case neither for the local nor for the nonlocal internal variables, for which the macroscopic variables correspond to representations of their microscale counterpart distribution, but not to their volume average.

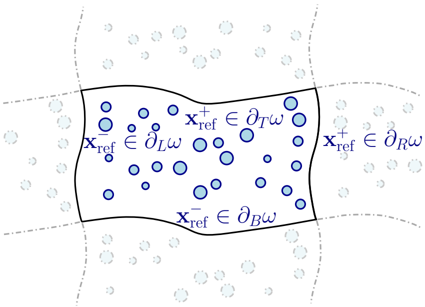

FIGURE 4.2: Graphical representation of the effect of the periodic boundary conditions on a loaded test sample.

The Hill Mandel condition, Eq. (4.6), and the evolution of the deformation gradient tensor, Eq. (4.8), have to be satisfied a priori by the microscopic boundary condition of the displacement field. In this Work, the periodic boundary condition is used: the periodic boundary condition decomposes the edges of ω into positive and negative edges, allowing the coincident nodes to be defined. Each point $\boldsymbol{x}^+_{\text{ref}}$ belonging to an edge $\boldsymbol{x}^+_{\text{ref}} \in \partial_+\omega$ will correspond to its negative counterpart $\boldsymbol{x}^-_{\text{ref}} \in \partial_-\omega$. In this way, the limit $\partial\omega$ of the volume ω will be distributed in these two subdivisions as: $\partial_+\omega = \partial_R\omega \cup \partial_T\omega$ and $\partial_-\omega = \partial_L\omega \cup \partial_B\omega$ (see Fig. 4.2). These distributions allow defining the condition of antiperiodicity in the traction field and periodicity in the displacement field for the coincident nodes:

$$\begin{cases} \dot{\boldsymbol{u}}\left(\boldsymbol{x}^+_{\text{ref}}\right) - \dot{\boldsymbol{u}}\left(\boldsymbol{x}^-_{\text{ref}}\right) = \dot{\mathbf{F}} \cdot \left(\boldsymbol{x}^+_{\text{ref}} - \boldsymbol{x}^-_{\text{ref}}\right), \\ \boldsymbol{T}\left(\boldsymbol{x}^+_{\text{ref}}\right) = -\boldsymbol{T}\left(\boldsymbol{x}^+_{\text{ref}}\right). \end{cases} \tag{4.9}$$

Fig. 4.2 shows a schematic representation of the effect of this periodic boundary condition (PBC) on a loaded sample. This expression implies a direct constraint between opposing nodes; however, this cannot be imposed in general non-periodic meshes. In order to solve this problem the PBC are approximated by an interpolation form (Nguyen et al., 2012). The effect of the BC choice for small periodic and non-periodic volume elements was studied in Firooz et al. (2019). By considering volume elements of increasing size, it was shown that for a periodic microstructure the kinematics uniform boundary condition and statistic uniform boundary condition respectively overestimates and underestimates the effective response predicted by the PBC, and that for a non-periodic microstructure, the same trend can be observed although some oscillations appear with respect to the volume element size. We thus select the PBC, although this introduces a boundary effect for the small SVEs considered in this Work. In order to study this boundary effect, we will consider two different SVE sizes during the analyses and will show that both sizes lead to the same statistical content in the macroscale response predictions. Periodic boundary condition is applied on the nonlocal variables as proposed by Nguyen, Wu, and Noels (2019), and we refer to the discussion in Section 4.1.4. A similar idea of the periodicity in the nonlocal variable can be found in the work by Khoei and Saadat (2019).

The use of PBC for problems involving failure is debatable, in particular when considering PBC for the nonlocal variables. Indeed, as discussed in the work by Nguyen, Wu, and Noels (2019), multiple localization bands can appear in the post-peak localization stage, which is considered to be a nonphysical result (Coenen, Kouznetsova, and Geers, 2012). Nevertheless, during the post-peak localization stage characterized by a loss of size objectivity, the stress-strain response cannot be used. In this Work, we consider the dissipated energy as a consistent value. For this value to be unaffected by the PBC, we consider tensile loading conditions, for which the failure band is perpendicular to the loading direction (Nguyen, Wu, and Noels, 2019), allowing to correctly capture the stress-strain relation before softening onset and the dissipated energy of the sample during failure. For this reason, the uniaxial tension condition will later be the preferred loading condition for the calibration of the post localization onset stage.

4.1.3 Information extracted from the SVE realizations

After defining the constitutive behaviors, the system of equations can then be solved by the multiplier elimination method (Nguyen, Wu, and Noels, 2017). From these SVE realizations, the fourth order homogenized macroscopic tensor $\bar{\boldsymbol{C}} = \frac{\partial\bar{\boldsymbol{\sigma}}}{\partial\bar{\boldsymbol{\varepsilon}}}$ can be extracted (where the Cauchy stress tensor $\bar{\boldsymbol{\sigma}}$ and the small strain tensor $\bar{\boldsymbol{\varepsilon}}$ write: $\bar{\boldsymbol{\sigma}} = \det(\bar{\mathbf{F}})^{-1}\bar{\boldsymbol{P}}\bar{\mathbf{F}}^T$ and $\bar{\boldsymbol{\varepsilon}} = 1/2(\bar{\mathbf{F}}^T + \bar{\mathbf{F}}) - \mathbf{1}$). In order to perform the inverse identification process, the SVE fiber volume fraction as well as the homogenized macro stress-strains ($\bar{\boldsymbol{\sigma}}$; $\bar{\boldsymbol{\varepsilon}}$) and the homogenized macroscopic damaged elastic tensors $\bar{\boldsymbol{C}}^{\text{elD}}$ are extracted. This macroscopic damaged elastic tensor $\bar{\boldsymbol{C}}^{\text{elD}}$ is computed as the homogenized composite material tensor during a virtual elastic unloading.

These quantities allow to perform the elastic and damaged-enhanced plastic regimes identifications (Wu et al., 2019), however, these quantities are not valid once the strain-softening onset is reached. Between the dissipation and the localization onset stages, the development of the damage of the composite material starts diffusing over the entire microstructure. However, once the SVE stress reaches its peak, the so-called localization onset, the dissipated energy released during this stage does not scale to the entire microstructure, as localization begins to unfold on a microscopic scale. A loss of the size objectivity is therefore encountered after the localization onset, meaning that a new objective value must be used in order to be able to recover this objectivity. To that end, the critical energy release rate G_c, computed from the SVE realization, is used. This quantity quantifies the fracture energy released per unit of crack surface, permitting to obtain an objective value to capture the failure characteristics of a given SVE. In order to compute this critical energy release rate, the dissipated energy $\mathcal{D}$ from the uniaxial tensile test is extracted at each iteration making it possible to evaluate its value through the failure diagram as shown in Fig. 4.3, in which we assume that $\mathcal{D}$ scales with the SVE volume before onset and with the SVE cross-section after onset.

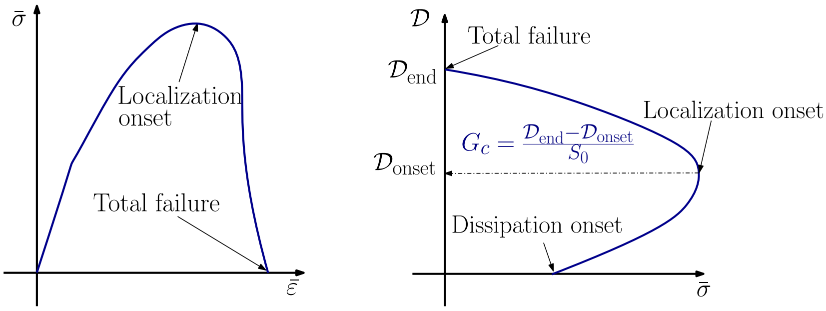

FIGURE 4.3: Stress ($\bar{\sigma}$) - strain ($\bar{\varepsilon}$) and energy dissipation ($\mathcal{D}$) - stress ($\bar{\sigma}$) plots used for the computation of the critical energy release rate G_c.

By obtaining the value of the total dissipated energy at the localization onset and at total failure, and by assuming a crack perpendicular to the loading direction with surface $S_0 = W \times 1\mu\text{m}^2$, being W the side length of the square SVE, it is possible to compute the critical energy release rate as:

$$G_c = \frac{\mathcal{D}_{\text{end}} - \mathcal{D}_{\text{onset}}}{S_0}. \tag{4.10}$$

4.1.4 Generation of full-field SVE simulations

In order to extract the microscale information needed to perform the multiscale analysis, the first step is the generation and simulation of stochastic volume elements of the composite material microstructure. The simulated unidirectional composite is composed of high strength carbon fibers UD300/CHS and a matrix of pure RTM6 epoxy resin. This Section will start defining the hardening and damage models used in the definition of the material, followed by the parameters used to model the inclusion and matrix phases of the composite in the full-field realizations. Then, the used geometries and boundary conditions will be presented, finishing with a brief summary of the methodology used to extract the critical energy release rate (G_c) from the full-field simulations.

4.1.4.1 Hardening and damage models for the SVE matrix

The matrix phase is modeled using the enhanced large strain constitutive pressure-dependent elasto-plastic model enhanced by a multi-mechanism nonlocal damage continuum presented in Chapter 2. This model allows good flexibility by permitting the introduction of different hardening and damage models, which allows to correctly capture the behavior of the studied material.

Hardening modeling The hardening evolution, as already introduced in Chapter 2, is modeled by three different hardening laws: the compressive isotropic hardening, which is governed by the compressive hardening modulus H_c, tensile isotropic hardening driven by the tensile hardening modulus H_t, and the kinematic hardening, whose evolution is dictated by the kinematic hardening modulus H_b.

The tensile, compressive and tensile hardening moduli evolution laws used for the different hardenings write:

$$H_j = \sum_{i=0}^{M_j} h_j^i p^i + h_j^0 \exp\left(-\Lambda_j p\right) \text{ where } j = t, c, b, \tag{4.11}$$

where M_j stands for the polynomial order, h_j^i, h_j^0 and Λ_j are the hardening material parameters and the subindex j indicates the tensile (t), compressive (c) or kinematic (b) cases.

Damage modeling As previously presented, the damage evolution will be governed by internal variables that will account for the history of the plasticity undergone by the material. As for the hardening, the internal variable used for the damage evolution will be equivalent plastic strain p, such that the softening internal variable p_s writes:

$$\dot{p}_s = \dot{p} \text{ and } p_s(t=0) = 0. \tag{4.12}$$

The saturation law D_s tends to the saturated value $D_{s\infty}$:

$$\begin{cases} \dot{D}_s(t) = H_s\left(p_s - p_{s0}\right)^{\zeta_s}\left(D_{s\infty} - D_s\right)\dot{p}_s, \\ p_s(t) = \max_{\tau\in[0,t]}\left(p_{s0}, \breve{p}_s\left(\tau\right)\right), \end{cases} \tag{4.13}$$

where p_{s0} is the damage threshold, $\breve{p}_s$ is the nonlocal counterpart of the softening equivalent plastic strain p_s following the Helmholtz-type Eq. (2.7) and H_s, ζ_s and $D_{s\infty}$ are material constants. Integrating Eq. (4.13), it is possible to obtain the expression of D_s as:

$$D_s = D_{s\infty}\left[1 - \exp\left(-\frac{H_s}{\zeta_s + 1}\left(p_s - p_{s0}\right)^{\zeta_s+1}\right)\right]. \tag{4.14}$$

Similarly, the failure damage is defined as:

$$\begin{cases} \dot{D}_f(t) = H_f\left(p_f\right)^{\zeta_f}\left(1 - D_f\right)^{-\zeta_d}\dot{r}_f, \\ r_f(t) = \max_{\tau\in[0,t]}\left(p_{f_0}, \breve{p}_f\left(\tau\right)\right), \end{cases} \tag{4.15}$$

where the failure strain r_f results from $\breve{p}_f$ the nonlocal failure plastic strain, p_{f_0} is the damage threshold and H_f, ζ_f and ζ_d are material constants. As for the case of the nonlocal plastic strain, the nonlocal failure plastic strain $\breve{p}_f$ is related to its local counterpart p_f, whose evolution is described below, with the Helmholtz-type Eq. (2.7). The constant H_f can be written in terms of other material quantities as:

$$H_f = \frac{\zeta_f + 1}{\zeta_d + 1}\frac{1 - \left(1 - D_{f_c}\right)^{\zeta_d+1}}{p_{f_c}^{\zeta_f+1} - p_{f_0}^{\zeta_f+1}}, \tag{4.16}$$

where $D_{f_c} = D_f(p_{f_c})$ stands for the critical failure damage value and p_{f_c} is the critical nonlocal failure plastic strain.

Integrating Eq. (4.15), one gets:

$$D_f = \begin{cases} 0 & \text{if } r_f \leq p_{f_0}\,; \\ 1 - \left[1 - H_f\frac{\zeta_d+1}{\zeta_f+1}\left(r_f^{\zeta_f+1} - p_{f_0}^{\zeta_f+1}\right)\right]^{\frac{1}{\zeta_d+1}} & \text{if } p_{f_0} \leq r_f \leq p_{f_c}\,; \\ D_{f_c} & \text{if } p_{f_c} \leq r_f\,. \end{cases} \tag{4.17}$$

The onset at which failure starts is controlled by a criterion based on the equivalent plastic strain as suggested by Morelle et al. (2017), which writes:

$$\Phi_f = p - a\exp(-bT) - c = 0, \tag{4.18}$$

where $T = \frac{\mathrm{tr}(\hat{\boldsymbol{\tau}})}{3\hat{\tau}^{eq}}$ refers to the stress triaxiality, and where a, b and c are material constants. Once the failure onset is reached, the evolution of the failure surface is defined by the Kuhn-Tucker condition:

$$\Phi_f - r \leq 0, \quad \dot{r} \geq 0, \quad \text{and} \quad \dot{r}\,(\Phi_f - r) = 0, \tag{4.19}$$

where r is a non-negative variable that allows to store the maximal failure criterion reached in the loading history. Using the Kuhn-Tucker condition (Eq. 4.19), it is possible to define the evolution of the failure plastic strain as:

$$\dot{p}_f = \begin{cases} 0 & \text{if } \dot{r} = 0, \\ \dot{p} & \text{if } \dot{r} > 0. \end{cases} \tag{4.20}$$

Concerning the boundary conditions used for the nonlocal variables, the equivalence to periodic boundary condition (Nguyen, Wu, and Noels, 2019) is used for both $\breve{p}_s$ and $\breve{p}_f$ at the SVE boundaries $\partial\omega$:

$$\begin{cases} [\![\boldsymbol{c}_{\mathrm{g}} \cdot \boldsymbol{\nabla}_0 \breve{p}_i]\!] \cdot \boldsymbol{N} = 0, \\ [\![\dot{\breve{p}}_i]\!] = 0, \end{cases} \quad \text{on} \quad \partial\omega, \quad \breve{p}_i = \breve{p}_s, \breve{p}_f, \tag{4.21}$$

where $[\![\bullet]\!]$ represents the jump operator between matching material points at opposite faces of the SVE, i.e. $[\![\bullet]\!] = \bullet\left(\boldsymbol{x}^+_{\mathrm{ref}}\right) - \bullet\left(\boldsymbol{x}^-_{\mathrm{ref}}\right)$.

At the internal boundary, $\partial_I\omega$ composed by the set of interfaces between the fibers and the matrix with outward normal $\boldsymbol{N}^I$, the following conditions are used for the nonlocal variable $\breve{p}_s$:

$$\begin{cases} [\![\boldsymbol{c}_{\mathrm{g}} \cdot \boldsymbol{\nabla}_0 \breve{p}_s]\!] \cdot \boldsymbol{N}^I = 0, \\ [\![\dot{\breve{p}}_s]\!] = 0, \end{cases} \quad \text{on} \quad \partial_I\omega, \tag{4.22}$$

where $[\![\bullet]\!]$ represents the jump operator at the interface between fibers and matrix $[\![\bullet]\!] = \bullet_{\mathrm{matrix}} - \bullet_{\mathrm{fiber}}$, since they allow the introduction of the length scale effect of the matrix response introduced by the fiber distribution (Nguyen, Wu, and Noels, 2019). However, for the nonlocal variable $\breve{p}_f$, at the internal boundary $\partial_I\omega$, the following condition is considered so that the damage can develop at the interface between the fibers and the matrix:

$$\boldsymbol{\nabla}_0 \breve{p}_f \cdot \boldsymbol{N}^I = 0, \text{ on } \quad \partial_I\omega. \tag{4.23}$$

4.1.4.2 Anisotropic inclusion model

A hyperelastic strain energy $\Psi_f = \Psi_f(\mathbf{C})$ ($\mathbf{C}$ stands for the right Cauchy-Green tensor) is used to describe the transversely isotropic hyperelastic model used for the modeling of the unidirectional fibers following the works by Bonet and Burton (1998), and Wu et al. (2013b). As transversely istropic properties are taken into account, the strain energy Ψ_f can be divided into isotropic (Ψ_f^{iso}) and transverse (Ψ_f^{trn}) components as:

$$\Psi_f = \Psi_f^{\mathrm{iso}} + \Psi_f^{\mathrm{trn}}. \tag{4.24}$$

The parameters characterizing such material are the transverse Young's modulus E^{T}, Poisson's ratio ν^{TT} and shear modulus μ^{TT}, the longitudinal-transverse Poisson's ratio ν^{LT} and shear modulus μ^{LT}, and the longitudinal Young's modulus E^{L}.

The isotropic and transverse parts of the strain energy write:

$$\begin{aligned}\Psi_f^{\text{iso}} &= \frac{1}{2}\mu^{\text{TT}}\left(I_1-3\right) - \mu^{\text{TT}}\log J + \frac{1}{2}\lambda\log^2 J,\\ \Psi_f^{trn} &= \left[\alpha_{\text{trn}} + 2\beta_{\text{trn}}\ln J + \gamma_{\text{trn}}\left(I_4-1\right)\right]\left(I_4-1\right) - \frac{1}{2}\alpha_{\text{trn}}\left(I_5-1\right),\end{aligned} \tag{4.25}$$

where $I_1 = \text{tr}\left(\mathbf{C}\right)$,$I_4 = \mathbf{A}\cdot\mathbf{C}\cdot\mathbf{A}$, $I_5 = \mathbf{A}\cdot\mathbf{C}^2\cdot\mathbf{A}$, being $\mathbf{A}$ the unit vector with the fibers direction in the original non-deformed configuration, $J = \sqrt{\det(\mathbf{C})}$. The quantities μ^{TT}, λ, $\alpha_{\text{trn}}, \beta_{\text{trn}}$, and γ_{trn} are material constants defined as:

$$\begin{aligned}\mu^{\text{TT}} &= \frac{E^{\text{T}}}{2\left(1+\nu^{\text{TT}}\right)},\\ \lambda &= \frac{E^{\text{T}}\left(\nu^{\text{TT}} + n\nu^{\text{TL}^2}\right)}{m^{\text{TL}}\left(1+\nu^{\text{TT}}\right)},\\ \alpha_{\text{trn}} &= \mu^{\text{TT}} - \mu^{\text{TL}},\\ \beta_{\text{trn}} &= \frac{E^{\text{T}}\left[n^{\text{TL}}\nu^{\text{TL}}\left(1+\nu^{\text{TT}}-\nu^{\text{TL}}\right)-\nu^{\text{TT}}\right]}{4m^{\text{TL}}\left(1+\nu^{\text{TT}}\right)},\\ \gamma_{\text{trn}} &= \frac{E^{\text{L}}\left(1-\nu^{\text{TT}}\right)}{8m^{\text{TL}}} - \frac{\lambda+2\mu^{\text{TT}}}{8} + \frac{\alpha_{\text{trn}}}{2} - \beta_{\text{trn}},\end{aligned} \tag{4.26}$$

where $m^{\text{TL}} = 1 - \nu^{\text{TT}} - 2n^{\text{TL}}\nu^{\text{TL}^2}$, and $n^{\text{TL}} = \frac{E^{\text{L}}}{E^{\text{T}}}$.

Finally, this strain energy Ψ_f allows the first Piola-Kirchhoff stress tensor to be written by computing the strain energy derivative with respect to the deformation gradient tensor $\mathbf{F}$ as:

$$\begin{aligned}\mathbf{P} = \frac{\partial\Psi_f}{\partial\mathbf{F}} = 2\mathbf{F}\cdot\frac{\partial\Psi_f}{\partial\mathbf{C}} =& 2\mathbf{F}\cdot\left\{\lambda\ln J\mathbf{C}^{-1} + \mu^{\text{TT}}\left(\boldsymbol{I}-\mathbf{C}^{-1}\right) + 2\beta_{\text{trn}}\left(I_4-1\right)\mathbf{C}^{-1}\right.\\ &+ 2\left[\alpha_{\text{trn}} + 2\beta_{\text{trn}}\ln J + 2\gamma_{\text{trn}}\left(I_4-1\right)\right]\mathbf{A}\otimes\mathbf{A}\\ &\left.-\alpha_{\text{trn}}(\mathbf{C}\cdot\mathbf{A}\otimes\mathbf{A} + \mathbf{A}\otimes\mathbf{C}\cdot\mathbf{A})\right\}.\end{aligned} \tag{4.27}$$

4.1.4.3 Phase parameters

The carbon fibers are modeled as a hyperelastic and transversely isotropic material, while the matrix phase is modeled using the large strain constitutive pressure-dependent elasto-plastic model enhanced by a multi-mechanism nonlocal damage continuum presented in Chapter 2 with the hardening and damage laws presented in Sectionsec:headings. This model allows to correctly capture the matrix failure (Nguyen et al., 2016; Nguyen, Wu, and Noels, 2019). Table 4.1 shows the parameters used for the UD300/CHS inclusions and Table 4.2 the parameters used to model the RTM6 matrix phase[2] following literature data.

The two phases properties are considered to be uniform across each UD-composite phase, being the geometrical distribution and fibers properties the only source of randomness on the SVE realizations.

---

[2] In the present work we neglect the viscous part of the model and thus we do not report the corresponding parameters

TABLE 4.1: UD300/CHS carbon fiber properties (Wu et al., 2013b) of the model reported in Section 4.1.4.2

Property of carbon fibers (Unit)	Value
Density ρ (kg/m^3)	1750
Longitudinal Young's modulus E^{L} (GPa)	230
Transverse Young's modulus E^{T} (GPa)	40
Transverse Poisson's ratio ν^{TT} (-)	0.2
Longitudinal-transverse Poisson's ratio $\nu^{\mathrm{LT}} = \nu^{\mathrm{TL}}\frac{E^{\mathrm{L}}}{E^{\mathrm{T}}}$ (-)	0.256
Transverse shear modulus μ^{TT} (GPa)	16.7
Longitudinal-transverse shear modulus μ^{LT} (GPa)	24

TABLE 4.2: RTM6 epoxy properties (Nguyen, Wu, and Noels, 2019) of the model reported in Chapter 2.

Property of RTM6 epoxy (Unit)	Value
Young's modulus E (MPa)	2450
Yield Exponent α (-)	3.5
Poisson's ratio ν (-)	0.39
Plastic Poisson's ratio ν_p (-)	0.45
Compressive yield σ_c^0 (MPa)	48
Tensile yield σ_t^0 (MPa)	40.8
Compressive hardening H_c (MPa)	$6475\exp(-37p)$
Tensile hardening H_t (MPa)	$5503.8\exp(-37p)$
Kinematic hardening H_b (MPa)	$1412.7p - 5484.8p^2 + 18283p^3$
Saturation damage law D_s (-)	$0.62[1-\exp(-30p_s)]$
Saturated damage $D_{s\infty}$ (-)	0.62
Saturation damage parameter H_s (-)	30
Saturation damage parameter ζ_s (-)	0
Saturation damage onset p_{s0} (-)	0
. Failure damage parameter ζ_f (-)	1
Failure damage parameter ζ_d (-)	0.3
Failure critical damage D_{f_c} (-)	0.999
Failure critical strain p_{f_c} (-)	0.117
Failure strain onset p_{f_0} (-)	0.
Failure surface parameter a (-)	0.03428
Failure surface parameter b (-)	7.815
Failure surface parameter c (-)	0.02169
Nonlocal length l_c (μm)	3

4.1.4.4 Finite element simulations

In order to carry the full-field simulations, transverse cross-sections of the UD composite are generated at the microscale from dependent variables represented within a copula framework built from SEM images, allowing the generation of microstructures by an inclusions additive process (Wu et al., 2018). This SVE generation process allows a realistic statistical distribution of the dependent microscale parameters to be obtained as shown in (Wu et al., 2018), ensuring the applicability of this Work to real-life applications. The statistical information of the microstructure parameters is provided in Appendix C.1.

One of the major constraints of this kind of approach, as already mentioned, is the size of the SVE used to build the dataset of random homogenized parameters. The use of a larger SVE would allow for a lower number of SVE realizations needed in order to obtain all the required

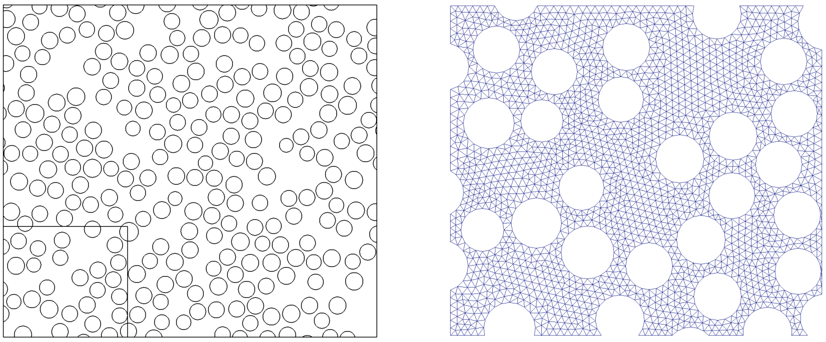

FIGURE 4.4: Composite window of 135×135 μm^2 with smaller 45×45 μm^2 SVE and full-field SVE mesh detail.

statistical information. To check the effect of the SVE size in the final obtained responses, two different SVE sizes were used. In order to obtain these SVEs, 100 windows of 135×135 μm^2 with an average of 40% fiber volume fraction were generated, from which small windows of 25×25 μm^2 or $45 \times 45 \mu$m^2 are extracted as shown in Fig. 4.4. Then, the extracted SVE is meshed with quadratic elements in order to perform the finite element simulations.

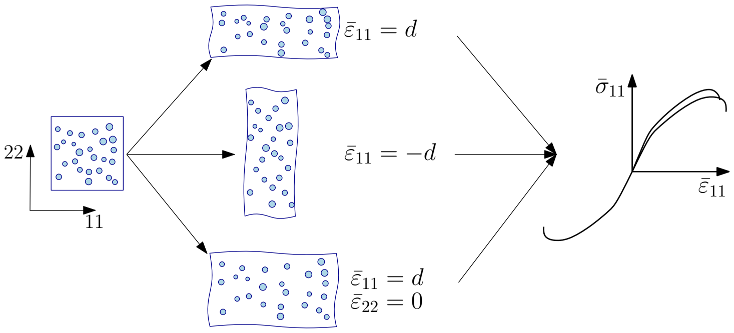

FIGURE 4.5: Schematic of the three loading conditions tested on each SVE realization. From top to bottom: Uniaxial tensile test, uniaxial compressive test and uniaxial strain test. Letter d stands for the imposed value.

In order to perform the inverse identification introduced in Section 4.2, three different tests are run for each SVE realization: Uniaxial tensile and compressive loading tests, and a uniaxial strain test (see Fig. 4.5). As presented in Section 4.1.2, periodic boundary conditions are used for these three tests and plane strain conditions are assumed.

Uniaxial tension and compression loadings provide a clear view of the material pressure dependence, as they offer two opposing points in the material internal state. A third test is added to the set of loading conditions. This test allows to complete the information required for the inverse parameter identification procedure at the onset of plasticity. Biaxial loading is chosen for this third test, providing a clear understanding of the effect of triaxiality on material behavior and representing an additional valuable result for the inverse identification procedure.

As Figs. 4.6 and 4.7 show, the used matrix model allows obtaining complex matrix behaviors, including total failure of the sample. The large strain matrix model used in this Work allows to accurately capture the behavior of the RTM6 matrix up to its complete failure thanks to the use of the critical energy release rate in the calibration of its failure parameters.

The SVEs are then deformed under tensile loading until reaching their total failure, being possible to extract the uniaxial tensile critical energy release rate G_c. As it is possible to observe in Fig. 4.8, each SVE will present different characteristics due to the inherent uncertainties contained in these SVEs. This extracted data will then allow us to scale the effect of these uncertainties to larger scales.

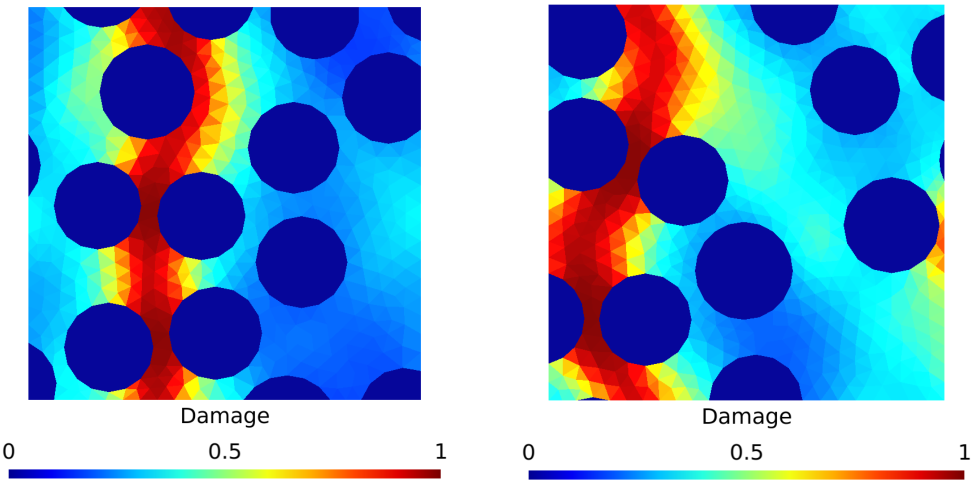

FIGURE 4.6: Matrix failure damage of two $25 \times 25\mu\text{m}^2$ SVEs under uniaxial tension loading at fracture. SVE 1 on the left and SVE 2 on the right.

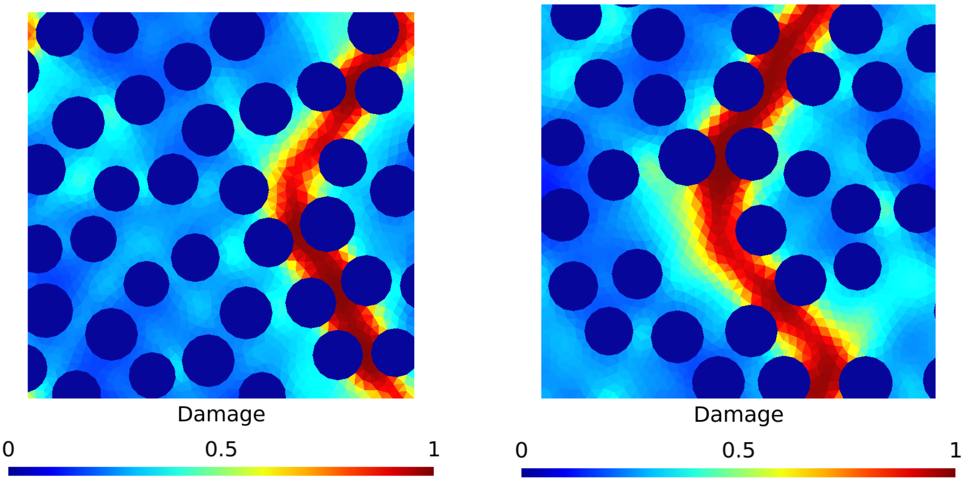

FIGURE 4.7: Matrix failure damage of two $45 \times 45\mu\text{m}^2$ SVEs under uniaxial tension loading at fracture. SVE 3 on the left and SVE 4 on the right.

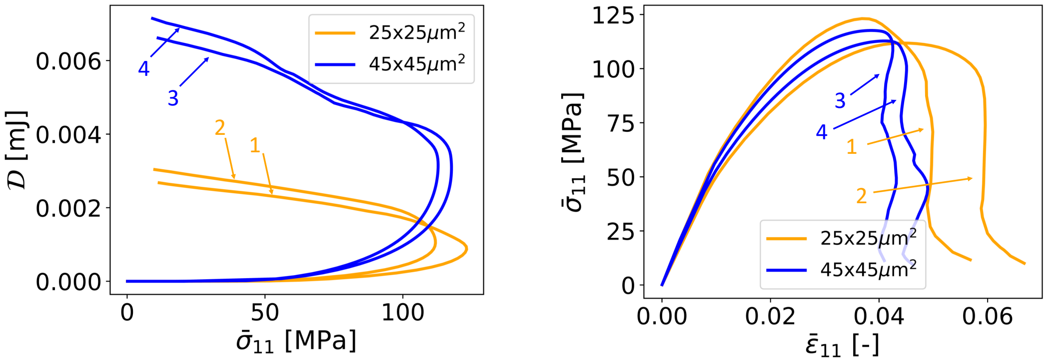

FIGURE 4.8: Dissipated energy in matrix vs. averaged stress component 11 for SVEs 1, 2, 3 and 4 on the left and averaged stress-strain of SVEs 1, 2, 3 and 4 for component 11 on the right (SVE numbering refers to Figs. 4.6 and 4.7).

As an example of the effect of these variabilities found in the material microstructure, the obtained distribution of the SVE G_c can be seen in Fig. 4.9, which shows the distribution for the two sizes of SVE used in this study. Similar distributions of the energy release rate are obtained for both cases, being the average value slightly higher for the $45 \times 45 \mu\text{m}^2$ SVE samples.

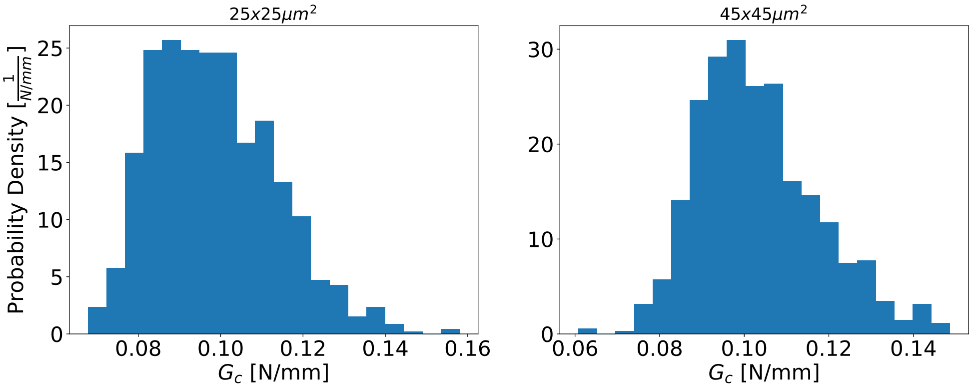

FIGURE 4.9: Probability density histograms of the energy release rate found in the 25×25 μm^2 and 45×45 μm^2 SVEs

4.2 Mean-Field Homogenization surrogate model and inverse identification process

In order to build a stochastic MF-ROM capable of capturing all the microstructure variabilities shown by each SVE, an identification process must be developed. The goal of this identification process is to find, for each SVE realization, the parameters of the MFH model that allow obtaining a homogenized material response that is as its full-field counterpart. As seen in Section 4.1.4.4, failure of the SVE occurs at few percents of deformation at the homogenized level. Therefore, the MF-ROM can be developed in a small strain setting. This Section summarizes the identification process by presenting the identification method for elastic behaviors first and then for pressure dependent damage-enhanced elasto-plastic behaviors; and finally for the post-strain softening phase up to complete failure.

4.2.1 Inverse identification

The developed inverse identification methodology consists in an extension to account for pressure-dependency and failure of the elastic (Wu, Adam, and Noels, 2018) and elasto-plastic (Wu et al., 2019) inverse identification approaches. To this end, in this Thesis, the MFH model developed in Chapter 3 is used for the MFH surrogate. For each SVE we will associate corresponding parameters yielding the same homogenized behavior. As this identification is performed for each SVE realization, as many values of each random descriptors as SVE realizations will be obtained. The notation $(\tilde{\bullet})$ will be used to make reference to the identified parameters. The parameters that will define the inclusion phase will be the fiber volume fraction $\tilde{v}_{\text{I}}$, the major and minor axes ratio of the single inclusion phase ellipsoid $\tilde{\text{I}}$, and its orientation $\tilde{\theta}$. The matrix phase is characterized by its elastic, pressure-dependent plastic and damage parameters. The Young's modulus $\tilde{E}_0$ and the Poisson's ratio $\tilde{\nu}_0$ describe the elastic matrix behavior. The pressure-dependent plasticity stage is defined by the initial compressive yield stress $\tilde{\sigma}_c^0$, the parameters $\tilde{\boldsymbol{H}} = \left[\tilde{h}_0, \, \tilde{h}_1, \, \tilde{m}_0\right]$ of the further described hardening law, the tension and compression yield stress ratio $\tilde{m}$, the plastic Poisson's ratio $\tilde{\nu}_p$ and the yield surface exponent $\tilde{\alpha}$. The damage of the matrix phase will depend on the softening damage parameters $\tilde{p}_{\text{onset}}$ and $\widetilde{D}_{\text{onset}}$ and its failure damage parameters $\tilde{\alpha}_{\text{Dam}}$

and $\tilde{\beta}_{\mathrm{Dam}}$. A total of 16^3 random effective parameters, which will form the vector $\boldsymbol{\beta}^D$ will be identified for each SVE realization:

$$\boldsymbol{\beta}^D = \left[\tilde{v}_{\mathrm{I}}, \tilde{\mathrm{I}}, \tilde{\theta}, \tilde{E}_0, \tilde{\nu}_0, \tilde{\sigma}_c^0, \tilde{h}_0, \tilde{h}_1, \tilde{m}_0, \tilde{m}, \tilde{\nu}_p, \tilde{\alpha}, \tilde{p}_{\mathrm{onset}}, \tilde{D}_{\mathrm{onset}}, \tilde{\alpha}_{\mathrm{Dam}}, \tilde{\beta}_{\mathrm{Dam}}\right]. \tag{4.28}$$

The inverse identification of a given SVE draws on the results extracted from the full-field simulations. As shown in Fig. 4.10, the information used for the identification process of each SVE realization is extracted from the three different loading conditions tested. The obtained effective parameter vectors from the full set of SVE realizations will form a realization of the random matrix of effective parameters vectors $[\beta^D]$ that will then serve as input for the generator of new data.

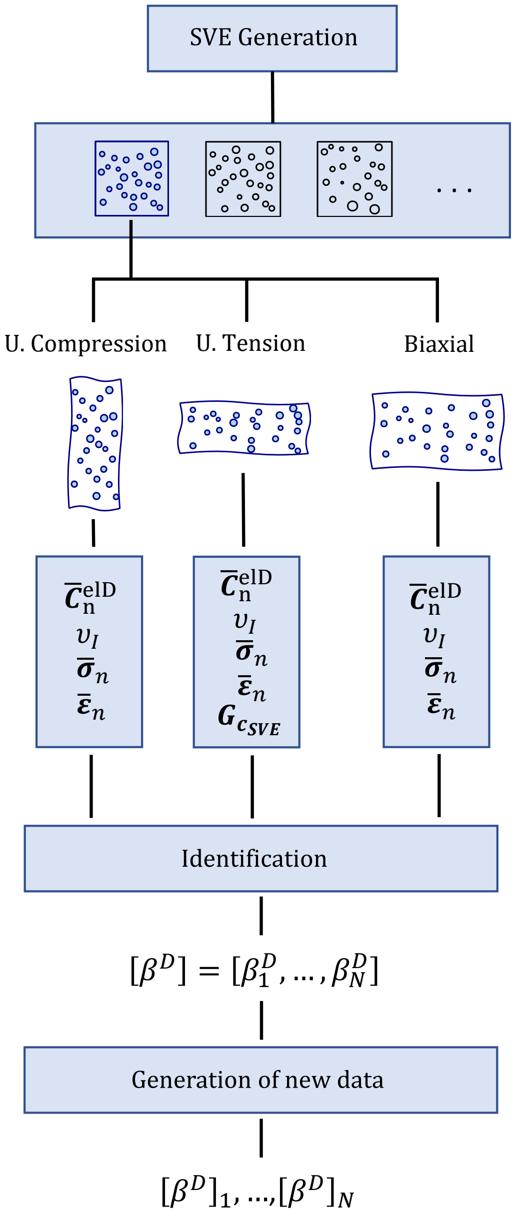

FIGURE 4.10: Flowchart of the complete methodology for the generation of the MF-ROM.

---

[3] Actually $\tilde{\beta}_{\mathrm{Dam}}$ has a fixed value

This methodology was implemented in the form of different Python file blocks that control each step of the process (See the provided data by Calleja Vázquez et al. (2023)). These Python files carry out the identification and data generation process, and make call to the core in-house C++ codes for performing the full-field and MFH simulations involved (As presented in Chapter 2 and Chapter 3). This modularity allows future users of the code to easily adapt the complete methodology to their own FEM code or even to new constitutive or evolution laws. Each code requires a clear input and will provide the output required for the next step in the MF-ROM methodology as indicated in the provided data (Calleja Vázquez et al., 2023). A fully novel identification procedure was developed and implemented inside the Python loop for which the SciPy library was used for the optimization steps.

This Section will start presenting the identification process for the elastic properties, followed with the nonlinear damaged-enhanced pressure dependent plasticity, and will end with the calibration of the model in order to recover the size objectivity encountered after the strain-softening stage. At the beginning of some key points of the identification process, a line specifying the already identified effective parameters and the parameters that will be identified at that specific point of the process will be introduced. This will allow the reader to more easily identify the MF-ROM parameters needed for its definition and follow the identification process.

4.2.1.1 Elastic Composites

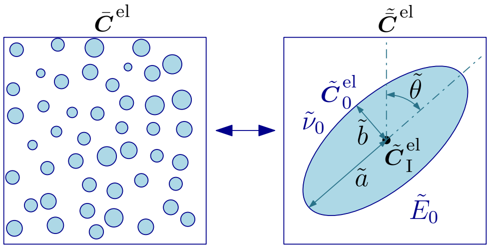

FIGURE 4.11: Schematic representation of the elastic full-field SVE and its MFH virtual counterpart.

At this stage, the known MF-ROM variable is: the fiber volume fraction $[\tilde{v}_{\text{I}}]$. This parameter is directly deduced from the SVE. In this step, the following variables will be identified: $\left[\tilde{\text{I}}, \tilde{\theta}, \tilde{E}_0, \tilde{\nu}_0\right]$.

The equivalent inclusion model (Wu, Adam, and Noels, 2018) substitutes the complex microstructure of the composite material by an SVE composed of matrix and a single elliptic inclusion (see Fig. 4.11). To define the inclusion, the volume fraction v_{I} and its effective anisotropic elasticity tensor $\boldsymbol{C}_{\text{I}}^{\text{el}}$, which is considered constant for all SVEs, are directly obtained from the SVE realizations. Then, the ratio between the major and minor axes of the inclusion's ellipsoid $\tilde{\text{I}}$, and its orientation, denoted by $\tilde{\theta}$, are obtained through the inverse identification process (hence the $\tilde{\bullet}$ notation). In this inverse identification process, the effective elasticity properties of the isotropic matrix $\tilde{\boldsymbol{C}}_0^{\text{el}}\left(\tilde{E}_0, \tilde{v}_0\right)$, as well as the effective Young's modulus and Poisson's ratio ($\tilde{E}_0, \tilde{v}_0$ respectively) are identified to characterize the matrix phase.

In order to identify the elastic random descriptors, the elasticity tensor of the equivalent composite ($\tilde{\bar{\boldsymbol{C}}}^{\text{el}}$), Eq. (3.7), which depends on the variables $\tilde{\text{I}}, \tilde{\theta}, \tilde{E}_0, \tilde{v}_0$, has to be as similar as possible to the homogenized elasticity tensor extracted from the SVE realizations ($\bar{\boldsymbol{C}}^{\text{el}}$). To that end, the following optimization process is performed:

$$\min_{\tilde{\text{I}}, \tilde{\theta}, \tilde{E}_0, \tilde{\nu}_0} \left\| \tilde{\bar{\boldsymbol{C}}}^{\text{el}}\left(\tilde{\text{I}}, \tilde{\theta}, \tilde{\boldsymbol{C}}_0^{\text{el}}\left(\tilde{E}_0, \tilde{\nu}_0\right); \boldsymbol{C}_{\text{I}}^{\text{el}}, v_{\text{I}}\right) - \bar{\boldsymbol{C}}^{\text{el}} \right\|, \tag{4.29}$$

where $\| \bullet \|$ stands for the Frobenius norm. By performing this minimization problem for each of the SVE realizations, the elastic random descriptors are identified.

4.2.1.2 Nonlinear damage-enhanced elasto-plastic composites up to strain softening

Once the geometrical information of the inclusion and the effective elastic descriptors of the matrix are identified, the nonlinear behavior descriptors of the matrix, including the plasticity onset, are still to be identified. To perform the identification of the pressure-dependent matrix model parameters, three different loading conditions are used in for the characterization of all its parameters. These different loading conditions allow obtaining information about the effect of different hydrostatic pressures on the composite material response. In this Work, uniaxial tension and compression and biaxial tension ($\bar{\varepsilon}_{22} = 0$) loading conditions are used for the identification of the material parameters (as previously shown in Fig. 4.5). Since the incremental-secant formulation is used, the loading curves will be divided into loading increments and virtual elastic unloading steps.

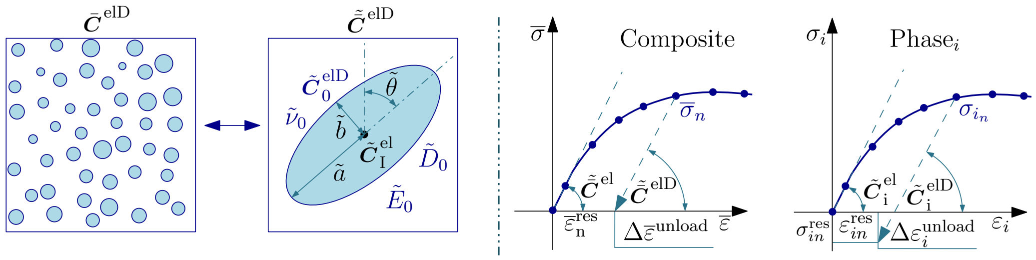

FIGURE 4.12: Schematic representation of the damaged elastic full-field SVE and its MFH virtual counterpart (left) and schematic unloading phase in a stress-strain plot (right).

Effective damage evolution The first step consists in identifying the effective damage D_0 present at each loading increment. To that end, as the damaged elastic tensor is extracted from the full-field simulation, the virtual elastic unloading step at each iteration can be used to extract the value of the damage evolution (Wu et al., 2019) (see Fig. 4.12). In this Work, damage is taken into account on the matrix phase of the composite through the scalar damage variable D_0. The effective damage $\tilde{D}_0$ of the matrix phase is obtained through the following minimization problem:

$$\min_{\tilde{D}_{0_n}} \left\| \tilde{\bar{\boldsymbol{C}}}_n^{\rm elD} \left(\tilde{\boldsymbol{C}}_{0_n}^{\rm elD} \left(\tilde{D}_{0_n}; \tilde{\rm I}, \tilde{\theta}, \tilde{E}_0, \tilde{\nu}_0 \right), \boldsymbol{C}_{\rm I}^{\rm el}, v_{\rm I} \right) - \bar{\boldsymbol{C}}_n^{\rm elD} \right\|, \tag{4.30}$$

where $\tilde{\boldsymbol{C}}_{0_n}^{\rm elD} \left(\tilde{D}_{0_n} \right)$ is the matrix damaged elastic tensor defined as:

$$\tilde{\boldsymbol{C}}_{0_n}^{\rm elD} = \left(1 - \tilde{D}_{0_n} \right) \tilde{\boldsymbol{C}}_0^{\rm el} \left(\tilde{E}_0, \tilde{\nu}_0 \right). \tag{4.31}$$

This procedure is performed for the three different loading conditions, obtaining the matrix damage evolution for each step increment of the three loading conditions.

Composite plastic onset identification The next step consists in identifying the composite plasticity onset stress-strain state ($\tilde{\bar{\boldsymbol{\sigma}}}_y$, $\tilde{\bar{\boldsymbol{\varepsilon}}}_y$) of the three loading conditions used for the parameter identification in order to be able to later characterize the matrix stress-strain state at this point. Using the already identified elastic tensor of the composite $\bar{\boldsymbol{C}}^{\rm el}$, it is possible to compute a theoretical elastic stress ($\bar{\boldsymbol{\sigma}}_n^{\rm th}$) of the composite as:

$$\bar{\boldsymbol{\sigma}}_n^{\rm th} = \bar{\boldsymbol{C}}^{\rm el} : \bar{\boldsymbol{\varepsilon}}_n. \tag{4.32}$$

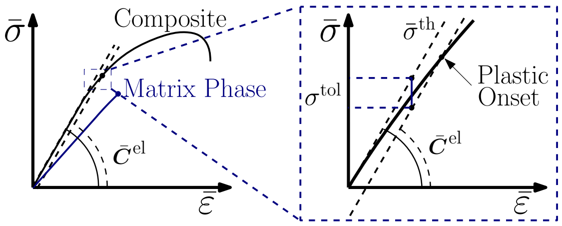

FIGURE 4.13: Composite yield identification scheme.

Due to the complex microstructure that is taken into account, localization points in which plasticity starts developing due to the fibers disposition do not allow to implement a straightforward analytical methodology to find a plasticity onset. As the homogenized composite macro stresses and strains $(\bar{\boldsymbol{\sigma}}, \bar{\boldsymbol{\varepsilon}})$ are known at all time steps from the full-field realizations, this theoretical elastic stress allows us to obtain a reference value to compare with these responses obtained from the full-field realizations and be able to assess the amount of plasticity that is developing in the SVE. In order to check when there is a meaningful amount of plasticity developing on the SVE, the plasticity onset is identified by defining a tolerance stress (σ^{tol}), *e.g.* 1 MPa, on the loading component of the composite as shown in Fig. 4.13. The plasticity onset iteration is then found as the first step satisfying:

$$|\bar{\sigma}_{11_n}| < |\bar{\sigma}^{\text{th}}_{11_n} - \sigma^{\text{tol}}|. \tag{4.33}$$

It is then possible to define the yield strain $\tilde{\bar{\boldsymbol{\varepsilon}}}_y$ and yield stress $\tilde{\bar{\boldsymbol{\sigma}}}_y$ as the stress-strain state in which the extracted SVE stress-strain curve crosses the tolerance line by using a linear interpolation between the values of $\bar{\boldsymbol{\sigma}}$ and $\bar{\boldsymbol{\varepsilon}}$ at the plasticity onset iteration and the previous strain state, such that: $(\bar{\boldsymbol{\varepsilon}}_{n-1} < \tilde{\bar{\boldsymbol{\varepsilon}}}_y < \bar{\boldsymbol{\varepsilon}}_n)$ and $(\bar{\boldsymbol{\sigma}}_{n-1} < \tilde{\bar{\boldsymbol{\sigma}}}_y < \bar{\boldsymbol{\sigma}}_n)$.

Phases plasticity onset and identification of pressure dependency parameters At this stage, the known MF-ROM variables are: $\left[\tilde{v}_{\text{I}}, \tilde{\text{I}}, \tilde{\theta}, \tilde{E}_0, \tilde{\nu}_0\right]$. In this step, the following variables will be identified: $\left[\tilde{\alpha}, \tilde{m}, \tilde{\sigma}^0_c\right]$. In addition, from the full-field simulations the macro-stresses and -strains $(\bar{\boldsymbol{\sigma}}, \bar{\boldsymbol{\varepsilon}})$ are known and from previous identification steps, the effective damage evolution $\tilde{D}_{0_n}$, and the plastic onset stress-strain state of the composite $(\tilde{\bar{\boldsymbol{\sigma}}}_y, \tilde{\bar{\boldsymbol{\varepsilon}}}_y)$ are known for the three loading cases.

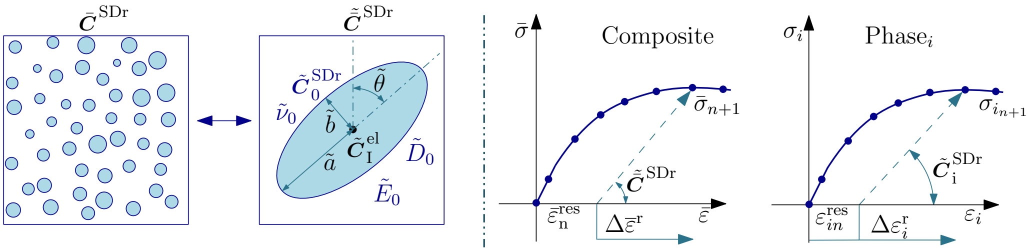

FIGURE 4.14: Schematic representation of the damaged plastic full-field SVE and its MFH virtual counterpart (left) and schematic loading phase in a stress-strain plot (right).

After identifying the plastic onset stress-strain state of the composite material under the three studied loading conditions, the matrix strain-stress state at the plastic onset (PO), i.e. $(\boldsymbol{\varepsilon}_{0_{\text{PO}}}, \boldsymbol{\sigma}_{0_{\text{PO}}})$, must be obtained, which will allow to have the needed information to compute the pressure-dependent parameters of the MF-ROM. To that end, the matrix strain and stress states at each iteration must be computed up to the identified composite plastic onset. It is important to point out that in order to obtain an accurate representation of the matrix stress-strain state at the plasticity onset of the three loading conditions, the damaged-enhanced nonlinear incremental-secant scheme is used to be able to account for the starting plasticity and damage effects in the

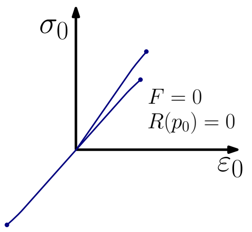

FIGURE 4.15: Matrix stress-strain curves for uniaxial tension and compression, and biaxial loading up to the plastic onset.

matrix phase. While it was shown that when using first statistical moments, cancelling the matrix residual stress could help improving the scheme accuracy for composites with stiff inclusions, we note that as the MFH model is used as a reduced order model whose parameters are identified to recover the full field results, the residual version of the incremental-secant scheme developed in the previous Chapter can be used in the developed MF-ROM. Let us consider a time step $[t_n, t_{n+1}]$:

- First, a virtual elastic unloading is performed. This step unloads the composite up to a stress-free state such that:

  $$0 = \bar{\boldsymbol{\sigma}}_n^{\mathrm{res}} = \bar{\boldsymbol{\sigma}}_n - \bar{\boldsymbol{C}}_n^{\mathrm{elD}} : \Delta\bar{\boldsymbol{\varepsilon}}_n^{\mathrm{unload}}. \tag{4.34}$$

  From this expression it is possible to obtain the residual strain tensor, allowing to write the strain increment $\Delta\bar{\boldsymbol{\varepsilon}}^{\mathrm{r}}$ (see Fig. 3.2) as:

  $$\Delta\bar{\boldsymbol{\varepsilon}}_{n+1}^{\mathrm{r}} = (\bar{\boldsymbol{\varepsilon}}_{n+1} - \bar{\boldsymbol{\varepsilon}}_n) + \bar{\boldsymbol{C}}_n^{\mathrm{elD}-1} : \bar{\boldsymbol{\sigma}}_n. \tag{4.35}$$

  As enough points are obtained from the full-field simulations, it is possible to assume that $\left(D_{0_{n+1}} - D_{0_n}\right) \hat{\boldsymbol{\sigma}}_{0_{n+1}}^{\mathrm{res}} \approx 0$, writing Eq. (3.23) as:

  $$\bar{\boldsymbol{\sigma}}_{n+1} = \bar{\boldsymbol{C}}_{n+1}^{\mathrm{SDr}} : \Delta\bar{\boldsymbol{\varepsilon}}_{n+1}^{\mathrm{r}}. \tag{4.36}$$

- Then, using Eq. (4.36), the material is reloaded up to the next composite state, see Fig. 4.14. Since this stress-strain state is known from the full-field simulation, it is possible to identify the matrix secant tensor $\boldsymbol{C}_0^{\mathrm{SDr}}$ by performing the following minimization problem using the definition of the composite secant tensor, Eq. (3.22), and of the phases, Eqs. (3.67, 3.74):

  $$\min_{\tilde{\mu}_s^{\mathrm{Dr}};\tilde{\kappa}_s^{\mathrm{Dr}}} \left\{ \left\| \tilde{\bar{\boldsymbol{C}}}_{n+1}^{\mathrm{SDr}} \left(\tilde{\boldsymbol{C}}_0^{\mathrm{SDr}} \left(\tilde{\mu}_s^{\mathrm{Dr}}(\tilde{D}_0), \tilde{\kappa}_s^{\mathrm{Dr}}(\tilde{D}_0); \tilde{E}_0, \tilde{\nu}_0 \right); \boldsymbol{C}_{\mathrm{I}}^{\mathrm{el}}, \tilde{\mathrm{I}}, \tilde{\theta}, v_{\mathrm{I}} \right) : \Delta\bar{\boldsymbol{\varepsilon}}_{n+1}^{\mathrm{r}} - \bar{\boldsymbol{\sigma}}_{n+1} \right\| \right\}. \tag{4.37}$$

  By computing the damaged matrix secant tensor $\tilde{\bar{\boldsymbol{C}}}_0^{\mathrm{SDr}}$ at each step, it is possible to obtain the stress-strain state of each of the phases at each step by using Eq. (3.26).

  Performing consecutive virtual unloading and loading steps until reaching the computed plastic onset, making use of the mean-field homogenization relations shown in Eqs. (3.15 and 3.26), the plastic onset state of the matrix phase ($\boldsymbol{\varepsilon}_{0_{\mathrm{PO}}}$, $\boldsymbol{\sigma}_{0_{\mathrm{PO}}}$) is determined for each of the three loading conditions as shown in Fig. 4.15.

  Once the stress state of the matrix is known at the plastic onset, the surrogate model yield surface function F is assumed to have reached a null value. By considering the hardening $R(p_0)$ is small enough to be considered null at this stage, the number of unknowns of the yield surface decreases to three. By minimizing the yield surface equation at this stage for the three tests, it is then possible to identify these three unknown parameters: $\tilde{\alpha}$, $\tilde{m}$ and the matrix compressive initial yield stress $\tilde{\sigma}_c^0$, as:

$$\min_{\tilde{\alpha},\tilde{m},\tilde{\sigma}_c^0} \left\{ \sum_{\text{Tests}} \left|F_{\text{PO}}(\tilde{\alpha},\tilde{m},\tilde{\sigma}_c^0)\right| = \sum \left| \left(\frac{((\hat{\boldsymbol{\sigma}}_{0_{\text{PO}}})^{\text{eq}})^{\tilde{\alpha}}}{(\tilde{\sigma}_c^0)^{\tilde{\alpha}}} - 3\frac{\tilde{m}^{\tilde{\alpha}}-1}{(\tilde{m}+1)\tilde{\sigma}_c^0}\hat{\phi}_{0_{\text{PO}}} - \frac{\tilde{m}^{\tilde{\alpha}}+\tilde{m}}{\tilde{m}+1} \right) \right| \right\}. \tag{4.38}$$

The minimization shown in Eq. (4.38) presents multiple minima, meaning the optimization algorithm can result in spurious values for the random parameters. Therefore, the initial guess values used for $\tilde{\alpha}, \tilde{m}$ and $\tilde{\sigma}_c^0$ as well as the introduction of fixed boundaries for each of the random parameters are of crucial importance for the correct identification of the parameters.

Now that $\tilde{\alpha}, \tilde{m}$ and $\tilde{\sigma}_c^0$ are identified, all the parameters defining the pressure-dependency of the material are known except the hardening laws. However, assuming the tensile and compressive hardenings are related through parameter $\tilde{m}$ as $\tilde{H}_c = \tilde{m}\tilde{H}_t$, it is no longer needed to use different loading conditions in order to identify the remaining parameters. As explained in the work by Nguyen et al. (2012), multiple localization bands can appear in the post-peak localization stage, which is considered to be a nonphysical result (Coenen, Kouznetsova, and Geers, 2012). This is not the case under tensile loading conditions, for which this condition is valid since in those cases the failure band is perpendicular to the loading direction (Nguyen, Wu, and Noels, 2019), allowing to correctly capture the dissipated energy of the sample during failure. For this reason, the uniaxial tension condition will later be the preferred loading condition for the calibration of the post localization onset stage. This uniaxial tension loading condition will therefore be used for the following identification steps.

Starting plastic flow: Initial plastic Poisson's ratio At this stage, the known MF-ROM variables are: $\left[\tilde{v}_{\text{I}}, \tilde{\text{I}}, \tilde{\theta}, \tilde{E}_0, \tilde{\nu}_0, \tilde{\alpha}, \tilde{m}, \tilde{\sigma}_c^0\right]$. In this step, the following variable will be identified: $[\tilde{\nu}_p]$. Apart from these variables, the macro-stress and strain ($\bar{\boldsymbol{\sigma}}$, $\bar{\boldsymbol{\varepsilon}}$) and the effective damage evolution $\tilde{D}_0$ are known for all steps. In addition, the phases stress-strain state ($\boldsymbol{\sigma}_0$, $\boldsymbol{\varepsilon}_0$, $\boldsymbol{\sigma}_{\text{I}}$, $\boldsymbol{\varepsilon}_{\text{I}}$) have been computed up to the plastic onset.

Once plasticity is found to be reached, the initial plastic Poisson's ratio of the given SVE can be identified. To that end, the relation between the material parameters $\tilde{\beta}$ and $\tilde{\nu}_p$, Eq. (3.30), is used. In order to reduce the source of errors that could be introduced numerically at a specific time step, the following procedure is performed for the first 5 loading increments after the plastic flow onset in order to find an averaged quantity.

Rewriting the incremental-secant scheme, Eq. (3.23), for the studied case with all identified parameters, it is possible to identify the effective virtual shear and bulk moduli ($\tilde{\mu}_0^{\text{SDr}}$, $\tilde{\kappa}_0^{\text{SDr}}$) of the matrix (defined in Eq. (3.68)) through the evaluation of the $\tilde{\boldsymbol{C}}_0^{\text{SDr}}$ tensor using Eqs. (3.22, 3.23):

$$\min_{\tilde{\mu}_s^{\text{Dr}};\tilde{\kappa}_s^{\text{Dr}}} \left\{ \left\| \tilde{\bar{\boldsymbol{C}}}_{n+1}^{\text{SDr}} \left(\tilde{\boldsymbol{C}}_0^{\text{SDr}} \left(\tilde{\mu}_s^{\text{Dr}}(\tilde{D}_0,\Gamma), \tilde{\kappa}_s^{\text{Dr}}(\tilde{D}_0,\Gamma,\beta); \tilde{E}_0, \tilde{\nu}_0 \right); \boldsymbol{C}_{\text{I}}^{\text{el}}, \tilde{\text{I}}, \tilde{\theta}, v_{\text{I}} \right) : \Delta\bar{\boldsymbol{\varepsilon}}_{n+1}^{\text{r}} - \bar{\boldsymbol{\sigma}}_{n+1} \right\| \right\}. \tag{4.39}$$

While similar to Eq. (4.37), the development of the plasticity in the matrix phase introduces a dependency of $\tilde{\mu}_s^{\text{Dr}}$ and $\tilde{\kappa}_s^{\text{Dr}}$ on Γ and β. The matrix secant tensor $\tilde{\boldsymbol{C}}_0^{\text{SDr}}$ is known to be isotropic, being possible to write it in terms of $\tilde{\mu}_s^{\text{Dr}}$ and $\tilde{\kappa}_s^{\text{Dr}}$ as $\tilde{\boldsymbol{C}}_0^{\text{SDr}} = 3\kappa_s^{\text{Dr}}\boldsymbol{I}^{\text{vol}} + 2\mu_s^{\text{Dr}}\boldsymbol{I}^{\text{dev}}$, where the plastic bulk and shear moduli write:

$$\begin{aligned} \tilde{\kappa}_{s_{n+1}}^{\text{Dr}} &= \left(1 - \tilde{D}_{0_{n+1}}\right)\left(\kappa^{\text{el}} - \frac{2\beta_{n+1}{\kappa^{\text{el}}}^2\Gamma_{n+1}}{1 + 2\kappa^{\text{el}}\Gamma_{n+1}\beta_{n+1}}\right) \quad ; \text{ and} \\ \tilde{\mu}_{s_{n+1}}^{\text{Dr}} &= \left(1 - \tilde{D}_{0_{n+1}}\right)\left(\mu^{\text{el}} - \frac{6{\mu^{\text{el}}}^2\Gamma_{n+1}}{1 + 6\mu^{\text{el}}\Gamma_{n+1}}\right). \end{aligned} \tag{4.40}$$

By solving the system of two equations formed by the definitions of the bulk and shear moduli, the unknown plastic multiplier Γ_{n+1} and the parameter β_{n+1} can be obtained directly as:

$$\Gamma_{n+1} = -\frac{\left(\tilde{D}_{0_{n+1}} - 1\right)\mu^{\mathrm{el}} + \tilde{\mu}^{\mathrm{Dr}}_{s_{n+1}}}{6\mu^{\mathrm{el}}\tilde{\mu}^{\mathrm{Dr}}_{s_{n+1}}}, \tag{4.41}$$

$$\beta_{n+1} = -\frac{\kappa^{\mathrm{el}}\left(\tilde{D}_{0_{n+1}} - 1\right) + \tilde{\kappa}^{\mathrm{Dr}}_{s_{n+1}}}{2\Gamma_{n+1}\tilde{\kappa}^{\mathrm{Dr}}_{s_{n+1}}\kappa^{\mathrm{el}}}. \tag{4.42}$$

In order to find a unique value of the parameter $\tilde{\beta}$, this is computed as the arithmetic mean of the identified β_i at each loading increment. Once the parameter $\tilde{\beta}$ is computed, the initial plastic Poisson's ratio $\tilde{\nu}_p$ can be identified as:

$$\tilde{\nu}_p = \frac{9 - 2\tilde{\beta}}{18 + 2\tilde{\beta}}. \tag{4.43}$$

Parameters $\tilde{\beta}$ and $\tilde{\nu}_p$ remain constant for the rest of the identification process.

Fig. 4.16 shows a flowchart of the inverse identification process up to the plastic flow with all the steps performed separated into the three tested loading conditions.

Plastic flow and damage evolution law up to strain softening onset At this stage, the known MF-ROM variables are: $\left[\tilde{v}_{\mathrm{I}}, \tilde{\mathrm{I}}, \tilde{\theta}, \tilde{E}_0, \tilde{\nu}_0, \tilde{\alpha}, \tilde{m}, \tilde{\sigma}^0_c, \tilde{\nu}_p\right]$. In this step, the following variables will be identified: $\left[\tilde{p}_{\mathrm{onset}}\ , \widetilde{D}_{\mathrm{onset}}\ \right]$. Apart from the MF-ROM variables, it is worth recalling that the macro-stress and strains ($\bar{\boldsymbol{\sigma}}$, $\bar{\boldsymbol{\varepsilon}}$) and the effective damage evolution $\tilde{D}_0$ are known for all steps, as well as the phases stress-strain states ($\boldsymbol{\sigma}_0$, $\boldsymbol{\varepsilon}_0$, $\boldsymbol{\sigma}_{\mathrm{I}}$, $\boldsymbol{\varepsilon}_{\mathrm{I}}$) up to the plastic onset and the matrix parameters $\tilde{\nu}_p$ and $\tilde{\beta}$, with $\tilde{\nu}_p$ and $\tilde{\beta}$ being linked through $\tilde{\nu}_p = \frac{9-2\tilde{\beta}}{18+2\tilde{\beta}}$.

Once all the parameters defining the plastic evolution of the material are identified, it is possible to compute the plastic strain evolution of the matrix phase by identifying the matrix damaged secant tensor $\tilde{\boldsymbol{C}}^{\mathrm{SDr}}_0$ using the reloading step of the incremental secant scheme as previously shown. Having identified and fixed the parameter $\tilde{\beta}$, the definition of the shear and bulk moduli, Eqs. (3.68, 3.74), will now only depend on one unknown: the plastic multiplier Γ through Eq. (4.41), reducing the evaluation of $\tilde{\boldsymbol{C}}^{\mathrm{SDr}}_0$ to the optimization of Γ. To that end, the following minimization is performed:

$$\min_{\Gamma_{n+1}} \left\{ \left\| \tilde{\bar{\boldsymbol{C}}}^{\mathrm{SDr}}_{n+1} \left(\tilde{\boldsymbol{C}}^{\mathrm{SDr}}_0 \left(\tilde{\mu}^{\mathrm{Dr}}_s(\Gamma_{n+1}); \tilde{\kappa}^{\mathrm{Dr}}_s(\Gamma_{n+1}) \right); \boldsymbol{C}^{\mathrm{el}}_{\mathrm{I}}, \tilde{\mathrm{I}}, \tilde{\theta}, v_{\mathrm{I}} \right) : \Delta\boldsymbol{\varepsilon}^{\mathrm{r}}_{n+1} - \bar{\boldsymbol{\sigma}}_{n+1} \right\| \right\}, \tag{4.44}$$

Once the plastic multiplier Γ is obtained, the value of the matrix, inclusions and composite secant tensors ($\tilde{\boldsymbol{C}}^{\mathrm{SDr}}_0$, $\tilde{\boldsymbol{C}}^{\mathrm{Sr}}_{\mathrm{I}}$ and $\tilde{\bar{\boldsymbol{C}}}^{\mathrm{SDr}}$ respectively) are known from Eqs. (3.22, 3.67, 3.68), being possible to compute the stress-strain state of each of the phases for all loading increments (see Fig. 4.17). This step allows us to identify the matrix localization onset iteration, which is defined as being the iteration in which the matrix stress reaches its maximum ($|\boldsymbol{\sigma}^{\mathrm{eq}}_{0_{n+1}}| \leq |\boldsymbol{\sigma}^{\mathrm{eq}}_{0_n}|$). This point is used to define the softening damage law parameters that define its evolution before the failure damage evolution law is triggered, see Fig. 4.18. Once this condition is reached, the iterative process is stopped, since the identification of the post-strain softening region is not needed in terms of the plastic flow evolution information.

As shown in Fig. 4.17, by identifying the value of the plastic multiplier, it is possible to obtain the increment of the accumulated plastic strain in the matrix $\Delta\tilde{p}_{0_{n+1}}$ from time t_n to t_{n+1}

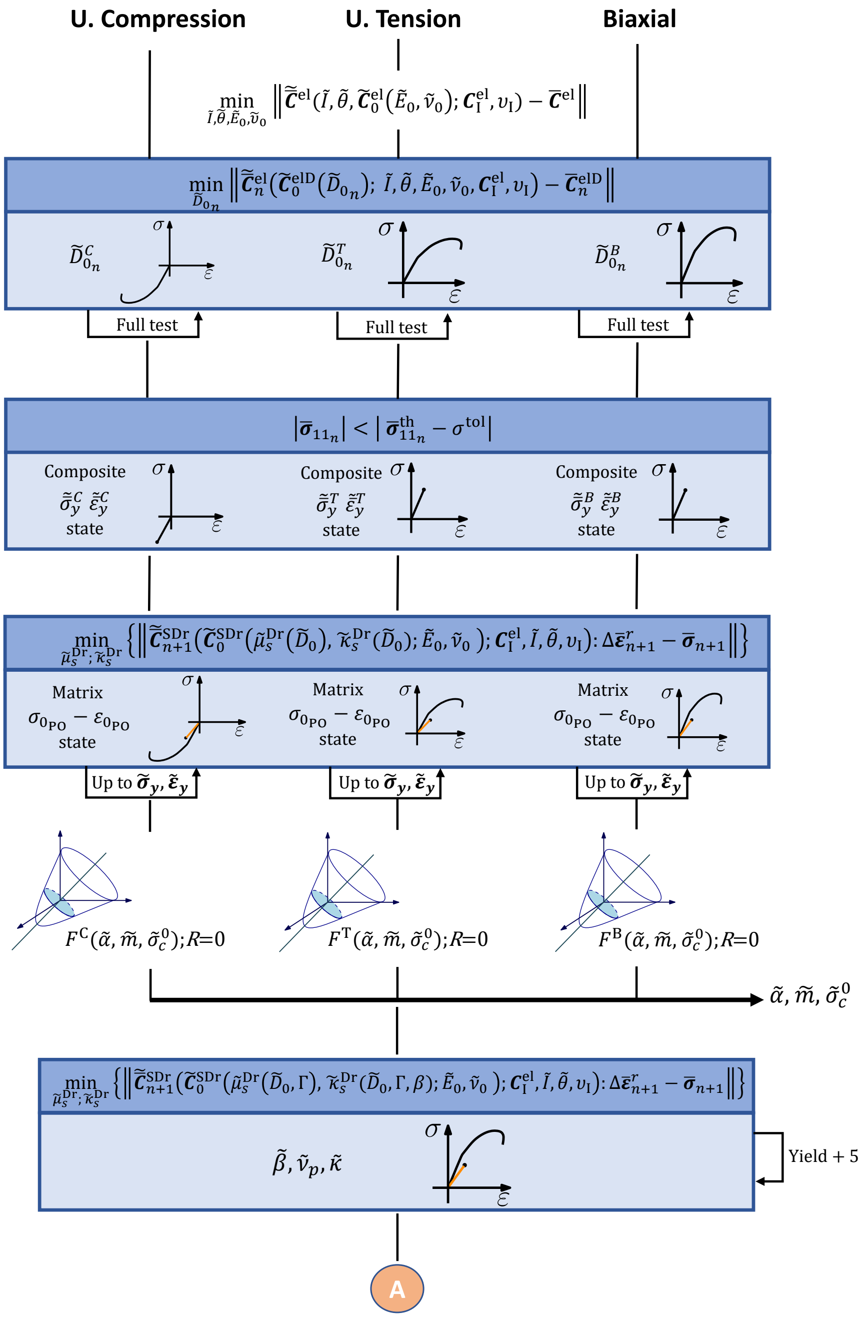

FIGURE 4.16: Flowchart of the inverse identification process up to plastic flow.

having:

$$\Delta\tilde{p}_{0_{n+1}} = \frac{\Gamma_{n+1}}{\sqrt{1+2\tilde{\nu}_p^2}}\sqrt{6\left(\left(\tilde{\boldsymbol{C}}_{0_{n+1}}^{\mathrm{Sr}} : \Delta\boldsymbol{\varepsilon}_{0_{n+1}}^{\mathrm{r}}\right)^{\mathrm{eq}}\right)^2 + \frac{4}{3}\tilde{\beta}^2\left(\frac{1}{3}\mathrm{tr}\left(\tilde{\boldsymbol{C}}_{0_{n+1}}^{\mathrm{Sr}} : \Delta\boldsymbol{\varepsilon}_{0_{n+1}}^{\mathrm{r}}\right)\right)^2}, \tag{4.45}$$

where the matrix equivalent increment strain $(\Delta\boldsymbol{\varepsilon}_0^{\mathrm{r}})^{\mathrm{eq}}$ is evaluated with the first statistical moment:

$$\begin{cases} \boldsymbol{\sigma}^{\mathrm{eq}} = \sqrt{\frac{3}{2}\boldsymbol{\sigma} : \boldsymbol{I}^{\mathrm{dev}} : \boldsymbol{\sigma}}, \\ \Delta\varepsilon^{\mathrm{eq}} = \sqrt{\frac{2}{3}\Delta\boldsymbol{\varepsilon} : \boldsymbol{I}^{\mathrm{dev}} : \Delta\boldsymbol{\varepsilon}}. \end{cases} \tag{4.46}$$

This accumulated plastic strain increment of the matrix phase allows to approximate the accumulated plastic strain by adding all steps increments $\tilde{p}_{0_{n+1}} = \sum_{l=0}^{n} \Delta\tilde{p}_{0_{l+1}}$.

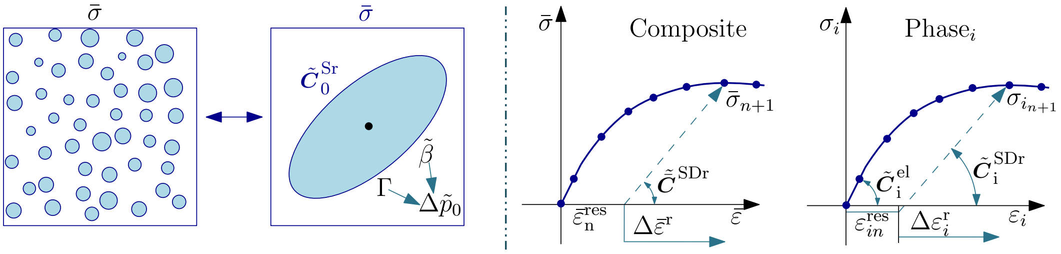

FIGURE 4.17: Schematic representation of the full-field SVE and its MFH virtual counterpart with computation of the plastic strain evolution (left) and schematic loading phase in a stress-strain plot (right).

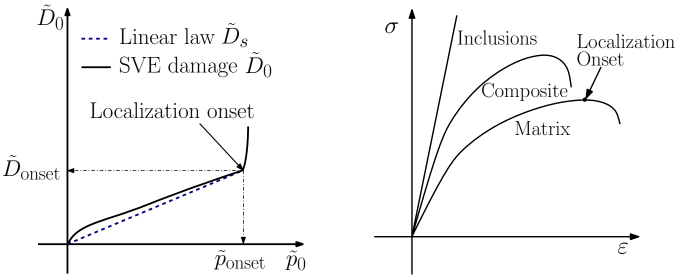

FIGURE 4.18: Damage-plastic strain plot representing the identified matrix damage from the SVE and the linear approximation used for the MFH surrogate on the left, and graphic representation of the composite, matrix and inclusions stress-strain curves with the location of the localization onset on the right.

A softening damage ($\tilde{D}_s$) evolution law is used to model the matrix damage. In this Work, this surrogate model softening damage $\tilde{D}_s$ is simplified to a linear evolution law allowing for an accurate representation of the damage value at the strain softening onset, meaning the maximum stress reached by the composite material and the strain at which it is reached will be accurately represented while simplifying the model. In order to be able to accurately capture the damage state at the beginning of the strain softening onset, the slope of the damage law is defined by the damage ($\tilde{D}_0$) and the accumulated plastic strain ($\tilde{p}_0$) values at the matrix localization onset iteration. These quantities will be called $\tilde{D}_{\mathrm{onset}}$ and $\tilde{p}_{\mathrm{onset}}$ respectively, see Fig. 4.18. The evolution law of the softening damage then writes:

$$\Delta\tilde{D}_s = \frac{\tilde{D}_{\mathrm{onset}}}{\tilde{p}_{\mathrm{onset}}} \Delta\tilde{p}_0. \tag{4.47}$$

It is worth highlighting that even though the damage representation during this stage does not represent the main focus of this Work, a more complex damage evolution law can be easily implemented in future works for a more complete damage representation.

Hardening identification At this stage, the known MF-ROM variables are: $\left[\tilde{v}_{\mathrm{I}}, \tilde{\mathrm{I}}, \tilde{\theta}, \tilde{E}_0, \tilde{\nu}_0, \tilde{\alpha}, \tilde{m}, \tilde{\sigma}_c^0, \tilde{\nu}_p, \tilde{p}_{\mathrm{onset}}\ , \tilde{D}_{\mathrm{onset}}\ \right]$. In this step, the following variables will be identified: $\left[\tilde{h}_0, \tilde{h}_1, \tilde{m}_0\right]$. Adding to the known MF-ROM variables, from which the softening damage $\tilde{D}_s(\tilde{p}_{\mathrm{onset}}\ , \tilde{D}_{\mathrm{onset}}\ )$ used in this step is defined, previous steps permitted the identification of the stress-strain state of the matrix phase ($\boldsymbol{\sigma}_0$, $\boldsymbol{\varepsilon}_0$) for all iterations as well as the plastic strain evolution $\tilde{p}_0$ up to the localization onset.

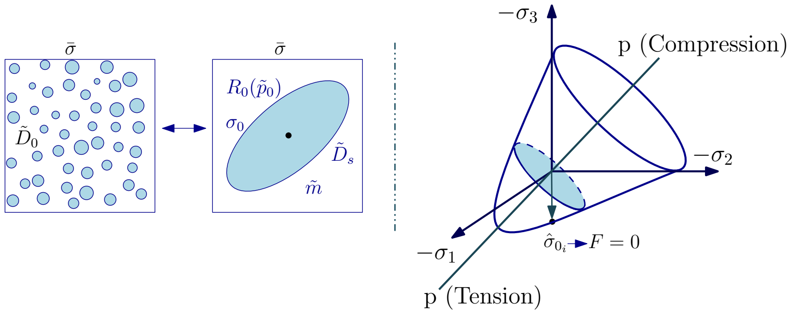

FIGURE 4.19: Schematic representation of the damaged plastic full-field SVE and its MFH virtual counterpart (left) and yield surface representation in the Haigh-Westergaard coordinate space and effective matrix stress at iteration i (right).

As already mentioned, in this Section the damage evolution law $\tilde{D}_s$ used for the MF-ROM will be defined and the hardening evolution of the matrix will be identified. The effective von Mises stress of the matrix phase can be computed using the first statistical formula, Eq. (4.46). As plastic flow occurs during the full loading, the yield function F has a null value at all steps, see Fig. 4.19.

Knowing the matrix stress and strain states at each loading increment, as well as the accumulated plastic strain evolution, it is then possible to identify the matrix effective hardening evolution $R\left(\tilde{p}_0\right)$ up to the strain softening onset by minimizing the yield surface function F at each time increment:

$$\begin{aligned}\min_{R_{n+1}\left(\tilde{p}_{0_{n+1}}\right)} \Bigg\{ \Bigg| F_{n+1}\left(R_{n+1}\left(\tilde{p}_{0_{n+1}}\right)\right) = & \frac{\left(\left(\hat{\boldsymbol{\sigma}}_{0_{n+1}}\right)^{\mathrm{eq}}\right)^{\tilde{\alpha}}}{\left(\tilde{\sigma}_c^0 + R_{n+1}\left(\tilde{p}_{0_{n+1}}\right)\right)^{\tilde{\alpha}}} \\ & - 3\frac{\tilde{m}^{\tilde{\alpha}} - 1}{\left(\tilde{m}+1\right)\left(\tilde{\sigma}_c^0 + R_{n+1}\left(\tilde{p}_{0_{n+1}}\right)\right)}\hat{\phi}_{0_{n+1}} - \frac{\tilde{m}^{\tilde{\alpha}} + \tilde{m}}{\tilde{m}+1}\Bigg|\Bigg\},\end{aligned} \tag{4.48}$$

where the effective stress is computed with the identified softening damage evolution $\tilde{D}_s$, such that:

$$\hat{\boldsymbol{\sigma}}_{0_{n+1}} = \frac{\boldsymbol{\sigma}_{0_{n+1}}}{\left(1 - \tilde{D}_{s_{n+1}}\right)}. \tag{4.49}$$

The use of the softening damage evolution law allows slightly increasing the accuracy of the MF-ROM, as it permits to compute the effective hardening evolution accounting for the damage law simplification.

Once the effective hardening evolution is computed, it is possible to identify the parameters ($\tilde{\boldsymbol{H}}$) governing the dedicated evolution law $\tilde{R}_0(\tilde{p}_{0_n}, \tilde{\boldsymbol{H}})$ used for the MFH model. In order to identify the hardening parameters that best suit a given SVE, a curve fitting problem is performed using the previously computed hardening evolution $R_n(\tilde{p}_{0_n})$.

$$\min_{\tilde{\boldsymbol{H}}} \left\{ \sum_n \left| R_n(\tilde{p}_{0_n}) - \tilde{R}_0(\tilde{\boldsymbol{H}}, \tilde{p}_{0_n}) \right| \right\}. \tag{4.50}$$

In this Thesis, a linear exponential law is used in order to model this evolution:

$$\tilde{R}_0\left(\tilde{p}_0\right) = \tilde{h}_0\tilde{p}_0 + \tilde{h}_1\left(1 - e^{-\tilde{m}_0\tilde{p}_0}\right). \tag{4.51}$$

With this evolution model, the set of hardening parameters ($\tilde{\boldsymbol{H}}$) that need to be identified consists of $\tilde{h}_0$, $\tilde{h}_1$ and $\tilde{m}_0$, which will be part of the set of random quantities in the final MFH-ROM. Considering two different hardening laws in tension and compression would allow intro-

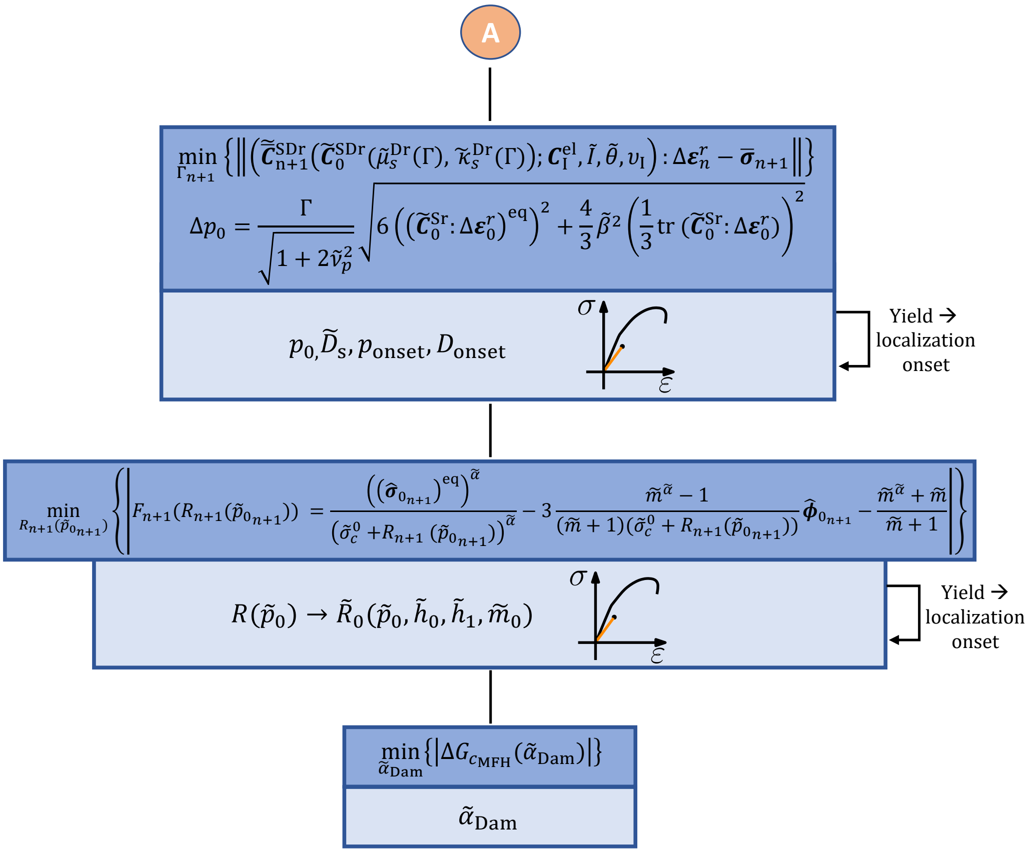

FIGURE 4.20: Flowchart of the inverse identification process during plastic flow.

ducing more parameters in the MFH surrogate in order to capture more accurately different loading modes. It is worth highlighting that this hardening identification process is applied up to the strain-softening onset, as the introduction of the post-strain softening onset would introduce spurious information due to the localization effects. A flowchart of the plastic flow stage identification process is shown in Fig. 4.20.

The identification process presented in this Section allows obtaining an accurate representation of the SVE behavior under different loading conditions independently of the SVE characteristics. A direct comparison between the response obtained with the full-field SVE realizations and their identified MFH counterparts for the three tested loading conditions, see Fig. 4.5, is shown in Fig. 4.21. As already observed in the work by Wu et al. (2019), the identified matrix behavior differs from the SVE matrix material. This is observed in the comparison between the tensile hardening evolution curves obtained from the identification process of different SVEs and the epoxy hardening law used to model the matrix behavior in the full-field realizations, see Fig. 4.21.

The capability of the identified surrogate model to capture the SVE behavior under a different loading to those used for the inverse process was checked by testing its performance under shear loading. We however note that the use of periodic boundary conditions for the cases different from tensile ones is debatable as discussed in Section 4.1.2. As seen in the results shown in Fig. 4.22, the MFH model yields less accurate results than for the previously tested loading conditions. However, the MFH simulations predict the composite strength within a 10% error. This result shows how the tests selected for the inverse identification procedure could impact the

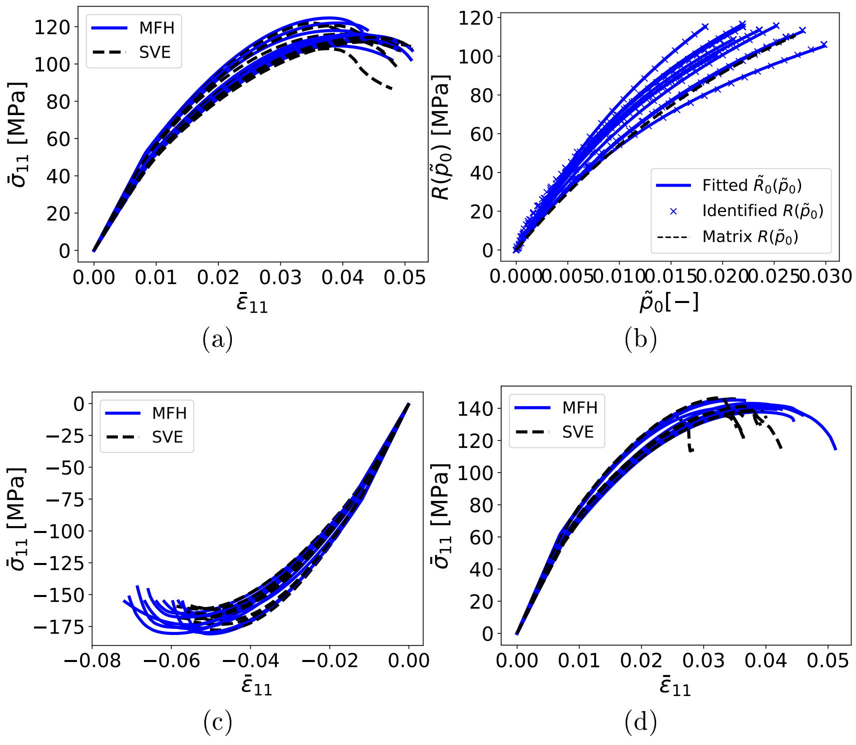

(a) (b)

(c) (d)

FIGURE 4.21: (a) Stress-strain curves of random picked SVEs under uniaxial tension. (b) Comparison between epoxy tensile hardening law and the identified hardening evolution. (c) Stress-strain curves of random picked SVEs under uniaxial compression. (d) Stress-strain curve of random picked SVEs under biaxial tension. MFH stands for the results obtained with the surrogate model. SVE stands for the results obtained in the full-field SVE realizations. The Identified $\tilde{R}(\tilde{p}_0)$ and Fitted $\tilde{R}_0(\tilde{p}_0)$ stand for the identified surrogate matrix hardening law. The Matrix $\tilde{R}_0(\tilde{p}_0)$ stands for the hardening law used in the full-field SVE realizations.

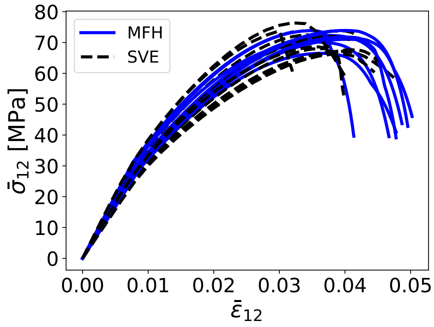

FIGURE 4.22: Stress-strain curves of random picked SVEs under shear loading. MFH stands for the results obtained with the surrogate model. SVE stands for the results obtained in the full-field SVE realizations.

ability of the model to capture different characteristics of the material behavior. The use of a different set of loading conditions, or the addition of more loading conditions to be used could be tested in future works to optimize the performance of the surrogate model.

4.2.1.3 Nonlinear damage-enhanced elasto-plastic composites accounting for loss of objectivity during local softening

At this stage, the known MF-ROM variables are: $\left[\tilde{v}_{\mathrm{I}}, \tilde{\mathrm{I}}, \tilde{\theta}, \tilde{E}_0, \tilde{\nu}_0, \tilde{\alpha}, \tilde{m}, \tilde{\sigma}_c^0, \tilde{\nu}_p, \tilde{p}_{\mathrm{onset}}, \tilde{D}_{\mathrm{onset}}, \tilde{h}_0, \tilde{h}_1, \tilde{m}_0\right]$. In this step, the following variables will be identified: $\left[\tilde{\alpha}_{\mathrm{Dam}}, \tilde{\beta}_{\mathrm{Dam}}\right]$. At this step, the critical energy release rate extracted from the full-field realization $G_{c_{\mathrm{SVE}}}$ will be used for the calibration of the failure stage of the damage law.

Up to now, the loss of objectivity that is encountered once the onset of strain softening occurs has not been taken into account. To that end, the energy release rate is used as objective value that will allow the recovery of the size objectivity (Nguyen, Wu, and Noels, 2019; Wu et al., 2013b). In order to estimate the critical energy release rate associated to the MFH model, similarly to the approach used in previous publications (Nguyen, Wu, and Noels, 2019; Wu et al., 2021), a uniaxial test with a loading direction perpendicular to the UD composite fiber orientation is performed on a 2D specimen with length L ten times bigger than the characteristic nonlocal length l_c used in the MFH model and width W four times smaller than the characteristic length of the homogenized composite material, see Fig. 4.23. A slight decrease of the bar diameter in its center is introduced through a curvature with radius $R >> L$ in order to generate a localization of the deformation while not affecting the pre-localization response of the material. A thorough convergence study of the solution with respect to the mesh was performed in order to ensure a correct identification of the critical energy release rates.

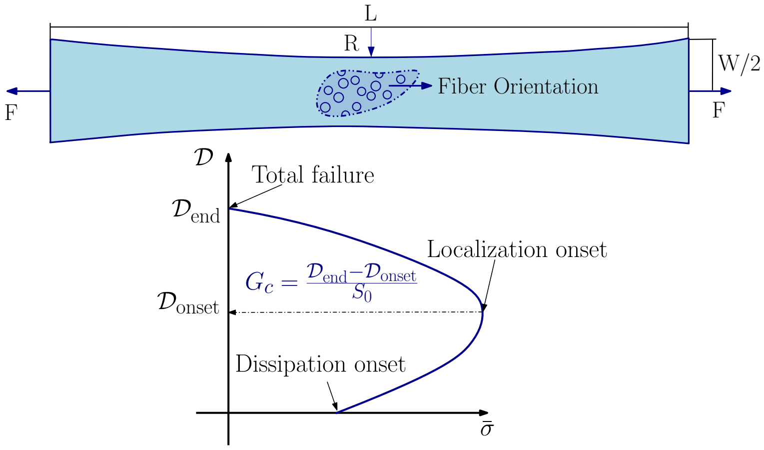

FIGURE 4.23: Schematic representation of the uniaxial test on the left and energy dissipation ($\mathcal{D}$) - stress ($\bar{\sigma}$) plot used for the computation of the MFH critical energy release rate G_c.

The failure stage of the composite response is considered to be started once $\tilde{p}_0 > \tilde{p}_{\mathrm{onset}}$. In order to be able to control the failure characteristics of the material, a new failure damage (D_f) contribution is introduced in the MFH surrogate model. This failure damage evolution law writes:

$$\Delta \tilde{D}_f = \tilde{\alpha}_{\mathrm{Dam}} \left(\tilde{p}_0 + \Delta \tilde{p}_0 - \tilde{p}_{\mathrm{onset}}\right)^{\tilde{\beta}_{\mathrm{Dam}}} \Delta \tilde{p}_0, \quad \text{if} \quad \tilde{p}_0 > \tilde{p}_{\mathrm{onset}}. \tag{4.52}$$

The total damage of the surrogate model during this post-strain softening point is then defined by the sum of both damage components: $\Delta \tilde{D}_{\mathrm{MFH}} = \Delta \tilde{D}_s + \Delta \tilde{D}_f$. As can be observed in Eq. (4.52), the failure damage evolution depends on two new parameters: $\tilde{\alpha}_{\mathrm{Dam}}$ and $\tilde{\beta}_{\mathrm{Dam}}$. These parameters will affect the ductility of the material, see Fig. 4.24, changing the resultant critical energy release rate. While the parameter $\tilde{\alpha}_{\mathrm{Dam}}$ directly affects the speed of the failure damage evolution and therefore the critical energy release rate, the parameter $\tilde{\beta}_{\mathrm{Dam}}$ allows modeling the shape of the failure stage. As the critical energy release rate remains the only objective parameter after the failure softening, the calibration of both parameters would not be possible. To this end, in this Thesis, $\tilde{\beta}_{\mathrm{Dam}}$ was fixed to a value of 2.5 $[-]$, value for which the post-softening averaged stress-strain evolution of the SVEs using the MFH model yielded a similar behavior to the averaged response of the full-field realizations for a wide range of G_c, allowing to reduce the optimization problem to a one-DOF problem.

The value of the characteristic length l_c introduced used for the definition of $\boldsymbol{c}_{\text{g}}$ (see Eq. (3.79)) directly impacts the required finite element discretization, as the size of the elements should remain lower than l_c in order to be able to correctly capture the damage evolution. This translates in a direct relation between the efficiency of the MF-ROM and the value of l_c. The higher the characteristic length, the more efficient the SFEM simulations are, as the amount of elements required to discretize the FEM simulation decreases. The chosen value for the characteristic length was fixed to a value of 25 μm, value which allows to capture the interaction between the different property spatial discretizations (which will be squares of 25x25 μm^2 or 45x45 μm^2 depending on the used SVE realizations to build the MF-ROM) while not having a negative impact on the required mesh. With the characteristic length l_c fixed, the value of the energy release rate now only depends on the post-strain softening damage characteristics of the composite material.

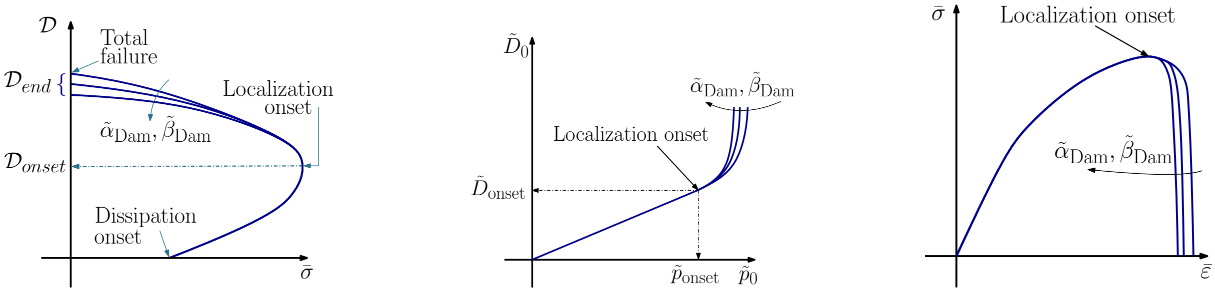

FIGURE 4.24: Schematic representation of the composite energy dissipation ($\mathcal{D}$) - stress ($\bar{\sigma}$) plot, the matrix damage evolution law with respect to its accumulated plastic strain and the composite averaged $\sigma-\varepsilon$ curve. The effect of the failure damage evolution law parameter ($\tilde{\alpha}_{\text{Dam}}$) is illustrated on each respective graph.

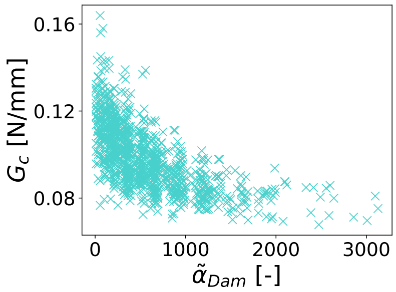

FIGURE 4.25: $G_c - \tilde{\alpha}_{\text{Dam}}$ distribution for the 25×25 μm^2 SVE realizations.

After the matrix softening strain onset is reached, the identification of the post-strain softening damage evolution law parameter ($\tilde{\alpha}_{\text{Dam}}$) is performed through an iterative process, in which the critical energy release rate obtained with the full-field SVE simulation is attempted to be recovered with its MFH model counterpart. These model parameters are then found through the following minimization problem:

$$\min_{\tilde{\alpha}_{\text{Dam}}} \left\{ \left| \Delta G_{c_{\text{MFH}}} \left(\tilde{\alpha}_{\text{Dam}} \right) \right| \right\}, \tag{4.53}$$

where $\Delta G_{c_{\text{MFH}}} \left(\tilde{\alpha}_{\text{Dam}} \right) = G_{c_{\text{MFH}}} \left(\tilde{\alpha}_{\text{Dam}} \right) - G_{c_{\text{SVE}}}$.

An initial guess value for $\tilde{\alpha}_{\text{Dam}}$ is used to start the iterative process, in which a finite element simulation from which the critical energy release rate $G_{c_{\text{MFH}}}$ will be computed is performed

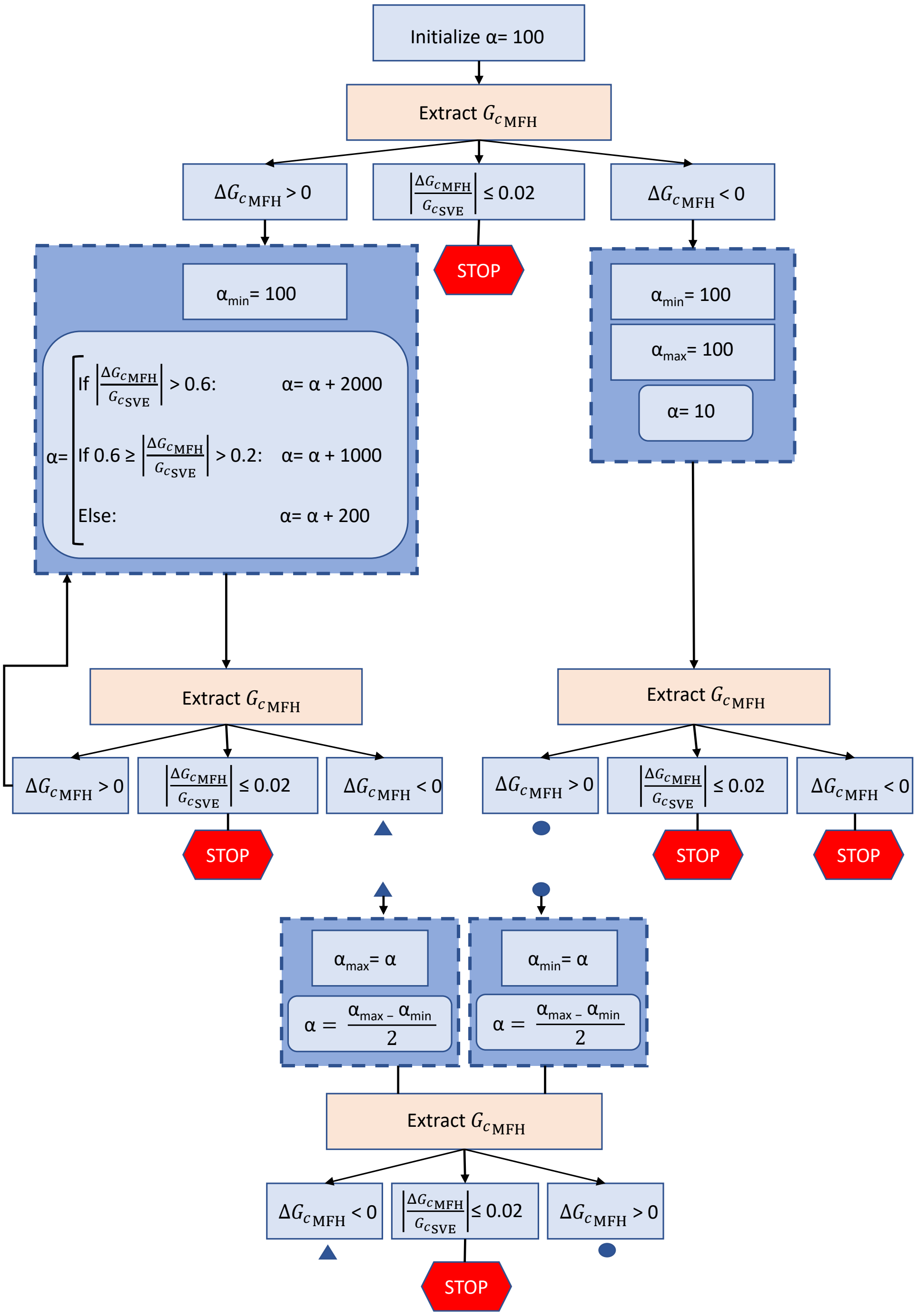

FIGURE 4.26: Flowchart of the optimization process of parameter $\tilde{\alpha}_{\mathrm{Dam}}$ (the subscript Dam is omitted for clarity) for the recovery of the size objectivity through the critical energy release rate.

at each iteration as shown by Fig. 4.23. Once the critical energy release rate is obtained, this value is compared to the critical energy release rate of SVE realization, being possible to implement an algorithm capable of finding a better guess of the set of parameters of the damage model for the next iteration. As shown by Fig. 4.24, a change in the matrix damage evolution law modifies the failure characteristics of the homogenized composite material response. This change in the failure characteristics has a direct impact in the dissipated energy after the localization onset, modifying the characteristic critical energy release rate of the studied material. This iterative process is performed until minimizing the $\Delta G_{c_{\mathrm{MFH}}}(\tilde{\alpha}_{\mathrm{Dam}})$ below a fixed tolerance value. In this Work, this tolerance is fixed to be 2% of the reference value $G_{c_{\mathrm{SVE}}}$, such that $\Delta G_{c_{\mathrm{MFH}}} \leq \text{tolerance} = 0.02 \cdot G_{c_{\mathrm{SVE}}}$. In the case reaching this tolerance would not be possible for a given SVE realization, the results of that realization would not be taken into account in the final data.

As the resultant effect of $\tilde{\alpha}_{\mathrm{Dam}}$ on the critical energy release rate $G_{c_{\mathrm{SVE}}}$ also depends on all other parameters defining the surrogate model, a direct relation between $G_{c_{\mathrm{SVE}}}$ and $\tilde{\alpha}_{\mathrm{Dam}}$ cannot be found explicitly as shown in Fig. 4.25, being necessary to iterate during this optimization problem until reaching a sufficiently low error $\Delta G_{c_{\mathrm{MFH}}}$. Fig. 4.26 shows a scheme of the optimization algorithm used to identify the parameter $\tilde{\alpha}_{\mathrm{Dam}}$ through a flowchart.

While the algorithm can be applicable to any type of studied material, the values used as increment or decrease of the parameter $\tilde{\alpha}_{\mathrm{Dam}}$ have been optimized for the here studied RTM6 matrix based UD composites. In case the MF-ROM is being built for another material, these values shall be revisited in order to check their validity or to optimize the failure stage identification process.

4.3 Stochastic MF-ROM for UD composite material

After the presentation of the identification process, this section will start with a study of the statistical properties of the identified effective random parameters used to define the MF-ROM. Then, the data-driven sampling method (Soize and Ghanem, 2016) used for the generation of proper random fields for the construction of the structural stochastic FEM (Wu et al., 2019) will be presented.

4.3.1 Analysis of the MF-ROM effective random parameters

As shown in Section 4.2, a total of 16 effective random parameters is needed for the definition of the MF-ROM. These random parameters constitute the vector $\boldsymbol{\beta}^D$ ($n = 16$) Eq. (4.28). A vector of 16 parameters is therefore identified for each SVE realization, meaning as many vectors $\boldsymbol{\beta}^D$ as SVE realizations are obtained. Fig. 4.27 shows the different distributions of the random effective material parameters obtained from the inverse identification process for the case with 25×25 $\mu\mathrm{m}^2$ and 45×45 $\mu\mathrm{m}^2$ SVEs by plotting their respective probability density histograms. It is possible to observe how in general, the parameters using the 45×45 $\mu\mathrm{m}^2$ SVEs present less widespread values of the effective random parameters, which is reflected in higher maxima of the probability density histograms, due to the higher size of the SVE. This lower standard deviation allows reducing the number of SVE realizations needed to obtain the complete distribution of the effective parameters compared to the 25×25 $\mu\mathrm{m}^2$ case. However, the effect of this lower heterogeneity of the effective parameter values is still to be verified afterwards during the verification of the MF-ROM performance. The probability density distribution of the remaining effective random parameters can be found in Appendix C.2.

As in the elasto-plastic case (Wu et al., 2019), the effective random parameters used to build the damage-enhanced pressure-dependent MF-ROM show a clear cross-dependence, as shown by the distance correlation (Székely, Rizzo, and Bakirov, 2007) values obtained in Figs. 4.28 and 4.29. This cross-dependence between the effective random parameters must be preserved by the data-driven sampling method in order to yield an accurate result when using the MF-ROM.

4.3.2 Generation of random parameters

This section will start by briefly introducing the data-driven sampling method presented in Soize and Ghanem (2016) and used for a stochastic MF-ROM developed in Wu et al. (2019), method that will serve to generate new data from the obtained dataset through the identification process,

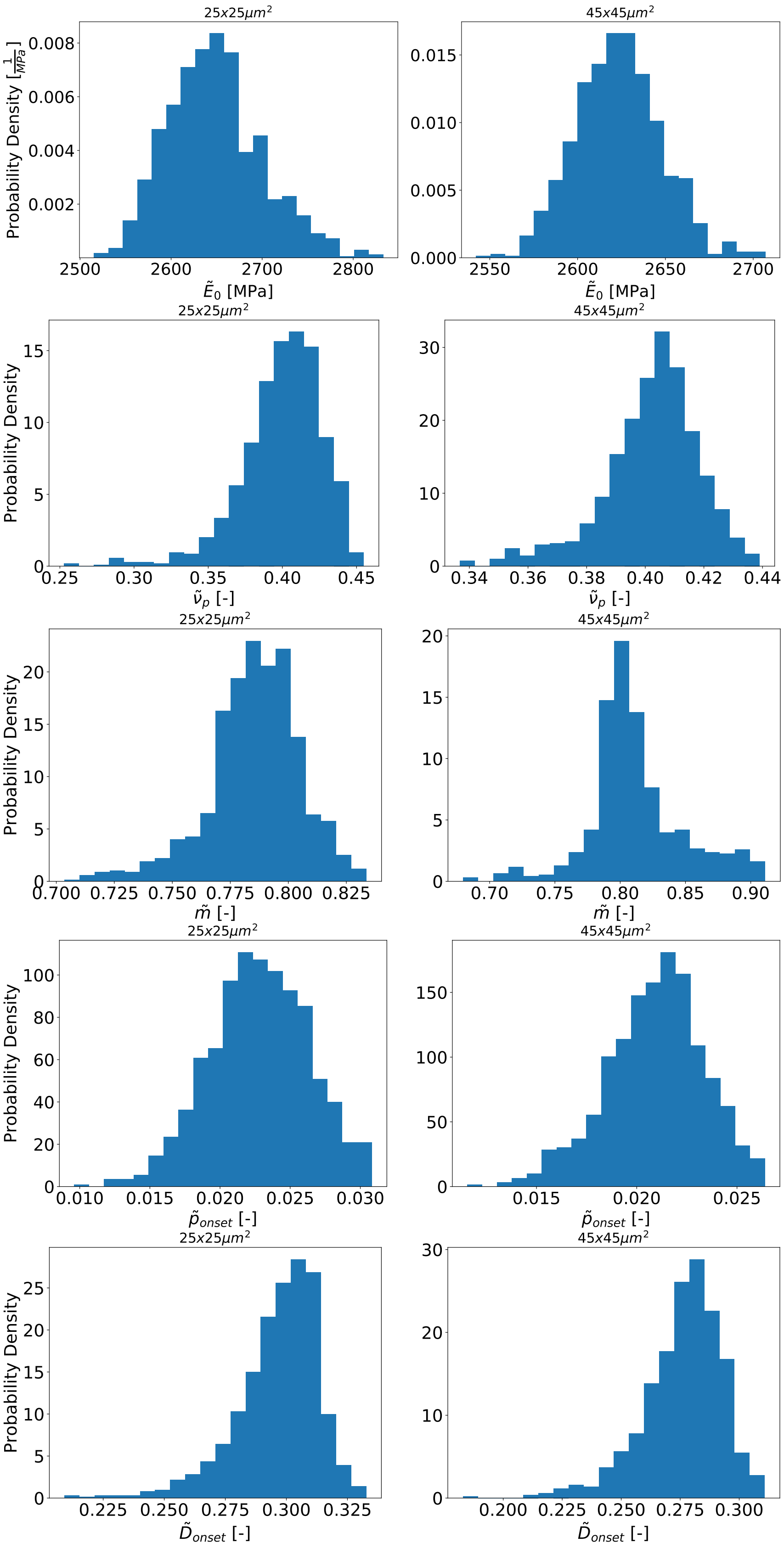

FIGURE 4.27: Probability density histograms of $\tilde{E}_0, \tilde{\nu}_p, \tilde{m}, \tilde{p}_{\text{onset}}$ and $\tilde{D}_{\text{onset}}$ for the $25 \times 25\mu\text{m}^2$ (left) and $45 \times 45\mu\text{m}^2$ (right) SVE cases.

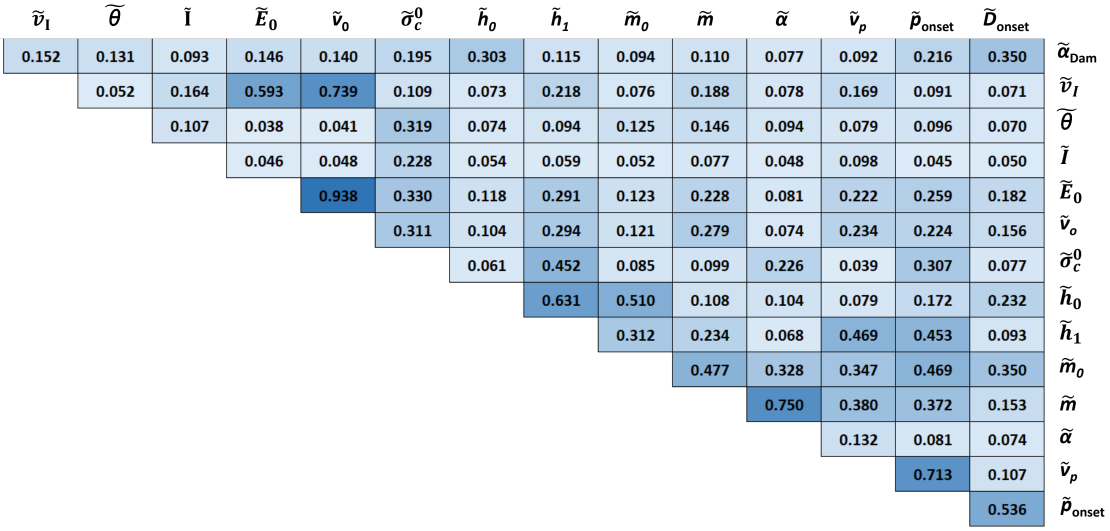

$\tilde{\nu}_I$	$\widetilde{\theta}$	$\tilde{I}$	$\tilde{E}_0$	$\tilde{\nu}_0$	$\tilde{\sigma}_c^0$	$\tilde{h}_0$	$\tilde{h}_1$	$\tilde{m}_0$	$\tilde{m}$	$\tilde{\alpha}$	$\tilde{\nu}_p$	$\tilde{p}_{onset}$	$\widetilde{D}_{onset}$	
0.152	0.131	0.093	0.146	0.140	0.195	0.303	0.115	0.094	0.110	0.077	0.092	0.216	0.350	$\tilde{\alpha}_{Dam}$
	0.052	0.164	0.593	0.739	0.109	0.073	0.218	0.076	0.188	0.078	0.169	0.091	0.071	$\tilde{\nu}_I$
		0.107	0.038	0.041	0.319	0.074	0.094	0.125	0.146	0.094	0.079	0.096	0.070	$\widetilde{\theta}$
			0.046	0.048	0.228	0.054	0.059	0.052	0.077	0.048	0.098	0.045	0.050	$\tilde{I}$
				0.938	0.330	0.118	0.291	0.123	0.228	0.081	0.222	0.259	0.182	$\tilde{E}_0$
					0.311	0.104	0.294	0.121	0.279	0.074	0.234	0.224	0.156	$\tilde{\nu}_0$
						0.061	0.452	0.085	0.099	0.226	0.039	0.307	0.077	$\tilde{\sigma}_c^0$
							0.631	0.510	0.108	0.104	0.079	0.172	0.232	$\tilde{h}_0$
								0.312	0.234	0.068	0.469	0.453	0.093	$\tilde{h}_1$
									0.477	0.328	0.347	0.469	0.350	$\tilde{m}_0$
										0.750	0.380	0.372	0.153	$\tilde{m}$
											0.132	0.081	0.074	$\tilde{\alpha}$
												0.713	0.107	$\tilde{\nu}_p$
													0.536	$\tilde{p}_{onset}$

FIGURE 4.28: Distance correlation of the effective random material parameters of the $25\times25\mu\text{m}^2$ SVEs.

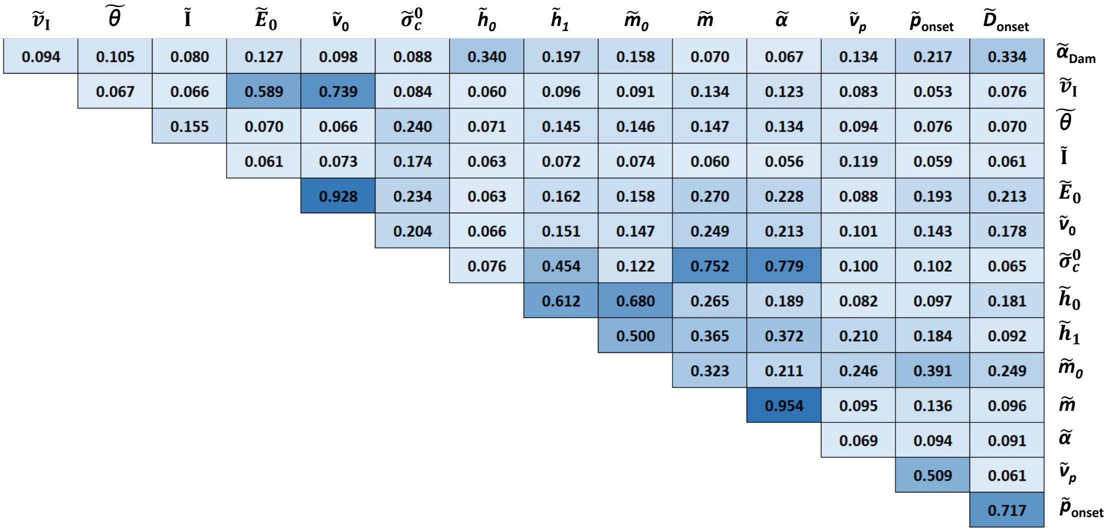

$\tilde{\nu}_I$	$\widetilde{\theta}$	$\tilde{I}$	$\tilde{E}_0$	$\tilde{\nu}_0$	$\tilde{\sigma}_c^0$	$\tilde{h}_0$	$\tilde{h}_1$	$\tilde{m}_0$	$\tilde{m}$	$\tilde{\alpha}$	$\tilde{\nu}_p$	$\tilde{p}_{onset}$	$\widetilde{D}_{onset}$	
0.094	0.105	0.080	0.127	0.098	0.088	0.340	0.197	0.158	0.070	0.067	0.134	0.217	0.334	$\tilde{\alpha}_{Dam}$
	0.067	0.066	0.589	0.739	0.084	0.060	0.096	0.091	0.134	0.123	0.083	0.053	0.076	$\tilde{\nu}_I$
		0.155	0.070	0.066	0.240	0.071	0.145	0.146	0.147	0.134	0.094	0.076	0.070	$\widetilde{\theta}$
			0.061	0.073	0.174	0.063	0.072	0.074	0.060	0.056	0.119	0.059	0.061	$\tilde{I}$
				0.928	0.234	0.063	0.162	0.158	0.270	0.228	0.088	0.193	0.213	$\tilde{E}_0$
					0.204	0.066	0.151	0.147	0.249	0.213	0.101	0.143	0.178	$\tilde{\nu}_0$
						0.076	0.454	0.122	0.752	0.779	0.100	0.102	0.065	$\tilde{\sigma}_c^0$
							0.612	0.680	0.265	0.189	0.082	0.097	0.181	$\tilde{h}_0$
								0.500	0.365	0.372	0.210	0.184	0.092	$\tilde{h}_1$
									0.323	0.211	0.246	0.391	0.249	$\tilde{m}_0$
										0.954	0.095	0.136	0.096	$\tilde{m}$
											0.069	0.094	0.091	$\tilde{\alpha}$
												0.509	0.061	$\tilde{\nu}_p$
													0.717	$\tilde{p}_{onset}$

FIGURE 4.29: Distance correlation of the effective random material parameters of the $45\times45\mu\text{m}^2$ SVEs.

and will then discuss the obtained identified and generated datasets that will be used to build the stochastic structural FEM.

The data-driven sampling method developed by Soize and Ghanem (2016) is used for the generation of proper random fields. This method accounts for the random properties of the material, which are defined in a probability space $(\Theta, \mathcal{T}, \mathcal{P})$ with a value in $\mathbb{R}^n$ through a random vector whose statistical information is supposed to belong to a subset $\mathcal{S}^n$ of $\mathbb{R}^n$ but whose distribution is unknown.

The random matrix $\left[\boldsymbol{\beta}^D\right] = \left[\boldsymbol{\beta}_1^D, ..., \boldsymbol{\beta}_N^D\right]$ with value in $\mathcal{M}_{n,N}$, where each column is an independent copy of the random vector defined in the space $(\Theta, \mathcal{T}, \mathcal{P})$, allows preserving the local structure of the dataset. In our case, the identification process permits us to obtain a matrix $[\boldsymbol{b}] = [\boldsymbol{b}_1, ..., \boldsymbol{b}_N]$, which is a realization of matrix $\left[\boldsymbol{\beta}^D\right]$ with a size of $N = 1037$ for the $25 \times 25\mu\text{m}^2$ SVE case and with a size of $N = 803$ for the $45 \times 45\mu\text{m}^2$ SVE case. The information contained in the matrix $[\boldsymbol{b}]$ allows then to generate n_{MC} new realizations of the random matrix $\left[\boldsymbol{\beta}^D\right]$ thanks to a Markov chain Monte Carlo (MCMC) process. To that end, first the mean is removed from the dataset values and a normalization of the variance is carried out, being then possible to generate a new random dataset. Once the new data is generated, this is re-scaled to the original dataset scale, obtaining the final data. This process is summarized in Wu et al. (2019).

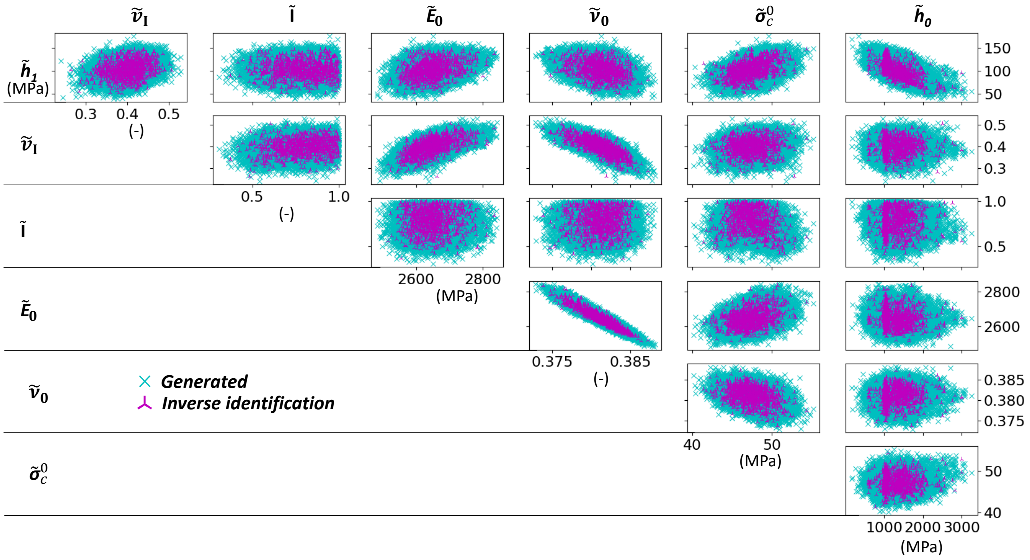

FIGURE 4.30: 25x25μm^2 effective random parameters distributions and their cross-dependence for the identified and generated $\tilde{v}_{\mathrm{I}}, \tilde{\mathrm{I}}, \tilde{E}_0, \tilde{\nu}_0, \tilde{\sigma}_c^0, \tilde{h}_0$ and $\tilde{h}_1$.

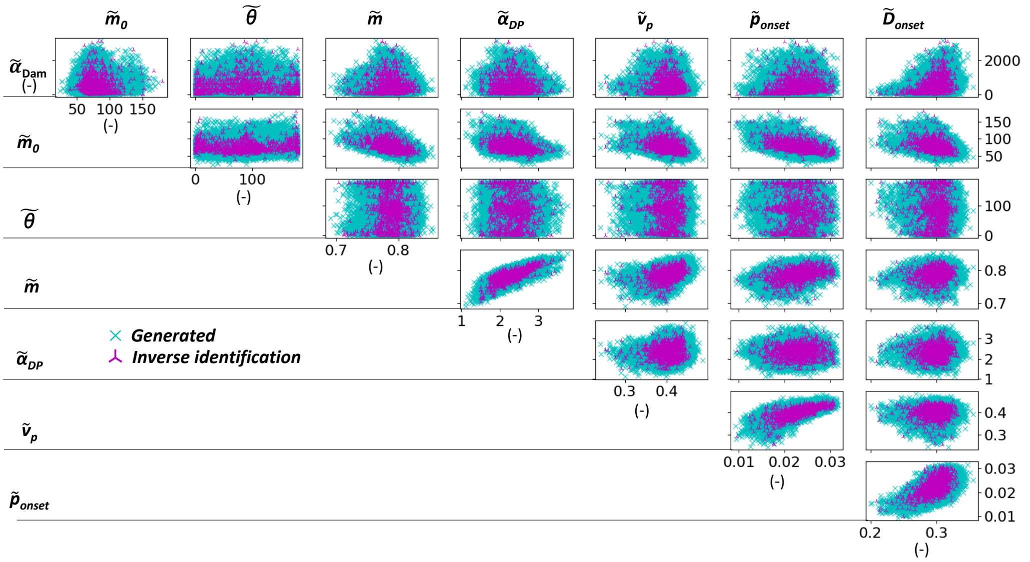

FIGURE 4.31: 25x25μm^2 effective random parameters distributions and their cross-dependence for the identified and generated $\tilde{m}_0, \tilde{\theta}, \tilde{m}, \tilde{\nu}_p, \tilde{\alpha}, \tilde{p}_{\mathrm{onset}}, \tilde{D}_{\mathrm{onset}}$ and $\tilde{\alpha}_{\mathrm{Dam}}$.

Figs. 4.30, 4.31 and 4.32 present a direct visual comparison between the generated data and the identified dataset. The number of needed realizations of the random vector $\boldsymbol{\beta}^D$ can vary with the application. The size of the studied geometry, or the number of desired stochastic simulations could increase or decrease the amount of needed realizations, meaning a larger set of realizations may be required. In this Work, a value of $n_{\mathrm{MC}} = 24$ was used in the generation of the new dataset for the $25 \times 25 \mu\mathrm{m}^2$ SVE case, meaning that a total of 24888 realizations are generated from the original dataset of 1037 SVE realizations. These plots show an excellent

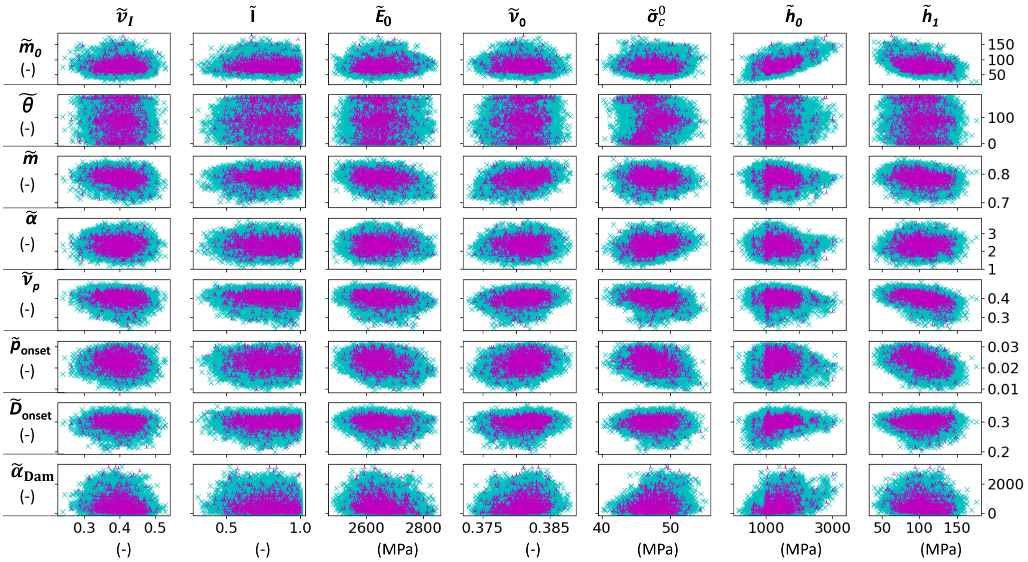

FIGURE 4.32: 25x25μm^2 effective random parameters distributions and their cross-dependence for the identified and generated $\tilde{v}_{\mathrm{I}}, \tilde{\mathrm{I}}, \tilde{\theta}, \tilde{E}_0, \tilde{\nu}_0, \tilde{\sigma}_y, \tilde{h}_0, \tilde{h}_1, \tilde{m}_0, \tilde{m}, \tilde{\nu}_p, \tilde{\alpha}, \tilde{p}_{\mathrm{onset}}$, $\widetilde{D}_{\mathrm{onset}}$ and $\tilde{\alpha}_{\mathrm{Dam}}$.

agreement between the identified and the generated distributions. Similar results were obtained for the $45 \times 45\mu\mathrm{m}^2$ SVE case, in which a value of $n_{\mathrm{MC}} = 29$ was used since less realizations were obtained from the full-field simulations, obtaining a total of 23287 realizations of the random vector $\boldsymbol{\beta}^D$.

As already observed with the distance correlation between the different effective random parameters, a cross-dependence between the different effective random parameters can be observed. It is worth mentioning the ability of the generator to successfully capture the different distributions of the different parameters. Similar results were obtained for the $45 \times 45\mu\mathrm{m}^2$ SVE, whose results are presented in Appendix C.3.

In addition to the previously presented distributions, let us obtain a more detailed view on the performance of the data-driven generator by focusing on probability density histograms of some of the parameters. To this end, Fig. 4.33 shows a direct comparison between the probability density histograms of the identified dataset and the generated data for some of the random material parameters. As it is possible to observe, this more precise comparison allows confirming the new data generated by the data-driven sampling method presents a good agreement with the identified distributions for the $25 \times 25\mu\mathrm{m}^2$ and the $25 \times 25\mu\mathrm{m}^2$ SVE cases.

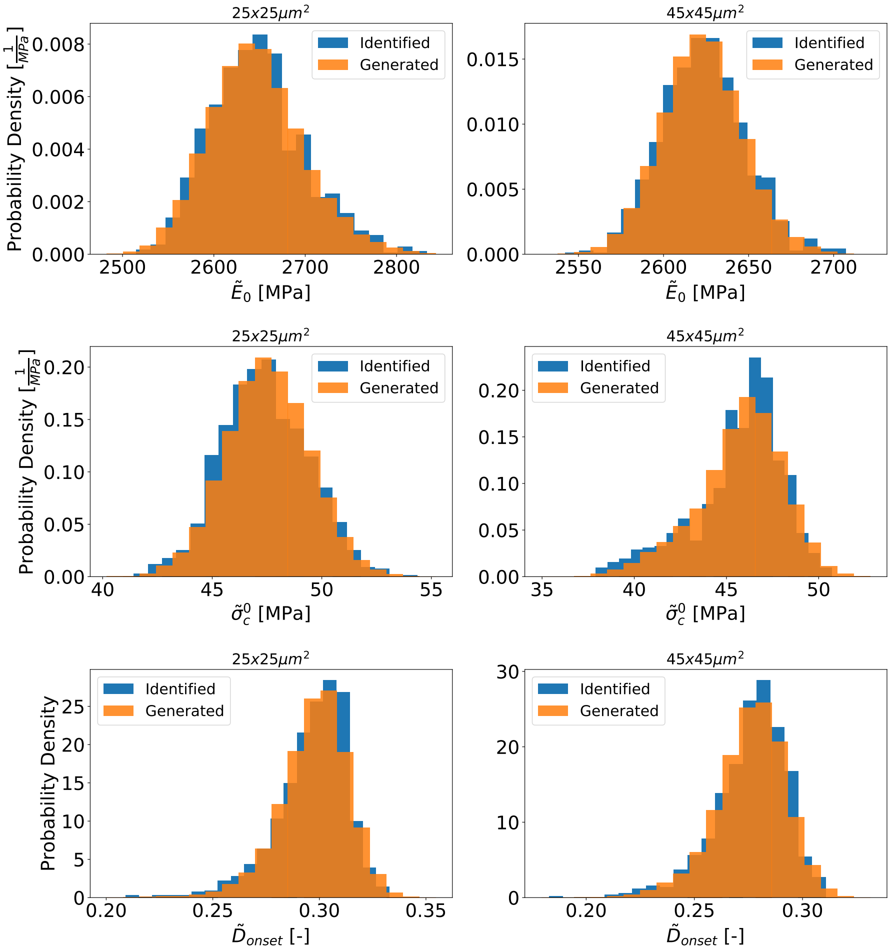

FIGURE 4.33: Direct comparison between the probability density histograms of the identified and generated $\tilde{E}_0, \tilde{\sigma}_c^0$ and $\tilde{D}_{\text{onset}}$ for the $25 \times 25\mu\text{m}^2$ (left) and $45 \times 45\mu\text{m}^2$ (right) SVE cases.

4.4 Application of the stochastic MF-ROM

Now that the dataset used to build the stochastic MF-ROM and the modeling strategy are presented, this section will directly test the performance of the ROM by comparing its results against full-field simulations and experimental results.

In order to test the consistency of the developed methodology, the two constructed MF-ROMs, one built with the $25 \times 25\mu\text{m}^2$ SVEs and the other built with the $45 \times 45\mu\text{m}^2$ SVEs are tested as input of the stochastic finite element simulations. As shown in Fig. 4.34, the random fields of the effective parameters, which are different realizations of the random vector $\boldsymbol{\beta}^D$, are discretized in squares with the same size as the SVEs used to construct the used MF-ROM, i.e. $25 \times 25\mu\text{m}^2$ or $45 \times 45\mu\text{m}^2$, determining the distribution of different effective random parameters on the integration points. Following the methodology developed in (Wu et al., 2018; Wu et al., 2019), due to the vanishing of the spatial correlation, the effective random parameters used at each random field discretization are independent of the parameters of adjacent squares. As in Wu et al. (2018) and Wu et al. (2019), smooth step functions are used at the random field discretization, avoiding possible artificial effects that could be introduced due to sharp changes in the material properties. The finite element discretization of the tested sample is performed with a mesh performed with quadratic elements whose characteristic size must be smaller than the random field discretization squares and the characteristic nonlocal length used in the MF-ROM

(Wu et al., 2019). The nonlocal equations governing the material at the ply level write:

$$\begin{cases} \boldsymbol{\nabla}_0 \cdot \bar{\boldsymbol{\sigma}} \left(\boldsymbol{\beta}^D(\boldsymbol{x}_{\text{ref}}), \boldsymbol{x}_{\text{ref}}\right) = 0 & \forall \boldsymbol{x}_{\text{ref}} \in \omega, \\ \breve{p}_0 - \boldsymbol{\nabla}_0 \cdot (\boldsymbol{c}_{\text{g}} \cdot \boldsymbol{\nabla}_0 \breve{p}_0) = p_0 & \forall \boldsymbol{x}_{\text{ref}} \in \omega. \end{cases} \tag{4.54}$$

At the ply level, the stress $\bar{\boldsymbol{\sigma}}$ is computed using the built MF-ROM. The resolution of this nonlocal MFH problem is detailed in Chapter 3.

This Section will start verifying the MF-ROM by applying it to the stochastic study of UD ply realizations under tensile loading. To this end, UD plies of $500 \times 250 \mu\text{m}^2$ will be tested by using the two constructed MF-ROMs, one built with the $25 \times 25\mu\text{m}^2$ SVEs and the other one with the $45 \times 45\mu\text{m}^2$ SVEs. Several UD ply realizations are tested under this loading condition in order to obtain a representative view of the MF-ROM performance. Then, this Section will end by validating the performance of the MF-ROM against real-life results. To this end, an experimental transverse compression test will be simulated, allowing not only to directly test the validity of the MF-ROM against the real behavior of the composite, but also to test the performance of the MF-ROM under multiple loading conditions.

4.4.1 UD ply under tensile loading

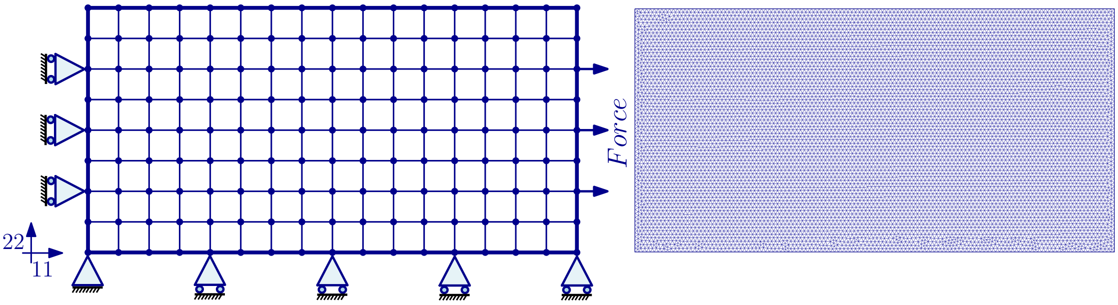

Figure 4.34: Boundary conditions and property discretization on the left and quadratic mesh used on the right.

In the tensile test, the sample will be stretched in the horizontal direction as shown in Fig. 4.34. Quadratic elements are used to discretize the sample with a size smaller than the squares used for the property discretization and smaller than the characteristic length, see Eq. (4.54), used in the nonlocal damage definition of the MFH. A convergence study with respect to the macroscale element size of the stochastic MF-ROM method is performed in Appendix C.4. It is shown that for elements of size lower than half of both the SVE size and the characteristic length l_c of the nonlocal MFH formulation, the predictions have converged.

The model is capable of capturing successfully the average response of the sample at all stages of loading as seen in Fig. 4.35. In this figure it can be seen how the stress variability in the solutions provided by the MF-ROM is able to represent the variability in the stress-strain curve that is observed when performing the full-field simulations.

It is also observed how the point at which the failure phase of the sample begins is correctly captured by the MF-ROM. However, it is worth noting the slightly stiffer behavior of the stochastic MFH simulations when reaching large strains. Enriching the damage modeling of the matrix by using more complex damage evolution laws that allow capturing more subtilities of the damage evolution of each SVE could help making the MF-ROM more accurate and able to find more complex behaviors of the material. The average runtimes of the ply analyses were respectively 5.3 hours and 124.4 hours on a i5 single processor for the stochastic simulation using the MF-ROM as surrogate and for the full-field simulation. In average, the ratio between both simulations is of 23.4 [-], demonstrating the interest of the method.

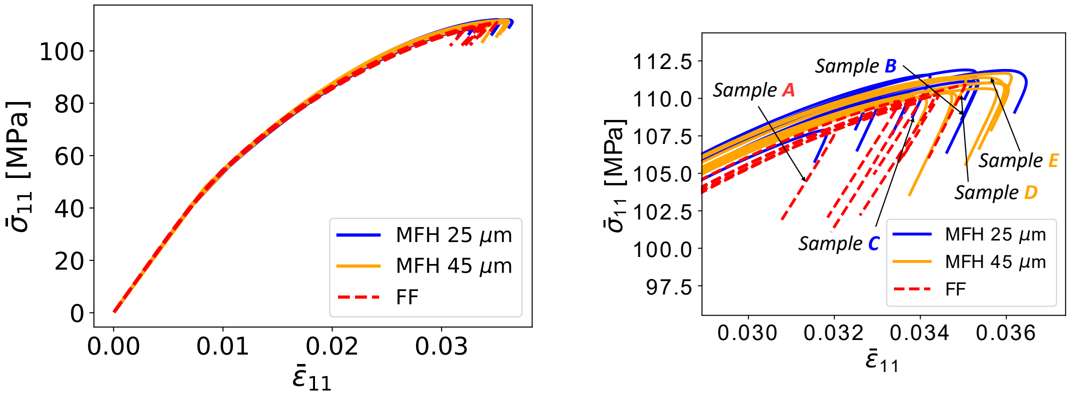

FIGURE 4.35: Ply stress-strain curves for samples using the $25 \times 25\mu\text{m}^2$ (MFH 25μm) and $45 \times 45\mu\text{m}^2$ (MFH 45μm) MF-ROM, and full-field simulations (FF).

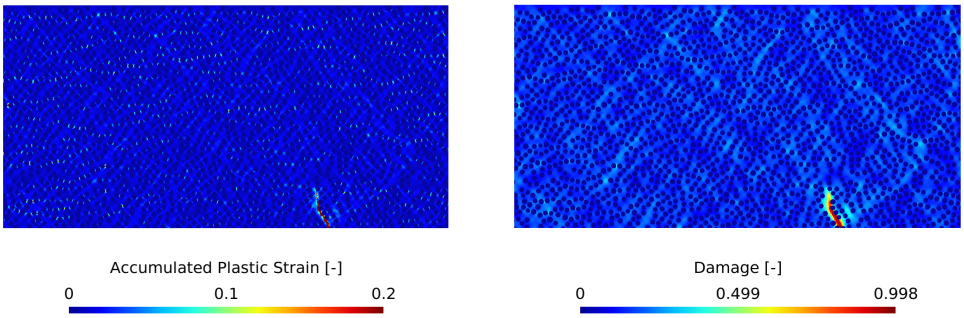

FIGURE 4.36: Accumulated plastic strain (left) and damage (right) field plots for the randomly picked full-field sample A whose response is reported in Fig. 4.35.

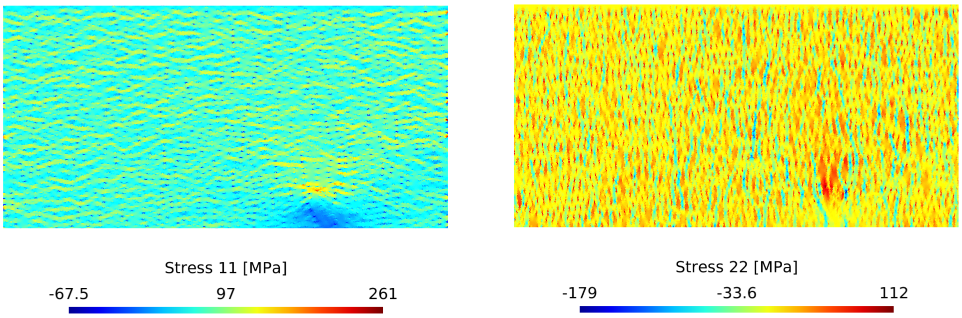

FIGURE 4.37: Stress 11 (left) and stress 22 (right) field plots for the randomly picked full-field sample A whose response is reported in Fig. 4.35.

Let us now discuss the resultant distribution of different quantities through field plots by considering four randomly picked samples (A, B, C, D and E) whose responses are represented in Fig. 4.35. The field plots obtained for the accumulated plastic strain, damage and stresses on the full-field sample A can be observed in Figs. 4.36 and 4.37. Figs. 4.38 and 4.39 show the obtained field distributions of the accumulated plastic strain, damage or stress for the picked $25 \times 25\mu\text{m}^2$ MF-ROM sample B. Figs. 4.40 and 4.41 allow comparing these results with another sample C using the $25 \times 25\mu\text{m}^2$ MF-ROM, and Figs. 4.42, 4.43, 4.44 and 4.45 shows the results obtained for the $45 \times 45\mu\text{m}^2$ MF-ROM samples D and E. The properties discretization can be easily observed, as quantities such as damage or the accumulated plastic strain show a uniform field inside each property sub-division of the sample.

In the accumulated plastic strain field plot, it is possible to observe shear bands emanating

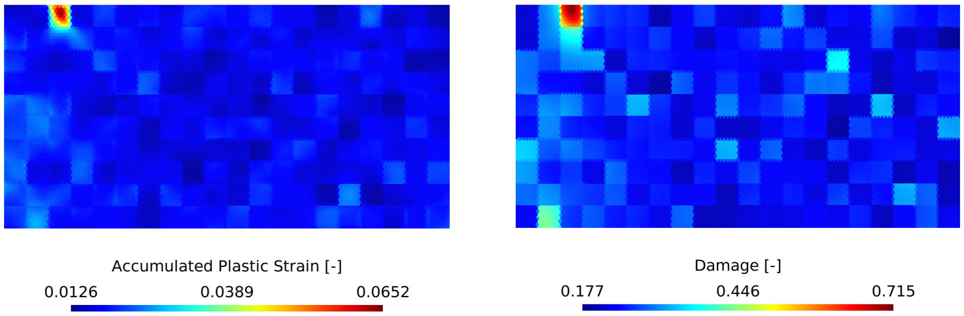

FIGURE 4.38: Accumulated plastic strain (left) and damage (right) field plots for the randomly picked $25 \times 25 \mu\mathrm{m}^2$ MF-ROM sample B whose response is reported in Fig. 4.35.

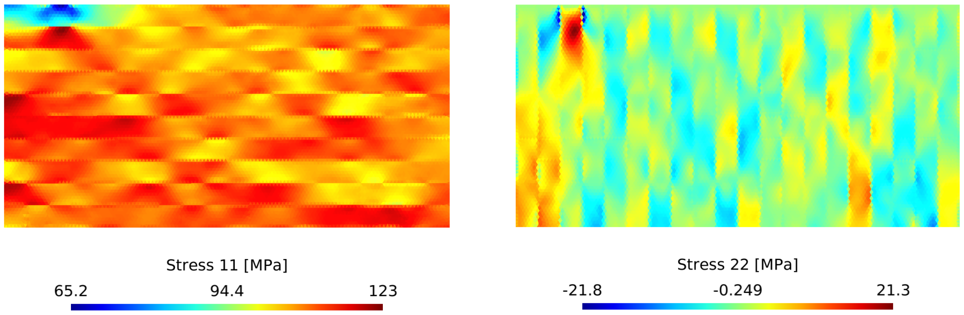

FIGURE 4.39: Stress 11 (left) and stress 22 (right) field plots for the random picked $25 \times 25 \mu\mathrm{m}^2$ MF-ROM sample B whose response is reported in Fig. 4.35.

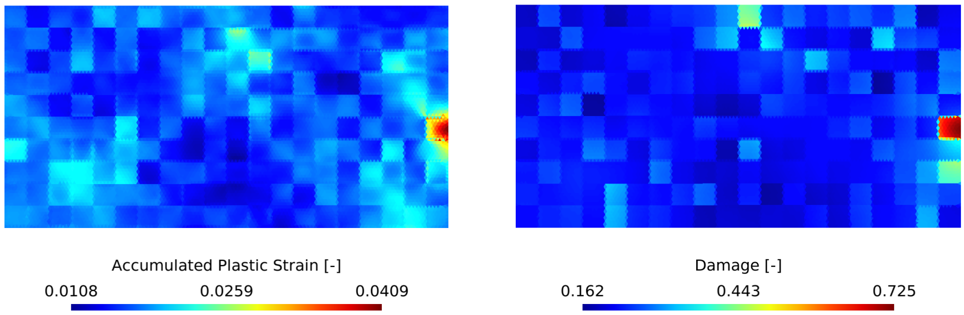

FIGURE 4.40: Accumulated plastic strain (left) and damage (right) field plots for the randomly picked $25 \times 25 \mu\mathrm{m}^2$ MF-ROM sample C whose response is reported in Fig. 4.35.

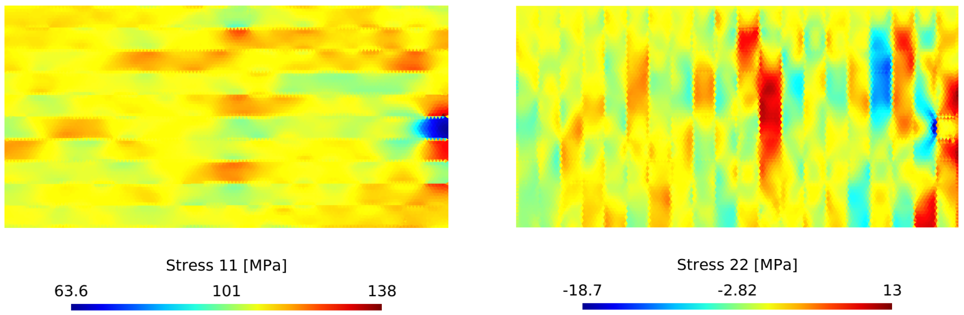

FIGURE 4.41: Stress 11 (left) and stress 22 (right) field plots for the randomly picked $25 \times 25 \mu\mathrm{m}^2$ MF-ROM sample C whose response is reported in Fig. 4.35.

from the location with the highest damage. This behavior can also be observed in the full-field simulations presented in Fig. 4.36. These bands are also seen in the damage field plots, see

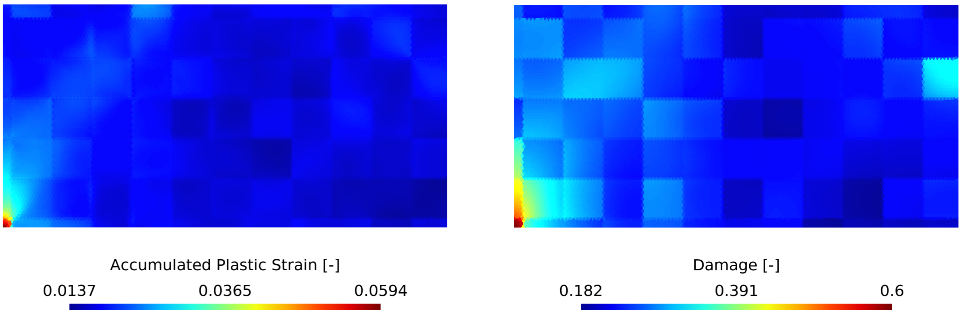

FIGURE 4.42: Accumulated plastic strain (left) and damage (right) field plots for the randomly picked $45 \times 45 \mu m^2$ MF-ROM sample D whose response is reported in Fig. 4.35.

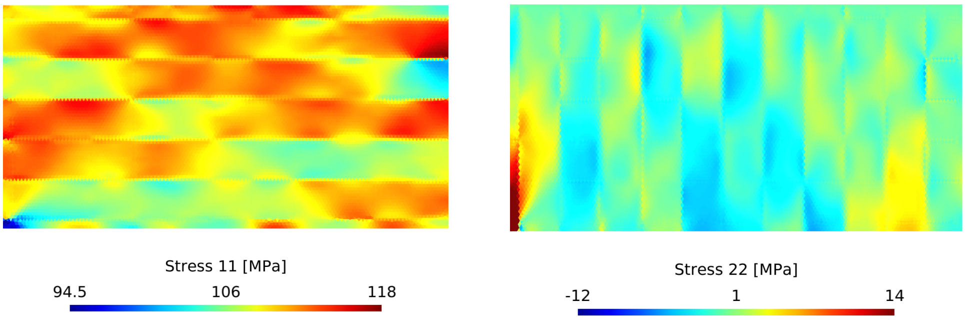

FIGURE 4.43: Stress 11 (left) and stress 22 (right) field plots for the randomly picked $45 \times 45 \mu m^2$ MF-ROM sample D whose response is reported in Fig. 4.35.

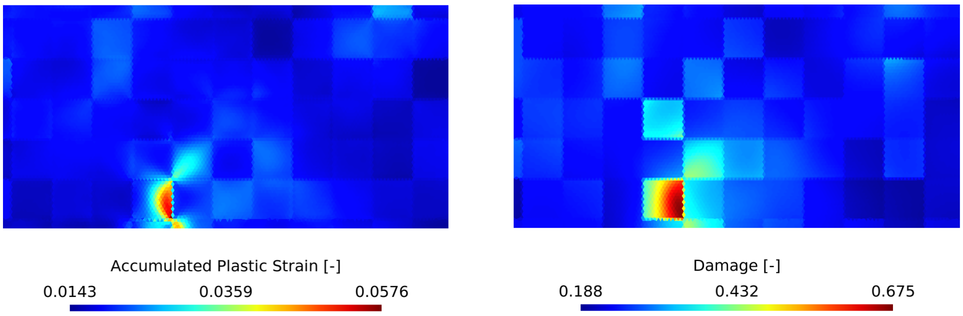

FIGURE 4.44: Accumulated plastic strain (left) and damage (right) field plots for the randomly picked $45 \times 45 \mu m^2$ MF-ROM sample E whose response is reported in Fig. 4.35.

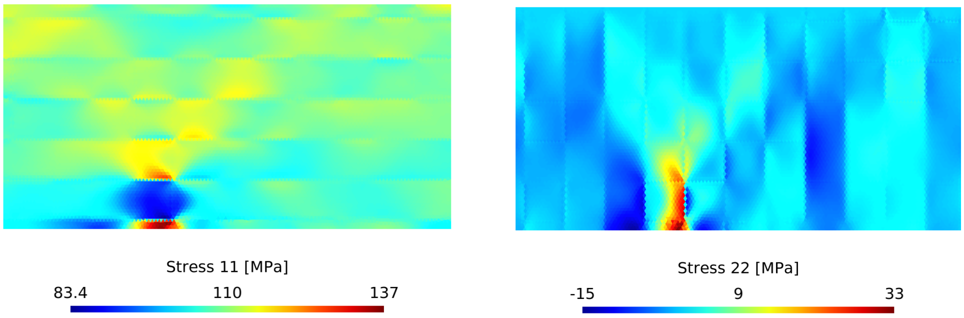

FIGURE 4.45: Stress 11 (left) and stress 22 (right) field plots for the randomly picked $45 \times 45 \mu m^2$ MF-ROM sample E whose response is reported in Fig. 4.35.

Figs. 4.38, 4.40 and 4.42, as the faster evolution of the plastic-strain causes a faster development of the damage. A strong localization of the damage can be seen in the stress graphs once the failure onset is reached. When looking at the component in the loading direction of the stress (Stress 11), the location in which one can find the highest damage suffers an abrupt decrease in its loading state, which provokes a high stress localization in its boundaries. Similarly, the high accumulated plastic strain and damage have a clear effect on the component 22 of the stress, which sees a sudden change in the localization zone and its surroundings.

Looking at Fig. 4.37, it is possible to observe a clear horizontal or vertical pattern in the stresses, depending whether the component 11 or 22 is studied. This effect is well captured by both MF-ROMs ($25 \times 25 \mu\text{m}^2$ and $45 \times 45 \mu\text{m}^2$) as shown by Figs. 4.39, 4.41 and 4.43. Focusing on the results obtained with the MF-ROM constructed from the $25 \times 25 \mu\text{m}^2$ and $45 \times 45 \mu\text{m}^2$ SVE realizations, it is possible to conclude that the methodology shows a good consistency on both cases, being both MF-ROMs capable of providing good predictions of the UD composite ply sample response up to its complete failure, where the model satisfactorily captures how the geometrical variabilities found at the microstructure level affect the failure characteristics of the sample.

4.4.2 Experimental compression test

In this Section, the MF-ROM will be tested against real life experiment results. For this purpose, the considered test is the same as the one used in Section 3.5. This time, the MF-ROM developed in this Chapter will permit to model the transverse compression test performed in the work by Chevalier, Camanho, and Pardoen (2019) accounting for the geometrical variabilities that can be found in these kind of specimens. In this Work, the transverse compression test is performed on a $10 \times 10 \times 10$ mm^3 cubic sample as shown in Fig. 4.46. In order to reduce the computational cost of the simulation, a 2D square sample of 10×10 mm^2 divided into two differentiated regions is used. As shown in Fig. 4.46, the 2D sample is divided into an inner and an outer region. As it was observed in the experimental results (Chevalier, Camanho, and Pardoen, 2019), the starting failure mechanism consists on a tensile stress driven failure at the center of the specimen, followed by a transition to shear failure. Therefore, numerical setup must be able to provide a good representation of the damage evolution in this inner region in order to correctly capture the failure mechanism of the sample. The inner part of the 2D geometry used for the test is meshed with quadratic triangular elements with a characteristic mesh length of 20μm and the behavior will be modeled with the developed stochastic MF-ROM. The outer part will be modeled with a deterministic MFH model with a characteristic mesh length of 200μm, meaning a coarser mesh can be used. For this region, the properties used correspond to realizations of fiber volume fractions close to the average of 40%. This division of the tested sample allows not only to reduce the computational cost of the simulation while retaining the ability to capture the starting failure mechanism, but also to mitigate the effect of the boundary conditions on the failure characteristics of the sample. Two different boundary conditions will be tested in order to represent two limit cases. First, a no-slip condition is tested, in which the upper and lower edges will be constrained along the horizontal direction (see Fig. 4.46). Then, a perfect slip test in which these constrains are removed is performed. Due to the impossibility to accurately model the real friction effect at the top and lower boundaries of the tested sample, these two conditions will allow us to obtain two limit cases, knowing the experimental conditions remain in between these two conditions. For this test, the MF-ROM built from 25×25 μm^2 SVEs is used.

As in the experimental test by Chevalier, Camanho, and Pardoen (2019), an average of 40% fiber volume fraction is used, and as in Section 3.5, the Young's modulus is corrected in order to account for the viscous effect seen on the real experiment.

Looking at the averaged behavior results shown in Fig. 4.47, we can observe how the behavior of the composite sample under these loading conditions is capable of correctly capturing the behavior observed in the real experiment, correctly capturing the minimum stress reached during the test. Looking at the blocked edges BC (where the no-slip condition is applied to the upper

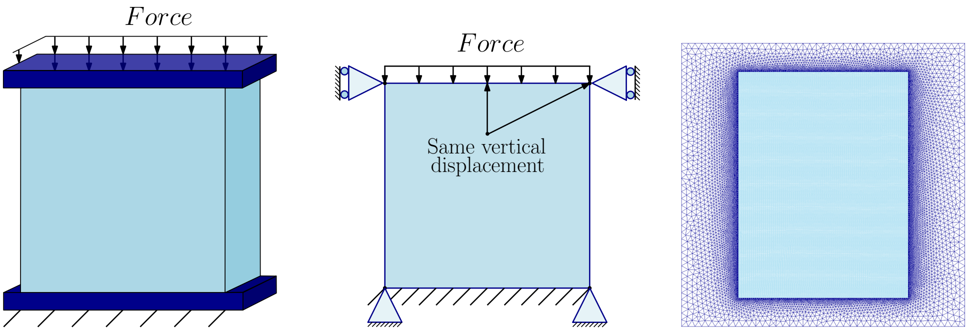

FIGURE 4.46: Schematic representation of the experimental setup built in Chevalier, Camanho, and Pardoen (2019) on the left, blocked case boundary conditions in the middle and second-order mesh with inner and outer regions on the right.

and lower edges), a stiffer behavior compared to the experiment is obtained. This is due to the stronger constraints introduced by the no-slip condition at the edges of the sample. Similarly, this stronger constraint yields a sooner fracture of the sample compared to the experiment results. In contrast, as expected, the free edges condition (BC in which the horizontal constraint is removed from the top and lower edges) yields a softer behavior and a later failure of the sample. As anticipated, the results obtained with both boundary conditions represent two limit cases, in which the experimental results yield between both results.

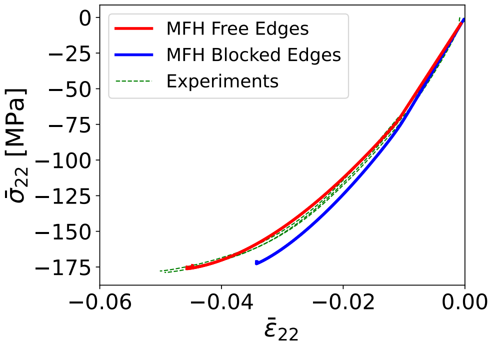

FIGURE 4.47: Stress-strain curve comparison between the MFH results and the experimental results obtained in Chevalier, Camanho, and Pardoen (2019) for a true strain rate of -10^{-4} s^{-1}.

As expected, a lower variability to the one observed in the previous ply stochastic study is observed due to the much larger size of the studied sample, size at which one obtains a representative response of the composite behavior. The use of the stochastic MF-ROM in the inner part of the sample allows to observe a variability in the damage evolution characteristics of each realization, as well as a slight variability in the elastic and nonlinear responses of the studied sample. Let us analyze the contour plots obtained from these simulations. First, Fig. 4.48 shows images from the real experiment results and a damage contour plot of the result obtained with a deterministic MFH at the dawn of failure in the test performed by Calleja Vázquez et al. (2022). Then, Figs. 4.49-4.51 show the field plots for the stress, the accumulated plastic strain and the damage evolution state at the start of the failure of the sample realizations under the blocked edges BC. Fig. 4.52 shows the damage field plots obtained with the two samples tested with the free edges BC. All the shown results are extracted at the starting of the failure stage, meaning the tensile stress driven failure observed at the center of the specimen can be observed to be developing.

The effect of the MF-ROM used in the inner part of the sample can be observed in the field plots of the stress and the accumulated plastic strain. However, the most interesting comparison can be seen in the damage field plots. As it is presented, the damage contour plot at the beginning

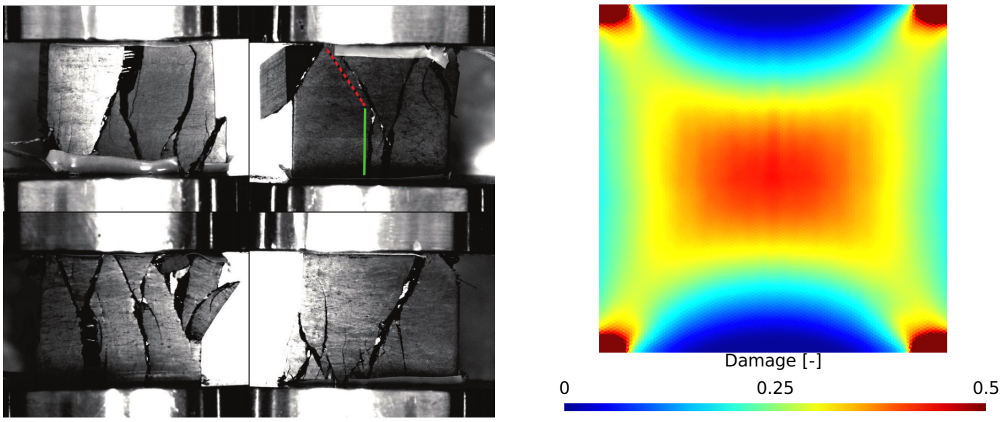

FIGURE 4.48: Surfaces of the cubic UD specimens after failure as shown in Chevalier, Camanho, and Pardoen (2019) on the left: the green and red lines emphasize the transition between a tensile stress dominated crack propagation to a shear one. Reprinted from Composite Structures, 209, J. Chevalier and P.P. Camanho and F. Lani and T. Pardoen, Multi-scale characterization and modelling of the transverse compression response of unidirectional carbon fiber reinforced epoxy, 160-176, Copyright (2019), with permission from Elsevier. Damage [-] contour plot of the deterministic multiscale MFH simulation with blocked upper and lower edges on the right.

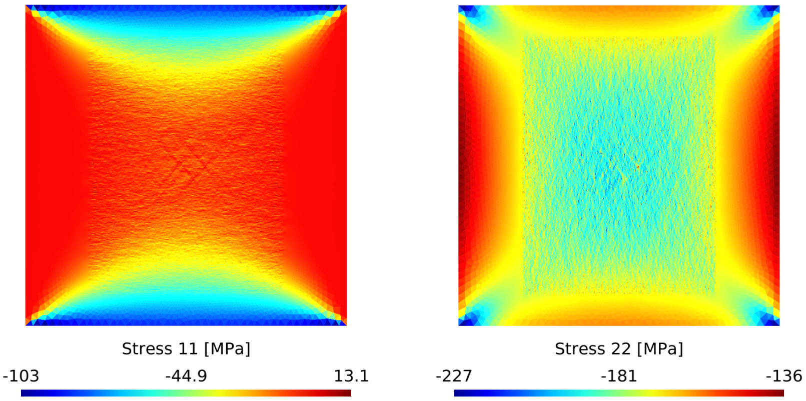

FIGURE 4.49: Stress 11 (left) and Stress 22 (right) field plots of realization A with constrained upper and lower edge.

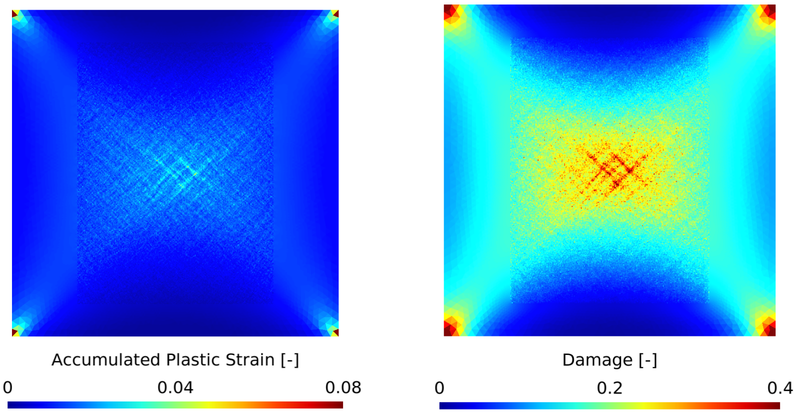

FIGURE 4.50: Accumulated plastic strain (left) and damage (right) field plots of realization A with constrained upper and lower edge.

of the failure stage, presented a smooth and very uniform distribution over the sample when using the deterministic material law (see Fig. 4.48), being possible to observe the concentration

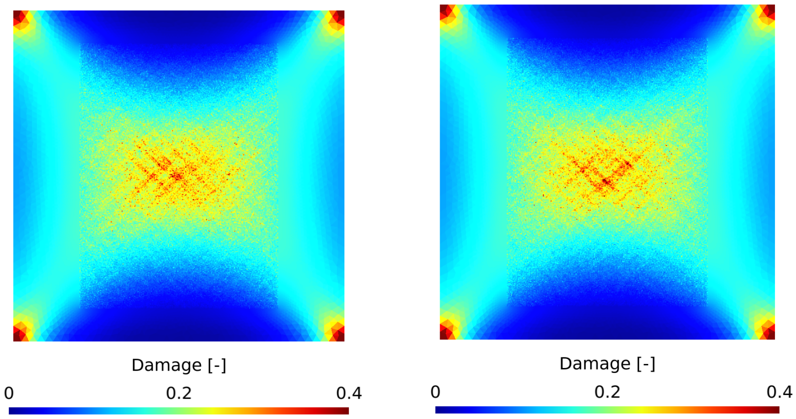

FIGURE 4.51: Damage field plots of realization B (left) and realization C (right) with constrained upper and lower edge.

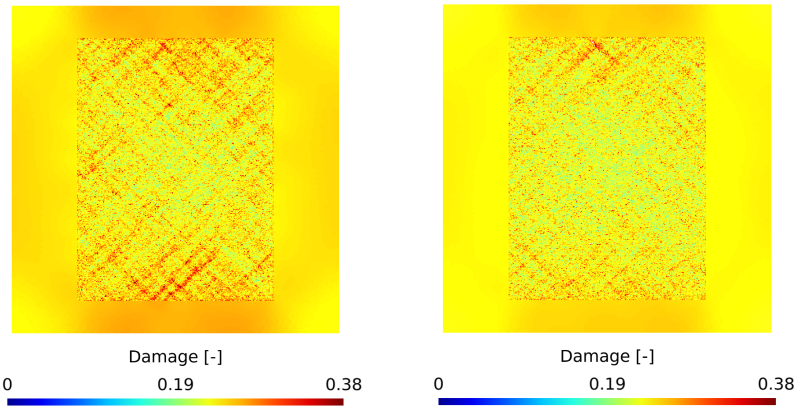

FIGURE 4.52: Damage field plots of realization D (left) and realization E (right) with slip conditions on upper and lower edge.

of damage at the center of the sample due to the tensile stress driven failure. Similar results are observed on the new stochastic results. However, these present a much complex distribution and a different behavior for each realization (see Figs. 4.49-4.52). Damage evolution can also be observed at the corners of the sample; however this is a result of the no-slip boundary condition used in the numerical setup. This is thought to be one of the main causes for the sooner failure observed with this boundary condition. As shown in Fig. 4.52, the free edges BC does not present this problem, allowing the material to undergo larger strains before failing.

4.5 Summary

The goal of this Chapter is to build a stochastic MF-ROM capable of capturing the pressure-dependent nonlinear behavior of two-phase UD composite materials with epoxy matrix, which remains valid after the strain-softening onset. In order to generate the stochastic MF-ROM, the information extracted from full-field SVE realizations is used as input of an inverse identification process that allows obtaining the effective random properties of a micromechanical MFH surrogate. The homogenized stress-strain responses and the damaged elastic tensor of the SVE realizations serve as input for this identification process. However, these quantities do not remain valid once the strain-softening onset is reached. Once this stage is reached, a loss of size objectivity is encountered, meaning that a new objective value that allows to recover it is needed. In this Work, the critical energy release rate is used as the target value that would allow this recovery of the size objectivity. By identifying the MFH surrogate parameters allowing to recover the same critical energy release rate as the one extracted from the full-field simulation, it is possible to correctly capture the behavior of each SVE up to its complete failure. Providing the model with the ability to maintain the size objectivity over the entire response of the material allows the uncertainties encountered in the material microstructure to be upscaled to the macroscale, making it possible to analyze the effect of these geometrical uncertainties in the failure characteristics of a material.

This stochastic MF-ROM paves the way for efficient stochastic virtual testing of composite materials by using an incremental-secant mean-field homogenization scheme as its basis. Two different SVE sizes are tested in the construction of the MF-ROM, being possible to study its impact in the performance of the stochastic simulations. The developed identification process is able to correctly capture the behavior of the studied SVEs under multiple loading conditions up to their complete failure. The identified parameters for each SVE represent a realization of a matrix of random vectors, which is used as the input of a data-driven-process that allows to obtain proper random fields by generating new data with the same statistical properties as the input matrix. The generated data obtained with this data-driven process show a good representation of not only the distribution of each random parameter, but also an accurate representation of the relation between them. We however note that for an identified set of parameters, the MF-ROM predictions show more discrepancies with the corresponding SVE model when loading under shearing, for which the use of periodic boundary condition under damage is debatable. To reduce this error, different loading modes should be considered in the future during the identification process as well as more parameters of the MF-ROM, for example by considering different hardening laws in tension and compression. The more complex identification would then have to be conducted through unsupervised learning to account for several loading cases altogether, for example using a Bayesian inference (BI) process as in Wu et al. (2020b).

Finally, the performance of the stochastic MF-ROM is verified against full-field simulations and real-life experiments. First, multiple UD plies under tensile loading are tested using successively full-field and the MF-ROM representations. The field distribution plots show how the MF-ROM models constructed with the two property discretizations ($25\times25\mu\text{m}^2$ and $45\times45\mu\text{m}^2$) are able to capture the overall patterns observed in the full-field simulations for quantities such as the stresses, the damage evolution or the accumulated plastic strain. It is possible to observe a correct representation of the ply response for both MF-ROMs, obtaining a good variability of the responses at low and medium strains and being able to capture the failure point of the samples. Secondly, a transverse compression test experiment was virtually modeled with the developed MF-ROM built from the $25 \times 25\mu\text{m}^2$ SVE realizations. Two different boundary conditions were used on the edges of the sample in order to test two limit cases (fully blocked upper and lower edges, simulating an infinite friction between the machine and the tested sample; and free upper and lower edges, simulating an idealized zero-friction condition). The obtained results show the ability of the methodology to capture the effects of the microscale variabilities into the macroscale response of the tested sample, confirming the good accuracy of the MF-ROM. This MF-ROM methodology allows for a high flexibility, making it easy to adapt it to other kinds of materials or to enrich the model with more complex evolution laws. This high flexibility mixed with the promising obtained results and the intrinsic advantages of the incremental-secant formulation, allow to confirm this stochastic reduced-order model as a basis for future works.

4.6 Data availabilities

The raw/processed data required to reproduce these findings are available under the Creative Commons Attribution 4.0 International (CC BY 4.0) license (Calleja Vázquez et al., 2023).

Chapter 5

Conclusion and future perspectives

This Thesis focuses on the modeling of polymeric matrix composites. Polymers are materials consisting of large molecules made of repeating units called monomers. This kind of material presents many advantages that make them widely used in multiple fields. Their durability and resistance to corrosion make them suitable for harsh environments and long-term uses. They are easy to process and to use, reducing the production time and costs, and thanks to their flexible nature, they can be easily molded. One of the most interesting aspects of these materials is the ability to give answer to multiple physical, chemical, electrical, or even biological needs thanks to their wide range of possible properties depending on the requirements of each application. These large horizons of possibilities, while making these materials highly attractive for their applicability to very diverse fields, represent a challenge to the scientific and industrial communities, which try to correctly capture their behavior in the virtual world. This Thesis provides new tools to further pave the way for a more efficient framework to virtually test polymer-based materials such epoxy-matrix composite materials.

In the pursue of a better representation of polymer-based materials, one of the first steps is the efficient and accurate modeling of polymers. These materials present viscous and highly nonlinear behaviors, meaning commonly used viscoelastic constitutive models, such as the generalized Kelvin (Zhang and Moore, 1997) and Maxwell (Reese and Govindjee, 1998; Buhan and Frey, 2011; Takagi et al., 2008) models, along with other well-known models like the Schapery (Haj-Ali and Muliana, 2004; Zhang et al., 2022) or fractional (Schiessel et al., 1995; Hajikarimi et al., 2022) models, are often found to be inadequate for the accurate simulation of polymers. Only complex constitutive models addressing rate-dependent elasticity and plasticity, softening, and failure stages are capable of representing the behavior of these materials under a wide range of loading conditions. This Thesis focuses on three main ingredients to improve the efficient modeling of the polymeric matrix composites. First, the viscoelastic response of an existing large strain polymer model is enhanced to permit the correct modeling of the behavior of highly nonlinear polymers. Then, this model is used as a basis for the development of a pressure dependent incremental-secant MFH model, permitting an accurate and efficient way of simulating these materials. Finally, this MFH model allows to develop an efficient stochastic MF-ROM that paves the way for the stochastic virtual testing of this kind of materials.

5.1 Polymer model

The complex behavior of glassy polymers was addressed by Van Dung Nguyen and his team (Nguyen et al., 2016) through a large strain nonlocal damaged-enhanced pressure-dependent viscoelastic-viscoplastic constitutive model, a model based on a multimechanism nonlocal damage continuum. The model has shown significant potential in replicating real epoxy materials, such as the high-crosslinked RTM6 epoxy resin, due to the incorporation of pressure-dependency. This model is based on hyperelastic large strain framework capable of capturing rate-dependent elastic behavior of the material. However, as presented through the literature review of this Work, some hyperelastic polymers exhibit an elastic stiffening at large strains (Srivastava, Chester, and Anand, 2010), making this model not valid for this application.

Chapter 2 enhances this model with the introduction of new strain dependent bulk and shear moduli stiffening terms, allowing the correct modeling of this nonlinear elastic behavior. The new enhanced generalized Maxwell model is used to capture the nonlinear viscoelastic behavior at small strains. Once the material reaches its viscoelastic limit, the viscoplastic region ensues. The viscoelastic limit is defined by an enhanced Drucker-Prager pressure-sensitive yield function. Viscoplasticity is modeled by non-associated pressure-dependent plasticity. To this end, a non-associated Perzyna-type with a quadratic flow potential is used to capture the volumetric deformation during the plastic process. As discussed in the literature review, a multi-stage damage evolution is characteristic of these kinds of materials. This behavior is captured within a continuum damage mechanics approach via the contribution of two different damage internal scalars. To avoid the loss of solution uniqueness, a nonlocal implicit gradient formulation is used for both internal variables, resulting in a multi-mechanism nonlocal damage continuum. The two internal damage scalars that compose the damage modeling of the material are:

- Softening: The first contribution is taken into account by the softening damage variable. This scalar evolves according to a saturation law, which models the post-peak softening. Once the softening variable is saturated, the model is capable of capturing the rehardening stage, as the isotropic and kinematic hardening phenomena continue to develop.
- Failure: Then, once the material reaches its failure onset, the second internal scalar starts developing. The failure onset is determined by a pressure-dependent failure criterion, after which the failure damage variable controls the failure stage of the material up to complete failure.

The new ability of the model to capture viscoelastic hardening behaviors was tested against isothermal experimental tests of the semicrystalline PCL76-4MAL/FUR 3 wt%CNT shape memory polymer. These tests clearly showed the efficiency of the new enhanced model to improve modeling of polymer materials showing this characteristic elastic stiffening. With the introduction of the bulk and shear moduli stiffening terms, the model presents a better basis for the modeling of highly-nonlinear polymers under isothermal conditions and opens the door to new applications, such as the modeling of one-way and two-way shape memory effects. The ability of this model to capture the elastic stiffening of some SMPs makes it a perfect candidate for a finite strain phenomenological model of semi-crystalline polymers under thermo-mechanical loading. As shown in the research carried out by Liege University (Gulasik et al., 2023), such finite strain phenomenological model is able to yield close results to the ones obtained during an experimental test campaign and for one and two-way shape memory effects.

5.2 MFH

While the model developed in Chapter 2 permits a complete and accurate modeling of the behavior of polymers, its direct use in the modeling of composite materials with epoxy matrices represents a challenge. The complex microstructure makes the use of direct numerical simulations unfeasible due to the high computational cost. For this reason, the scientific community has worked over the years on new homogenization techniques (Doghri et al., 2011; Yvonnet, Monteiro, and He, 2013; Wu et al., 2012; Kanouté et al., 2009; Geers, Kouznetsova, and Brekeclmans, 2010; Llorca et al., 2011; Nemat-Nasser and Hori, 2013; Noels, Wu, and Adam, 2016). Homogenization allows to retain the composite constituents behavior while avoiding the need of resolving all the details of the complex microstructure. One methodology is the incremental-secant approach. This mean field homogenization method was developed by Wu et al. (Wu et al., 2013c; Wu et al., 2013a) by considering J2 plasticity in the different phases, meaning this approach was only valid for pressure insensitive materials. Chapter 3 takes the model developed in Chapter 2 and uses it as a basis of a new, possibly damage-enhanced, pressure-dependent based incremental-secant mean-field homogenization (MFH) scheme for two-phase composites. The incremental-secant formulation consists on a fictitious unloading of the composite material up to a stress-free state, in which a residual stress is attained in its phases. The secant method allows then to compute the mean stress fields of each phase at the next step after a virtual reloading of the material. One of the main advantages of the incremental-secant method presented in the works by L. Wu et al. (Wu et al., 2013c; Wu et al., 2013a), was the natural isotropicity of the secant tensors that allows defining the linear-comparison-composite (LCC). In this Work, it was shown how this isotropic nature is preserved for the case of a non-associated pressure dependent plastic flow, making possible the direct definition of the LCC without the need of the isotropization step that is commonly required in other formulations. This new pressure-dependent incremental-secant MFH model is thus able to represent the physics of real polymeric composites.

The homogenization efficiency was tested against full-field simulations in several cases, including cyclic and non-proportional loading involving perfectly elastic phases, elasto-plastic and damage-enhanced elasto-plastic phases in random representative volume elements (RVE) of unidirectional (UD) composites and of composites reinforced with spherical inclusions. Finally, the model was tested against an experimental test, in which the model showed its capabilities to represent real-life composite behaviors.

5.3 Stochastic MF-ROM

While the pressure-dependent mean-field homogenization model allows the reduction of the computational time burden that the large strain nonlocal full-field simulations represent by several orders of magnitude, this model is not able to capture the inherent uncertainty introduced by the complex microstructure of these composite materials. The complexity of the microstructure of composite materials poses a significant challenge for industries that have recently adopted their use. These industries often require a detailed analysis of the material properties for certification, which typically involves a long test campaign. This expensive process can be significantly reduced through virtual testing without the necessity for long and costly testing campaigns.

Several approaches have been developed over the years to circumvent this burden through stochastic simulations, but the introduction of nonlinearity and failure in these proved to be challenging. Wu et al. developed a stochastic nonlinear micromechanics model that acts as a mesoscale surrogate model for UD composite materials. This surrogate model was then utilized as input for a stochastic finite element method (SFEM) analysis. The microscale geometric information was derived from scanning electron microscope (SEM) images of actual UD composite materials. This information was subsequently used to construct synthetic microstructures or statistical volume elements (SVEs) of any size and quantity. This model showed great capabilities capturing the effect introduced by the geometrical uncertainties. However, the model was not able to capture the pressure-dependent behavior or the failure of the matrix that composes these materials.

This Thesis presents the construction of a mean-field homogenization (MFH) surrogate for nonlinear stochastic multiscale analyses of two-phase composites that allows the material response to be studied up to its failure. To this end, the homogenized stochastic behavior of the studied unidirectional composite material was first characterized through full-field simulations on stochastic volume elements of the material microstructure, for which the model presented in Chapter 2 was used, permitting to capture the effect of the microstructural geometric uncertainties on the material response. Then, in order to conduct the stochastic nonlinear multiscale simulations, the microscale problem was substituted by a pressure-dependent MFH reduced order micromechanical model based on the model developed in Chapter 3, that is, a MF-ROM, whose properties are identified by an inverse process from the full-field SVE realizations. This Work presents a new inverse identification process that allows to capture the full behavior of the SVE. While the homogenized stress-strain curves can be used for the identification process of the nonlinear range, a calibration of the energy release rate obtained with a nonlocal MFH micromechanical model was implemented to circumvent the loss of size objectivity encountered after the strain softening onset. This novelty permits to scale the variability found on each SVE failure characteristics to the macroscale.

The random effective properties obtained by performing the identification process were then used as input of the data-driven stochastic model to generate the complete random fields used to feed the stochastic MF-ROM. To show the consistency of the methodology, two MF-ROMs constructed from SVEs of two different sizes ($25 \times 25 \mu\mathrm{m}^2$ and $45 \times 45 \mu\mathrm{m}^2$) were studied. The built MF-ROMs were tested against full-field simulations and an experimental test. First, several UD plies under tensile loading were simulated using full-field simulations and the MF-ROMs constructed from the full-field SVEs. The results showed very promising results, being the MF-ROM simulations able to capture the overall patterns observed in the full-field simulations for quantities such as the stresses, the damage evolution or the accumulated plastic strain, and good correlation between the full-field and MF-ROM simulations was found in the averaged responses of the UD composite plies. Secondly, the performance of the new developed MF-ROM built from the $25 \times 25 \mu\mathrm{m}^2$ SVE realizations was tested against a transverse compression test experiment. The results showed the ability of the new constructed MF-ROM to capture the effects of the microscale variabilities into the macroscale response of the tested sample, confirming the good accuracy of the MF-ROM.

5.4 Perspectives

This thesis had as objective to pave the way for more polyvalent, affordable, and accurate modeling of polymer composite materials. This was successfully achieved thanks to the key novelties introduced in the large strain polymer model, the newly developed MFH model and the MF-ROM constructed upon it. The simplicity, modularity and flexibility of the developed approaches were always paramount during the development of this Thesis in order to facilitate future tasks to improve and complete the models presented here. This Section will provide the reader some guidance of the main potential improvements that could benefit from the work carried out during this Thesis:

- In the present Work, even though the damage is modeled through the contribution of a softening and a failure damage evolution laws, both are used to compute the damage variable, meaning a single scalar damage model was used for the large-strain polymer model and the small-strain based implementation used for the MFH approach. It was shown in the works by V.D. Nguyen et al. (Nguyen et al., 2016; Nguyen, Wu, and Noels, 2019), a single that a single scalar damage model is capable of accurately capturing the failure response of the RTM6 under multiple tests including failure for 3D test with barreling effect using the base model of the here enhanced large-strain polymer constitutive model. The same principle was chosen for the matrix modeling of the here developed MFH model, where the response at the composite level inherits from the homogenization scheme. When only the polymer phase is considered, as it is the case for the large-strain polymer model and the MFH model, the models developed in the literature consider scalar damage, most of the time a single damage scale parameter. Even for the specific case of polymer matrix composite materials, single scalar damage variables formulated in a Lemaitre-Chaboche style yield successful results as in the case of Nguyen et al. (2016) or Montesano et al. (2013). An accurate representation of the damage was never the main focus of this Thesis, but just a showcase of the capability of the developed models to account for damage on the polymer phase. In future works, more complex damage evolution laws could further improve the modeling capabilities of the different models, especially for MFH, where a simple damage evolution law was chosen for the sake of simplicity. The introduction of damage approaches other than the Lemaitre-Chaboche, as well as the introduction of more damage scalars permitting the modeling of more complex damage behaviors could also be studied in future works.

- The modeling of the pressure-dependency of materials with a Drucker-Prager yield criterion mixed with a non-associated plastic flow is a quite widespread approach in the research community (see as example the works by Li and Tang (2005), Chevalier, Camanho, and Pardoen (2019) or Lee et al. (2021)) thanks to the accurate results it is able to reach. However, while most models consider the pressure and equivalent stress in a similar approach as the one used in this work, this is not the only widely used model to capture this kind of behavior as pointed out in this Thesis (Raghava, Caddell, and Yeh, 1973; Balieu et al., 2013; Balieu et al., 2014; Gao et al., 2011; Roscoe and Burland, 1968; Islam and Gnanendran, 2020). The implementation of new plastic potentials, testing with other yield surfaces or the introduction of new enhancements could be studied in future works, which could help continuing improving the capabilities and accuracy of the large-strain polymer model and the MFH composite model.

- Another point to enrich future models is the MFH surrogate model used for the MF-ROM. Currently, a constant ratio between the compressive and tensile hardening was taken into account $\hat{H}_c/\widetilde{H}_t = \tilde{m}$. This assumption has been used in this Work to be able to represent realistic behaviors while not shifting the focus of the thesis from the capturing of the material failure. A variable ratio between the tensile and compressive hardening could be introduced in future works, as it could help to obtain more accurate material behaviors, allowing the model to better represent the homogenized material under a wider range of loads. However, this would be at the expense of an added complexity to the developed MF-ROM methodology, as the amount of required parameters and the complexity of the identification steps would increase.

- The implementation of the MFH in this Work focused on the modeling of uni-directional composites. However, this model could be used in the modeling of more complex materials such as woven composites. MFH blocks made of equivalent fibers of different orientations and aspect ratio values could be combined following the approach presented in Wu, Adam, and Noels (2021),where the reduced order model parameters for pseudo-grains number and micro-structural features, including orientation, aspect ratio, and volume fraction, are identified using the deep material network (DMN) approach. This data-driven approach developed by Liu et al. (Liu, Wu, and Koishi, 2019; Liu and Wu, 2019; Liu, 2020) is based on analytical micro-mechanics models, and uses mechanistic building blocks organized in a binary hierarchical topological structure to define the microstructure. As in the work by Wu, Adam, and Noels (2021), the pressure-dependent MFH could be used in the mechanistic building blocks of the woven composite material, reducing the needed number of building blocks and improving the accuracy of the model.

- Another approach used for the two-step homogenization of woven composites is the clustering analysis based homogenization (CAH). As an example of applicability of the MFH method, in the work by Spilker et al. (2023), the homogenized behavior of the woven unit cell was computed using TFA. In this publication, the fact that the composite yarn material could be treated as a piecewise uniform UD fiber composite per subdomain was exploited to make use of the MFH method to compute their homogenized nonlinear behavior during the online stage. The use of the MFH for micro to mesoscopic scale bridging allowed the consideration of arbitrary plastic responses of the phases of the yarns microstructure and loading conditions. A new procedure could be developed using the MFH model developed in this Thesis, where the eigenstrains of the subdomains would be deduced from the homogenized response computed by the pressure-dependent MFH.

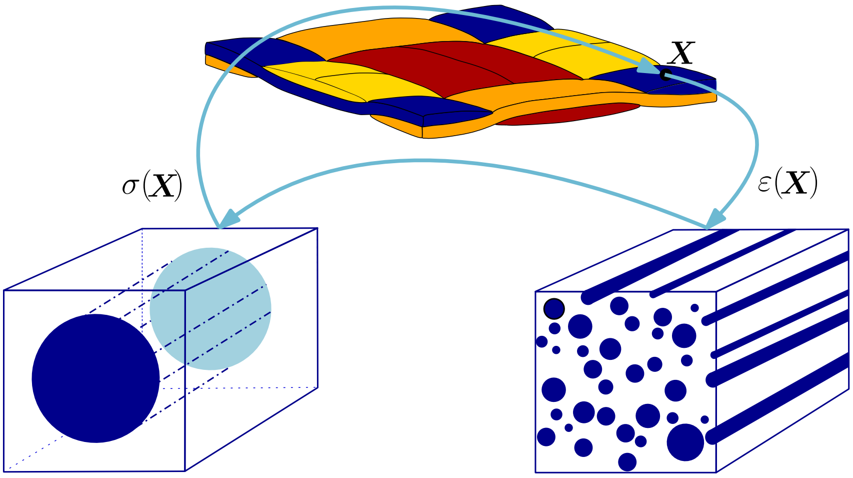

FIGURE 5.1: Schematic representation of woven cell yarns homogenization for two-step homogenization of woven composites.

- The high flexibility of the developed MFH surrogate translated directly into an equal flexibility of the stochastic MF-ROM method. This high modularity together with the promising results obtained makes it an ideal basis for future works. As previously mentioned, the use of new hardening or damage evolution laws in the MFH surrogate used to build the stochastic model could be taken into account in the identification steps and the parameters of the MF-ROM, allowing to capture different behaviors or to improve the accuracy of the model. In addition, the use of different loading modes can be considered during the identification process in order to reduce the error found when loading the material in different conditions to the used in the identification process. However, this would imply, on the one hand to increase the number of parameters of the MF-ROM –for example by considering different hardening laws in tension and compression, and on the other hand to consider unsupervised learning for the parameters identification to account for several loading cases altogether –for example using a Bayesian inference (BI) process as in the work by Wu et al. (2020b).

Nowadays data-driven ROMs seems to be gaining interest in the research community. One has to bear in mind that MF-ROM represents a semi-analytical approach that relies on some assumptions and approximations and therefore may not be valid for complex non-linear behaviors or microstructures, while data-driven ROMs are nowadays able to capture complex and non-linear responses. However, MF-ROMs are computationally efficient and, because of their micro-mechanical foundation, requires a much smaller data-set to build than data-driven ROMs. MF-ROMs therefore avoid the large amount of data required for training and validation of data-driven ROMs, which is costly and time-consuming to generate.

It is therefore possible to conclude that no single ROM approach represents the optimal method for stochastic multi-scale analyzes, as this statement depends on the specific problem, the available data, and the desired accuracy. In future works, an increasing interest in the development of hybrid methods could be observed, allowing to combine different approaches, and extracting the best characteristics of each approach. The development of MF based ROMs is therefore still relevant and important for the future development of material ROMs.

As exposed, flexibility and modularity have been paramount throughout the entire process of this Thesis, allowing future research projects to work upon the developed models. As author of this Work, I firmly believe this Thesis can serve as a solid starting step to develop mode accurate and complete models that mimic the real behavior of polymer-based materials in an efficient way.

Appendix A

Appendix related to Chapter 2

A.1 Derivatives of the extended yield surface

The first derivative to be computed is $\frac{\partial \bar{F}}{\partial \Delta p}$. Using Eq. (2.105), we obtain:

$$\frac{\partial \bar{F}}{\partial \Delta p} = H_2 \left(\frac{((\boldsymbol{\phi}^{\mathrm{tr}})^{\mathrm{dev}} + \Delta(\hat{\boldsymbol{\tau}}_c)^{\mathrm{dev}})^{\mathrm{eq}}}{u} \right)^{\alpha} - H_1 \frac{\hat{\phi}^{\mathrm{tr}} + \Delta(\frac{1}{3}\,\mathrm{tr}\,\hat{\boldsymbol{\tau}}_c)}{v} - H_0, \tag{A.1}$$

where:

$$H_2 = \frac{\partial a_2}{\partial \Delta p} = -\frac{\alpha}{\sigma_c^{\alpha+1}} H_c, \tag{A.2}$$

$$H_1 = \frac{\partial a_1}{\partial \Delta p} = \frac{3}{\sigma_c} \left[\frac{\alpha m^{\alpha-1}}{m+1} - \frac{m^{\alpha}-1}{(m+1)^2} \right] \frac{H_t \sigma_c - H_c \sigma_t}{\sigma_c^2} - 3 \frac{m^{\alpha}-1}{m+1} \frac{H_c}{\sigma_c^2}, \tag{A.3}$$

and

$$H_0 = \frac{\partial a_0}{\partial \Delta p} = \frac{\left(\alpha m^{\alpha-1} + 1\right)(m+1) - m^{\alpha} - m}{(m+1)^2} \frac{H_t \sigma_c - H_c \sigma_t}{\sigma_c^2}. \tag{A.4}$$

Then, in order to compute $\frac{\partial \Delta p}{\partial \Gamma}$ let us develop the expression of the equivalent plastic deformation increment ($\Delta p = p - p_n$). Using Eq. (2.101) and applying the correction, the plastic deformation increment writes:

$$\Delta p = k \Gamma A = k \Gamma \sqrt{\underbrace{6 \left(\frac{((\boldsymbol{\phi}^{\mathrm{tr}})^{\mathrm{dev}} + \Delta(\hat{\boldsymbol{\tau}}_c)^{\mathrm{dev}})^{\mathrm{eq}}}{u} \right)^2 + \frac{4}{3}\beta^2 \left(\frac{\hat{\phi}^{\mathrm{tr}} + \Delta(\frac{1}{3}\,\mathrm{tr}\,\hat{\boldsymbol{\tau}}_c)}{v} \right)^2}_{\mathcal{Z}}}. \tag{A.5}$$

Its partial derivative with respect to Γ is then written as:

$$\frac{\partial \Delta p}{\partial \Gamma} = k \left(A + \Gamma \frac{\partial A}{\partial \Gamma} \right), \tag{A.6}$$

where:

$$\frac{\partial A}{\partial \Gamma} = \frac{1}{2A} \frac{\partial \mathcal{Z}}{\partial \Gamma}. \tag{A.7}$$

The derivative $\frac{\partial \mathcal{Z}}{\partial \Gamma}$ writes:

$$\begin{aligned}\frac{\partial \mathcal{Z}}{\partial \Gamma} = & -\frac{72\breve{\mu}\left[((\boldsymbol{\phi}^{\mathrm{tr}})^{\mathrm{dev}} + \Delta(\hat{\boldsymbol{\tau}}_c)^{\mathrm{dev}})^{\mathrm{eq}}\right]^2}{u^3} - \frac{16\beta^3\breve{\kappa}\left(\hat{\phi}^{\mathrm{tr}} + \Delta(\frac{1}{3}\,\mathrm{tr}\,\hat{\boldsymbol{\tau}}_c)\right)^2}{3v^3} \\ & + \frac{8\beta^2(\hat{\phi}^{\mathrm{tr}} + \Delta(\frac{1}{3}\,\mathrm{tr}\,\hat{\boldsymbol{\tau}}_c))}{3v^2}\frac{\partial(\frac{1}{3}\,\mathrm{tr}\,\hat{\boldsymbol{\tau}}_c)}{\partial\Gamma} + \frac{18}{u^2}((\boldsymbol{\phi}^{\mathrm{tr}})^{\mathrm{dev}} + \Delta(\hat{\boldsymbol{\tau}}_c)^{\mathrm{dev}}) : \frac{\partial(\hat{\boldsymbol{\tau}}_c)^{\mathrm{dev}}}{\partial\Gamma},\end{aligned} \tag{A.8}$$

where $\frac{\partial(\hat{\boldsymbol{\tau}}_c)^{\mathrm{dev}}}{\partial\Gamma}$ and $\frac{\partial(\frac{1}{3}\,\mathrm{tr}\,\hat{\boldsymbol{\tau}}_c)}{\partial\Gamma}$ are given in Appendix A.

Finally, using Eq. (2.105), the derivative $\frac{\partial \bar{F}}{\partial\Gamma}$ can be computed as:

$$\frac{\partial \bar{F}}{\partial\Gamma} = \frac{\partial}{\partial\Gamma}\left[\underbrace{a_2\left(\frac{((\boldsymbol{\phi}^{\mathrm{tr}})^{\mathrm{dev}} + \Delta(\hat{\boldsymbol{\tau}}_c)^{\mathrm{dev}})^{\mathrm{eq}}}{u}\right)^{\alpha}}_{\mathbf{1}^{\star}} \underbrace{-a_1\frac{\hat{\phi}^{\mathrm{tr}} + \Delta(\frac{1}{3}\,\mathrm{tr}\,\hat{\boldsymbol{\tau}}_c)}{v}}_{\mathbf{2}^{\star}} - \underbrace{a_0}_{\mathbf{3}^{\star}} - \underbrace{\left(\eta\frac{\Gamma}{\Delta t}\right)^{\gamma}}_{\mathbf{4}^{\star}}\right]. \tag{A.9}$$

The first two terms follow from:

$$\begin{aligned}\frac{\partial \mathbf{1}^{\star}}{\partial\Gamma} = & \frac{a_2\alpha}{u^2}\left(\frac{((\boldsymbol{\phi}^{\mathrm{tr}})^{\mathrm{dev}} + \Delta(\hat{\boldsymbol{\tau}}_c)^{\mathrm{dev}})^{\mathrm{eq}}}{u}\right)^{\alpha-1}\left[u\frac{\partial((\boldsymbol{\phi}^{\mathrm{tr}})^{\mathrm{dev}} + \Delta(\hat{\boldsymbol{\tau}}_c)^{\mathrm{dev}})^{\mathrm{eq}}}{\partial\Gamma} - ((\boldsymbol{\phi}^{\mathrm{tr}})^{\mathrm{dev}} + \Delta(\hat{\boldsymbol{\tau}}_c)^{\mathrm{dev}})^{\mathrm{eq}}\frac{\partial u}{\partial\Gamma}\right] \\ = & -a_2\left(\frac{((\boldsymbol{\phi}^{\mathrm{tr}})^{\mathrm{dev}} + \Delta(\hat{\boldsymbol{\tau}}_c)^{\mathrm{dev}})^{\mathrm{eq}}}{u}\right)^{\alpha}\frac{6\alpha\breve{\mu}}{u} + \frac{3a_2\alpha}{2u^2}\left(\frac{((\boldsymbol{\phi}^{\mathrm{tr}})^{\mathrm{dev}} + \Delta(\hat{\boldsymbol{\tau}}_c)^{\mathrm{dev}})^{\mathrm{eq}}}{u}\right)^{\alpha-2} \\ & ((\boldsymbol{\phi}^{\mathrm{tr}})^{\mathrm{dev}} + \Delta(\hat{\boldsymbol{\tau}}_c)^{\mathrm{dev}}) : \frac{\partial(\hat{\boldsymbol{\tau}}_c)^{\mathrm{dev}}}{\partial\Gamma},\end{aligned} \tag{A.10}$$

$$\begin{aligned}\frac{\partial \mathbf{2}^{\star}}{\partial\Gamma} = & \frac{a_1 2\beta\breve{\kappa}(\hat{\phi}^{\mathrm{tr}} + \Delta(\frac{1}{3}\,\mathrm{tr}\,\hat{\boldsymbol{\tau}}_c))}{v^2} - \frac{a_1}{v}\frac{\partial\Delta(\frac{1}{3}\,\mathrm{tr}\,\hat{\boldsymbol{\tau}}_c)}{\partial\Gamma} \\ = & a_1\left(\frac{\hat{\phi}^{\mathrm{tr}} + \Delta(\frac{1}{3}\,\mathrm{tr}\,\hat{\boldsymbol{\tau}}_c)}{v}\right)\frac{2\beta\breve{\kappa}}{v} - \frac{a_1}{v}\frac{\partial(\frac{1}{3}\,\mathrm{tr}\,\hat{\boldsymbol{\tau}}_c)}{\partial\Gamma},\end{aligned} \tag{A.11}$$

where $\frac{\partial(\hat{\boldsymbol{\tau}}_c)^{\mathrm{dev}}}{\partial\Gamma}$ and $\frac{\partial(\frac{1}{3}\,\mathrm{tr}\,\hat{\boldsymbol{\tau}}_c)}{\partial\Gamma}$ are given in Appendix A.2.

The last two term follow from:

$$\frac{\partial \mathbf{3}^{\star}}{\partial\Gamma} = 0, \tag{A.12}$$

$$\frac{\partial \mathbf{4}^{\star}}{\partial\Gamma} = -\gamma\Gamma^{\gamma-1}\left(\frac{\eta}{\Delta t}\right)^{\gamma}. \tag{A.13}$$

A.2 Derivatives of the corrector terms

First, let us obtain the derivative of $\hat{\boldsymbol{\tau}}_c^{\mathrm{dev}}$, which is described in Eq. (2.88). As $\mathbf{Q}$ depends also on Γ, this derivative writes:

$$\begin{aligned}\frac{\partial(\hat{\boldsymbol{\tau}}_c)^{\mathrm{dev}}}{\partial\Gamma} = & 2\hat{\mu}_{\infty}\mathbf{f}'_{\mu}(\mathbf{E}^{\mathrm{ve\,tr}} - \Gamma\mathbf{Q})^{\mathrm{dev}} : \frac{\partial(\mathbf{E}^{\mathrm{ve}})^{\mathrm{dev}}}{\partial\Gamma}(\mathbf{E}^{\mathrm{ve\,tr}} - \Gamma\mathbf{Q})^{\mathrm{dev}} \\ & + 2\hat{\mu}_{\infty}f_{\mu}(\mathbf{E}^{\mathrm{ve\,tr}} - \Gamma\mathbf{Q})^{\mathrm{dev}}\frac{\partial(\mathbf{E}^{\mathrm{ve}})^{\mathrm{dev}}}{\partial\Gamma},\end{aligned} \tag{A.14}$$

where $\mathbf{f}_{\mu}$ and $\mathbf{f}'_{\mu}$ are given in Eqs. (2.31) and (2.114) respectively. By using the definition of the corrected normal (2.100), one has:

$$(\mathbf{E}^{\mathrm{ve}})^{\mathrm{dev}} = (\mathbf{E}^{\mathrm{ve\,tr}})^{\mathrm{dev}} - 3\Gamma\frac{(\boldsymbol{\phi}^{\mathrm{tr}})^{\mathrm{dev}} + \Delta(\hat{\boldsymbol{\tau}}_c)^{\mathrm{dev}}}{u}. \tag{A.15}$$

The derivative $\frac{\partial(\mathbf{E}^{\mathrm{ve}})^{\mathrm{dev}}}{\partial\Gamma}$ therefore writes:

$$\frac{\partial(\mathbf{E}^{\mathrm{ve}})^{\mathrm{dev}}}{\partial\Gamma} = -\frac{3((\boldsymbol{\phi}^{\mathrm{tr}})^{\mathrm{dev}} + \Delta(\hat{\boldsymbol{\tau}}_c)^{\mathrm{dev}}) + 3u\Gamma\frac{\partial(\hat{\boldsymbol{\tau}}_c)^{\mathrm{dev}}}{\partial\Gamma}}{u^2}. \tag{A.16}$$

Let us then write the system of equations in a compact way to compute the derivative (A.14):

$$\begin{aligned}&\left[\boldsymbol{I} + \frac{6\Gamma}{u}\hat{\mu}_\infty\left[(\mathbf{E}^{\mathrm{ve\,tr}} - \Gamma\mathbf{Q})^{\mathrm{dev}}\otimes\mathbf{f}'_\mu + f_\mu\boldsymbol{I}\right]\right] : \frac{\partial(\hat{\boldsymbol{\tau}}_c)^{\mathrm{dev}}}{\partial\Gamma} = \\ &-\left[\frac{6}{u^2}\hat{\mu}_\infty\left[(\mathbf{E}^{\mathrm{ve\,tr}} - \Gamma\mathbf{Q})^{\mathrm{dev}}\otimes\mathbf{f}'_\mu + f_\mu\boldsymbol{I}\right]\right] : ((\boldsymbol{\phi}^{\mathrm{tr}})^{\mathrm{dev}} + \Delta(\hat{\boldsymbol{\tau}}_c)^{\mathrm{dev}}),\end{aligned} \tag{A.17}$$

where $\boldsymbol{I}$ stands for the fourth order identity tensor, yielding the solution $\frac{\partial(\hat{\boldsymbol{\tau}}_c)^{\mathrm{dev}}}{\partial\Gamma}$.

Similarly starting from Eq. (2.110), for the volumetric term one has:

$$\frac{\partial(\frac{1}{3}\operatorname{tr}\hat{\boldsymbol{\tau}}_c)}{\partial\Gamma} = \hat{\kappa}_\infty f'_\kappa(\operatorname{tr}(\mathbf{E}^{\mathrm{ve\,tr}} - \Gamma\mathbf{Q}))\operatorname{tr}(\mathbf{E}^{\mathrm{ve\,tr}} - \Gamma\mathbf{Q})\frac{\partial\operatorname{tr}\mathbf{E}^{\mathrm{ve}}}{\partial\Gamma} + \hat{\kappa}_\infty f_\kappa(\operatorname{tr}(\mathbf{E}^{\mathrm{ve\,tr}} - \Gamma\mathbf{Q}))\frac{\partial\operatorname{tr}\mathbf{E}^{\mathrm{ve}}}{\partial\Gamma}, \tag{A.18}$$

where f'_κ and f_κ are given in Eqs. (2.110) and (2.31). Finally, using Eq. (2.100), $\operatorname{tr}\mathbf{E}^{\mathrm{ve}}$ writes:

$$\operatorname{tr}\mathbf{E}^{\mathrm{ve}} = \operatorname{tr}\mathbf{E}^{\mathrm{ve\,tr}} - \frac{2\beta\Gamma}{v}\left(\hat{\phi}^{\mathrm{tr}} + \Delta(\frac{1}{3}\operatorname{tr}\hat{\boldsymbol{\tau}}_c)\right), \tag{A.19}$$

being possible to compute the derivative:

$$\frac{\partial\operatorname{tr}\mathbf{E}^{\mathrm{ve}}}{\partial\Gamma} = -\frac{2\beta}{v^2}\left(\hat{\phi}^{\mathrm{tr}} + \Delta(\frac{1}{3}\operatorname{tr}\hat{\boldsymbol{\tau}}_c) + \Gamma v\frac{\partial\Delta(\frac{1}{3}\operatorname{tr}\hat{\boldsymbol{\tau}}_c)}{\partial\Gamma}\right). \tag{A.20}$$

Finally, it is possible to obtain derivative $\frac{\partial(\frac{1}{3}\operatorname{tr}\hat{\boldsymbol{\tau}}_c)}{\partial\Gamma}$ as:

$$\frac{\partial(\frac{1}{3}\operatorname{tr}\hat{\boldsymbol{\tau}}_c)}{\partial\Gamma} = -\frac{2\beta\hat{\kappa}_\infty}{v^2}\frac{(f'_\kappa\operatorname{tr}(\mathbf{E}^{\mathrm{ve\,tr}} - \Gamma\mathbf{Q}) + f_\kappa)\left(\hat{\phi}^{\mathrm{tr}} + \Delta(\frac{1}{3}\operatorname{tr}\hat{\boldsymbol{\tau}}_c)\right)}{1 + \frac{2\beta\Gamma}{v}\hat{\kappa}_\infty(f'_\kappa\operatorname{tr}(\mathbf{E}^{\mathrm{ve\,tr}} - \Gamma\mathbf{Q}) + f_\kappa)}. \tag{A.21}$$

A.3 Tangent operator

A.3.1 Derivation of the tangent operator

In order to complete the definition of the effective tangent operator $\hat{\mathbf{L}}$, Eq. (2.115), it is necessary to compute the derivatives with respect to $\mathbf{F}$. Having that $\mathbf{F}^{\mathrm{ve}} = \mathbf{F}\cdot\mathbf{F}^{\mathrm{vp}^{-1}}$, one has:

$$\frac{\partial\mathbf{F}^{\mathrm{ve}}}{\partial\mathbf{F}} = (\mathbf{1}\otimes\mathbf{1})^2\cdot\mathbf{F}^{\mathrm{vp}^{-1}} + \mathbf{F}\cdot\frac{\partial\mathbf{F}^{\mathrm{vp}^{-1}}}{\partial\mathbf{F}}, \tag{A.22}$$

where:

$$\frac{\partial\mathbf{F}^{\mathrm{vp}^{-1}}}{\partial\mathbf{F}} = -\mathbf{F}^{\mathrm{vp}^{-1}}\cdot\frac{\partial\mathbf{F}^{\mathrm{vp}}}{\partial\mathbf{F}}{}_2\cdot\mathbf{F}^{\mathrm{vp}^{-1}}. \tag{A.23}$$

The derivatives $\frac{\partial \mathbf{S}^{\mathrm{ve}}}{\partial \mathbf{F}}$ and $\frac{\partial \mathbf{F}^{\mathrm{vp}}}{\partial \partial \mathbf{F}}$ are still required to complete the computation of $\hat{\mathbf{L}}$. Knowing the right Cauchy strain tensor writes $\mathbf{C} = \mathbf{F}^{\mathrm{ve\,pr}^T}$, and making use of its symmetrical nature, it is possible to write:

$$\frac{\partial \bullet}{\partial \mathbf{F}} = \frac{\partial \bullet}{\partial \mathbf{C}} : \frac{\partial \mathbf{C}}{\partial \mathbf{F}} = 2 \frac{\partial \bullet}{\partial \mathbf{C}} : {}^4\mathbf{F}^T, \tag{A.24}$$

where $\bullet$ represents an arbitrary tensor field. The predictor values $\mathbf{F}^{\mathrm{ve\,tr}}$ and $\mathbf{C}^{\mathrm{ve\,tr}}$ can be written as:

$$\mathbf{F}^{\mathrm{ve\,tr}} = \mathbf{F} \cdot \mathbf{F}_n^{\mathrm{vp}^{-1}}, \tag{A.25}$$

and:

$$\mathbf{C}^{\mathrm{ve\,tr}} = \mathbf{F}_n^{\mathrm{vp}^{-T}} \cdot \mathbf{C} \cdot \mathbf{F}_n^{\mathrm{vp}^{-1}}, \tag{A.26}$$

which allows to define the derivative of an arbitrary tensor field with respect to $\mathbf{C}$ as:

$$\frac{\partial \bullet}{\partial \mathbf{C}} = \mathbf{F}_n^{\mathrm{vp}^{-1}} \cdot \frac{\partial \bullet}{\partial \mathbf{C}^{\mathrm{ve\,tr}}} \cdot \mathbf{F}_n^{\mathrm{vp}^{-T}}. \tag{A.27}$$

The material operator can thus be expressed in terms of the derivatives with respect to $\mathbf{C}^{\mathrm{ve\,tr}}$.

A.3.2 Derivatives w.r.t. predictor strain

Dividing the corotational Kirchhoff predictor stress into its volumetric and deviatoric parts, the derivative of its volumetric part with respect to the predictor strain writes:

$$\frac{\partial(\frac{1}{3}\operatorname{tr}\hat{\boldsymbol{\tau}}^{\mathrm{tr}})}{\partial \mathbf{C}^{\mathrm{ve\,tr}}} = \frac{\partial(\frac{1}{3}\operatorname{tr}\hat{\boldsymbol{\tau}}_0^{\mathrm{tr}})}{\partial \mathbf{E}^{\mathrm{ve\,tr}}} : \frac{\partial \mathbf{E}^{\mathrm{ve\,tr}}}{\partial \mathbf{C}^{\mathrm{ve\,tr}}} + \frac{\partial(\frac{1}{3}\operatorname{tr}\hat{\boldsymbol{\tau}}_c^{\mathrm{tr}})}{\partial \mathbf{E}^{\mathrm{ve\,tr}}} : \frac{\partial \mathbf{E}^{\mathrm{ve\,tr}}}{\partial \mathbf{C}^{\mathrm{ve\,tr}}} = \frac{\kappa_e}{2}\mathbf{1} : \mathcal{L}^{\mathrm{tr}} + \frac{\partial(\frac{1}{3}\operatorname{tr}\hat{\boldsymbol{\tau}}_c^{\mathrm{tr}})}{\partial \mathbf{C}^{\mathrm{ve\,tr}}}, \tag{A.28}$$

where $\mathcal{L}^{\mathrm{tr}}$ writes:

$$\mathcal{L}^{\mathrm{tr}} = \left.\frac{\partial \ln \mathbf{C}^{\mathrm{ve}}}{\partial \mathbf{C}^{\mathrm{ve}}}\right|_{\mathbf{C}^{\mathrm{ve\,tr}}}, \tag{A.29}$$

and where the derivative $\frac{\partial(\frac{1}{3}\operatorname{tr}\hat{\boldsymbol{\tau}}_c^{\mathrm{tr}})}{\partial \mathbf{C}^{\mathrm{ve\,tr}}}$ yields:

$$\frac{\partial(\frac{1}{3}\operatorname{tr}\hat{\boldsymbol{\tau}}_c^{\mathrm{tr}})}{\partial \mathbf{C}^{\mathrm{ve\,tr}}} = \frac{\hat{\kappa}_\infty}{2}\left[f_\kappa + f'_\kappa \operatorname{tr}\mathbf{E}^{\mathrm{ve\,tr}}\right] \mathbf{1} : \mathcal{L}^{\mathrm{tr}}. \tag{A.30}$$

Equivalently, for the deviatoric part of the Kirchhoff predictor stress one has:

$$\frac{\partial(\hat{\boldsymbol{\tau}}^{\mathrm{tr}})^{\mathrm{dev}}}{\partial \mathbf{C}^{\mathrm{ve\,tr}}} = \frac{\partial(\hat{\boldsymbol{\tau}}_0^{\mathrm{tr}})^{\mathrm{dev}}}{\partial \mathbf{E}^{\mathrm{ve\,tr}}} : \frac{\partial \mathbf{E}^{\mathrm{ve\,tr}}}{\partial \mathbf{C}^{\mathrm{ve\,tr}}} + \frac{\partial(\hat{\boldsymbol{\tau}}_c^{\mathrm{tr}})^{\mathrm{dev}}}{\partial \mathbf{E}^{\mathrm{ve\,tr}}} : \frac{\partial \mathbf{E}^{\mathrm{ve\,tr}}}{\partial \mathbf{C}^{\mathrm{ve\,tr}}} = \mu_e \left(\boldsymbol{I} - \frac{1}{3}\mathbf{1} \otimes \mathbf{1}\right) : \mathcal{L}^{\mathrm{tr}} + \frac{\partial(\hat{\boldsymbol{\tau}}_c^{\mathrm{tr}})^{\mathrm{dev}}}{\partial \mathbf{C}^{\mathrm{ve\,tr}}}, \tag{A.31}$$

where the derivative $\frac{\partial(\hat{\boldsymbol{\tau}}^{\mathrm{tr}})^{\mathrm{dev}}}{\partial \mathbf{C}^{\mathrm{ve\,tr}}}$ writes:

$$\frac{\partial(\hat{\boldsymbol{\tau}}_c^{\mathrm{tr}})^{\mathrm{dev}}}{\partial \mathbf{C}^{\mathrm{ve\,tr}}} = \hat{\mu}_\infty[f_\mu \boldsymbol{I} + (\mathbf{E}^{\mathrm{ve\,tr}})^{\mathrm{dev}} \otimes \mathbf{f}'_\mu] : \left(\boldsymbol{I} - \frac{1}{3}\mathbf{1} \otimes \mathbf{1}\right) : \mathcal{L}^{\mathrm{tr}}. \tag{A.32}$$

The total derivative of the extended yield condition with respect to the logarithm strain predictor yields:

$$\left.\frac{d\bar{F}}{d\mathbf{E}^{\mathrm{ve\,tr}}}\right|_{\Gamma} = \frac{\partial \bar{F}}{\partial \Delta p}\frac{\partial \Delta p}{\partial \mathbf{E}^{\mathrm{ve\,tr}}} + \frac{\partial \bar{F}}{\partial \mathbf{E}^{\mathrm{ve\,tr}}}, \tag{A.33}$$

where the derivative $\frac{\partial \bar{F}}{\partial \Delta p}$ is solved in Eq. (A.1). Derivatives $\frac{\partial \Delta p}{\partial \mathbf{E}^{\mathrm{ve\,tr}}}$ and $\frac{\partial \bar{F}}{\partial \mathbf{E}^{\mathrm{ve\,tr}}}$ are solved hereafter.

→ $\frac{\partial \Delta p}{\partial \mathbf{E}^{\mathrm{ve\,tr}}}$:

$$\frac{\partial \Delta p}{\partial \mathbf{E}^{\mathrm{ve\,tr}}} = k\Gamma \frac{\partial A}{\partial \mathbf{E}^{\mathrm{ve\,tr}}}, \tag{A.34}$$

where A is given in Eq. (2.102). Its derivative writes:

$$\frac{\partial A}{\partial \mathbf{E}^{\mathrm{ve\,tr}}} = \frac{1}{2A}\frac{\partial}{\partial \mathbf{E}^{\mathrm{ve\,tr}}}\left[6\left(\frac{((\boldsymbol{\phi}^{\mathrm{tr}})^{\mathrm{dev}} + \Delta(\hat{\boldsymbol{\tau}}_c)^{\mathrm{dev}})^{\mathrm{eq}}}{u}\right)^2\right] + \frac{1}{2A}\frac{\partial}{\partial \mathbf{E}^{\mathrm{ve\,tr}}}\left[\frac{4}{3}\beta^2\left(\frac{\hat{\phi}^{\mathrm{tr}} + \Delta(\frac{1}{3}\operatorname{tr}\hat{\boldsymbol{\tau}}_c)}{v}\right)^2\right], \tag{A.35}$$

where:

$$\frac{\partial}{\partial \mathbf{E}^{\mathrm{ve\,tr}}}\left[6\left(\frac{((\boldsymbol{\phi}^{\mathrm{tr}})^{\mathrm{dev}} + \Delta(\hat{\boldsymbol{\tau}}_c)^{\mathrm{dev}})^{\mathrm{eq}}}{u}\right)^2\right] = \frac{18((\boldsymbol{\phi}^{\mathrm{tr}})^{\mathrm{dev}} + \Delta(\hat{\boldsymbol{\tau}}_c)^{\mathrm{dev}})}{u^2} : \frac{\partial((\boldsymbol{\phi}^{\mathrm{tr}})^{\mathrm{dev}} + \Delta(\hat{\boldsymbol{\tau}}_c)^{\mathrm{dev}})}{\partial \mathbf{E}^{\mathrm{ve\,tr}}} = \\ \frac{18((\boldsymbol{\phi}^{\mathrm{tr}})^{\mathrm{dev}} + \Delta(\hat{\boldsymbol{\tau}}_c)^{\mathrm{dev}})}{u^2} : \left[2\mu_e\left(\boldsymbol{I} - \frac{1}{3}\mathbf{1}\otimes\mathbf{1}\right) + \frac{\partial(\hat{\boldsymbol{\tau}}_c)^{\mathrm{dev}}}{\partial \mathbf{E}^{\mathrm{ve\,tr}}}\right], \tag{A.36}$$

and:

$$\frac{\partial}{\partial \mathbf{E}^{\mathrm{ve\,tr}}}\left[\frac{4}{3}\beta^2\left(\frac{\hat{\phi}^{\mathrm{tr}} + \Delta(\frac{1}{3}\operatorname{tr}\hat{\boldsymbol{\tau}}_c)}{v}\right)^2\right] = \frac{8\beta^2(\hat{\phi}^{\mathrm{tr}} + \Delta(\frac{1}{3}\operatorname{tr}\hat{\boldsymbol{\tau}}_c))}{3v^2}\frac{\partial(\hat{\phi}^{\mathrm{tr}} + \Delta(\frac{1}{3}\operatorname{tr}\hat{\boldsymbol{\tau}}_c))}{\partial \mathbf{E}^{\mathrm{ve\,tr}}} = \\ \frac{8\beta^2(\hat{\phi}^{\mathrm{tr}} + \Delta(\frac{1}{3}\operatorname{tr}\hat{\boldsymbol{\tau}}_c))}{3v^2}\left(\kappa_e\mathbf{1} + \frac{\partial(\frac{1}{3}\operatorname{tr}\hat{\boldsymbol{\tau}}_c)}{\partial \mathbf{E}^{\mathrm{ve\,tr}}}\right). \tag{A.37}$$

→ $\frac{\partial \bar{F}}{\partial \mathbf{E}^{\mathrm{ve\,tr}}}$:

$$\frac{\partial \bar{F}}{\partial \mathbf{E}^{\mathrm{ve\,tr}}} = \frac{\partial}{\partial \mathbf{E}^{\mathrm{ve\,tr}}}\left(\underbrace{a_2\left(\frac{((\boldsymbol{\phi}^{\mathrm{tr}})^{\mathrm{dev}} + \Delta(\hat{\boldsymbol{\tau}}_c)^{\mathrm{dev}})^{\mathrm{eq}}}{u}\right)^{\alpha}}_{*1*}\underbrace{-a_1\frac{\hat{\phi}^{\mathrm{tr}} + \Delta(\frac{1}{3}\operatorname{tr}\hat{\boldsymbol{\tau}}_c)}{v}}_{*2*}\underbrace{-a_0}_{=0}-\underbrace{\left(\eta\frac{\Gamma}{\Delta t}\right)^{\gamma}}_{=0}\right), \tag{A.38}$$

where:

$$\frac{\partial(*1*)}{\partial \mathbf{E}^{\mathrm{ve\,tr}}} = \frac{a_2\alpha\left(((\boldsymbol{\phi}^{\mathrm{tr}})^{\mathrm{dev}} + \Delta(\hat{\boldsymbol{\tau}}_c)^{\mathrm{dev}})^{\mathrm{eq}}\right)^{\alpha-1}}{u^{\alpha}}\frac{\partial((\boldsymbol{\phi}^{\mathrm{tr}})^{\mathrm{dev}} + \Delta(\hat{\boldsymbol{\tau}}_c)^{\mathrm{dev}})^{\mathrm{eq}}}{\partial \mathbf{E}^{\mathrm{ve\,tr}}} = \\ \frac{3a_2\alpha\left(((\boldsymbol{\phi}^{\mathrm{tr}})^{\mathrm{dev}} + \Delta(\hat{\boldsymbol{\tau}}_c)^{\mathrm{dev}})^{\mathrm{eq}}\right)^{\alpha-2}}{2u^{\alpha}}((\boldsymbol{\phi}^{\mathrm{tr}})^{\mathrm{dev}} + \Delta(\hat{\boldsymbol{\tau}}_c)^{\mathrm{dev}}) : \left[2\mu_e\left(\boldsymbol{I} - \frac{1}{3}\mathbf{1}\otimes\mathbf{1}\right) + \frac{\partial(\hat{\boldsymbol{\tau}}_c)^{\mathrm{dev}}}{\partial \mathbf{E}^{\mathrm{ve\,tr}}}\right], \tag{A.39}$$

and

$$\frac{\partial(*2*)}{\partial \mathbf{E}^{\mathrm{ve\,tr}}} = -\frac{a_1}{v}\left(\kappa_e\mathbf{1} + \frac{\partial(\frac{1}{3}\operatorname{tr}\hat{\boldsymbol{\tau}}_c)}{\partial \mathbf{E}^{\mathrm{ve\,tr}}}\right). \tag{A.40}$$

Starting from Eq. (2.91), it is possible to find the derivative $\frac{\partial(\frac{1}{3}\operatorname{tr}\hat{\boldsymbol{\tau}}_c)}{\partial \mathbf{E}^{\mathrm{ve\,tr}}}$ which writes:

$$\frac{\partial(\frac{1}{3}\operatorname{tr}\hat{\boldsymbol{\tau}}_c)}{\partial \mathbf{E}^{\mathrm{ve\,tr}}} = \hat{\kappa}_\infty f'_\kappa(\operatorname{tr}(\mathbf{E}^{\mathrm{ve\,tr}} - \Gamma\mathbf{Q}))\operatorname{tr}(\mathbf{E}^{\mathrm{ve\,tr}} - \Gamma\mathbf{Q})\frac{\partial \operatorname{tr}\mathbf{E}^{\mathrm{ve}}}{\partial \mathbf{E}^{\mathrm{ve\,tr}}} + \hat{\kappa}_\infty f_\kappa(\operatorname{tr}(\mathbf{E}^{\mathrm{ve\,tr}} - \Gamma\mathbf{Q}))\frac{\partial \operatorname{tr}\mathbf{E}^{\mathrm{ve}}}{\partial \mathbf{E}^{\mathrm{ve\,tr}}}, \tag{A.41}$$

where f'_κ is given in Eq. (2.110). By making use of Eq. (2.100) one gets:

$$\frac{\partial \operatorname{tr}\mathbf{E}^{\mathrm{ve}}}{\partial \mathbf{E}^{\mathrm{ve\,tr}}} = \mathbf{1} - \frac{2\beta\Gamma}{v}\frac{\partial}{\partial \mathbf{E}^{\mathrm{ve\,tr}}}\left(\hat{\phi}^{\mathrm{tr}} + \Delta(\frac{1}{3}\operatorname{tr}\hat{\boldsymbol{\tau}}_c)\right) = \mathbf{1} - \frac{2\beta\Gamma\kappa_e}{v}\mathbf{1} - \frac{2\beta\Gamma}{v}\frac{\partial(\frac{1}{3}\operatorname{tr}\hat{\boldsymbol{\tau}}_c)}{\partial \mathbf{E}^{\mathrm{ve\,tr}}}. \tag{A.42}$$

Eq. (A.41) can then be written as:

$$\frac{\partial(\frac{1}{3}\operatorname{tr}\hat{\boldsymbol{\tau}}_c)}{\partial \mathbf{E}^{\mathrm{ve\,tr}}} = \frac{\hat{\kappa}_\infty\left(1 - \frac{2\beta\Gamma\kappa_e}{v}\right)\left(f_\kappa + f'_\kappa\operatorname{tr}(\mathbf{E}^{\mathrm{ve\,tr}} - \Gamma\mathbf{Q})\right)}{1 + \frac{2\beta\Gamma\hat{\kappa}_\infty}{v}\left(f_\kappa + f'_\kappa\operatorname{tr}(\mathbf{E}^{\mathrm{ve\,tr}} - \Gamma\mathbf{Q})\right)}\mathbf{1}. \tag{A.43}$$

Equivalently, using Eq. (2.88) one has:

$$\begin{aligned}\frac{\partial(\hat{\boldsymbol{\tau}}_c)^{\mathrm{dev}}}{\partial \mathbf{E}^{\mathrm{ve\,tr}}} =& 2\hat{\mu}_\infty(\mathbf{E}^{\mathrm{ve\,tr}} - \Gamma\mathbf{Q})^{\mathrm{dev}} \otimes \mathbf{f}'_\mu(\mathbf{E}^{\mathrm{ve\,tr}} - \Gamma\mathbf{Q})^{\mathrm{dev}} : \frac{\partial}{\partial \mathbf{E}^{\mathrm{ve\,tr}}}(\mathbf{E}^{\mathrm{ve\,tr}} - \Gamma\mathbf{Q})^{\mathrm{dev}} \\ &+ 2\hat{\mu}_\infty f_\mu(\mathbf{E}^{\mathrm{ve\,tr}} - \Gamma\mathbf{Q})^{\mathrm{dev}}\frac{\partial}{\partial \mathbf{E}^{\mathrm{ve\,tr}}}(\mathbf{E}^{\mathrm{ve\,tr}} - \Gamma\mathbf{Q})^{\mathrm{dev}}.\end{aligned} \tag{A.44}$$

The derivative $\frac{\partial(\mathbf{E}^{ve})^{\mathrm{dev}}}{\partial \mathbf{E}^{\mathrm{ve\,tr}}}$ writes:

$$\begin{aligned}\frac{\partial(\mathbf{E}^{ve})^{\mathrm{dev}}}{\partial \mathbf{E}^{\mathrm{ve\,tr}}} &= \left(\boldsymbol{I} - \frac{1}{3}\mathbf{1}\otimes\mathbf{1}\right) - \frac{3\Gamma}{u}\frac{\partial}{\partial \mathbf{E}^{\mathrm{ve\,tr}}}(\boldsymbol{\phi}^{\mathrm{tr}} + \Delta\operatorname{dev}\hat{\boldsymbol{\tau}}_c)^{\mathrm{dev}} = \\ &\left(1 - \frac{6\mu_e\Gamma}{u}\right)\left(\boldsymbol{I} - \frac{1}{3}\mathbf{1}\otimes\mathbf{1}\right) - \frac{3\Gamma}{u}\frac{\partial(\hat{\boldsymbol{\tau}}_c)^{\mathrm{dev}}}{\partial \mathbf{E}^{\mathrm{ve\,tr}}},\end{aligned} \tag{A.45}$$

which allows writing Eq. (A.44) as:

$$\mathcal{S} : \frac{\partial(\hat{\boldsymbol{\tau}}_c)^{\mathrm{dev}}}{\partial \mathbf{E}^{\mathrm{ve\,tr}}} = 2\hat{\mu}_\infty\left(1 - \frac{6\mu_e\Gamma}{u}\right)\left[(\mathbf{E}^{\mathrm{ve\,tr}} - \Gamma\mathbf{Q})^{\mathrm{dev}} \otimes \mathbf{f}'_\mu : \left(\boldsymbol{I} - \frac{1}{3}\mathbf{1}\otimes\mathbf{1}\right) + f_\mu\left(\boldsymbol{I} - \frac{1}{3}\mathbf{1}\otimes\mathbf{1}\right)\right], \tag{A.46}$$

where $\mathcal{S}$ is the fourth order tensor:

$$\mathcal{S} = \left(1 + \frac{6\hat{\mu}_\infty\Gamma}{u}f_\mu\right)\left(\boldsymbol{I} - \frac{1}{3}\mathbf{1}\otimes\mathbf{1}\right) + \frac{6\hat{\mu}_\infty\Gamma}{u}(\mathbf{E}^{\mathrm{ve\,tr}} - \Gamma\mathbf{Q}) \otimes \mathbf{f}'_\mu : \left(\boldsymbol{I} - \frac{1}{3}\mathbf{1}\otimes\mathbf{1}\right). \tag{A.47}$$

Let us now compute the derivative $\frac{d\Delta p}{d\mathbf{E}^{\mathrm{ve\,tr}}}$ which writes:

$$\frac{d\Delta p}{d\mathbf{E}^{\mathrm{ve\,tr}}} = \frac{\partial\Delta p}{\partial\Gamma}\frac{\partial\Gamma}{\partial \mathbf{E}^{\mathrm{ve\,tr}}} + \frac{\partial\Delta p}{\partial \mathbf{E}^{\mathrm{ve\,tr}}} = k\left(A + \Gamma\frac{\partial A}{\partial\Gamma}\right)\frac{\partial\Gamma}{\partial \mathbf{E}^{\mathrm{ve\,tr}}} + k\Gamma\frac{\partial A}{\partial \mathbf{E}^{\mathrm{ve\,tr}}}, \tag{A.48}$$

where $\frac{\partial A}{\partial \mathbf{E}^{\mathrm{ve\,tr}}}$ is computed in Eq. (A.35), $\frac{\partial A}{\partial\Gamma}$ in Eq. (A.7) and $\frac{\partial\Gamma}{\partial \mathbf{E}^{\mathrm{ve\,tr}}}$ comes from the consistency condition of the yield condition: $\mathrm{d}\bar{F}\left(\mathbf{C}^{\mathrm{ve\,tr}}, \Delta p, \Gamma\right) = 0$:

$$\frac{\partial\Gamma}{\partial \mathbf{E}^{\mathrm{ve\,tr}}} = -\left(\frac{d\bar{F}}{d\Gamma}\right)^{-1}\left.\frac{d\bar{F}}{d\mathbf{E}^{\mathrm{ve\,tr}}}\right|_{\Gamma}, \tag{A.49}$$

where $\frac{d\bar{F}}{d\Gamma}$ is computed in Eq. (2.106) and $\left.\frac{d\bar{F}}{d\mathbf{E}^{\mathrm{ve\,tr}}}\right|_{\Gamma}$ in Eq. (A.33).

The derivatives of the normal $\mathbf{Q}$ (see Eq. (2.100)) with respect to the logarithmic strain predictor measure can then be computed by dividing it into its deviatoric and volumetric terms as:

$$\begin{aligned}\frac{\partial(\mathbf{Q})^{\mathrm{dev}}}{\partial\mathbf{E}^{\mathrm{ve\,tr}}} =& \frac{3}{u}\left[2\mu_e\left(\boldsymbol{I}-\frac{1}{3}\mathbf{1}\otimes\mathbf{1}\right)+\frac{\partial(\hat{\boldsymbol{\tau}}_c)^{\mathrm{dev}}}{\partial\mathbf{E}^{\mathrm{ve\,tr}}}\right]+\\ &\left[\frac{3}{u}\frac{\partial(\hat{\boldsymbol{\tau}}_c)^{\mathrm{dev}}}{\partial\Gamma}-\frac{18}{u^2}\breve{\mu}\left((\boldsymbol{\phi}^{\mathrm{tr}})^{\mathrm{dev}}+\Delta(\hat{\boldsymbol{\tau}}_c)^{\mathrm{dev}}\right)\right]\otimes\frac{\partial\Gamma}{\partial\mathbf{E}^{\mathrm{ve\,tr}}},\end{aligned} \tag{A.50}$$

and

$$\frac{\partial\,\mathrm{tr}\,\mathbf{Q}}{\partial\mathbf{E}^{\mathrm{ve\,tr}}}=\frac{2\beta}{v}\left(\kappa_e\mathbf{1}+\frac{\partial(\frac{1}{3}\,\mathrm{tr}\,\hat{\boldsymbol{\tau}}_c)}{\partial\mathbf{E}^{\mathrm{ve\,tr}}}\right)+\left[\frac{2\beta}{v}\frac{\partial(\frac{1}{3}\,\mathrm{tr}\,\hat{\boldsymbol{\tau}}_c)}{\partial\Gamma}-\frac{4\beta^2\breve{\kappa}}{v^2}\left(\hat{\phi}^{\mathrm{tr}}+\Delta(\frac{1}{3}\,\mathrm{tr}\,\hat{\boldsymbol{\tau}}_c)\right)\right]\frac{\partial\Gamma}{\partial\mathbf{E}^{\mathrm{ve\,tr}}}. \tag{A.51}$$

Finally, the updated $\hat{\boldsymbol{\tau}}$ write:

$$\hat{\boldsymbol{\tau}}=(\hat{\boldsymbol{\tau}})^{\mathrm{dev}}+(\hat{\boldsymbol{\tau}})^{\mathrm{vol}}=(\hat{\boldsymbol{\tau}}^{\mathrm{tr}})^{\mathrm{dev}}-2\mu_e\Gamma(\mathbf{Q})^{\mathrm{dev}}+((\frac{1}{3}\,\mathrm{tr}\,\hat{\boldsymbol{\tau}}^{\mathrm{tr}})-\kappa_e\Gamma\,\mathrm{tr}\,\mathbf{Q})\mathbf{1}, \tag{A.52}$$

being possible to compute $\frac{\partial(\hat{\boldsymbol{\tau}})^{\mathrm{dev}}}{\partial\mathbf{E}^{\mathrm{ve\,tr}}}$ and $\frac{\partial(\frac{1}{3}\,\mathrm{tr}\,\hat{\boldsymbol{\tau}})}{\partial\mathbf{E}^{\mathrm{ve\,tr}}}$ as:

$$\begin{aligned}\frac{\partial(\hat{\boldsymbol{\tau}})^{\mathrm{dev}}}{\partial\mathbf{E}^{\mathrm{ve\,tr}}}=&\frac{\partial((\hat{\boldsymbol{\tau}}^{\mathrm{tr}})^{\mathrm{dev}}-(\hat{\boldsymbol{\tau}}_c^{\mathrm{tr}})^{\mathrm{dev}})}{\partial\mathbf{E}^{\mathrm{ve\,tr}}}+\frac{\partial(\hat{\boldsymbol{\tau}}_c)^{\mathrm{dev}}}{\partial\mathbf{E}^{\mathrm{ve\,tr}}}+\frac{\partial(\hat{\boldsymbol{\tau}}_c)^{\mathrm{dev}}}{\partial\Gamma}\otimes\frac{\partial\Gamma}{\partial\mathbf{E}^{\mathrm{ve\,tr}}}-\\ &2\mu_e\Gamma\frac{\partial(\mathbf{Q})^{\mathrm{dev}}}{\partial\mathbf{E}^{\mathrm{ve\,tr}}}-2\mu_e(\mathbf{Q})^{\mathrm{dev}}\otimes\frac{\partial\Gamma}{\partial\mathbf{E}^{\mathrm{ve\,tr}}},\end{aligned} \tag{A.53}$$

and:

$$\frac{\partial(\frac{1}{3}\,\mathrm{tr}\,\hat{\boldsymbol{\tau}})}{\partial\mathbf{E}^{\mathrm{ve\,tr}}}=\kappa_e\mathbf{1}-\kappa_e\Gamma\frac{\partial\,\mathrm{tr}\,\mathbf{Q}}{\partial\mathbf{E}^{\mathrm{ve\,tr}}}-\kappa_e\,\mathrm{tr}\,\mathbf{Q}\frac{\partial\Gamma}{\partial\mathbf{E}^{\mathrm{ve\,tr}}}+\frac{\partial(\frac{1}{3}\,\mathrm{tr}\,\hat{\boldsymbol{\tau}}_c)}{\partial\Gamma}\frac{\partial\Gamma}{\partial\mathbf{E}^{\mathrm{ve\,tr}}}+\frac{\partial(\frac{1}{3}\,\mathrm{tr}\,\hat{\boldsymbol{\tau}}_c)}{\partial\mathbf{E}^{\mathrm{ve\,tr}}}. \tag{A.54}$$

It is then possible to compute $\frac{\partial\hat{\boldsymbol{\tau}}}{\partial\mathbf{E}^{\mathrm{ve\,tr}}}$ which yields:

$$\frac{\partial\hat{\boldsymbol{\tau}}}{\partial\mathbf{E}^{\mathrm{ve\,tr}}}=\mathbf{1}\otimes\frac{\partial(\frac{1}{3}\,\mathrm{tr}\,\hat{\boldsymbol{\tau}})}{\partial\mathbf{E}^{\mathrm{ve\,tr}}}+\frac{\partial(\hat{\boldsymbol{\tau}})^{\mathrm{dev}}}{\partial\mathbf{E}^{\mathrm{ve\,tr}}}. \tag{A.55}$$

This, allows to write:

$$\frac{\partial\mathbf{S}}{\partial\mathbf{C}^{\mathrm{ve\,tr}}}=\frac{\partial\mathcal{L}}{\partial\mathbf{C}^{\mathrm{ve\,tr}}}^{3,4}:\hat{\boldsymbol{\tau}}+\mathcal{L}:\frac{\partial\hat{\boldsymbol{\tau}}}{\partial\mathbf{C}^{\mathrm{ve\,tr}}}. \tag{A.56}$$

Finally, by using Eq. (2.79), the derivative of the plastic deformation gradient $\frac{\partial\mathbf{F}^{\mathrm{vp}}}{\partial\mathbf{C}^{\mathrm{ve\,tr}}}$ can be estimated as:

$$\frac{\partial\mathbf{F}^{\mathrm{vp}}}{\partial\mathbf{C}^{\mathrm{ve\,tr}}}=\left[\boldsymbol{\mathcal{E}}:\left(\mathbf{Q}\otimes\frac{\partial\Gamma}{\partial\mathbf{C}^{\mathrm{ve\,tr}}}+\Gamma\frac{\partial(\mathbf{Q})^{\mathrm{dev}}}{\partial\mathbf{C}^{\mathrm{ve\,tr}}}+\frac{\Gamma}{3}\mathbf{1}\otimes\frac{\partial\,\mathrm{tr}\,\mathbf{Q}}{\partial\mathbf{C}^{\mathrm{ve\,tr}}}\right)\right]^{2}\cdot\mathbf{F}_n^{\mathrm{vp}}, \tag{A.57}$$

where $\boldsymbol{\mathcal{E}}$ writes:

$$\boldsymbol{\mathcal{E}}=\left.\frac{\partial\exp\mathbf{A}}{\partial\mathbf{A}}\right|_{\Gamma\mathbf{Q}}. \tag{A.58}$$

Appendix B

Appendix related to Chapter 3

B.1 Algorithmic operators of the phases material responses in the incremental secant formulation

For the sake of conciseness, in this section the subscript referring to the phase is omitted.

B.1.1 Residual incremental-secant case

The operator $\boldsymbol{C}^{\text{alg}}$ is defined as:

$$\boldsymbol{C}^{\text{alg}} = \frac{\partial \hat{\boldsymbol{\sigma}}}{\partial \Delta \boldsymbol{\varepsilon}} = \frac{\partial}{\partial \Delta \boldsymbol{\varepsilon}^{\text{r}}} \left[\Delta \hat{\boldsymbol{\sigma}}^{\text{r}} \right] : \frac{\partial \Delta \boldsymbol{\varepsilon}^{\text{r}}}{\partial \Delta \boldsymbol{\varepsilon}} = \frac{\partial \Delta \hat{\boldsymbol{\sigma}}^{\text{r}}}{\partial \Delta \boldsymbol{\varepsilon}^{\text{r}}}. \tag{B.1}$$

The term $\frac{\partial}{\partial \Delta \boldsymbol{\varepsilon}^{\text{r}}} \left[\Delta \hat{\boldsymbol{\sigma}}^{\text{r}} \right]$ can be obtained from Equation (3.65), yielding:

$$\begin{aligned} \frac{\partial}{\partial \Delta \boldsymbol{\varepsilon}^{\text{r}}} \left[\Delta \hat{\boldsymbol{\sigma}}^{\text{r}} \right] = \boldsymbol{C}^{\text{el}} - 6\mu^{\text{el}} & \left[\left(\hat{\boldsymbol{\sigma}}^{\text{tr}}_{n+1} - \hat{\boldsymbol{\sigma}}^{\text{res}}_{n} \right)^{\text{dev}} \otimes \left(\frac{\frac{\partial \Gamma}{\partial \Delta \boldsymbol{\varepsilon}^{\text{r}}}}{\left(1 + 6\mu^{\text{el}} \Gamma\right)^2} \right) + \frac{\Gamma}{1 + 6\mu^{\text{el}}\Gamma} \left(2\mu^{\text{el}} \boldsymbol{I}^{\text{dev}} \right) \right] \\ - 2\kappa^{\text{el}}\beta & \left[\left(\hat{\boldsymbol{\sigma}}^{\text{tr}}_{n+1} - \hat{\boldsymbol{\sigma}}^{\text{res}}_{n} \right)^{\text{vol}} \otimes \left(\frac{\frac{\partial \Gamma}{\partial \Delta \boldsymbol{\varepsilon}^{\text{r}}}}{\left(1 + 2\kappa^{\text{el}}\beta \Gamma\right)^2} \right) + \frac{\Gamma}{1 + 2\beta\kappa^{\text{el}}\Gamma} \left(3\kappa^{\text{el}} \boldsymbol{I}^{\text{vol}} \right) \right], \end{aligned} \tag{B.2}$$

where $\frac{\partial \Gamma}{\partial \Delta \boldsymbol{\varepsilon}^{\text{r}}} = \frac{\partial \Gamma}{\partial \Delta \boldsymbol{\varepsilon}}$ is obtained from Equation (3.53) from which one can write:

$$0 = \delta F = \left(\frac{\partial F}{\partial \Delta \boldsymbol{\varepsilon}} + \frac{\partial F}{\partial \Delta p} \underbrace{\frac{\partial \Delta p}{\partial \Delta \varepsilon}}_{= \frac{\partial \Delta p}{\partial \Gamma} \frac{\partial \Gamma}{\partial \Delta \varepsilon}} + \frac{dF}{d\Gamma} \frac{\partial \Gamma}{\partial \Delta \boldsymbol{\varepsilon}} \right) : \delta \Delta \boldsymbol{\varepsilon}, \tag{B.3}$$

yielding:

$$\frac{\partial \Gamma}{\partial \Delta \boldsymbol{\varepsilon}} = - \left(\frac{dF}{d\Gamma} \right)^{-1} \left(\frac{\partial F}{\partial \Delta \boldsymbol{\varepsilon}} + \frac{\partial F}{\partial \Delta p} \frac{\partial \Delta p}{\partial \Gamma} \frac{\partial \Gamma}{\partial \Delta \varepsilon} \right). \tag{B.4}$$

One finally find:

$$\frac{\partial \Gamma}{\partial \Delta \boldsymbol{\varepsilon}} = - \left(\frac{dF}{d\Gamma} \right)^{-1} \frac{\partial F}{\partial \Delta \boldsymbol{\varepsilon}} \left[1 + \left(\frac{dF}{d\Gamma} \right)^{-1} \frac{\partial F}{\partial \Delta p} \frac{\partial \Delta p}{\partial \Gamma} \right]^{-1}. \tag{B.5}$$

The terms $\frac{dF}{d\Gamma}$ and $\frac{\partial F}{\partial \Delta p}$ come from the return mapping (Eq. (3.54)), the term $\frac{\partial \Delta p}{\partial \Gamma}$ comes from Eq. (3.55) and the term $\frac{\partial F}{\partial \Delta \boldsymbol{\varepsilon}}$ reads

$$\frac{\partial F}{\partial \Delta \boldsymbol{\varepsilon}} = \frac{1}{\sigma_c^{\alpha}} \underbrace{\frac{\partial \left[\left(\frac{\hat{\boldsymbol{\sigma}}_{n+1}^{\text{tr}} - \hat{\boldsymbol{\sigma}}_n^{\text{res}}}{1+6\mu^{\text{el}}\Gamma} + \hat{\boldsymbol{\sigma}}_n^{\text{res}}\right)^{\text{eq}}\right]^{\alpha}}{\partial \Delta \boldsymbol{\varepsilon}}}_{\mathbf{1*}} - 3 \frac{m^{\alpha} - 1}{(m+1)\,\sigma_c} \underbrace{\frac{\partial \left(\frac{\hat{\phi}_{n+1}^{\text{tr}} - \hat{\phi}_n^{\text{res}}}{1+2\kappa^{\text{el}}\Gamma\beta} + \hat{\phi}_n^{\text{res}}\right)}{\partial \Delta \boldsymbol{\varepsilon}}}_{\mathbf{2*}}, \tag{B.6}$$

where

$$\begin{aligned} \mathbf{1*} &= \alpha \left[\left(\frac{\hat{\boldsymbol{\sigma}}_{n+1}^{\text{tr}} - \hat{\boldsymbol{\sigma}}_n^{\text{res}}}{1 + 6\mu^{\text{el}}\Gamma} + \hat{\boldsymbol{\sigma}}_n^{\text{res}}\right)^{\text{eq}}\right]^{\alpha-1} \frac{\frac{3}{2}\left[\frac{\boldsymbol{I}^{\text{dev}}:\boldsymbol{C}^{\text{el}}}{1+6\mu^{\text{el}}\Gamma} : \left(\frac{\hat{\boldsymbol{\sigma}}_{n+1}^{\text{tr}} - \hat{\boldsymbol{\sigma}}_n^{\text{res}}}{1+6\mu^{\text{el}}\Gamma} + \hat{\boldsymbol{\sigma}}_n^{\text{res}}\right)^{\text{dev}}\right]}{\sqrt{\frac{3}{2}\left(\frac{\hat{\boldsymbol{\sigma}}_{n+1}^{\text{tr}} - \hat{\boldsymbol{\sigma}}_n^{\text{res}}}{1+6\mu^{\text{el}}\Gamma} + \hat{\boldsymbol{\sigma}}_n^{\text{res}}\right)^{\text{dev}} : \left(\frac{\hat{\boldsymbol{\sigma}}_{n+1}^{\text{tr}} - \hat{\boldsymbol{\sigma}}_n^{\text{res}}}{1+6\mu^{\text{el}}\Gamma} + \hat{\boldsymbol{\sigma}}_n^{\text{res}}\right)^{\text{dev}}}}; \\ \mathbf{2*} &= \frac{\kappa^{\text{el}}\mathbf{1}}{1 + 2\kappa^{\text{el}}\Gamma\beta}. \end{aligned} \tag{B.7}$$

Finally, one has directly $\boldsymbol{C}_p = \frac{\partial p}{\partial \breve{p}} = 0$.

B.1.2 Zero incremental-secant case

In the zero incremental-secant case, the residual stress is not taken into account. The term $\frac{\partial}{\partial \Delta \boldsymbol{\varepsilon}^{\text{r}}}\left[\Delta \hat{\boldsymbol{\sigma}}^{\text{r}}\right]$ is thus written:

$$\begin{aligned} \frac{\partial}{\partial \Delta \boldsymbol{\varepsilon}^{\text{r}}}\left[\Delta \hat{\sigma}^{\text{r}}\right] = &\boldsymbol{C}^{\text{el}} - 6\mu^{\text{el}}\left[\left(\hat{\boldsymbol{\sigma}}_{n+1}^{\text{tr}}\right)^{\text{dev}} \otimes \left(\frac{\frac{\partial \Gamma}{\partial \Delta \boldsymbol{\varepsilon}^{\text{r}}}}{\left(1 + 6\mu^{\text{el}}\Gamma\right)^2}\right) + \frac{\Gamma}{1 + 6\mu^{\text{el}}\Gamma}\left(2\mu^{\text{el}}\boldsymbol{I}^{\text{dev}}\right)\right] \\ &- 2\kappa^{\text{el}}\beta\left[\left(\hat{\boldsymbol{\sigma}}_{n+1}^{\text{tr}}\right)^{\text{vol}} \otimes \left(\frac{\frac{\partial \Gamma}{\partial \Delta \boldsymbol{\varepsilon}^{\text{r}}}}{\left(1 + 2\kappa^{\text{el}}\beta\Gamma\right)^2}\right) + \frac{\Gamma}{1 + 2\beta\kappa^{\text{el}}\Gamma}\left(3\kappa^{\text{el}}\boldsymbol{I}^{\text{vol}}\right)\right], \end{aligned} \tag{B.8}$$

where the terms defining $\frac{\partial \Gamma}{\partial \Delta \boldsymbol{\varepsilon}} = -\left(\frac{dF}{d\Gamma}\right)^{-1}\left(\frac{\partial F}{\partial \Delta \boldsymbol{\varepsilon}} + \frac{\partial F}{\partial \Delta p}\frac{\partial \Delta p}{\partial \Gamma}\frac{\partial \Gamma}{\partial \Delta \varepsilon}\right)$ read

$$\frac{\partial F}{\partial \Delta \boldsymbol{\varepsilon}} = \frac{1}{\sigma_c^{\alpha}} \underbrace{\frac{\partial \left[\left(\frac{\boldsymbol{\sigma}_{n+1}^{\text{tr}}}{1+6\mu^{\text{el}}\Gamma}\right)^{\text{eq}}\right]^{\alpha}}{\partial \Delta \boldsymbol{\varepsilon}}}_{\mathbf{1*}} - 3 \frac{m^{\alpha} - 1}{(m+1)\,\sigma_c} \underbrace{\frac{\partial \left(\frac{\phi_{n+1}^{\text{tr}}}{1+2\kappa^{\text{el}}\Gamma\beta}\right)}{\partial \Delta \boldsymbol{\varepsilon}}}_{\mathbf{2*}}, \tag{B.9}$$

with

$$\begin{aligned} \mathbf{1*} &= \alpha \left[\left(\frac{\hat{\boldsymbol{\sigma}}_{n+1}^{\text{tr}}}{1 + 6\mu^{\text{el}}\Gamma}\right)^{\text{eq}}\right]^{\alpha-1} \frac{\frac{3}{2}\left[\frac{\boldsymbol{I}^{\text{dev}}:\boldsymbol{C}^{\text{el}}}{1+6\mu^{\text{el}}\Gamma} : \left(\frac{\hat{\boldsymbol{\sigma}}_{n+1}^{\text{tr}}}{1+6\mu^{\text{el}}\Gamma}\right)^{\text{dev}}\right]}{\sqrt{\frac{3}{2}\left(\frac{\hat{\boldsymbol{\sigma}}_{n+1}^{\text{tr}}}{1+6\mu^{\text{el}}\Gamma}\right)^{\text{dev}} : \left(\frac{\hat{\boldsymbol{\sigma}}_{n+1}^{\text{tr}}}{1+6\mu^{\text{el}}\Gamma}\right)^{\text{dev}}}}, \\ \mathbf{2*} &= \frac{\kappa^{\text{el}}\mathbf{1}}{1 + 2\kappa^{\text{el}}\Gamma\beta}; \end{aligned} \tag{B.10}$$

and

$$\begin{aligned}\frac{dF}{d\Gamma} = \Bigg[&- \frac{\alpha}{\sigma_c^{\alpha+1}} \frac{\partial R(\Delta p)}{\partial \Delta p} \left(\left(\frac{\hat{\boldsymbol{\sigma}}^{\mathrm{tr}}_{n+1}}{1+6\mu^{\mathrm{el}}\Gamma} \right)^{\mathrm{eq}} \right)^{\alpha} \\ &+ 3 \frac{m^{\alpha}-1}{(m+1)\sigma_c^2} \frac{\partial R(\Delta p)}{\partial \Delta p} \left(\frac{\hat{\phi}^{\mathrm{tr}}_{n+1}}{1+2\kappa^{\mathrm{el}}\Gamma\beta} \right) \Bigg] \frac{\partial \Delta p}{\partial \Gamma} + \frac{\partial F}{\partial \Gamma}\,;\end{aligned} \tag{B.11}$$

$$\begin{aligned}\frac{\partial \Delta p}{\partial \Gamma} &= k \sqrt{6 \left(\left(\frac{\hat{\sigma}^{\mathrm{tr}}_{n+1}}{1+6\mu^{\mathrm{el}}\Gamma} \right)^{\mathrm{eq}} \right)^2 + \frac{4\beta^2}{3} \left(\frac{\hat{\phi}^{\mathrm{tr}}_{n+1}}{1+2\kappa^{\mathrm{el}}\Gamma\beta} \right)^2} \\ &- \frac{k\Gamma \left[72\mu^{\mathrm{el}} \frac{\left(\left(\hat{\sigma}^{\mathrm{tr}}_{n+1} \right)^{\mathrm{eq}} \right)^2}{\left(1+6\mu^{\mathrm{el}}\Gamma \right)^3} + \frac{16\beta^3\kappa^{\mathrm{el}}}{3} \frac{\left(\hat{\phi}^{\mathrm{tr}}_{n+1} \right)^2}{\left(1+2\kappa^{\mathrm{el}}\Gamma\beta \right)^3} \right]}{2\sqrt{6 \left(\left(\frac{\hat{\sigma}^{\mathrm{tr}}_{n+1}}{1+6\mu^{\mathrm{el}}\Gamma} \right)^{\mathrm{eq}} \right)^2 + \frac{4\beta^2}{3} \left(\frac{\hat{\phi}^{\mathrm{tr}}_{n+1}}{1+2\kappa^{\mathrm{el}}\Gamma\beta} \right)^2}};\end{aligned} \tag{B.12}$$

$$\begin{aligned}\frac{\partial F}{\partial \Gamma} = &- \alpha \left(\frac{\left(\frac{\hat{\boldsymbol{\sigma}}^{\mathrm{tr}}_{n+1}}{1+6\mu^{\mathrm{el}}\Gamma} \right)^{\mathrm{eq}}}{\sigma_c} \right)^{\alpha-1} \frac{9\mu^{\mathrm{el}} \left(\hat{\boldsymbol{\sigma}}^{\mathrm{tr}}_{n+1} \right)^{\mathrm{dev}} : \left(\frac{\hat{\boldsymbol{\sigma}}^{\mathrm{tr}}_{n+1}}{1+6\mu^{\mathrm{el}}\Gamma} \right)^{\mathrm{dev}}}{\sigma_c \left(1+6\mu^{\mathrm{el}}\Gamma \right)^2 \left(\frac{\hat{\boldsymbol{\sigma}}^{\mathrm{tr}}_{n+1}}{1+6\mu^{\mathrm{el}}\Gamma} \right)^{\mathrm{eq}}} \\ &+ 3 \frac{m^{\alpha}-1}{(m+1)\,\sigma_c} \left(\frac{\hat{\phi}^{\mathrm{tr}}_{n+1}}{\left(1+2\kappa^{\mathrm{el}}\Gamma\beta \right)^2} 2\kappa^{\mathrm{el}}\beta \right).\end{aligned} \tag{B.13}$$

Finally, one has directly $\boldsymbol{C}_p = \frac{\partial p}{\partial \breve{p}} = 0$.

B.2 Stress residual vector of the MFH

In this section, $\boldsymbol{C}^{\mathrm{S}}$, κ_s, μ_s and $\boldsymbol{C}^{\mathrm{SD}}$, κ_s^{D} and μ_s^{D} respectively stand either for $\boldsymbol{C}^{\mathrm{Sr}}$, Equation (3.67), κ_s^{r}, μ_s^{r}, Equation (3.68), $\boldsymbol{C}^{\mathrm{SDr}}$, Equation (3.72), κ_s^{Dr} and μ_s^{Dr}, Equation (3.74), or for $\boldsymbol{C}^{\mathrm{S0}}$, Equation (3.70), κ_s^{0}, μ_s^{0}, Equation (3.71), $\boldsymbol{C}^{\mathrm{SD0}}$, Equation (3.75), κ_s^{D0} and μ_s^{D0}, Equation (3.77).

At the end of the MFH scheme we must satisfy:

$$\Delta\boldsymbol{\varepsilon}^{\mathrm{r}}_{\mathrm{I}_{n+1}} = \boldsymbol{B}^{\epsilon}\left(\mathrm{I}, \boldsymbol{C}_0^{\mathrm{SD}}, \boldsymbol{C}_{\mathrm{I}}^{\mathrm{S}}\right) : \Delta\boldsymbol{\varepsilon}^{\mathrm{r}}_{0_{n+1}}. \tag{B.14}$$

For a two-phase composite, the relation of the variation of strains in the full composite and each of its phases writes

$$\Delta\bar{\boldsymbol{\varepsilon}}^{\mathrm{r}}_{n+1} = v_0 \Delta\boldsymbol{\varepsilon}^{\mathrm{r}}_{0_{n+1}} + v_{\mathrm{I}} \Delta\boldsymbol{\varepsilon}^{\mathrm{r}}_{\mathrm{I}_{n+1}}. \tag{B.15}$$

Multiplying Equation (B.15) by the concentration strain tensor and using Equation (B.14), one has

$$v_0 \Delta\boldsymbol{\varepsilon}^{\mathrm{r}}_{\mathrm{I}_{n+1}} + v_{\mathrm{I}} \boldsymbol{B}^{\epsilon}\left(\mathrm{I}, \boldsymbol{C}_0^{\mathrm{SD}}, \boldsymbol{C}_{\mathrm{I}}^{\mathrm{S}}\right) : \Delta\boldsymbol{\varepsilon}^{\mathrm{r}}_{\mathrm{I}_{n+1}} = \boldsymbol{B}^{\epsilon}\left(\mathrm{I}, \boldsymbol{C}_0^{\mathrm{SD}}, \boldsymbol{C}_{\mathrm{I}}^{\mathrm{S}}\right) : \Delta\bar{\boldsymbol{\varepsilon}}^{\mathrm{r}}_{n+1}. \tag{B.16}$$

Using the Mori-Tanaka assumption of Eq. (3.10) for $\boldsymbol{B}^{\epsilon}$, Eq. (B.16) is rewritten

$$\Delta\boldsymbol{\varepsilon}^{\mathrm{r}}_{\mathrm{I}_{n+1}} + v_0 \boldsymbol{S} : \left[\left(\boldsymbol{C}_0^{\mathrm{SD}} \right)^{-1} : \boldsymbol{C}_{\mathrm{I}}^{\mathrm{S}} - \boldsymbol{I} \right] : \Delta\boldsymbol{\varepsilon}^{\mathrm{r}}_{\mathrm{I}_{n+1}} = \Delta\bar{\boldsymbol{\varepsilon}}^{\mathrm{r}}_{n+1}\,. \tag{B.17}$$

It is then possible to write the stress residual vector $\boldsymbol{F} = 0$ as

$$\boldsymbol{F} = \boldsymbol{C}_0^{\mathrm{SD}} : \left[\Delta\boldsymbol{\varepsilon}^{\mathrm{r}}_{\mathrm{I}_{n+1}} - \frac{1}{v_0} \boldsymbol{S}^{-1} : \left(\Delta\boldsymbol{\varepsilon}^{\mathrm{r}}_{\mathrm{I}_{n+1}} - \Delta\bar{\boldsymbol{\varepsilon}}^{\mathrm{r}}_{n+1} \right) \right] - \boldsymbol{C}_{\mathrm{I}}^{\mathrm{S}} : \Delta\boldsymbol{\varepsilon}^{\mathrm{r}}_{\mathrm{I}_{n+1}}. \tag{B.18}$$

This residual can be linearized as

$$\mathrm{d}\boldsymbol{F} = \frac{\partial \boldsymbol{F}}{\partial \boldsymbol{\varepsilon}_{\mathrm{I}}} : \mathrm{d}\Delta\boldsymbol{\varepsilon}_{\mathrm{I}}^{\mathrm{r}} + \frac{\partial \boldsymbol{F}}{\partial \boldsymbol{\varepsilon}_{0}} : \mathrm{d}\Delta\boldsymbol{\varepsilon}_{0}^{\mathrm{r}} + \frac{\partial \boldsymbol{F}}{\partial \bar{\boldsymbol{\varepsilon}}} : \mathrm{d}\Delta\bar{\boldsymbol{\varepsilon}}^{\mathrm{r}} + \frac{\partial \boldsymbol{F}}{\partial \breve{p}_{0}} \,\mathrm{d}\breve{p}_{0}. \tag{B.19}$$

In order to solve $\boldsymbol{F} = 0$, we consider constant $\Delta\bar{\boldsymbol{\varepsilon}}^{\mathrm{r}}$ and $\breve{p}_0$ values. The process therefore yields $\mathrm{d}\boldsymbol{F} = \boldsymbol{J} : \mathrm{d}\boldsymbol{\varepsilon}_{\mathrm{I}}$, where $\boldsymbol{J}$ writes:

$$\begin{aligned}\boldsymbol{J} =& \frac{\partial \boldsymbol{F}}{\partial \boldsymbol{\varepsilon}_{\mathrm{I}}} + \frac{\partial \boldsymbol{F}}{\partial \boldsymbol{\varepsilon}_{0}} : \frac{\partial \boldsymbol{\varepsilon}_{0}}{\partial \boldsymbol{\varepsilon}_{\mathrm{I}}} = \boldsymbol{C}^{\mathrm{SD}}_{0_{n+1}} : \left[\boldsymbol{I} - \boldsymbol{S}^{-1}\right] - \boldsymbol{C}^{\mathrm{S}}_{\mathrm{I}_{n+1}} - \frac{\partial \boldsymbol{C}^{\mathrm{S}}_{\mathrm{I}_{n+1}}}{\partial \boldsymbol{\varepsilon}_{\mathrm{I}}} : \Delta\boldsymbol{\varepsilon}^{\mathrm{r}}_{\mathrm{I}_{n+1}} \\ &- \frac{v_{\mathrm{I}}}{v_0}\left(\frac{\partial \boldsymbol{C}^{\mathrm{SD}}_{0_{n+1}}}{\partial \boldsymbol{\varepsilon}_{0}} + \frac{\partial \boldsymbol{C}^{\mathrm{SD}}_{0_{n+1}}}{\partial D_0}\frac{\partial D_0}{\partial \boldsymbol{\varepsilon}_{0}}\right) : \left[\Delta\boldsymbol{\varepsilon}^{\mathrm{r}}_{\mathrm{I}_{n+1}} - \boldsymbol{S}^{-1} : \frac{\left(\Delta\boldsymbol{\varepsilon}^{\mathrm{r}}_{\mathrm{I}_{n+1}} - \Delta\bar{\boldsymbol{\varepsilon}}^{\mathrm{r}}_{n+1}\right)}{v_0}\right] \\ &- \frac{v_{\mathrm{I}}}{v_0^2}\boldsymbol{C}^{\mathrm{SD}}_{0_{n+1}} \otimes \left(\Delta\boldsymbol{\varepsilon}^{\mathrm{r}}_{\mathrm{I}_{n+1}} - \Delta\bar{\boldsymbol{\varepsilon}}^{\mathrm{r}}_{n+1}\right) :: \left(\boldsymbol{S}^{-1} \otimes \boldsymbol{S}^{-1}\right) :: \left(\frac{\partial \boldsymbol{S}}{\partial \boldsymbol{\varepsilon}_{0}} + \frac{\partial \boldsymbol{S}}{\partial D_0}\frac{\partial D_0}{\partial \boldsymbol{\varepsilon}_{0}}\right) \\ &- \frac{v_{\mathrm{I}}}{v_0}\boldsymbol{C}^{\mathrm{SD}}_{0_{n+1}} : \boldsymbol{S}^{-1},\end{aligned} \tag{B.20}$$

where the derivative of the Eshelby tensor is given in Appendix B.4.

Then, the strain increment of the inclusion phase coming from the variations of $\mathrm{d}\Delta\bar{\boldsymbol{\varepsilon}}^{\mathrm{r}}$ and of $\mathrm{d}\breve{p}_0$ is computed by constraining $d\boldsymbol{F} = 0$, being possible to write:

$$\frac{\partial \boldsymbol{\varepsilon}_{\mathrm{I}}}{\partial \bar{\boldsymbol{\varepsilon}}} = -\boldsymbol{J}^{-1} : \frac{\partial \boldsymbol{F}}{\partial \bar{\boldsymbol{\varepsilon}}}\,, \text{ and } \frac{\partial \boldsymbol{\varepsilon}_{\mathrm{I}}}{\partial \breve{p}_0} = -\boldsymbol{J}^{-1} : \frac{\partial \boldsymbol{F}}{\partial \breve{p}_0}\,. \tag{B.21}$$

The set of equations is completed with the use of the relation between the strains increments $\mathrm{d}\bar{\boldsymbol{\varepsilon}}^{\mathrm{r}} = v_0 \mathrm{d}\boldsymbol{\varepsilon}_0^{\mathrm{r}} + v_{\mathrm{I}} \mathrm{d}\boldsymbol{\varepsilon}_{\mathrm{I}}^{\mathrm{r}}$, yielding

$$\frac{\partial \boldsymbol{\varepsilon}_{0}}{\partial \bar{\boldsymbol{\varepsilon}}} = \frac{1}{v_0}\left(\boldsymbol{I} - v_1 \frac{\partial \boldsymbol{\varepsilon}_{\mathrm{I}}}{\partial \bar{\boldsymbol{\varepsilon}}}\right)\,, \text{ and } \frac{\partial \boldsymbol{\varepsilon}_{0}}{\partial \breve{p}_0} = -\frac{v_{\mathrm{I}}}{v_0}\frac{\partial \boldsymbol{\varepsilon}_{\mathrm{I}}}{\partial \breve{p}_0}. \tag{B.22}$$

Appendix B.3 details the derivative of $\boldsymbol{C}^{\mathrm{Sr}}$ and $\boldsymbol{C}^{\mathrm{S0}}$ with respect to $\boldsymbol{\varepsilon}$, which completes the process.

B.3 Derivatives of the phase secant operators in the incremental secant framework

For the sake of conciseness, in this section the subscript referring to the phase is omitted. Besides, $\boldsymbol{C}^{\mathrm{S}}$, κ_s, μ_s and $\boldsymbol{C}^{\mathrm{SD}}$, κ_s^{D} and μ_s^{D} respectively stand either for $\boldsymbol{C}^{\mathrm{Sr}}$, Equation (3.67), κ_s^{r}, μ_s^{r}, Equation (3.68), $\boldsymbol{C}^{\mathrm{SDr}}$, Equation (3.72), κ_s^{Dr} and μ_s^{Dr}, Equation (3.74), or for $\boldsymbol{C}^{\mathrm{S0}}$, Equation (3.70), κ_s^{0}, μ_s^{0}, Equation (3.71), $\boldsymbol{C}^{\mathrm{SD0}}$, Equation (3.75), κ_s^{D0} and μ_s^{D0}, Equation (3.77).

The derivative of $\boldsymbol{C}^{\mathrm{S}}$ writes

$$\frac{\partial \boldsymbol{C}^{\mathrm{S}}}{\partial \boldsymbol{\varepsilon}} = \frac{\partial}{\partial \Delta\boldsymbol{\varepsilon}^{\mathrm{r}}}\left(3\kappa_s \boldsymbol{I}^{\mathrm{vol}} + 2\mu_s \boldsymbol{I}^{\mathrm{dev}}\right) : \frac{\partial \Delta\boldsymbol{\varepsilon}^{\mathrm{r}}}{\partial \boldsymbol{\varepsilon}} = \left(3\boldsymbol{I}^{\mathrm{vol}}\frac{\partial \kappa_s}{\partial \Gamma} + 2\boldsymbol{I}^{\mathrm{dev}}\frac{\partial \mu_s}{\partial \Gamma}\right) \otimes \frac{\partial \Gamma}{\partial \boldsymbol{\varepsilon}}, \tag{B.23}$$

where the derivative $\frac{\partial \Gamma}{\partial \boldsymbol{\varepsilon}}$ is given in appendix B.1 and the derivatives of the bulk and shear moduli read

$$\frac{\partial \mu_s}{\partial \Gamma} = -\frac{6{\mu^{\mathrm{el}}}^2}{\left(1 + 6\mu^{\mathrm{el}}\Gamma\right)^2}, \text{ and } \frac{\partial \kappa_s}{\partial \Gamma} = -\frac{2\beta{\kappa^{\mathrm{el}}}^2}{\left(1 + 2\kappa^{\mathrm{el}}\Gamma\beta\right)^2}. \tag{B.24}$$

In the damaged enhanced case, the derivative of the damaged secant tensors become

$$\frac{\mathrm{d}\boldsymbol{C}^{\mathrm{SD}}}{\mathrm{d}\boldsymbol{\varepsilon}} = \frac{\partial \boldsymbol{C}^{\mathrm{SD}}}{\partial \boldsymbol{\varepsilon}} + \frac{\partial \boldsymbol{C}^{\mathrm{SD}}}{\partial D}\frac{\partial D}{\partial \boldsymbol{\varepsilon}} = (1-D)\frac{\partial \boldsymbol{C}^{\mathrm{S}}}{\partial \boldsymbol{\varepsilon}} - \boldsymbol{C}^{\mathrm{S}} \otimes \frac{\partial D}{\partial \boldsymbol{\varepsilon}}, \tag{B.25}$$

where the derivative $\frac{\partial D}{\partial \boldsymbol{\varepsilon}}$ is given in Appendix B.5.

B.4 Eshelby tensor derivatives

For the sake of conciseness, in this section the subscript referring to the phase is omitted. Besides, $\boldsymbol{C}^{\mathrm{S}}$, κ_s, μ_s and $\boldsymbol{C}^{\mathrm{SD}}$, κ_s^{D} and μ_s^{D} respectively stand either for $\boldsymbol{C}^{\mathrm{Sr}}$, Equation (3.67), κ_s^{r}, μ_s^{r}, Equation (3.68), $\boldsymbol{C}^{\mathrm{SDr}}$, Equation (3.72), κ_s^{Dr} and μ_s^{Dr}, Equation (3.74), or for $\boldsymbol{C}^{\mathrm{S0}}$, Equation (3.70), κ_s^0, μ_s^0, Equation (3.71), $\boldsymbol{C}^{\mathrm{SD0}}$, Equation (3.75), κ_s^{D0} and μ_s^{D0}, Equation (3.77).

For the elasto-plastic case, the derivative of the Eshelby tensor writes:

$$\frac{\partial \boldsymbol{S}}{\partial \Delta \boldsymbol{\varepsilon}^{\mathrm{r}}} = \frac{\partial \boldsymbol{S}}{\partial \nu} \otimes \left(\frac{\partial \nu}{\partial \kappa_s}\frac{\partial \kappa_s}{\partial \Gamma} + \frac{\partial \nu}{\partial \mu_s}\frac{\partial \mu_s}{\partial \Gamma}\right)\frac{\partial \Gamma}{\partial \Delta \boldsymbol{\varepsilon}^{\mathrm{r}}}, \tag{B.26}$$

where the derivative $\frac{\partial \Gamma}{\partial \boldsymbol{\varepsilon}}$ is given in Appendix B.1 and the derivatives of the bulk and shear moduli are given in Equation (B.24).

For the damage-enhanced elasto-plastic case, in which the damaged secant moduli are used, the derivative of the Eshelby tensor is written as

$$\begin{aligned}\frac{\partial \boldsymbol{S}}{\partial \Delta \boldsymbol{\varepsilon}^{\mathrm{r}}} =& \frac{\partial \boldsymbol{S}}{\partial \nu} \otimes \left[\frac{\partial \nu}{\partial \kappa_s^D}\left(-\frac{\partial D}{\partial \varepsilon^{\mathrm{r}}}\kappa_s + (1-D)\frac{\partial \kappa_s}{\partial \Gamma}\frac{\partial \Gamma}{\partial \Delta \varepsilon^{\mathrm{r}}}\right)\right.\\ &\left. + \frac{\partial \nu}{\partial \mu_s^D}\left(-\frac{\partial D}{\partial \varepsilon^{\mathrm{r}}}\mu_s + (1-D)\frac{\partial \mu_s}{\partial \Gamma}\frac{\partial \Gamma}{\partial \Delta \varepsilon^{\mathrm{r}}}\right)\right],\end{aligned} \tag{B.27}$$

where $\frac{\partial D}{\partial \boldsymbol{\varepsilon}^{\mathrm{r}}}$ is given in Appendix B.5.

B.5 Derivatives of the damage law used in Section 3

For the sake of conciseness, in this section the subscript referring to the phase is omitted.

By using the damage evolution law depicted in Equation (3.101), the derivatives needed for the incremental-secant based MFH implementation write

$$\frac{\partial D}{\partial \boldsymbol{\varepsilon}} = \frac{\partial D}{\partial \Delta \boldsymbol{\varepsilon}^{\mathrm{r}}} = 0, \tag{B.28}$$

and

$$\frac{\partial D}{\partial \breve{p}} = \begin{cases} \frac{D_{\mathrm{onset}}}{\breve{p}_{\mathrm{onset}}}, & \text{if} \quad \breve{p}_0 \leq \breve{p}_{\mathrm{onset}}\,; \\[2ex] \frac{D_{\mathrm{onset}}}{\breve{p}_{\mathrm{onset}}} + \alpha_{\mathrm{Dam}}\beta_{\mathrm{Dam}}\left(\breve{p}_0 + \Delta\breve{p}_0 - \breve{p}_{\mathrm{onset}}\right)^{\beta_{\mathrm{Dam}}-1}\Delta\breve{p}_0 & \text{if} \quad \breve{p}_0 > \breve{p}_{\mathrm{onset}}. \\ +\alpha_{\mathrm{Dam}}\left(\breve{p}_0 + \Delta\breve{p}_0 - \breve{p}_{\mathrm{onset}}\ \right)^{\beta_{\mathrm{Dam}}} & \end{cases} \tag{B.29}$$

B.6 Damage-Enhanced 2D MFH vs direct finite element simulations

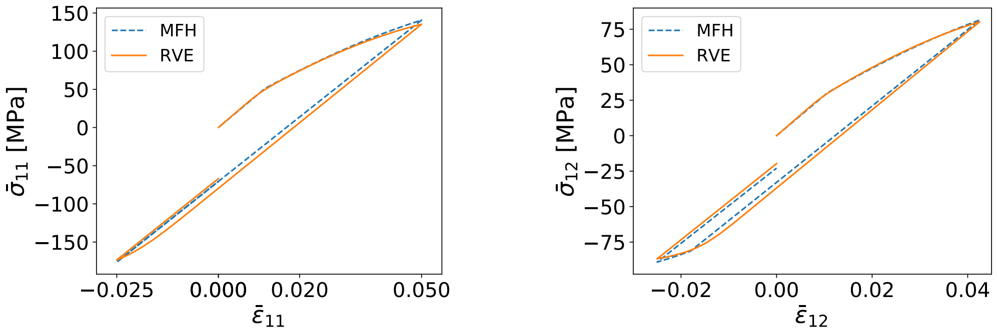

FIGURE B.1: Stress-strain curves for the damage-enhanced uniaxial loading test ($\bar{\boldsymbol{\sigma}}_{22} = 0$) on a 40% fiber volume fraction 2D UD sample(left), and stress-strain curves for the damage-enhanced shear loading test on a 40% fiber volume fraction 2D UD sample (right).

Uniaxial, shear and biaxial loading Concerning the uniaxial cyclic test, looking at Figure B.1 the same comments as on the elasto-plastic case can be applied to this simulation since an overestimation of the stress is seen by the material on the final stage of the loading path. As shown in Figure B.1, similar results are obtained again for the low strain shear cyclic loading, proving once again that the presence of damage in the matrix has no impact in the MFH prediction capabilities. A slight difference in the slope is seen as in the previous cases in the unloading path, but one can conclude that the damaged matrix case under shear loading is well captured by the MFH scheme.

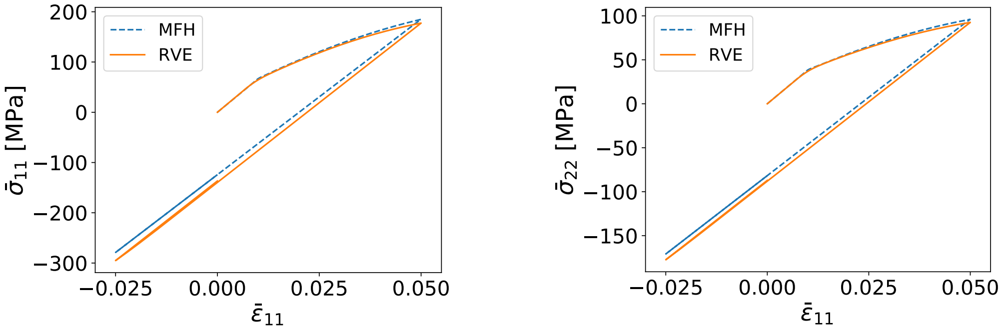

FIGURE B.2: Loading and transverse direction stress-strain curves for the damage-enhanced biaxial loading test ($\bar{\varepsilon}_{22} = 0$) on the 40% fiber volume fraction 2D UD RVE sample.

The next test used to compare the MFH performance with the full-field simulation is biaxial tension. This simulation allows assessing how the MFH scheme is able to correctly represent the pressure-dependent behavior in the case where damage is present in the matrix. Figure B.2 proves the accuracy of the MFH simulation is not impacted by the presence of damage in the matrix and it is able to correctly capture the behavior of the composite on both in-plane directions.

Nonproportional Loading The same nonproportional loading test as the one performed for the elasto-plastic case is now performed taking damage into account, so that the impact of damage on the obtained result can be addressed. Figures B.3 and B.4 show a good behavior of the MFH prediction under nonproportional loading conditions when damage is taken into account. For the first half of the simulation in which the loading occurs, the composite behavior is correctly captured for both tests, where a slightly stiffer behavior is encountered, overestimating the stress

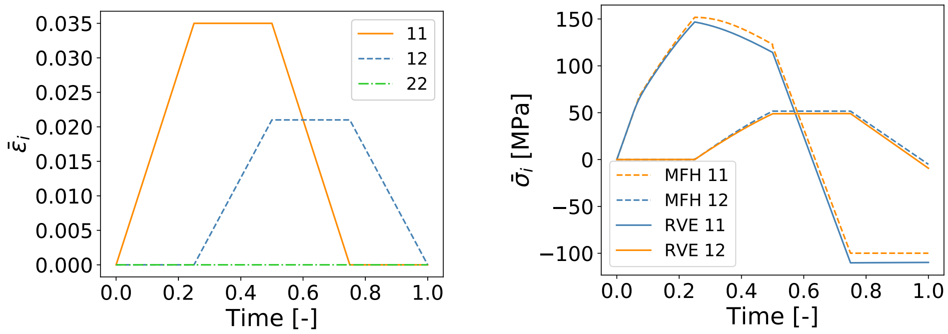

FIGURE B.3: Strain-time evolution (left) and stress-time evolution (right) of the damage-enhanced nonproportional loading with zero-transverse strain, $\bar{\varepsilon}_{22} = 0$, on a 40% fiber volume fraction 2D UD sample.

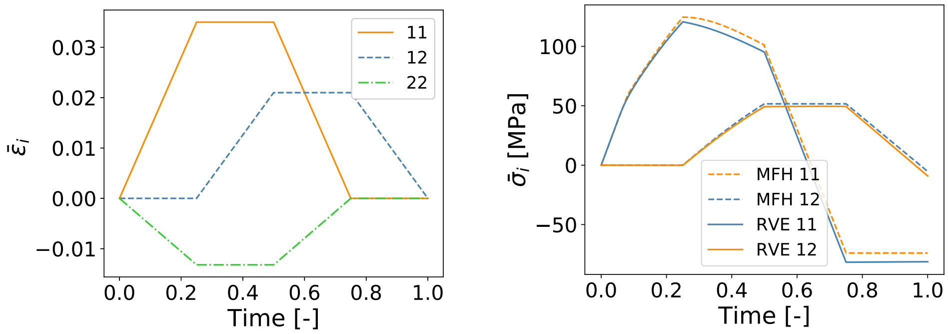

FIGURE B.4: Strain-time evolution (left) and stress-time evolution (right) of the damage-enhanced nonproportional loading with transverse compression, $\bar{\varepsilon}_{22} \neq 0$, on a 40% fiber volume fraction 2D UD sample.

seen by the composite. As already discussed, the difference in the slope during the unloading phases of the cycle is still present; however, the obtained MFH prediction can be said to be satisfactory.

Appendix C

Appendix related to Chapter 4

C.1 : Statistical properties of the microstructure

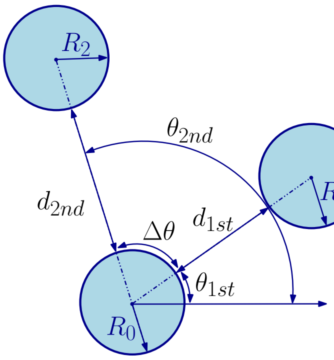

FIGURE C.1: Schematic representation of the statistical characteristics of the generated microstructure and its descriptors.

The generated microstructures were built using the algorithm developed by Wu et al. (2018), where the empirical statistical parameters of the microstructures extracted from SEM images were use as dependent variables. Five different random variables are used for the characterization of these microstructures: the fiber radius R, the nearest/neighbor net distance d_{1st}, the orientation θ_{1st} of the undirected line connecting these two fiber center points, the difference Δd between the net distances to the second neighbor (d_{2nd}) and the first /neighbor (d_{1st}), and the difference $\Delta\theta$ between the orientations of the second neighbor (θ_{2nd}) and the first nearest neighbor (θ_{1st}). A schematic representation of these descriptors is shown in Fig. C.1. Besides their distribution, their correlation was evaluated from the SEM images information. The fiber radius was found to be independent while the other parameters had a correlation matrix $\mathbf{R}$ as:

$$\mathbf{R} = \begin{array}{c} \\ d_{\mathrm{1st}} \\ \theta_{\mathrm{1st}} \\ \Delta d \\ \Delta\theta \end{array} \begin{array}{c} \begin{array}{cccc} d_{\mathrm{1st}} & \theta_{\mathrm{1st}} & \Delta d & \Delta\theta \end{array} \\ \begin{pmatrix} 1.0 & 0.014 & 0.205 & 0.022 \\ & 1.0 & 0.002 & 0.020 \\ \text{symmetric} & & 1.0 & -0.005 \\ & & & 1.0 \end{pmatrix} \end{array} . \tag{C.1}$$

However, since the distributions exhibit non-Gaussianity, the statistical dependence of these random variables were assessed by their distance correlations matrix $\mathbf{dR}$ following Székely, Rizzo, and Bakirov (2007), which reads in this case

$$\mathbf{dR} = \begin{array}{ccccc} & d_{1\text{st}} & \Theta_{1\text{st}} & \Delta d & \Delta\theta \\ d_{1\text{st}} & 1.0 & 0.040 & 0.273 & 0.075 \\ \theta_{1\text{st}} & & 1.0 & 0.048 & 0.046 \\ \Delta d & \text{symmetric} & & 1.0 & 0.064 \\ \Delta\theta & & & & 1.0 \end{array}, \tag{C.2}$$

showing that two parameters should be considered as dependent.

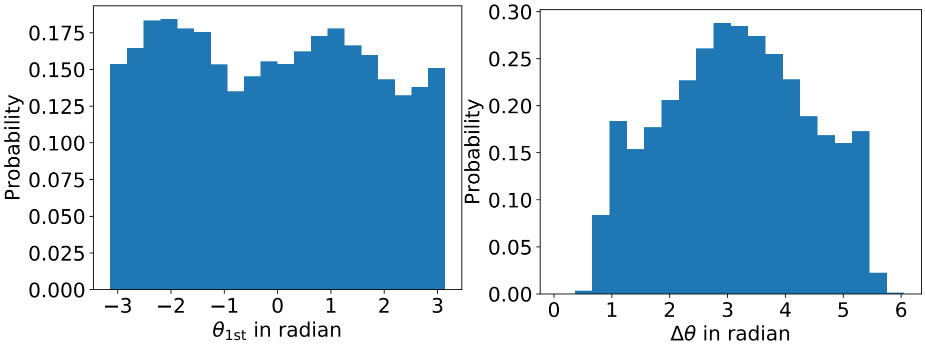

(a) Nearest-neighbor orientation (b) Difference between nearest-neighbor orientations

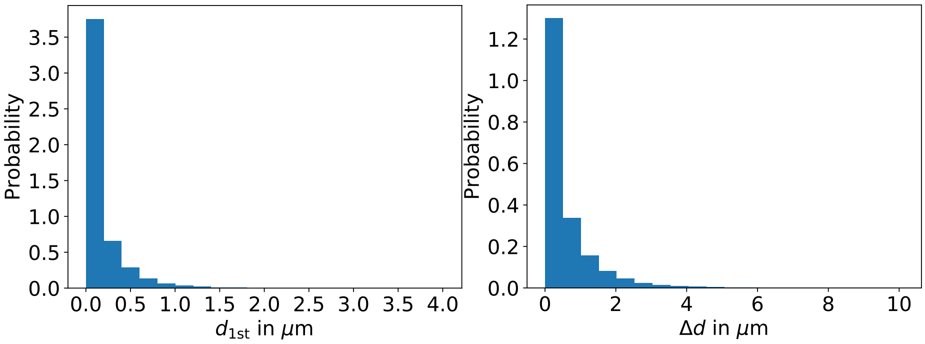

(c) Nearest-neighbor net distance (d) Net distances difference

FIGURE C.2: Probability density histograms for the parameters characterizing the fibers spatial properties of the generated microstructures: (a) Nearest-neighbor orientation $\theta_{1\text{st}}$ distribution (b) Difference between nearest-neighbor orientations $\Delta\theta$ distribution (c) Nearest-neighbor net distance $d_{1\text{st}}$ distribution (d) Difference between the net distances to the second and to the first nearest-neighbors Δd distribution.

Using the copula constructed from their cumulative distributions for the two dependent variables and using the inverse transform sampling method based on their cumulative distribution for the three independent variables, a generator was constructed by Wu et al. (2018), in which the targeted volume fraction can be tuned, see also Noels (2022). In the present work, a targeted volume fraction of 40% was set, and the resulting distributions of the microstructure descriptors are provided in Figs. C.2 and C.3.

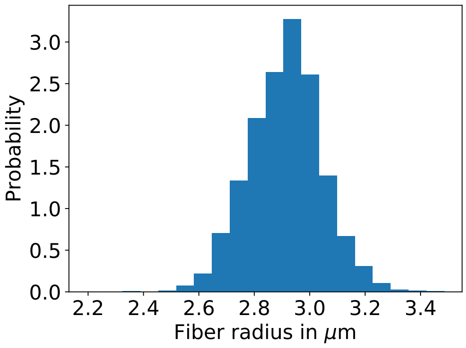

FIGURE C.3: Probability density histograms of fiber radius from the generated microstructures.

C.2 : Effective random parameter probability density distribution

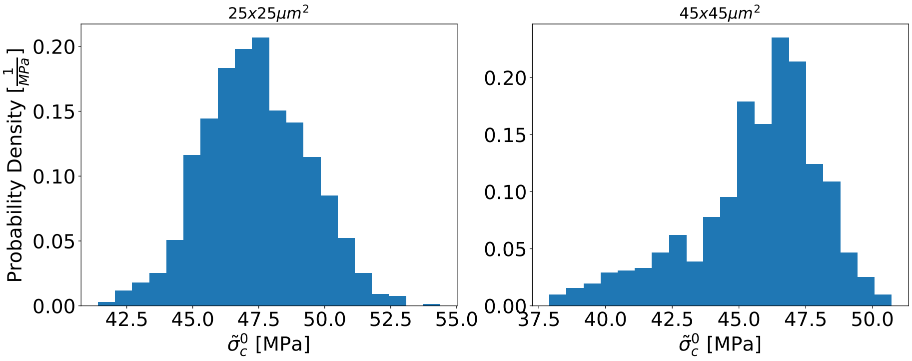

FIGURE C.4: Probability density function of the effective compressive initial yield stress for the $25 \times 25\mu m^2$ and $45 \times 45\mu m^2$ SVE cases.

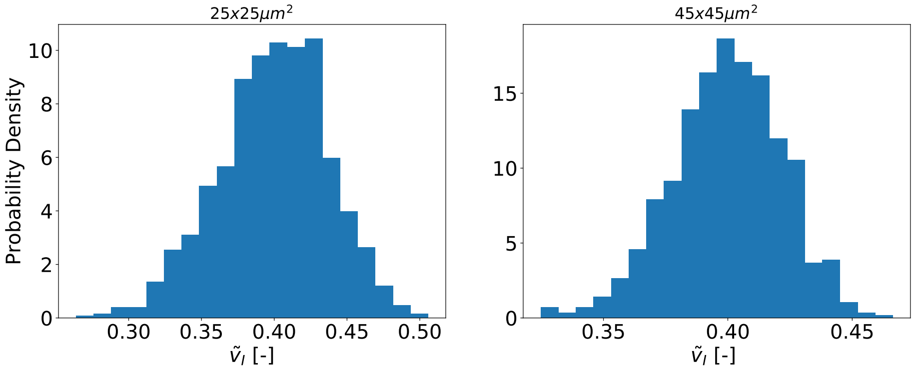

FIGURE C.5: Probability density histogram of the effective fiber volume fraction for the $25 \times 25\mu m^2$ and $45 \times 45\mu m^2$ SVE cases.

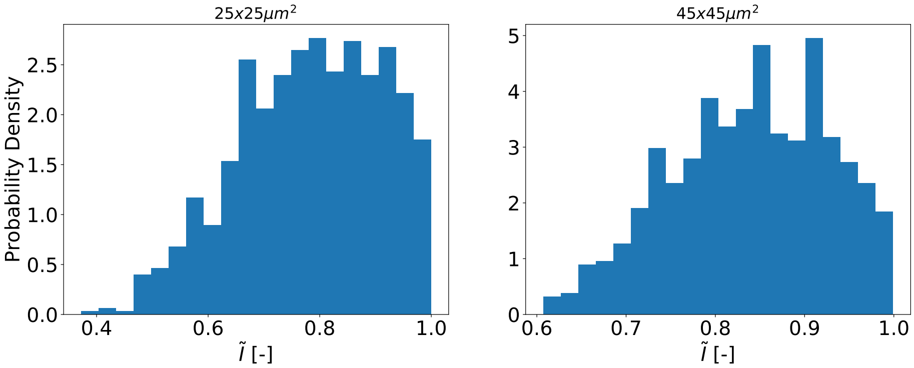

FIGURE C.6: Probability density histogram of the effective aspect ratio for the $25 \times 25\mu m^2$ and $45 \times 45\mu m^2$ SVE cases.

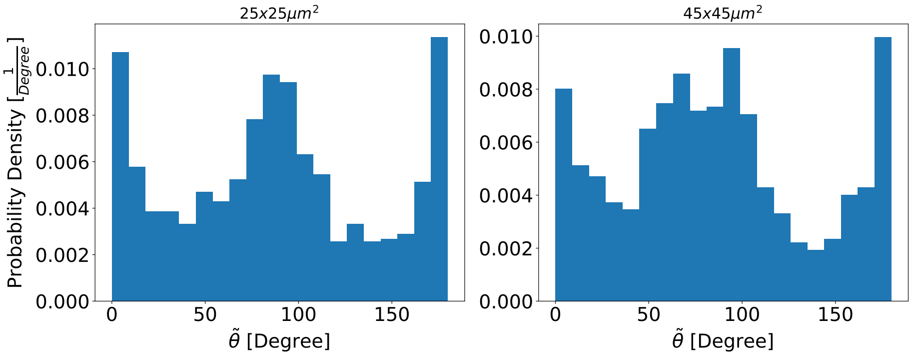

FIGURE C.7: Probability density histogram of the effective angle for the $25 \times 25\mu m^2$ and $45 \times 45\mu m^2$ SVE cases.

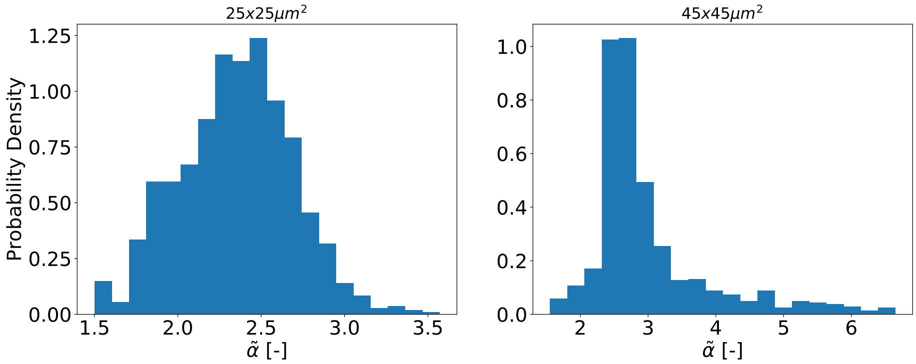

FIGURE C.8: Probability density histogram of the exponent $\tilde{\alpha}$, $25 \times 25 \mu m^2$ and $45 \times 45 \mu m^2$ SVE cases.

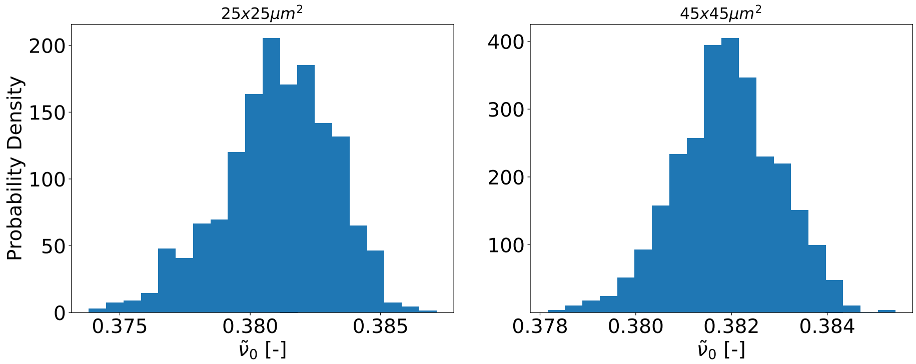

FIGURE C.9: Probability density histogram of the effective Poisson's ratio for the $25 \times 25 \mu m^2$ and $45 \times 45 \mu m^2$ SVE cases.

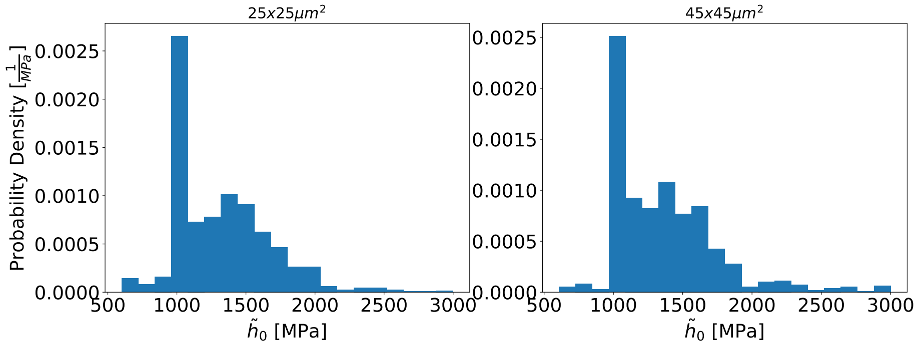

FIGURE C.10: Probability density histogram of the effective hardening parameter h_0 for the $25 \times 25 \mu m^2$ and $45 \times 45 \mu m^2$ SVE cases.

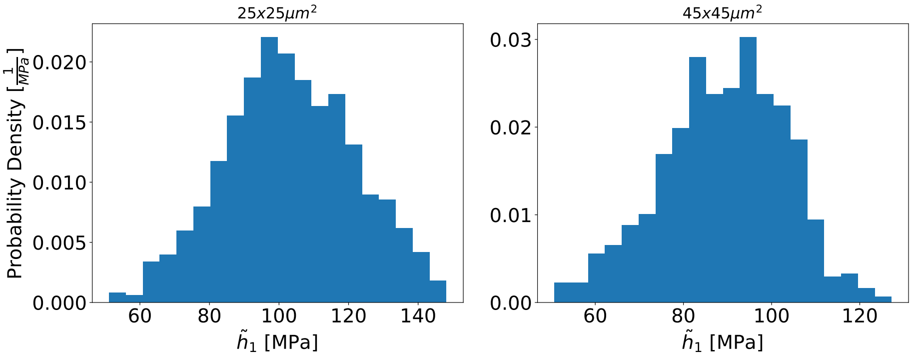

FIGURE C.11: Probability density histogram of the effective hardening parameter h_1 for the $25 \times 25\mu m^2$ and $45 \times 45\mu m^2$ SVE cases.

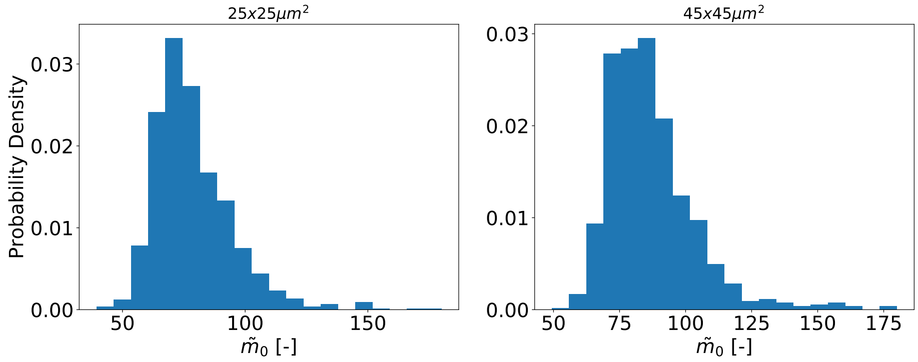

FIGURE C.12: Probability density histogram of the effective hardening parameter m_0 for the $25 \times 25\mu m^2$ and $45 \times 45\mu m^2$ SVE cases.

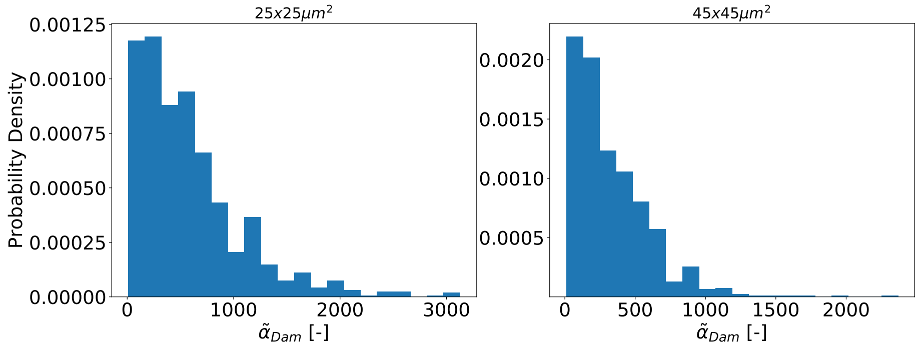

FIGURE C.13: Probability density histogram of the effective parameter α_{Dam} for the $25 \times 25\mu m^2$ and $45 \times 45\mu m^2$ SVE cases.

C.3 : Results of the 45×45 square micrometers SVE MF-ROM

C.3.1 Statistical analysis of random effective parameters

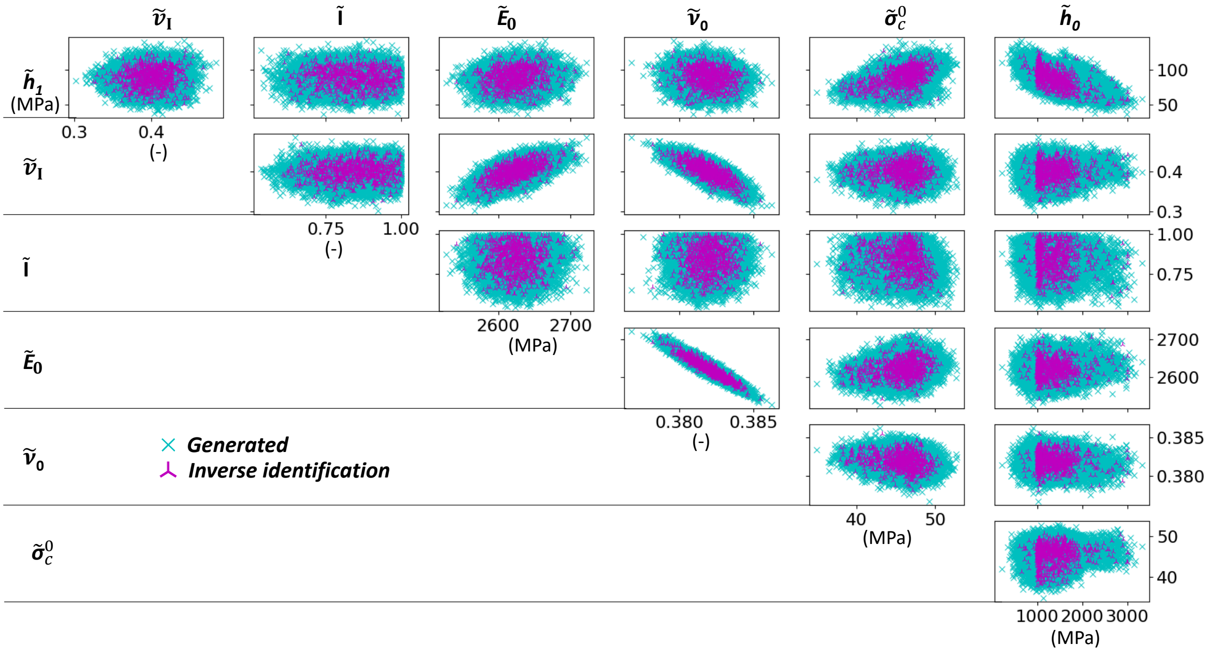

FIGURE C.14: $45\times45\mu m^2$ effective random parameters distributions and their cross-dependence for the identified and generated $\tilde{v}_{\mathrm{I}}, \tilde{\mathrm{I}}, \tilde{E}_0, \tilde{\nu}_0, \tilde{\sigma}_c^0, \tilde{h}_0$ and $\tilde{h}_1$.

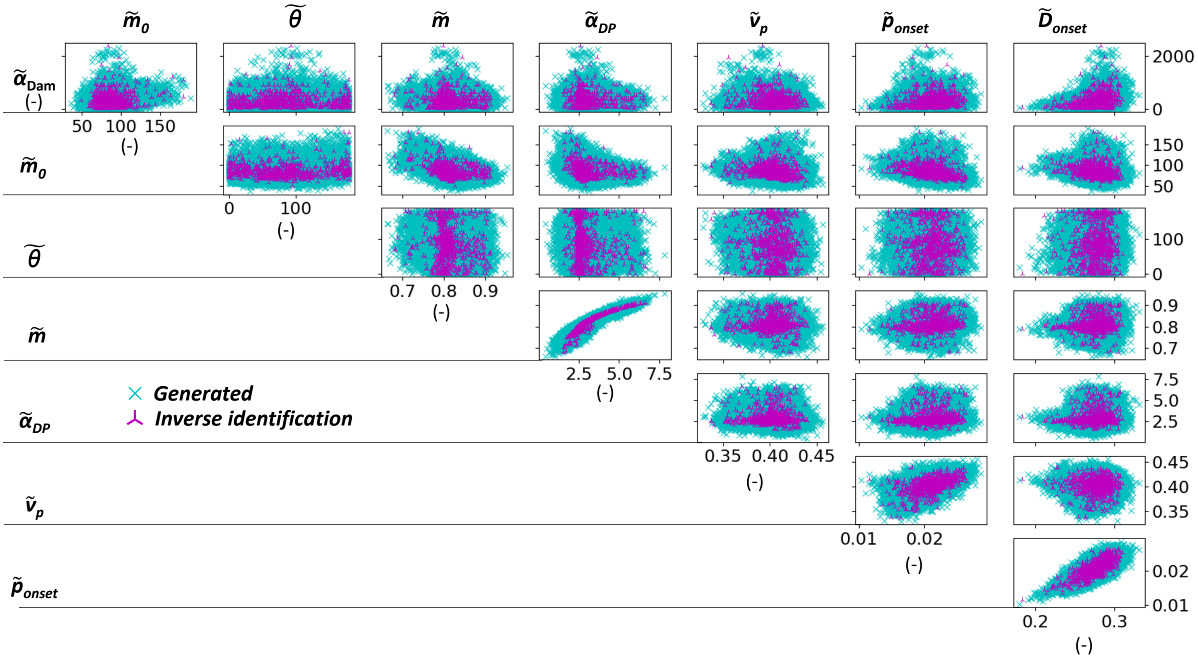

FIGURE C.15: $45\times45\mu m^2$ effective random parameters distributions and their cross-dependence for the identified and generated $\tilde{m}_0, \tilde{\theta}, \tilde{m}, \tilde{\nu}_p, \tilde{\alpha}, \tilde{p}_{\text{onset}}$, $\widetilde{D}_{\text{onset}}$ and $\tilde{\alpha}_{\text{Dam}}$.

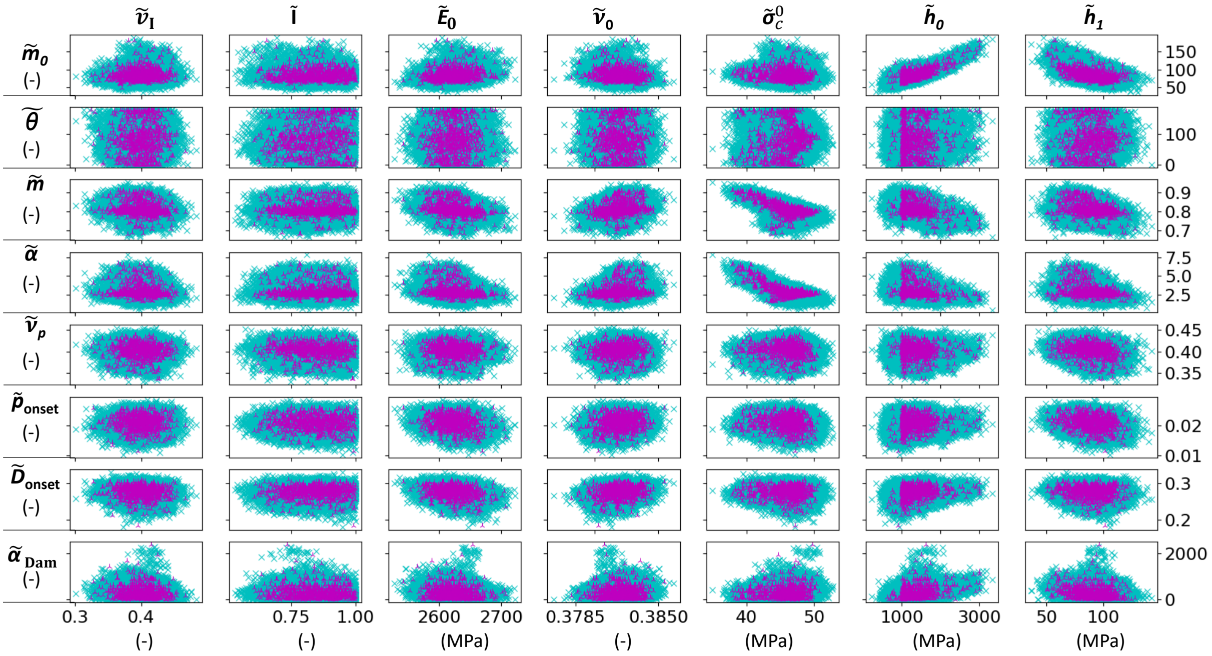

FIGURE C.16: $45\text{x}45\mu m^2$ effective random parameters distributions and their cross-dependence for the identified and generated $\tilde{\upsilon}_{\text{I}}, \tilde{\text{I}}, \tilde{\theta}, \tilde{E}_0, \tilde{\nu}_0, \tilde{\sigma}_c^0, \tilde{h}_0, \tilde{h}_1, \tilde{m}_0, \tilde{m}, \tilde{\nu}_p, \tilde{\alpha}, \tilde{p}_{\text{onset}}$, $\widetilde{D}_{\text{onset}}$ and $\tilde{\alpha}_{\text{dam}}$.

C.4 Stochastic MF-ROM mesh convergence study

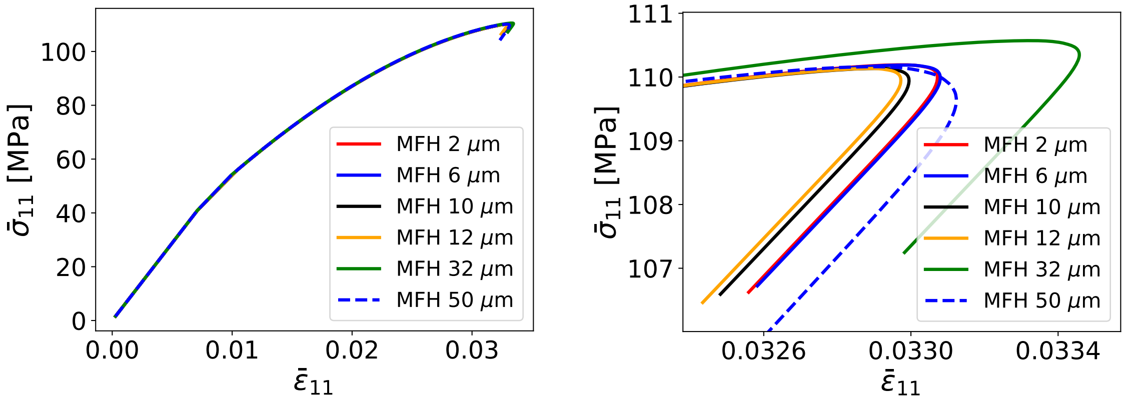

FIGURE C.17: Effect of the macroscale mesh size on a uniaxial loading test conducted on a 500x250μm^2 ply with the MF-ROM defined using 25x25μm^2 SVEs. Results on the left are zoomed on the right.

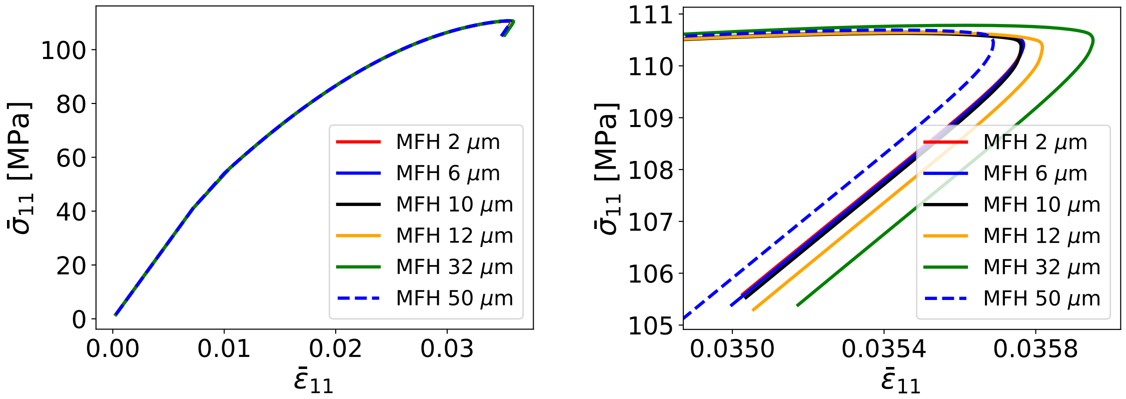

FIGURE C.18: Effect of the macroscale mesh size on a uniaxial loading test conducted on a 500x250μm^2 ply with the MF-ROM defined using 45x45μm^2 SVEs. Results on the left are zoomed on the right.

A convergence study is performed for the stochastic MF-ROM by considering different sizes of the macroscale finite elements ranging from 2μm to 50μm. To this end, we consider two ply realizations, one using 25x25μm^2 SVEs, Fig. C.17 and another one using 45x45μm^2 SVEs, Fig. C.18. As a reminder, the characteristic length l, of the nonlocal MFH formulation was fixed to a value of 25 μm for both SVE sizes. It clearly appears that for finite elements larger or close to the SVE size, i.e. 32μm and 50μm for the 25x25μm^2 SVEs and the 45x45μm^2 SVEs, and larger than the nonlocal length l the results are outliers when analyzing the maximum reached stress. For the other mesh sizes, the results are close, within a 0.3% in terms of the maximum stress, which is well below the variability observed for different ply realizations, see e.g. in Fig. 4.35. The observed variability in the results is mainly explained by the variable step length of the path-following method, which yields slight inaccuracy when performing the time integration.

Bibliography

Aboudi, Jacob (Oct. 1996). "Micromechanical Analysis of Composites by the Method of Cells - Update". In: *Applied Mechanics Reviews* 49(10S), S83–S91. ISSN: 0003-6900. DOI: 10.1115/1.3101981. eprint: https://asmedigitalcollection.asme.org/appliedmechanicsreviews/article-pdf/49/10S/S83/5437472/s83_1.pdf. URL: https://doi.org/10.1115/1.3101981.

Aifantis, E. (1992). "On the role of gradients in the localization of deformation and fracture". In: *Int. Journal Eng. Sci.* 30, pp. 1279–1299.

Al-Rub, R. K. Abu, A. H. Tehrani, and M. K. Darabi (2015). "Application of a large deformation nonlinear-viscoelastic viscoplastic viscodamage constitutive model to polymers and their composites". In: *International Journal of Damage Mechanics* 24(2), pp. 198–244. DOI: 10.1177/1056789514527020. eprint: https://doi.org/10.1177/1056789514527020. URL: https://doi.org/10.1177/1056789514527020.

Arruda, E. M., M. C. Boyce, and R. Jayachandran (1995). "Effects of strain rate, temperature and thermomechanical coupling on the finite strain deformation of glassy polymers". In: *Mechanics of Materials* 19(2), pp. 193–212. ISSN: 0167-6636. DOI: https://doi.org/10.1016/0167-6636(94)00034-E. URL: https://www.sciencedirect.com/science/article/pii/016766369400034E.

Balieu, R. et al. (2013). "A fully coupled elastoviscoplastic damage model at finite strains for mineral filled semi-crystalline polymer". In: *Int. Journ. of Plast.*

Balieu, R. et al. (2014). "Non associated viscoplasticity coupled with an integral type nonlocal damage model for mineral filled semi crystalline polymers". In: *Comp. and Struct.*

Barbero, EJ., GF. Abdelal, and A. Caceres (2005). "A micromechanics approach for damage modeling of polymer matrix composites". In: *Comp. Struct.*

Bažant, Z.P., T.B. Belytchko, and T.P. Chang (1984). "Continuum theory for strain-softening". In: *Journal. Eng. Mech.* 110, pp. 1666–1692.

Benveniste, Y. (1987). "A new approach to the application of Mori-Tanaka's theory in composite materials". In: *Mechanics of Materials* 6(2), pp. 147–157. ISSN: 0167-6636. DOI: https://doi.org/10.1016/0167-6636(87)90005-6. URL: https://www.sciencedirect.com/science/article/pii/0167663687900056.

Berveiller, M. and A. Zaoui (1978). "An extension of the self-consistent scheme to plastically-flowing polycrystals". In: *Journal of the Mechanics and Physics of Solids* 26(5), pp. 325–344. ISSN: 0022-5096. DOI: https://doi.org/10.1016/0022-5096(78)90003-0. URL: https://www.sciencedirect.com/science/article/pii/0022509678900030.

Bessa, M.A. et al. (2017). "A framework for data-driven analysis of materials under uncertainty: Countering the curse of dimensionality". In: *Computer Methods in Applied Mechanics and Engineering* 320, pp. 633–667. ISSN: 0045-7825. DOI: https://doi.org/10.1016/j.cma.2017.03.037. URL: https://www.sciencedirect.com/science/article/pii/S0045782516314803.

Blacklock, M. et al. (2012). "Generating virtual textile composite specimens using statistical data from micro-computed tomography: 1D tow representations for the Binary Model". In: *Journal of the Mechanics and Physics of Solids* 60(3), pp. 451–470. ISSN: 0022-5096. DOI: https://doi.org/10.1016/j.jmps.2011.11.010. URL: https://www.sciencedirect.com/science/article/pii/S0022509611002225.

Bodner, S. R. and Y. Partom (June 1975). “Constitutive Equations for Elastic-Viscoplastic Strain-Hardening Materials”. In: *Journal of Applied Mechanics* 42(2), pp. 385–389. ISSN: 0021-8936. DOI: `10.1115/1.3423586`. eprint: `https://asmedigitalcollection.asme.org/appliedmechanics/article-pdf/42/2/385/5454575/385\_1.pdf`. URL: `https://doi.org/10.1115/1.3423586`.

Bonet, J. and A.J. Burton (1998). “A simple orthotropic, transversely isotropic hyperelastic constitutive equation for large strain computations”. In: *Computer Methods in Applied Mechanics and Engineering* 162(1), pp. 151–164. ISSN: 0045-7825. DOI: `https://doi.org/10.1016/S0045-7825(97)00339-3`. URL: `https://www.sciencedirect.com/science/article/pii/S0045782597003393`.

Bornert, M., T. Bretheau, and P. Gilormini (2001). “Homogénéisation des milieux aléatoires : bornes et estimations.” In: *Homogénéisation en mécanique des matériaux* 1, pp. 133–222.

Boudet, J. et al. (2016). “An incremental variational formulation for the prediction of the effective work-hardening behavior and field statistics of elasto-(visco)plastic composites”. In: *International Journal of Solids and Structures* 83, pp. 90–113. ISSN: 0020-7683. DOI: `https://doi.org/10.1016/j.ijsolstr.2016.01.003`. URL: `https://www.sciencedirect.com/science/article/pii/S0020768316000068`.

Boyce, M. C., D. M. Parks, and A. S. Argon (1988). “Large inelastic deformation of glassy polymers. part I: rate dependent constitutive model”. In: *Mechanics of Materials* 7, pp. 15–33.

Boyce, M.C., E.M. Arruda, and R. Jayachandran (1994). “The large strain compression, tension, and simple shear of polycarbonate”. In: *Polym. Eng. Sci.*

Brassart, L. et al. (2011). “A variational formulation for the incremental homogenization of elasto-plastic composites”. In: *Journal of the Mechanics and Physics of Solids* 59(12), pp. 2455–2475. ISSN: 0022-5096. DOI: `https://doi.org/10.1016/j.jmps.2011.09.004`. URL: `https://www.sciencedirect.com/science/article/pii/S0022509611001712`.

Brassart, L. et al. (2012). “Homogenization of elasto-(visco) plastic composites based on an incremental variational principle”. In: *International Journal of Plasticity* 36, pp. 86–112. ISSN: 0749-6419. DOI: `https://doi.org/10.1016/j.ijplas.2012.03.010`. URL: `https://www.sciencedirect.com/science/article/pii/S0749641912000502`.

Brunner, Andreas J., René Alderliesten, and John-Alan Pascoe (2023). “In-Service Delaminations in FRP Structures under Operational Loading Conditions: Are Current Fracture Testing and Analysis on Coupons Sufficient for Capturing the Essential Effects for Reliable Predictions?” In: *Materials* 16(1). ISSN: 1996-1944. DOI: `10.3390/ma16010248`. URL: `https://www.mdpi.com/1996-1944/16/1/248`.

Buckley, C. et al. (1994). “Deformation of thermosetting resins at impact rates of strain. part i: Experimental study”. In: *Journ. Mech. Phys. Sol.*

Buhan, M. de and P. Frey (2011). “A generalized model of non-linear viscoelasticity: numerical issues and applications”. In: *International Journal for Numerical Methods in Engineering* 86(13), pp. 1544–1557. DOI: `https://doi.org/10.1002/nme.3115`. eprint: `https://onlinelibrary.wiley.com/doi/pdf/10.1002/nme.3115`. URL: `https://onlinelibrary.wiley.com/doi/abs/10.1002/nme.3115`.

Calleja Vázquez, J. M. et al. (2022). “An incremental-secant mean-field homogenization model enhanced with a non-associated pressure-dependent plasticity model”. In: *International Journal for Numerical Methods in Engineering* 123(19), pp. 4616–4654. DOI: `https://doi.org/10.1002/nme.7048`. eprint: `https://onlinelibrary.wiley.com/doi/pdf/10.1002/nme.7048`. URL: `https://onlinelibrary.wiley.com/doi/abs/10.1002/nme.7048`.

Calleja Vázquez, Juan Manuel et al. (2023). *Data of A micromechanical Mean-Field Homogenization surrogate for the stochastic multiscale analysis of composite materials failure.* DOI: `10.5281/zenodo.7998798`. URL: `https://doi.org/10.5281/zenodo.7998798`.

Calleja Vázquez, Juan Manuel et al. (2023). “A micromechanical mean-field homogenization surrogate for the stochastic multiscale analysis of composite materials failure”. In: *International Journal for Numerical Methods in Engineering* 124(23), pp. 5200–5262. DOI: `https://doi.org/10.1002/nme.7344`. eprint: `https://onlinelibrary.wiley.com/doi/pdf/10.1002/nme.7344`. URL: `https://onlinelibrary.wiley.com/doi/abs/10.1002/nme.7344`.

Carrere, N. et al. (2004). “Multiscale analysis of the transverese properties of ti-based matrix composites reinforced by sic fibres: from the grain scale to the macroscopic scale”. In: *Int. J. Plasticity* 20, pp. 783–810.

Carvalho, P.R.P., H.B. Coda, and R.A.K. Sanches (2023). “A large strain thermodynamically-based viscoelastic-viscoplastic model with application to finite element analysis of polytetrafluoroethylene (PTFE)”. In: *European Journal of Mechanics - A/Solids* 97, p. 104850. ISSN: 0997-7538. DOI: `https://doi.org/10.1016/j.euromechsol.2022.104850`. URL: `https://www.sciencedirect.com/science/article/pii/S0997753822002807`.

Castaneda, P. Ponte (1991). “The effective mechanical properties of nonlinear isotropic composites”. In: *Journal of the Mechanics and Physics of Solids* 39(1), pp. 45–71. ISSN: 0022-5096. DOI: `https://doi.org/10.1016/0022-5096(91)90030-R`. URL: `https://www.sciencedirect.com/science/article/pii/002250969190030R`.

Castaneda, P. Ponte (1992). “A New Variational Principle and its Application to Nonlinear Heterogeneous Systems”. In: *SIAM Journal on Applied Mathematics* 52(5), pp. 1321–1341. ISSN: 00361399. URL: `http://www.jstor.org/stable/2102311` (visited on 09/08/2022).

Chaboche, J.L., P. Kanouté, and A. Roos (2005). “On the capabilities of mean-field approaches for the description of plasticity in metal matrix composites”. In: *International Journal of Plasticity* 21(7), pp. 1409–1434. ISSN: 0749-6419. DOI: `https://doi.org/10.1016/j.ijplas.2004.07.001`. URL: `https://www.sciencedirect.com/science/article/pii/S0749641904001433`.

Charmpis, D.C., G.I. Schuëller, and M.F. Pellissetti (2007). “The need for linking micromechanics of materials with stochastic finite elements: A challenge for materials science”. In: *Computational Materials Science* 41(1), pp. 27–37. ISSN: 0927-0256. DOI: `https://doi.org/10.1016/j.commatsci.2007.02.014`. URL: `https://www.sciencedirect.com/science/article/pii/S0927025607000602`.

Chen, W., F. Lu, and M. Cheng (2002). “Tension and compression tests of two polymers under quasi-static and dynamic loading”. In: *Polym. Test.*

Cheng, L. et al. (2015). “A bipotential-based limit analysis and homogenization of ductile porous materials with non-associated Drucker-Prager matrix”. In: *Journal of the Mechanics and Physics of Solids* 77, pp. 1–26.

Chevalier, J., P.P. Camanho, and T. Pardoen (2019). “Multi-scale characterization and modelling of the transverse compression response of unidirectional carbon fiber reinforced epoxy”. In: *Comp. Struct.*

Chowdhury, K. A., R. Talreja, and A. A. Benzerga (Mar. 2008). “Effects of Manufacturing-Induced Voids on Local Failure in Polymer-Based Composites”. In: *Journal of Engineering Materials and Technology* 130(2). 021010. ISSN: 0094-4289. DOI: `10.1115/1.2841529`. eprint: `https://asmedigitalcollection.asme.org/materialstechnology/article-pdf/130/2/021010/5726673/021010\_1.pdf`. URL: `https://doi.org/10.1115/1.2841529`.

Chowdhury, K.A., A.A. Benzerga, and R. Talreja (2008). “An analysis of impact-induced deformation and fracture modes in amorphous glassy polymers”. In: *Engineering Fracture Mechanics* 75(11). Local Approach to Fracture (1986-2006): Selected papers from the 9th European Mechanics of Materials Conference, pp. 3328–3342. ISSN: 0013-7944. DOI: `https://doi.org/10.1016/j.engfracmech.2007.08.007`. URL: `https://www.sciencedirect.com/science/article/pii/S0013794407003451`.

Christensen, R.M. and K.H. Lo (1979). “Solutions for effective shear properties in three phase sphere and cylinder models”. In: *Mech. Phys. Solids* 27, pp. 315–330.

Clément, A., C. Soize, and J. Yvonnet (2012). "Computational nonlinear stochastic homogenization using a nonconcurrent multiscale approach for hyperelastic heterogeneous microstructures analysis". In: *International Journal for Numerical Methods in Engineering* 91(8), pp. 799–824. DOI: https://doi.org/10.1002/nme.4293. eprint: https://onlinelibrary.wiley.com/doi/pdf/10.1002/nme.4293. URL: https://onlinelibrary.wiley.com/doi/abs/10.1002/nme.4293.

Coenen, E., V. Kouznetsova, and M. Geers (2011a). "Enabling microstructure-based damage and localization analyses and upscaling". In: *Model. Simul. Mater. Sci. Eng.* 19, pp. 1–15.

Coenen, E., V. Kouznetsova, and M. Geers (2011b). "Novel boundary conditions for strain localization analyses in microstructural volume elements". In: *Int. Journal Numer. Meth. Eng.* 90, pp. 1–21.

Coenen, E.W.C., V.G. Kouznetsova, and M.G.D. Geers (2012). "Novel boundary conditions for strain localization analyses in microstructural volume elements". In: *International Journal for Numerical Methods in Engineering* 90(1), pp. 1–21. DOI: https://doi.org/10.1002/nme.3298. eprint: https://onlinelibrary.wiley.com/doi/pdf/10.1002/nme.3298. URL: https://onlinelibrary.wiley.com/doi/abs/10.1002/nme.3298.

Colak, O. U. (2005). "Modeling deformation behavior of polymers with viscoplasticity theory based on overstress". English. In: *International Journal of Plasticity* 21(1), pp. 145–160. DOI: 10.1016/j.ijplas.2004.04.004.

Costa, S. et al. (2021). "Modelling damage growth in composites using a unified physically-based finite deformation model". In: *ECCOMAS Them. Conf. on the Mech. Resp. of Comp.*

De Borst, R. (1991). "Simulation of strain localization: a reapprisal of the Cosserat continuum". In: *Eng. Comput.* 8, pp. 317–332.

De Borst, R. et al. (1993). "Fundamental issues in finite element analyses of localization of deformation". In: *Eng. Comput.* 10, pp. 99–121.

Defize, T. et al. (2012). "Multifunctional Poly(e-caprolactone)-Forming Networks by Diels-Alder Cycloaddition: Effect of the Adduct on the Shape-Memory Properties". In: *Macromolecular Chemistry and Physics* 213(2), pp. 187–197. DOI: https://doi.org/10.1002/macp.201100408. eprint: https://onlinelibrary.wiley.com/doi/pdf/10.1002/macp.201100408. URL: https://onlinelibrary.wiley.com/doi/abs/10.1002/macp.201100408.

Division, William J. Hughes Technical Center Aviation Research (2017). "Certification by Analysis - A building Block Methodology for Composite and Metallic Aircraft Crashworthy Structures - Coupon Level". In:

Doghri, I., L. Adam, and N. Bilger (2010). "Mean-field homogenization of elasto-viscoplastic composites based on a general incrementally affine linearization method". In: *International Journal of Plasticity* 26(2), pp. 219–238. ISSN: 0749-6419. DOI: https://doi.org/10.1016/j.ijplas.2009.06.003. URL: https://www.sciencedirect.com/science/article/pii/S0749641909000849.

Doghri, I. and A. Ouaar (2003). "Homogenization of two-phase elasto-plastic composite materials and structures: Study of tangent operators, cyclic plasticity and numerical algorithms". In: *International Journal of Solids and Structures* 40(7), pp. 1681–1712. ISSN: 0020-7683. DOI: https://doi.org/10.1016/S0020-7683(03)00013-1. URL: https://www.sciencedirect.com/science/article/pii/S0020768303000131.

Doghri, I. et al. (2011). "A second-moment incremental formulation for the mean-field homogenization of elasto-plastic composites." In: *International Journal of Plasticity* 27, pp. 352–371.

Drucker, D. C. and W. Prager (1952). "SOIL MECHANICS AND PLASTIC ANALYSIS OR LIMIT DESIGN". In: *Quarterly of Applied Mathematics* 10(2), pp. 157–165. ISSN: 0033569X, 15524485. URL: http://www.jstor.org/stable/43633942 (visited on 11/15/2023).

Dvorak, G.J., A.M. Wafa, and Y.A. Bahei-El-Din (1994). "Implementation of the transformation field analysis for inelastic composite materials". In: *Computational Mechanics* 14(3), pp. 201–228. DOI: 10.1007/BF00370073. URL: https://doi.org/10.1007/BF00370073.

Eshelby, J. D. and R. E. Peierls (1957). "The determination of the elastic field of an ellipsoidal inclusion, and related problems". In: *Proceedings of the Royal Society of London. Series A. Mathematical and Physical Sciences* 241(1226), pp. 376–396. DOI: 10.1098/rspa.1957.0133. eprint: https://royalsocietypublishing.org/doi/pdf/10.1098/rspa.1957.0133. URL: https://royalsocietypublishing.org/doi/abs/10.1098/rspa.1957.0133.

Feyel, F. (1999). "Multiscale FE2 elastoviscoplastic analysis of composite structures". In: *Computational Materials Science* 16, pp. 344–354.

Fiedler, B. et al. (2001). "Failure behavior of an epoxy matrix under different kinds of static loading". In: *Composites Sci. Technol.*

Firooz, Soheil et al. (2019). "Systematic study of homogenization and the utility of circular simplified representative volume element". In: *Mathematics and Mechanics of Solids* 24(9), pp. 2961–2985. DOI: 10.1177/1081286518823834.

Frank, G. J. and R. A. Brockman (2001). "A viscoelastic-viscoplastic constitutive model for glassy polymers". In: *International Journal of Solids and Structures* 38(30), pp. 5149–5164. ISSN: 0020-7683. DOI: https://doi.org/10.1016/S0020-7683(00)00339-5. URL: https://www.sciencedirect.com/science/article/pii/S0020768300003395.

Fritzen, F., M. Fernández, and F. Larsson (2019). "On-the-Fly Adaptivity for Nonlinear Twoscale Simulations Using Artificial Neural Networks and Reduced Order Modeling". In: *Frontiers in Materials* 6. ISSN: 2296-8016. DOI: 10.3389/fmats.2019.00075. URL: https://www.frontiersin.org/articles/10.3389/fmats.2019.00075.

Furukawa, Tomonari and Genki Yagawa (1998). "Implicit constitutive modelling for viscoplasticity using neural networks". In: *International Journal for Numerical Methods in Engineering* 43(2), pp. 195–219. DOI: https://doi.org/10.1002/(SICI)1097-0207(19980930)43:2<195::AID-NME418>3.0.CO;2-6. eprint: https://onlinelibrary.wiley.com/doi/pdf/10.1002/%28SICI%291097-0207%2819980930%2943%3A2%3C195%3A%3AAID-NME418%3E3.0.CO%3B2-6. URL: https://onlinelibrary.wiley.com/doi/abs/10.1002/%28SICI%291097-0207%2819980930%2943%3A2%3C195%3A%3AAID-NME418%3E3.0.CO%3B2-6.

Gajek, Sebastian, Matti Schneider, and Thomas Böhlke (2020). "On the micromechanics of deep material networks". In: *Journal of the Mechanics and Physics of Solids* 142, p. 103984. ISSN: 0022-5096. DOI: https://doi.org/10.1016/j.jmps.2020.103984. URL: https://www.sciencedirect.com/science/article/pii/S0022509620302192.

Gao, X. et al. (2011). "On stress-state dependent plasticity modeling: Significance of the hydrostatic stress, the third invariant of stress deviator and the non-associated flow rule". In: *Int. Journ. of Plast.*

Geers, M. (1997). "Experimental analysis and computational modelling of damage and fracture". In: *Ph.D. thesis. University of Technology, Eindhoven (Netherlands).*

Geers, M.G.D., V.G. Kouznetsova, and W.A.M. Brekeclmans (2010). "Multi-scale computational homogenization: Trends and challenges". In: *Journal of Comp. and Appl. Math.* 234, pp. 20175–2182.

Geers, M.G.D. et al. (1998). "Strain-based transient-gradient damage model for failure analyses". In: *Computer Methods in Applied Mechanics and Engineering* 160(1), pp. 133–153. ISSN: 0045-7825. DOI: https://doi.org/10.1016/S0045-7825(98)80011-X. URL: https://www.sciencedirect.com/science/article/pii/S004578259880011X.

Geers, Marc G. D. et al. (2017). "Homogenization Methods and Multiscale Modeling: Nonlinear Problems". In: *Encyclopedia of Computational Mechanics Second Edition.* John Wiley and Sons, Ltd, pp. 1–34. ISBN: 9781119176817. DOI: https://doi.org/10.1002/9781119176817.ecm2107. eprint: https://onlinelibrary.wiley.com/doi/pdf/10.1002/9781119176817.

ecm2107. URL: https://onlinelibrary.wiley.com/doi/abs/10.1002/9781119176817.ecm2107.

Ghaboussi, J. and D.E. Sidarta (1998). “New nested adaptive neural networks (NANN) for constitutive modeling”. In: *Computers and Geotechnics* 22(1), pp. 29–52. ISSN: 0266-352X. DOI: https://doi.org/10.1016/S0266-352X(97)00034-7. URL: https://www.sciencedirect.com/science/article/pii/S0266352X97000347.

Ghanem, R. and P. Spanos (1991). “Stochastic Finite Elements: A Spectral Approach”. In: *Springer Verlag*.

Ghavamian, F. and A. Simone (2019). “Accelerating multiscale finite element simulations of history-dependent materials using a recurrent neural network”. In: *Computer Methods in Applied Mechanics and Engineering* 357, p. 112594. ISSN: 0045-7825. DOI: https://doi.org/10.1016/j.cma.2019.112594. URL: https://www.sciencedirect.com/science/article/pii/S0045782519304700.

Ghosh, Somnath, Kyunghoon Lee, and Suresh Moorthy (1995). “Multiple scale analysis of heterogeneous elastic structures using homogenization theory and voronoi cell finite element method”. In: *International Journal of Solids and Structures* 32(1), pp. 27–62.

Gorji, Maysam B. et al. (2020). “On the potential of recurrent neural networks for modeling path dependent plasticity”. In: *Journal of the Mechanics and Physics of Solids* 143, p. 103972. ISSN: 0022-5096. DOI: https://doi.org/10.1016/j.jmps.2020.103972. URL: https://www.sciencedirect.com/science/article/pii/S0022509620302076.

Govaert, L. E., P. H. M. Timmermans, and W. A. M. Brekelmans (Nov. 1999). “The Influence of Intrinsic Strain Softening on Strain Localization in Polycarbonate: Modeling and Experimental Validation ”. In: *Journal of Engineering Materials and Technology* 122(2), pp. 177–185. ISSN: 0094-4289. DOI: 10.1115/1.482784. eprint: https://asmedigitalcollection.asme.org/materialstechnology/article-pdf/122/2/177/5880300/177_1.pdf. URL: https://doi.org/10.1115/1.482784.

G'Sell, C. and J.J. Jonas (1995). “Yield and transient effects during the plastic deformation of solid polymers”. In: *Journ. of Mat. Sci.* 16, pp. 1956–1974.

Guéry, A. Abou-Chakra et al. (2008). “A micromechanical model of elastoplastic and damage behavior of a cohesive geomaterial”. In: *International Journal of Solids and Structures* 45, pp. 1406–1429.

Gulasik, Hasan et al. (2023). “A Thermo-Mechanical, Viscoelasto-Plastic Model for Semi-Crystalline Polymers Exhibiting One-Way and Two-Way Shape Memory Effects Under Phase Change”. In: *Journal of the Mechanics and Physics of Solids* Under review.

Gurson, A. L. (1977). “Continuum theory of ductile rupture by void nucleation and growth: Part I yield criteria and flow rules for porous ductile media”. In: *J. Eng. Mater. Technol.*

Hachemi, A. et al. (2014). “Limit state of structures made of heterogeneous materials”. In: *International Journal of Plasticity* 63. Deformation Tensors in Material Modeling in Honor of Prof. Otto T. Bruhns, pp. 124–137. ISSN: 0749-6419. DOI: https://doi.org/10.1016/j.ijplas.2014.03.019. URL: https://www.sciencedirect.com/science/article/pii/S0749641914000862.

Haddad, M., I. Doghri, and O. Pierard (2022). “Viscoelastic-viscoplastic polymer composites: Development and evaluation of two very dissimilar mean-field homogenization models”. In: *International Journal of Solids and Structures* 236-237, p. 111354. ISSN: 0020-7683. DOI: https://doi.org/10.1016/j.ijsolstr.2021.111354. URL: https://www.sciencedirect.com/science/article/pii/S0020768321004273.

Haj-Ali, R. M. and A. H. Muliana (2004). “Numerical finite element formulation of the Schapery non-linear viscoelastic material model”. In: *International Journal for Numerical Methods in Engineering* 59(1), pp. 25–45. DOI: https://doi.org/10.1002/nme.861. eprint: https://onlinelibrary.wiley.com/doi/pdf/10.1002/nme.861. URL: https://onlinelibrary.wiley.com/doi/abs/10.1002/nme.861.

Hajikarimi, P. et al. (2022). “Fractional viscoelastic modeling of modified asphalt mastics using response surface method”. In: *Construction and Building Materials* 317, p. 125958. ISSN: 0950-0618. DOI: https://doi.org/10.1016/j.conbuildmat.2021.125958. URL: https://www.sciencedirect.com/science/article/pii/S0950061821036904.

Hashemi, M. S., M. Safdari, and A. Sheidaei (2021). “A supervised machine learning approach for accelerating the design of particulate composites: Application to thermal conductivity”. In: *Computational Materials Science* 197, p. 110664. DOI: 10.48550/ARXIV.2010.00041. URL: https://arxiv.org/abs/2010.00041.

Hashin, Z. (1962). “The elastic moduli of heterogeneous materials”. In: *ASME J. Appl. Mech.* 29, pp. 143–150.

Hashin, Z. and S. Shtrikman (1963). “A variational approach to the theory of the elastic behaviour of multiphase materials”. In: *Journal of the Mechanics and Physics of Solids* 11(2), pp. 127–140. ISSN: 0022-5096. DOI: https://doi.org/10.1016/0022-5096(63)90060-7. URL: https://www.sciencedirect.com/science/article/pii/0022509663900607.

Hernandez, J.A. et al. (2014). “High-performance model reduction techniques in computational multiscale homogenization”. In: *Computer Methods in Applied Mechanics and Engineering* 276, pp. 149–189. ISSN: 0045-7825. DOI: https://doi.org/10.1016/j.cma.2014.03.011. URL: https://www.sciencedirect.com/science/article/pii/S0045782514000978.

Hill, R. (1963). “Elastic properties of reinforced solids: some theoretical principles”. In: *Journal Mech. Phys. Solids* 11, pp. 357–372.

Hill, R. (1965a). “A self-consistent mechanics of composite materials”. In: *Journal of the Mechanics and Physics of Solids* 13(4), pp. 213–222. ISSN: 0022-5096. DOI: https://doi.org/10.1016/0022-5096(65)90010-4. URL: https://www.sciencedirect.com/science/article/pii/0022509665900104.

Hill, R. (1965b). “Continuum micro-mechanics of elastoplastic polycrystals”. In: *Journal of the Mechanics and Physics of Solids* 13(2), pp. 89–101. ISSN: 0022-5096. DOI: https://doi.org/10.1016/0022-5096(65)90023-2. URL: https://www.sciencedirect.com/science/article/pii/0022509665900232.

Hine, P. et al. (2005). “The effect of hydro-static pressure on the mechanical properties of glass fibre/epoxy unidirectional composites”. In: *Comp. Part A: App. Sci. and Man.*

Hori, M. and S. Nemat-Nasser (1993). “Double-inclusion model and overall moduli of multi-phase composites”. In: *Mech. of Mech.* 14, pp. 189–206.

Houbben, Maxime et al. (2023). “MWCNTs filled PCL covalent adaptable networks: Towards reprocessable, self-healing and fast electrically-triggered shape-memory composites”. In: *Polymer* 278, p. 125992. ISSN: 0032-3861. DOI: https://doi.org/10.1016/j.polymer.2023.125992. URL: https://www.sciencedirect.com/science/article/pii/S0032386123003221.

Huang, Dengpeng et al. (2020). “A machine learning based plasticity model using proper orthogonal decomposition”. In: *Computer Methods in Applied Mechanics and Engineering* 365, p. 113008. ISSN: 0045-7825. DOI: https://doi.org/10.1016/j.cma.2020.113008. URL: https://www.sciencedirect.com/science/article/pii/S0045782520301924.

Huang, T. et al. (2022). “Microstructure-guided deep material network for rapid nonlinear material modeling and uncertainty quantification”. In: *Computer Methods in Applied Mechanics and Engineering* 398, p. 115197. ISSN: 0045-7825. DOI: https://doi.org/10.1016/j.cma.2022.115197. URL: https://www.sciencedirect.com/science/article/pii/S0045782522003498.

Hun, Darith-Anthony et al. (2019). “Stochastic multiscale modeling of crack propagation in random heterogeneous media”. In: *International Journal for Numerical Methods in Engineering* 119(13), pp. 1325–1344. DOI: https://doi.org/10.1002/nme.6093. eprint: https://onlinelibrary.wiley.com/doi/pdf/10.1002/nme.6093. URL: https://onlinelibrary.wiley.com/doi/abs/10.1002/nme.6093.

Hutchinson, J. W. (1977). “Bounds and self-consistent estimates for creep of polycrystalline metals”. In: *Proc. of the Roy. Soc. of London. A. Math. and Phys. Sci.*

Hutchinson, J. W. and R. Hill (1970). “Elastic-plastic behaviour of polycrystalline metals and composites”. In: *Proceedings of the Royal Society of London. A. Mathematical and Physical Sciences* 319(1537), pp. 247–272. DOI: 10.1098/rspa.1970.0177. eprint: https://royalsocietypublishing.org/doi/pdf/10.1098/rspa.1970.0177. URL: https://royalsocietypublishing.org/doi/abs/10.1098/rspa.1970.0177.

IATA (2021). “Annual Review 2021”. In: *IATA.org*.

Islam, M. and C. Gnanendran (2020). “Non-Associated Flow Rule-Based Elasto-Viscoplastic Model for Clay”. In: *Geosciences*.

Ju, B. and T. Wang (2003). “Plastic constitutive behavior of short-fiber particle reinforced composites”. In: *Int. J. Plasticity* 19, pp. 565–581.

Jung, S. and J. Ghaboussi (2006). “Neural network constitutive model for rate-dependent materials”. In: *Computers and Structures* 84(15), pp. 955–963. ISSN: 0045-7949. DOI: https://doi.org/10.1016/j.compstruc.2006.02.015. URL: https://www.sciencedirect.com/science/article/pii/S0045794906000563.

Kaiser, J.M. and M Stommel (2014). “Modified mean-field formulations for the improved simulation of short fiber reinforced thermoplastics”. In: *Composites Science and Technology* 99, pp. 75–81.

Kanouté, P. et al. (2009). “Multiscale Methods for Composites: A Review”. In: *Archives of Computational Methods in Engineering* 16, pp. 31–75.

Khoei, Amir R. and Mohammad A. Saadat (2019). “A nonlocal computational homogenization of softening quasi-brittle materials”. In: *International Journal for Numerical Methods in Engineering* 119(8), pp. 712–736. DOI: https://doi.org/10.1002/nme.6070. eprint: https://onlinelibrary.wiley.com/doi/pdf/10.1002/nme.6070. URL: https://onlinelibrary.wiley.com/doi/abs/10.1002/nme.6070.

Kim, J.-S. and A. H. Muliana (2010). “A combined viscoelastic-viscoplastic behavior of particle reinforced composites”. In: *International Journal of Solids and Structures* 47(5), pp. 580–594. ISSN: 0020-7683. DOI: https://doi.org/10.1016/j.ijsolstr.2009.10.019. URL: https://www.sciencedirect.com/science/article/pii/S0020768309004120.

Knockaert, R. and I. Doghri (1999). “Nonlocal consitutive models with gradients of internal variables derived from a micro/macro homogenization procedure”. In: *Comput. Meth. Appl. Mech. Eng.* 174, pp. 121–136.

Kolling, S. et al. (2005). “SAMP-1: a semi-analytical model for the simulation of polymers”. In: *4. LS-DYNA Anwenderforum, Bamberg*.

Kouznetsova, V., W.A.M. Brekelmans, and F.P.T. Baaijens (2001). “An approach to micro-macro modeling of heterogeneous materials”. In: *Computational Mechanics* 27(1), pp. 37–48.

Kouznetsova, V., M. Geers, and W. Brekelmans (2002). “Multi-scale constitutive modelling of heterogeneous materials with a gradient-enhanced computational homogenization scheme”. In: *Int. J. Numer. Meth. Eng.* 54, pp. 1235–1260.

Kouznetsova, V., M. Geers, and W. Brekelmans (2004). “Multi-scale second-order computational homogenization of muli-phase materials: a nested finite element solution strategy”. In: *Comput. Methods Appl. Mech. Eng.* 193, pp. 5525–5550.

Krairi, A. (2015). “Multiscale modeling of the damage and failure of homogeneous and short-fiber reinforced thermoplastics under monotonic and fatigue loadings”. In: *Ph.D. Thesis*.

Krairi, A. and I. Doghri (2014). “A thermodynamically-based constitutive model for thermoplastic polymers coupling viscoelasticity, viscoplasticity and ductile damage”. In: *International Journal of Plasticity* 60, pp. 163–181. ISSN: 0749-6419. DOI: https://doi.org/10.1016/j.ijplas.2014.04.010. URL: https://www.sciencedirect.com/science/article/pii/S074964191400093X.

Krempl, E., J.J. McMahon, and D. Yao (1986). “Viscoplasticity based on overstress with a differential growth law for the equilibrium stress”. In: *Mechanics of Materials* 5(1), pp. 35–48. ISSN: 0167-6636. DOI: https://doi.org/10.1016/0167-6636(86)90014-1. URL: https://www.sciencedirect.com/science/article/pii/0167663686900141.

Kröner, E. (1958). “Berechnung der elastischen Konstanten des Vielkristalls aus den Konstanten des Einkristalls”. In: *Zeitschrift für Physik* 151, pp. 504–518.

Lahellec, N. and P. Suquet (2007a). “On the effective behavior of nonlinear inelastic composites: I. Incremental variational principles”. In: *Journal of the Mechanics and Physics of Solids* 55(9), pp. 1932–1963. ISSN: 0022-5096. DOI: https://doi.org/10.1016/j.jmps.2007.02.003. URL: https://www.sciencedirect.com/science/article/pii/S0022509607000312.

Lahellec, N. and P. Suquet (2007b). “On the effective behavior of nonlinear inelastic composites: II: A second-order procedure”. In: *Journal of the Mechanics and Physics of Solids* 55(9), pp. 1964–1992. ISSN: 0022-5096. DOI: https://doi.org/10.1016/j.jmps.2007.02.004. URL: https://www.sciencedirect.com/science/article/pii/S0022509607000324.

Le, B. A., J. Yvonnet, and Q.-C. He (2015). “Computational homogenization of nonlinear elastic materials using neural networks”. In: *International Journal for Numerical Methods in Engineering* 104(12), pp. 1061–1084. DOI: https://doi.org/10.1002/nme.4953. eprint: https://onlinelibrary.wiley.com/doi/pdf/10.1002/nme.4953. URL: https://onlinelibrary.wiley.com/doi/abs/10.1002/nme.4953.

Lee, K. et al. (2021). “Enhancement of Drucker-Prager yield model by adding corner points for pressure-dependent materials”. In: *Journ. of Mech. Sci. and Tech.*

Lefik, M. and B.A. Schrefler (2003). “Artificial neural network as an incremental non-linear constitutive model for a finite element code”. In: *Computer Methods in Applied Mechanics and Engineering* 192(28). Multiscale Computational Mechanics for Materials and Structures, pp. 3265–3283. ISSN: 0045-7825. DOI: https://doi.org/10.1016/S0045-7825(03)00350-5. URL: https://www.sciencedirect.com/science/article/pii/S0045782503003505.

Lemaitre, J. (1985). “Coupled elasto-plasticity and damage constitutive equations”. In: *Computer Methods in Applied Mechanics and Engineering* 51(1), pp. 31–49. ISSN: 0045-7825. DOI: https://doi.org/10.1016/0045-7825(85)90026-X. URL: https://www.sciencedirect.com/science/article/pii/004578258590026X.

Lemaitre, J. and J.-L. Chaboche (1994). *Mechanics of Solid Materials*. Cambridge University Press. DOI: 10.1017/CBO9781139167970.

Lesser, A.J. and R.S. Kody (1997). “A generalized model for the yield behavior of epoxy networks in multiaxial stress states”. In: *Journ. Polym. Sci. Part B*.

Li, X. and H. Tang (2005). “A consistent return mapping algorithm for pressure-dependent elastoplastic Cosserat continua and modelling of strain localisation”. In: *Comp. and Struct.*

Lissenden, C. and S. Arnold (1997). “Theoretical and experimental considerations in representing macroscale flow/damage surfaces for metal matrix composites”. In: *Int. J. Plasticity* 13, pp. 327–358.

Liu, C. et al. (2022). “A viscoelastic-viscoplastic constitutive model for nanoparticle-reinforced epoxy composites: Particle, temperature, and strain rate effects”. In: *Materials Today Communications* 33, p. 104849. ISSN: 2352-4928. DOI: https://doi.org/10.1016/j.mtcomm.2022.104849. URL: https://www.sciencedirect.com/science/article/pii/S2352492822016907.

Liu, X. and G. Hu (2005). “A continuum micromechanical theory of overall plasticity for particulate composites including particle size effect”. In: *Int. Journal Plast.* 21, pp. 777–799.

Liu, Z. (2020). “Deep material network with cohesive layers: Multi-stage training and interfacial failure analysis”. In: *Computer Methods in Applied Mechanics and Engineering* 363, p. 112913. ISSN: 0045-7825. DOI: https://doi.org/10.1016/j.cma.2020.112913. URL: https://www.sciencedirect.com/science/article/pii/S0045782520300967.

Liu, Z., M.A. Bessa, and W. K. Liu (2016). "Self-consistent clustering analysis: An efficient multi-scale scheme for inelastic heterogeneous materials". In: *Computer Methods in Applied Mechanics and Engineering* 306, pp. 319–341. ISSN: 0045-7825. DOI: `https://doi.org/10.1016/j.cma.2016.04.004`. URL: `https://www.sciencedirect.com/science/article/pii/S0045782516301499`.

Liu, Z. and C.T. Wu (2019). "Exploring the 3D architectures of deep material network in data-driven multiscale mechanics". In: *Journal of the Mechanics and Physics of Solids* 127, pp. 20–46. ISSN: 0022-5096. DOI: `https://doi.org/10.1016/j.jmps.2019.03.004`. URL: `https://www.sciencedirect.com/science/article/pii/S0022509618310688`.

Liu, Z., C.T. Wu, and M. Koishi (2019). "A deep material network for multiscale topology learning and accelerated nonlinear modeling of heterogeneous materials". In: *Computer Methods in Applied Mechanics and Engineering* 345, pp. 1138–1168. ISSN: 0045-7825. DOI: `https://doi.org/10.1016/j.cma.2018.09.020`. URL: `https://www.sciencedirect.com/science/article/pii/S0045782518304729`.

Llorca, J. et al. (2011). "Multiscale modeling of composite materials: a roadmap towards virtual testing". In: *Adv. Mat.* 23, pp. 5130–5147.

Logarzo, H. J., German Capuano, and Julian J. Rimoli (2021). "Smart constitutive laws: Inelastic homogenization through machine learning". In: *Computer Methods in Applied Mechanics and Engineering* 373, p. 113482. ISSN: 0045-7825. DOI: `https://doi.org/10.1016/j.cma.2020.113482`. URL: `https://www.sciencedirect.com/science/article/pii/S0045782520306678`.

Lu, J. and K. Ravi-Chandar (1999). "Inelastic deformation and localization in polycarbonate under tension". In: *Int. Journ. of Sol and Struct.* 36, pp. 391–425.

Lu, X. et al. (2019). "A data-driven computational homogenization method based on neural networks for the nonlinear anisotropic electrical response of graphene/polymer nanocomposites". In: *Computational Mechanics* 64, pp. 307–321. ISSN: 1432-0924. DOI: `10.1007/s00466-018-1643-0`. URL: `https://doi.org/10.1007/s00466-018-1643-0`.

Lu, X. et al. (2021). "A Stochastic FE2 Data-Driven Method for Nonlinear Multiscale Modeling". In: *Materials* 14(11). ISSN: 1996-1944. DOI: `10.3390/ma14112875`. URL: `https://www.mdpi.com/1996-1944/14/11/2875`.

Lucas, V. et al. (2015). "A stochastic computational multiscale approach; Application to MEMS resonators". In: *Computer Methods in Applied Mechanics and Engineering* 294, pp. 141–167. ISSN: 0045-7825. DOI: `https://doi.org/10.1016/j.cma.2015.05.019`. URL: `https://www.sciencedirect.com/science/article/pii/S0045782515001929`.

Lucchetta, A. et al. (2019). "A double incremental variational procedure for elastoplastic composites with combined isotropic and linear kinematic hardening". In: *International Journal of Solids and Structures* 158, pp. 243–267. ISSN: 0020-7683. DOI: `https://doi.org/10.1016/j.ijsolstr.2018.09.012`. URL: `https://www.sciencedirect.com/science/article/pii/S0020768318303688`.

Lucchetta, A. et al. (2021). "Incremental variational homogenization of elastoplastic composites with isotropic and Armstrong-Frederick type nonlinear kinematic hardening". In: *International Journal of Solids and Structures* 222-223, p. 111000. ISSN: 0020-7683. DOI: `https://doi.org/10.1016/j.ijsolstr.2021.02.011`. URL: `https://www.sciencedirect.com/science/article/pii/S0020768321000652`.

Maalej, Y., M. Imene El Ghezal, and I. Doghri (2013). "Elasticity and viscoelasticity of open cellular material: micromechanical approach". In: *M. Haddar et al. (Eds.): Design and Modeling of Mechanical Systems*, pp. 531–540.

Massart, T., R. Peerlings, and M. Geers (2005). "A dissipation-based control method for the multi-scale modelling of quasi-brittle materials". In: *C.R. Méca.* 333, pp. 521–527.

Massart, T., R. Peerlings, and M. Geers (2007). "An enhanced multi-scale approach for masonry wall computations". In: *Int. Journal Numer. Meth. Eng.* 69, pp. 1022–1059.

Masson, R. et al. (2000). "An affine formulation for the prediction of the effective properties of nonlinear composites and polycrystals". In: *Journal of the Mechanics and Physics of Solids* 48(6), pp. 1203–1227. ISSN: 0022-5096. DOI: `https://doi.org/10.1016/S0022-5096(99)00071-X`. URL: `https://www.sciencedirect.com/science/article/pii/S002250969900071X`.

Matous, K. et al. (2017). "A review of predictive nonlinear theories for multiscale modeling of heterogeneous materials". In: *Journal of Computational Physics* 330, pp. 192–220. ISSN: 0021-9991. DOI: `https://doi.org/10.1016/j.jcp.2016.10.070`. URL: `https://www.sciencedirect.com/science/article/pii/S0021999116305782`.

Maxwell, J.C. (1867). "On the dynamical theory of gases". In: *Royal Society*.

McDowell, David L. (2010). "A perspective on trends in multiscale plasticity". In: *International Journal of Plasticity* 26(9). Special Issue In Honor of D. L. McDowell, pp. 1280–1309. ISSN: 0749-6419. DOI: `https://doi.org/10.1016/j.ijplas.2010.02.008`. URL: `https://www.sciencedirect.com/science/article/pii/S0749641910000306`.

Melro, A.R., P.P. Camanho, and S.T. Pinho (2008). "Generation of random distribution of fibres in long-fibre reinforced composites". In: *Composites Science and Technology* 68(9), pp. 2092–2102. ISSN: 0266-3538. DOI: `https://doi.org/10.1016/j.compscitech.2008.03.013`. URL: `https://www.sciencedirect.com/science/article/pii/S0266353808001048`.

Melro, A.R. et al. (2013). "Micromechanical analysis of polymer composites reinforced by unidirectional fibres: Part I - Constitutive modelling". In: *International Journal of Solids and Structures* 50(11), pp. 1897–1905. ISSN: 0020-7683. DOI: `https://doi.org/10.1016/j.ijsolstr.2013.02.009`. URL: `https://www.sciencedirect.com/science/article/pii/S0020768313000747`.

Mercier, S., K. Kowalczyk-Gajewska, and C. Czarnota (2019). "Effective behavior of composites with combined kinematic and isotropic hardening based on additive tangent Mori-Tanaka scheme". In: *Composites Part B: Engineering* 174, p. 107052. ISSN: 1359-8368. DOI: `https://doi.org/10.1016/j.compositesb.2019.107052`. URL: `https://www.sciencedirect.com/science/article/pii/S1359836819308352`.

Michel, J.-C. and P. Suquet (2009). "Non-uniform transformation field analysis: A reduced model for multiscale non-linear problems in solid mechanics". In: pp. 159–206. DOI: `10.1142/9781848163089/0004`. URL: `https://www.worldscientific.com/doi/abs/10.1142/9781848163089/0004`.

Michel, J.-C. and P. Suquet (2016). "A model-reduction approach in micromechanics of materials preserving the variational structure of constitutive relations". In: *Journal of the Mechanics and Physics of Solids* 90, pp. 254–285. ISSN: 0022-5096. DOI: `https://doi.org/10.1016/j.jmps.2016.02.005`. URL: `https://www.sciencedirect.com/science/article/pii/S0022509616300928`.

Michel, J., H. Moulinec, and P. Suquet (1999). "Effective properties of composite materials with periodic microstructure: a computational approach". In: *Computer Methods in Applied Mechanics and Engineering* 172, pp. 109–143.

Michel, J.C. and P. Suquet (2003). "Nonuniform transformation field analysis". In: *International Journal of Solids and Structures* 40(25). Special issue in Honor of George J. Dvorak, pp. 6937–6955. ISSN: 0020-7683. DOI: `https://doi.org/10.1016/S0020-7683(03)00346-9`. URL: `https://www.sciencedirect.com/science/article/pii/S0020768303003469`.

Miehe, C. (2002). "Strain-driven homogenization of inelastic microstructures and composites based on an incremental variational formulation". In: *International Journal for Numerical Methods in Engineering* 55(11), pp. 1285–1322. DOI: `https://doi.org/10.1002/nme.515`. eprint: `https://onlinelibrary.wiley.com/doi/pdf/10.1002/nme.515`. URL: `https://onlinelibrary.wiley.com/doi/abs/10.1002/nme.515`.

Miled, B. et al. (2013). "Micromechanical modeling of coupled viscoelastic-viscoplastic composites based on an incrementally affine formulation". In: *International Journal of Solids and*

Structures 50(10), pp. 1755–1769. ISSN: 0020-7683. DOI: https://doi.org/10.1016/j.ijsolstr.2013.02.004. URL: https://www.sciencedirect.com/science/article/pii/S0020768313000693.

Mises, R. Von (1913). “Mechanik der festen Körper im plastisch-deformablen Zustand”. In: *Nach. von der Gese. der Wiss. zu Gött.*, pp. 582–592.

Molinari, A., G.R. Canova, and S. Ahzi (1987). “A self consistent approach of the large deformation polycrystal viscoplasticity”. In: *Acta Metallurgica* 35(12), pp. 2983–2994. ISSN: 0001-6160. DOI: https://doi.org/10.1016/0001-6160(87)90297-5. URL: https://www.sciencedirect.com/science/article/pii/0001616087902975.

Montesano, John et al. (2013). “Fatigue damage characterization and modeling of a triaxially braided polymer matrix composite at elevated temperatures”. In: *Composite Structures* 101, pp. 129–137. ISSN: 0263-8223. DOI: https://doi.org/10.1016/j.compstruct.2013.01.030. URL: https://www.sciencedirect.com/science/article/pii/S0263822313000780.

Morelle, C.P. et al. (2017). “Mechanical characterization and modeling of the deformation and failure of the highly crosslinked RTM6 epoxy resin”. In: *Mechanics of Time-Dependent Materials* 21, pp. 419–454. ISSN: 1573-2738. DOI: https://doi.org/10.1007/s11043-016-9336-6.

Morelle, X., T. Pardoen, and C. Bailly (2015). “Mechanical characterization and physics-based modeling of highly-crosslinked epoxy resin”. In: *Ecole Polytechnique de Louvain, PhD thesis.*

Mori, T. and K. Tanaka (1973). “Average stress in matrix and average elastic energy of materials with misfitting inclusions”. In: *Acta Metallurgica* 21(5), pp. 571–574. ISSN: 0001-6160. DOI: https://doi.org/10.1016/0001-6160(73)90064-3. URL: https://www.sciencedirect.com/science/article/pii/0001616073900643.

Mosby, M. and K. Matous (2015). “On mechanics and material length scales of failure in heterogeneous interfaces using a finite strain high performance solver”. In: *Modelling and Simulation in Materials Science and Engineering* 23. DOI: https://doi.org/10.1088/0965-0393/23/8/085014.

Mozaffar, M et al. (2019). “Deep learning predicts path-dependent plasticity”. In: *Proceedings of the National Academy of Sciences* 116(52), pp. 26414–26420.

Mulliken, A. and M. Boyce (2006). “Mechanics of the rate-dependent elastic-plastic deformation of glassy polymers from low to high strain rates”. In: *Int. J. Solids Struct.*

Naili, Chiheb and Issam Doghri (2023). “Combined mean-field and full-field homogenization of porous elasto-plastic materials and composites under arbitrary stress triaxialities”. In: *Mechanics of Materials* 187, p. 104818. ISSN: 0167-6636. DOI: https://doi.org/10.1016/j.mechmat.2023.104818. URL: https://www.sciencedirect.com/science/article/pii/S0167663623002648.

Narayanan, P., R. Pramanik, and A. Arockiarajan (2023). “A hyperelastic viscoplastic damage model for large deformation mechanics of rate-dependent soft materials”. In: *European Journal of Mechanics - A/Solids* 98, p. 104874. ISSN: 0997-7538. DOI: https://doi.org/10.1016/j.euromechsol.2022.104874. URL: https://www.sciencedirect.com/science/article/pii/S0997753822003047.

Nemat-Nasser, S. and M. Hori (2013). “Micromechanics: overall properties of heterogeneous materials”. In: 37.

Nemat-Nasser, S. and M. Obata (1986). “Rate-dependent finite elasto-plastic deformation of polycrystals”. In: *Proc. of the Roy. Soc. of London. A. Math. and Phys. Sci.*

Nguyen, V. D. and L. Noels (2022). “Micromechanics-based material networks revisited from the interaction viewpoint; robust and efficient implementation for multi-phase composites”. In: *European Journal of Mechanics - A/Solids* 91, p. 104384. ISSN: 0997-7538. DOI: https://doi.org/10.1016/j.euromechsol.2021.104384. URL: https://www.sciencedirect.com/science/article/pii/S0997753821001431.

Nguyen, V.-D., L. Wu, and L. Noels (2017). “Unified treatment of microscopic boundary conditions and efficient algorithms for estimating tangent operators of the homogenized behavior in the computational homogenization method”. In: *Computational Mechanics* 59, pp. 483–505. DOI: `10.1007/s00466-016-1358-z`. URL: `https://doi.org/10.1007/s00466-016-1358-z`.

Nguyen, V.-D., L. Wu, and L. Noels (2019). “A micro-mechanical model of reinforced polymer failure with length scale effects and predictive capabilities. Validation on carbon fiber reinforced high-crosslinked RTM6 epoxy resin”. In: *Mechanics of Materials* 133, pp. 193–213. ISSN: 0167-6636. DOI: `https://doi.org/10.1016/j.mechmat.2019.02.017`. URL: `https://www.sciencedirect.com/science/article/pii/S0167663618306975`.

Nguyen, V.-D. et al. (2012). “Imposing periodic boundary condition on arbitrary meshes by polynomial interpolation”. In: *Computational Materials Science* 55, pp. 390–406. ISSN: 0927-0256. DOI: `https://doi.org/10.1016/j.commatsci.2011.10.017`. URL: `https://www.sciencedirect.com/science/article/pii/S0927025611005866`.

Nguyen, V.-D. et al. (2016). “A large strain hyperelastic viscoelastic-viscoplastic-damage constitutive model based on a multi-mechanism non-local damage continuum for amorphous glassy polymers”. In: *International Journal of Solids and Structures* 96, pp. 192–216. ISSN: 0020-7683. DOI: `https://doi.org/10.1016/j.ijsolstr.2016.06.008`. URL: `https://www.sciencedirect.com/science/article/pii/S0020768316301238`.

Nguyen, Van-Dung, Thomas Pardoen, and Ludovic Noels (2020). “A nonlocal approach of ductile failure incorporating void growth, internal necking, and shear dominated coalescence mechanisms”. In: *Journal of the Mechanics and Physics of Solids* 137, p. 103891. ISSN: 0022-5096. DOI: `https://doi.org/10.1016/j.jmps.2020.103891`. URL: `https://www.sciencedirect.com/science/article/pii/S0022509619309275`.

Noels, L. (2022). “Chapter One - Toward stochastic multiscale methods in continuum solid mechanics”. In: ed. by Stéphane P.A. Bordas. Vol. 55. Advances in Applied Mechanics. Elsevier, pp. 1–254. DOI: `https://doi.org/10.1016/bs.aams.2022.03.001`. URL: `https://www.sciencedirect.com/science/article/pii/S0065215622000011`.

Noels, L., L. Wu, and L. Adam (2016). “Review of homogenization methods for heterogeneous materials”. In: *Handbook of Software Solutions for ICME* 6.1.1. Pp. 433–441.

Oliver, J. et al. (2017). “Reduced order modeling strategies for computational multiscale fracture”. In: *Computer Methods in Applied Mechanics and Engineering* 313, pp. 560–595. ISSN: 0045-7825. DOI: `https://doi.org/10.1016/j.cma.2016.09.039`. URL: `https://www.sciencedirect.com/science/article/pii/S0045782516303322`.

Östlund, R. et al. (2014). “Evaluation of localization and failure of boron alloyed steels with different microstructure compositions”. In: *Journal of Mat. Process. Tech.*

Ostoja-Starzewski, M. (2005). “Scale effects in plasticity of random media: status and challenges”. In: *International Journal of Plasticity* 21(6). Plasticity of Multiphase Materials, pp. 1119–1160. ISSN: 0749-6419. DOI: `https://doi.org/10.1016/j.ijplas.2004.06.008`. URL: `https://www.sciencedirect.com/science/article/pii/S0749641904001391`.

Ostoja-Starzewski, M. and X. Wang (1999). “Stochastic finite elements as a bridge between random material microstructure and global response”. In: *Computer Methods in Applied Mechanics and Engineering* 168(1), pp. 35–49. ISSN: 0045-7825. DOI: `https://doi.org/10.1016/S0045-7825(98)00105-4`. URL: `https://www.sciencedirect.com/science/article/pii/S0045782598001054`.

Ostoja-Starzewski, M. et al. (2007). “Comparisons of the Size of the Representative Volume Element in Elastic, Plastic, Thermoelastic, and Permeable Random Microstructures”. In: *International Journal for Multiscale Computational Engineering* 5(2), pp. 73–82. ISSN: 1543-1649.

Peerlings, R. H. J. et al. (1996). “Gradient enhanced damage for quasi-brittle materials”. In: *International Journal for Numerical Methods in Engineering* 39(19), pp. 3391–3403. DOI: `https://doi.org/10.1002/(SICI)1097-0207(19961015)39:19<3391::AID-NME7>3.0.`

CO;2-D. eprint: https://onlinelibrary.wiley.com/doi/pdf/10.1002/%28SICI%291097-0207%2819961015%2939%3A19%3C3391%3A%3AAID-NME7%3E3.0.CO%3B2-D. URL: https://onlinelibrary.wiley.com/doi/abs/10.1002/%28SICI%291097-0207%2819961015%2939%3A19%3C3391%3A%3AAID-NME7%3E3.0.CO%3B2-D.

Peerlings, R. H. J. et al. (1998). “Gradient-enhanced damage modelling of concrete fracture”. In: *Mechanics of Cohesive-frictional Materials* 3(4), pp. 323–342. DOI: https://doi.org/10.1002/(SICI)1099-1484(1998100)3:4<323::AID-CFM51>3.0.CO;2-Z. eprint: https://onlinelibrary.wiley.com/doi/pdf/10.1002/%28SICI%291099-1484%281998100%293%3A4%3C323%3A%3AAID-CFM51%3E3.0.CO%3B2-Z. URL: https://onlinelibrary.wiley.com/doi/abs/10.1002/%28SICI%291099-1484%281998100%293%3A4%3C323%3A%3AAID-CFM51%3E3.0.CO%3B2-Z.

Peerlings, R.H.J. et al. (2001). “A critical comparison of nonlocal and gradient-enhanced softening continua”. In: *International Journal of Solids and Structures* 38(44), pp. 7723–7746. ISSN: 0020-7683. DOI: https://doi.org/10.1016/S0020-7683(01)00087-7. URL: https://www.sciencedirect.com/science/article/pii/S0020768301000877.

Perzyna, P. (1971). “Thermodynamic Theory of Viscoplasticity”. In: ed. by Chia-Shun Yih. Vol. 11. Advances in Applied Mechanics. Elsevier, pp. 313–354. DOI: https://doi.org/10.1016/S0065-2156(08)70345-4. URL: https://www.sciencedirect.com/science/article/pii/S0065215608703454.

Phu Nguyen, V. et al. (2010). “On the existence of representative volumes for softening quasi-brittle materials - A failure zone averaging scheme”. In: *Computer Methods in Applied Mechanics and Engineering* 199(45), pp. 3028–3038. ISSN: 0045-7825. DOI: https://doi.org/10.1016/j.cma.2010.06.018. URL: https://www.sciencedirect.com/science/article/pii/S0045782510001854.

Pierard, O. and I. Doghri (2006). “An enhanced affine formulation and the corresponding numerical algorithms for the mean-field homogenization of elasto-viscoplastic composites”. In: *International Journal of Plasticity* 22(1), pp. 131–157. ISSN: 0749-6419. DOI: https://doi.org/10.1016/j.ijplas.2005.04.001. URL: https://www.sciencedirect.com/science/article/pii/S0749641905000549.

Pierard, O. et al. (2007). “Micromechanics of particle-reinforced elasto-viscoplastic composites: Finite element simulations versus affine homogenization”. In: *Int. Journal of Plast.* 23, pp. 1041–1060.

Pingaro, M., E. Reccia, and P. Trovalusci (June 2019). “Homogenization of Random Porous Materials With Low-Order Virtual Elements”. In: *ASCE-ASME J Risk and Uncert in Engrg Sys Part B Mech Engrg* 5(3). 030905. ISSN: 2332-9017. DOI: 10.1115/1.4043475. eprint: https://asmedigitalcollection.asme.org/risk/article-pdf/5/3/030905/6412921/risk_005_03_030905.pdf. URL: https://doi.org/10.1115/1.4043475.

Pingaro, M. et al. (2019). “Fast statistical homogenization procedure (FSHP) for particle random composites using virtual element method”. In: *Computational Mechanics* 64(1), pp. 197–210.

Pingaro, M. et al. (2023). “Fast Statistical Homogenization Procedure for estimation of effective properties of Ceramic Matrix Composites (CMC) with random microstructure”. In: *Composite Structures* 304, p. 116265. ISSN: 0263-8223. DOI: https://doi.org/10.1016/j.compstruct.2022.116265. URL: https://www.sciencedirect.com/science/article/pii/S0263822322009977.

Pivovarov, D., P. Steinmann, and K. Willner (2020). “Acceleration of the spectral stochastic FEM using POD and element based discrete empirical approximation for a micromechanical model of heterogeneous materials with random geometry”. In: *Computer Methods in Applied Mechanics and Engineering* 360. DOI: 10.1016/j.cma.2019.112689. URL: https://www.scopus.com/inward/record.uri?eid=2-s2.0-85075485475&doi=10.1016%2fj.cma.2019.112689&partnerID=40&md5=9d22ace6176eb400fb29455d0b3532b4.

Poulton, G. (2009). “Notice of proposed amendement (NPA) No 2009-06”. In: *Airbus Newsroom.*

Poulton, G. (2017). “Aviation´s material evolution”. In: *Airbus Newsroom*.

Radermacher, Annika et al. (2016). “Displacement-based multiscale modeling of fiber-reinforced composites by means of proper orthogonal decomposition”. In: *Advanced Modeling and Simulation in Engineering Sciences* 3(1). ISSN: 2213-7467. URL: `https://doi.org/10.1186/s40323-016-0082-8`.

Raghava, R., R.M. Caddell, and G.S.Y. Yeh (1973). “The macroscopic yield behaviour of polymers”. In: *Journ. of Mat. Sci.*

Rao, Chengping and Yang Liu (2020). “Three-dimensional convolutional neural network (3D-CNN) for heterogeneous material homogenization”. In: *Computational Materials Science* 184, p. 109850. ISSN: 0927-0256. DOI: `https://doi.org/10.1016/j.commatsci.2020.109850`. URL: `https://www.sciencedirect.com/science/article/pii/S0927025620303414`.

Reccia, E. et al. (2018). “Sensitivity to material contrast in homogenization of random particle composites as micropolar continua”. In: *Composites Part B: Engineering* 136, pp. 39–45. ISSN: 1359-8368. DOI: `https://doi.org/10.1016/j.compositesb.2017.10.017`. URL: `https://www.sciencedirect.com/science/article/pii/S1359836817325088`.

Reese, S. and S. Govindjee (1998). “A theory of finite viscoelasticity and numerical aspects”. In: *International Journal of Solids and Structures* 35(26), pp. 3455–3482. ISSN: 0020-7683. DOI: `https://doi.org/10.1016/S0020-7683(97)00217-5`. URL: `https://www.sciencedirect.com/science/article/pii/S0020768397002175`.

Roscoe, K.H. and J.B. Burland (1968). “On the generalized stress-strain behaviour of wet clay”. In: *Eng. Plast.*

Salmi, M. et al. (2012). “Apparent and effective mechanical properties of linear matrix-inclusion random composites: Improved bounds for the effective behavior”. In: *International Journal of Solids and Structures* 49(10), pp. 1195–1211. ISSN: 0020-7683. DOI: `https://doi.org/10.1016/j.ijsolstr.2012.01.018`. URL: `https://www.sciencedirect.com/science/article/pii/S0020768312000340`.

Sánchez, Clara Pereira et al. (2022). “Review of Thermoresponsive Electroactive and Magnetoactive Shape Memory Polymer Nanocomposites”. In: *ACS omega* 7(45), pp. 40701–40723.

Santo, Loredana et al. (2014). “Shape Memory Composites for Self-deployable Structures in Aerospace Applications”. In: *Procedia Engineering* 88. International Symposium on Dynamic Response and Failure of Composite Materials, DRaF2014, pp. 42–47. ISSN: 1877-7058. DOI: `https://doi.org/10.1016/j.proeng.2014.11.124`. URL: `https://www.sciencedirect.com/science/article/pii/S1877705814021857`.

Schiessel, H. et al. (1995). “Generalized viscoelastic models: their fractional equations with solutions”. In: *Journal of Physics A: Mathematical and General* 28(23), p. 6567. DOI: `10.1088/0305-4470/28/23/012`. URL: `https://dx.doi.org/10.1088/0305-4470/28/23/012`.

Segurado, J., J. Llorca, and C. González (2002). “On the accuracy of mean field approaches to simulate the plastic deformation of composites”. In: *Scripta Mater* 46, pp. 525–529.

Settgast, C. et al. (2020). “A hybrid approach to simulate the homogenized irreversible elastic-plastic deformations and damage of foams by neural networks”. In: *International Journal of Plasticity* 126, p. 102624. ISSN: 0749-6419. DOI: `https://doi.org/10.1016/j.ijplas.2019.11.003`. URL: `https://www.sciencedirect.com/science/article/pii/S074964191930381X`.

Sharma, Keshav and G. Srinivas (2020). “Flying smart: Smart materials used in aviation industry”. In: *Materials Today: Proceedings* 27. First International Conference on Recent Advances in Materials and Manufacturing 2019, pp. 244–250. ISSN: 2214-7853. DOI: `https://doi.org/10.1016/j.matpr.2019.10.115`. URL: `https://www.sciencedirect.com/science/article/pii/S2214785319336247`.

Shen, W.Q. et al. (2012). “A micro-macro model for clayey rocks with a plastic compressible porous matrix”. In: *International Journal of Plasticity* 36, pp. 64–85.

Simo, J. C. and T. J. Hughes (2006). *Computational inelasticity.* Springer Science and Business Media.

Simo, J.C. (1987). “On a fully three-dimensional finite-strain viscoelastic damage model: Formulation and computational aspects”. In: *Computer Methods in Applied Mechanics and Engineering* 60(2), pp. 153–173. ISSN: 0045-7825. DOI: `https://doi.org/10.1016/0045-7825(87)90107-1`. URL: `https://www.sciencedirect.com/science/article/pii/0045782587901071`.

Soize, C. and R. Ghanem (2016). “Data-driven probability concentration and sampling on manifold”. In: *Journal of Computational Physics* 321, pp. 242–258. ISSN: 0021-9991. DOI: `https://doi.org/10.1016/j.jcp.2016.05.044`. URL: `https://www.sciencedirect.com/science/article/pii/S0021999116301899`.

Soldner, D. et al. (2017). “A numerical study of different projection-based model reduction techniques applied to computational homogenisation”. In: *Computational Mechanics volume* 60, pp. 613,625. ISSN: 1432-0924. DOI: `10.1007/s00466-017-1428-x`. URL: `https://doi.org/10.1007/s00466-017-1428-x`.

Spilker, Kevin et al. (2023). “Three-scale bridging for woven composites using homogenization techniques”. In: *European Journal of Mechanics - A/Solids* 100, p. 104974. ISSN: 0997-7538. DOI: `https://doi.org/10.1016/j.euromechsol.2023.104974`. URL: `https://www.sciencedirect.com/science/article/pii/S0997753823000669`.

Squibb, Carson Owen (2023). “Investigation of Polymer-Filled Honeycomb Composites with Applications as Variable Stiffness Morphing Aircraft Structures”. PhD thesis. Virginia Tech.

Srivastava, V., S. A. Chester, and L. Anand (2010). “Thermally actuated shape-memory polymers: Experiments, theory, and numerical simulations”. In: *Journal of the Mechanics and Physics of Solids* 58(8), pp. 1100–1124. ISSN: 0022-5096. DOI: `https://doi.org/10.1016/j.jmps.2010.04.004`. URL: `https://www.sciencedirect.com/science/article/pii/S0022509610000736`.

Stefanou, George, Dimitrios Savvas, and Manolis Papadrakakis (2015). “Stochastic finite element analysis of composite structures based on material microstructure”. In: *Composite Structures* 132, pp. 384–392. ISSN: 0263-8223. DOI: `https://doi.org/10.1016/j.compstruct.2015.05.044`. URL: `https://www.sciencedirect.com/science/article/pii/S0263822315004183`.

Stefanou, George et al. (2022). “The effect of random field parameter uncertainty on the response variability of composite structures”. In: *Composites Part C: Open Access* 9, p. 100324. ISSN: 2666-6820. DOI: `https://doi.org/10.1016/j.jcomc.2022.100324`. URL: `https://www.sciencedirect.com/science/article/pii/S2666682022000871`.

Svedberg, T. and K. Runesson (1997). “A thermodynamically consistent theory of gradient-regularized plasticity coupled to damage”. In: *Int. Journal Plast.* 13, pp. 669–696.

Székely, Gábor J., Maria L. Rizzo, and Nail K. Bakirov (Dec. 2007). “Measuring and testing dependence by correlation of distances”. In: *Ann. Statist.* 35(6), pp. 2769–2794. DOI: `10.1214/009053607000000505`.

Sánchez, Clara Pereira et al. (2022). “Experimental characterization of the thermo-electro-mechanical properties of a shape memory composite during electric activation”. In: *Smart Materials and Structures* 31(9), p. 095029. DOI: `10.1088/1361-665X/ac8297`. URL: `https://dx.doi.org/10.1088/1361-665X/ac8297`.

Takagi, H. et al. (2008). “Analysis of time dependent polymer deformation based on a viscoelastic model in thermal imprint process”. In: *Microelectronic Engineering* 85(5). Proceedings of the Micro- and Nano-Engineering 2007 Conference, pp. 902–906. ISSN: 0167-9317. DOI: `https://doi.org/10.1016/j.mee.2008.01.018`. URL: `https://www.sciencedirect.com/science/article/pii/S016793170800049X`.

Tal, D. and J. Fish (2016). “Generating a statistically equivalent representative volume element with discrete defects”. In: *Composite Structures* 153, pp. 791–803. ISSN: 0263-8223.

DOI: https://doi.org/10.1016/j.compstruct.2016.06.077. URL: https://www.sciencedirect.com/science/article/pii/S0263822316310790.

Talbot, D.R.S. and J.R. Willis (July 1985). “Variational Principles for Inhomogeneous Nonlinear Media”. In: *IMA Journal of Applied Mathematics* 35(1), pp. 39–54. ISSN: 0272-4960. DOI: 10.1093/imamat/35.1.39. eprint: https://academic.oup.com/imamat/article-pdf/35/1/39/2037184/35-1-39.pdf. URL: https://doi.org/10.1093/imamat/35.1.39.

Tandon, G. P. and G. J. Weng (Mar. 1988). “A Theory of Particle-Reinforced Plasticity”. In: *Journal of Applied Mechanics* 55(1), pp. 126–135. ISSN: 0021-8936. DOI: 10.1115/1.3173618. eprint: https://asmedigitalcollection.asme.org/appliedmechanics/article-pdf/55/1/126/5459681/126_1.pdf. URL: https://doi.org/10.1115/1.3173618.

Terada, K. et al. (2000). “Simulation of the multi-scale convergence in computational homogenization approaches”. In: *International Journal of Solids and Structures* 37, pp. 2285–2311.

Tervoort, T.A. et al. (1997). “A Constitutive Equation for the Elasto-Viscoplastic Deformation of Glassy Polymers”. In: *Mechanics of Time-Dependent Materials* 1(2), pp. 269–291. ISSN: 1573-2738. DOI: https://doi.org/10.1023/A:1009720708029.

Tomita, Y. and T. Adachi (1997). “Network models for glassy polymer and prediction of instability propagation”. In: *Journ. of the Soc. of Mat. Sci.* 46, pp. 125–136.

Tomita, Y. and W. Lu (2002). “Computational characterization of micro-to macroscopic mechanical behavior and damage of polymers containing second-phase particles”. In: *Int. Journ. of Dam. Mech.* 11, pp. 129–149.

Tresca, H. (1864). “Memoir on the flow of solid bodies under strong pressure”. In: *Compt. ren. de l’acad. des sci.* 59, p. 754.

Trovalusci, P. et al. (2015). “Scale-dependent homogenization of random composites as micropolar continua”. In: *European Journal of Mechanics - A/Solids* 49, pp. 396–407. ISSN: 0997-7538. DOI: https://doi.org/10.1016/j.euromechsol.2014.08.010. URL: https://www.sciencedirect.com/science/article/pii/S0997753814001223.

Tvergaard, V. and A. Needleman (1995). “Effects of nonlocal damage in porous plastic solids”. In: *Int. Journ. of Sol. and Struct.*

Tvergaard, V. and A. Needleman (1998). “Dynamic crack growth in a nonlocal progressively cavitating solid”. In: *Eu. Journ. of Mech.*

Van Der Sluis, O., P.J.G. Schreurs, and H.E.H. Meijer (2001). “Homogenisation of structured elastoviscoplastic solids at finite strains”. In: *Mechanics of Materials* 33(9), pp. 499–522. ISSN: 0167-6636. DOI: https://doi.org/10.1016/S0167-6636(01)00066-7. URL: https://www.sciencedirect.com/science/article/pii/S0167663601000667.

Vanaerschot, A. et al. (2013). “Stochastic multi-scale modelling of textile composites based on internal geometry variability”. In: *Computers & Structures* 122. Computational Fluid and Solid Mechanics 2013, pp. 55–64. ISSN: 0045-7949. DOI: https://doi.org/10.1016/j.compstruc.2012.10.026. URL: https://www.sciencedirect.com/science/article/pii/S0045794912002647.

Vaughan, T.J. and C.T. McCarthy (2010). “A combined experimental-numerical approach for generating statistically equivalent fibre distributions for high strength laminated composite materials”. In: *Composites Science and Technology* 70(2), pp. 291–297. ISSN: 0266-3538. DOI: https://doi.org/10.1016/j.compscitech.2009.10.020. URL: https://www.sciencedirect.com/science/article/pii/S0266353809003832.

Verhoosel, C. V. et al. (2010). “Computational homogenization for adhesive and cohesive failure in quasi-brittle solids”. In: *International Journal for Numerical Methods in Engineering* 83(8-9), pp. 1155–1179. DOI: https://doi.org/10.1002/nme.2854. eprint: https://onlinelibrary.wiley.com/doi/pdf/10.1002/nme.2854. URL: https://onlinelibrary.wiley.com/doi/abs/10.1002/nme.2854.

Vernon, Lester B. and Harold M. Vernon (U.S. Patent , 1941). *Process of manufacturing articles of thermoplastic synthetic resins.*

Vogler, M., R. Rolfes, and P.P. Camanho (2013). “Modeling the inelastic deformation and fracture of polymer composites - Part I: Plasticity model”. In: *Mechanics of Materials* 59, pp. 50–64. ISSN: 0167-6636. DOI: `https://doi.org/10.1016/j.mechmat.2012.12.002`. URL: `https://www.sciencedirect.com/science/article/pii/S016766361200213X`.

Wieckowski, Z. (2000). “Dual finite element methods in homogenization for elasticplastic fibrous composite material”. In: *Int. J. Plasticity* 16, pp. 199–221.

Willis, J. R. (1977a). “Bounds on self-consistent estimates for the overall properties of anisotropic composites”. In: *Journ. of the Mech and Phys. of Sol.*

Willis, J. R. (1977b). “Upper and lower bounds for nonlinear composite behaviour”. In: *Mat. Sci. and Eng.*

Wilson, Vincent Herald et al. (2020). “A Development of Innovative Shape Memory Polymers and Their Nanocomposites to Resist the Load Aircraft High Lift Devices”. In: *International Journal of Advanced Research in Engineering and Technology* 11(9).

Wu, L., L. Adam, and L. Noels (2018). “A micromechanics-based inverse study for stochastic order reduction of elastic UD fiber reinforced composites analyses”. In: *International Journal for Numerical Methods in Engineering* 115(12), pp. 1430–1456. DOI: `https://doi.org/10.1002/nme.5903`. eprint: `https://onlinelibrary.wiley.com/doi/pdf/10.1002/nme.5903`. URL: `https://onlinelibrary.wiley.com/doi/abs/10.1002/nme.5903`.

Wu, L., L. Adam, and L. Noels (2021). “Micro-mechanics and data-driven based reduced order models for multi-scale analyses of woven composites”. In: *Composite Structures* 270, p. 114058. ISSN: 0263-8223. DOI: `https://doi.org/10.1016/j.compstruct.2021.114058`. URL: `https://www.sciencedirect.com/science/article/pii/S0263822321005183`.

Wu, L., I. Doghri, and L. Noels (2015). “An incremental-secant mean-field homogenization method with second statistical moments for elasto-plastic composite materials”. In: *Philosophical Magazine* 95, pp. 1–37.

Wu, L and L. Noels (2022). “Recurrent Neural Networks (RNNs) with dimensionality reduction and break down in computational mechanics; application to multi-scale localization step”. In: *Computer Methods in Applied Mechanics and Engineering* 390, p. 114476. ISSN: 0045-7825. DOI: `https://doi.org/10.1016/j.cma.2021.114476`. URL: `https://www.sciencedirect.com/science/article/pii/S0045782521006940`.

Wu, L. et al. (2012). “A multiscale mean-field homogenization method for fiber-reinforced composites with gradient-enhanced damage models”. In: *Comp. Meth. in Appl. Mech. and Eng.* 233-236, pp. 164–179.

Wu, L. et al. (2013a). “A combined incremental-secant mean-field homogenization scheme with per-phase residual strains for elasto-plastic composites”. In: *International Journal of Plasticity* 51, pp. 80–102. ISSN: 0749-6419. DOI: `https://doi.org/10.1016/j.ijplas.2013.06.006`. URL: `https://www.sciencedirect.com/science/article/pii/S0749641913001174`.

Wu, L. et al. (2013b). “A micro-meso-model of intra-laminar fracture in fiber-reinforced composites based on a discontinuous Galerkin/cohesive zone method”. In: *Engineering Fracture Mechanics* 104, pp. 162–183. ISSN: 0013-7944. DOI: `https://doi.org/10.1016/j.engfracmech.2013.03.018`. URL: `https://www.sciencedirect.com/science/article/pii/S0013794413001252`.

Wu, L. et al. (2013c). “An implicit-gradient-enhanced incremental-secant mean-field homogenization scheme for elasto-plastic composites with damage”. In: *International Journal of Solids and Structures* 50(24), pp. 3843–3860. ISSN: 0020-7683. DOI: `https://doi.org/10.1016/j.ijsolstr.2013.07.022`. URL: `https://www.sciencedirect.com/science/article/pii/S0020768313003028`.

Wu, L. et al. (2015). “A study of composite laminates failure using an anisotropic gradient-enhanced damage mean-field homogenization model”. In: *Composite Structures* 126, pp. 246–264. ISSN: 0263-8223. DOI: `https://doi.org/10.1016/j.compstruct.2015.02.070`. URL: `https://www.sciencedirect.com/science/article/pii/S0263822315001580`.

Wu, L. et al. (2017). “An incremental-secant mean-field homogenization method with second statistical moments for elasto-visco-plastic composite materials”. In: *Mechanics of Materials* 114, pp. 180–200. ISSN: 0167-6636. DOI: https://doi.org/10.1016/j.mechmat.2017.08.006. URL: https://www.sciencedirect.com/science/article/pii/S0167663617300698.

Wu, L. et al. (2018). “From SEM images to elastic responses: A stochastic multiscale analysis of UD fiber reinforced composites”. In: *Composite Structures* 189, pp. 206 –227. ISSN: 0263-8223. DOI: https://doi.org/10.1016/j.compstruct.2018.01.051. URL: http://www.sciencedirect.com/science/article/pii/S0263822317327770.

Wu, L. et al. (2019). “An inverse micro-mechanical analysis toward the stochastic homogenization of nonlinear random composites”. In: *Computer Methods in Applied Mechanics and Engineering* 348, pp. 97–138. ISSN: 0045-7825. DOI: https://doi.org/10.1016/j.cma.2019.01.016. URL: https://www.sciencedirect.com/science/article/pii/S0045782519300210.

Wu, L. et al. (2020a). “A recurrent neural network-accelerated multi-scale model for elasto-plastic heterogeneous materials subjected to random cyclic and non-proportional loading paths”. In: *Computer Methods in Applied Mechanics and Engineering* 369, p. 113234. ISSN: 0045-7825. DOI: https://doi.org/10.1016/j.cma.2020.113234. URL: https://www.sciencedirect.com/science/article/pii/S0045782520304199.

Wu, L. et al. (2021). “Per-phase spatial correlated damage models of UD fibre reinforced composites using mean-field homogenisation; applications to notched laminate failure and yarn failure of plain woven composites”. In: *Computers and Structures* 257, p. 106650. ISSN: 0045-7949. DOI: https://doi.org/10.1016/j.compstruc.2021.106650. URL: https://www.sciencedirect.com/science/article/pii/S0045794921001723.

Wu, Ling et al. (2020b). “Bayesian inference of non-linear multiscale model parameters accelerated by a Deep Neural Network”. In: *Computer Methods in Applied Mechanics and Engineering* 360, p. 112693. DOI: 10.1016/j.cma.2019.112693.

Yang H.and Guo, X., S. Tang, and W. K. Liu (2019). “Derivation of heterogeneous material laws via data-driven principal component expansions”. In: *Computational Mechanics* 64(2), pp. 365–379.

Yvonnet, J. and Q.-C. He (2007). “The reduced model multiscale method (R3M) for the non-linear homogenization of hyperelastic media at finite strains”. In: *Journal of Computational Physics* 223(1), pp. 341–368. ISSN: 0021-9991. DOI: https://doi.org/10.1016/j.jcp.2006.09.019. URL: https://www.sciencedirect.com/science/article/pii/S0021999106004402.

Yvonnet, J., E. Monteiro, and Q.-C. He (2013). “Computational homogenization method and reduced database model for hyperelastic heterogeneous structures”. In: *International Journal for Multiscale Computational Engineering* 11(3), pp. 201–225. ISSN: 1543-1649.

Zahr, M.J., P. Avery, and C. Farhat (2017). “A multilevel projection-based model order reduction framework for nonlinear dynamic multiscale problems in structural and solid mechanics”. In: *International Journal for Numerical Methods in Engineering* 112(8), pp. 855–881. DOI: https://doi.org/10.1002/nme.5535. eprint: https://onlinelibrary.wiley.com/doi/pdf/10.1002/nme.5535. URL: https://onlinelibrary.wiley.com/doi/abs/10.1002/nme.5535.

Zaïri, F., K. Woznica, and M. Naït-Abdelaziz (2005). “Phenomenological nonlinear modelling of glassy polymers”. In: *Compt. Ren. Mec.* 333, pp. 359–364.

Zairi, F. et al. (2008). “Modelling of the elasto-viscoplastic damage behaviour of glassy polymers”. In: *International Journal of Plasticity* 24(6), pp. 945–965. ISSN: 0749-6419. DOI: https://doi.org/10.1016/j.ijplas.2007.08.001. URL: https://www.sciencedirect.com/science/article/pii/S074964190700112X.

Zaoui, A. and R. Masson (2000). “Micromechanics based modelling of plastic polycrystals: An affine formulation”. In: *Proc. of the Roy. Soc. of London. A. Math. and Phys. Sci.*

Zbib, H.M. and E.C. Aifantis (1989). “A gradient-dependent flow theory of plasticity: Application to metal and soil instabilities”. In: *Appl. Mech. Rev.-T* 42, S295–S304.

Zende, R., V. Ghase, and Vandana Jamdar (2023). "A review on shape memory polymers". In: *Polymer-Plastics Technology and Materials* 62(4), pp. 467–485. DOI: `10.1080/25740881.2022.2121216`. eprint: `https://doi.org/10.1080/25740881.2022.2121216`. URL: `https://doi.org/10.1080/25740881.2022.2121216`.

Zhang, C. and I. D. Moore (1997). "Nonlinear mechanical response of high density polyethylene. Part II: Uniaxial constitutive modeling". In: *Polymer Engineering & Science* 37(2), pp. 414–420. DOI: `https://doi.org/10.1002/pen.11684`. eprint: `https://4spepublications.onlinelibrary.wiley.com/doi/pdf/10.1002/pen.11684`. URL: `https://4spepublications.onlinelibrary.wiley.com/doi/abs/10.1002/pen.11684`.

Zhang, Y.-Y. et al. (2022). "Experimental and theoretical investigations of the viscoelastic behaviour of short carbon fiber reinforced polyetherimide composites". In: *Composite Structures* 298, p. 116016. ISSN: 0263-8223. DOI: `https://doi.org/10.1016/j.compstruct.2022.116016`. URL: `https://www.sciencedirect.com/science/article/pii/S026382232200767X`.

Zhao, LY. et al. (2019). "Homogenization of rock-like materials with plastic matrix based on an incremental variational principle". In: *International Journal of Plasticity* 123, pp. 145–164.

Zhao, W. et al. (2021). "A viscoelastic-viscoplastic constitutive model for glassy polymers informed by molecular dynamics simulations". In: *International Journal of Solids and Structures* 226-227, p. 111071. ISSN: 0020-7683. DOI: `https://doi.org/10.1016/j.ijsolstr.2021.111071`. URL: `https://www.sciencedirect.com/science/article/pii/S002076832100161X`.